

INTERNATIONAL PHYSICAL SCIENCE CONFERENCE

FEDERAL UNIVERSITY DUTSIN-MA

BOOK OF PROCEEDINGS

Theme: Panacea To Global Energy Crises

The Role Of Innovative Science And Technology

4th-8th August, 2025

IPSCFUDINA 2025



Foreword

It is with great pleasure and a deep sense of responsibility that I welcome you to the 2nd International Physical Sciences Conference, proudly hosted by Faculty of Physical Sciences, Federal University Dutsin-Ma titled: *Panacea for Global Energy Crises: The Role of Innovative Science and Technology.* This gathering serves as a crucial nexus for brilliant minds from across the globe, uniting scientists, researchers, academics, and students who are passionately dedicated to unraveling the mysteries and harnessing the power of the physical world. In an era defined by rapid technological advancements and complex global challenges, the role of physical sciences has never been more critical. This conference provides an unparalleled platform for the exchange of ground-breaking ideas, the dissemination of cutting-edge research, and the fostering of collaborations that will undoubtedly shape the future of scientific discovery.

On behalf of the Local Organizing Committee, I extend a warm and heartfelt welcome to all participants. Whether you are a seasoned scientist, an emerging researcher, or an enthusiastic student, your presence enriches this intellectual tapestry. We are particularly honoured to host distinguished guests and keynote speakers whose profound insights and pioneering work have significantly advanced various fields within the physical sciences. Your contributions to this conference will undoubtedly inspire new perspectives and ignite further inquiry. We trust that your time here will be both intellectually stimulating and personally rewarding, fostering new connections and strengthening existing ones within our vibrant scientific community.

This conference has been meticulously designed with several key objectives in mind. Our primary aim is to promote robust collaboration among diverse scientific disciplines, recognizing that many of the most profound breakthroughs occur at the intersections of different fields. We seek to provide a dynamic forum for sharing the latest research findings, encouraging open dialogue, and critically evaluating new methodologies. Furthermore, a core goal is to foster innovative ideas that can translate theoretical knowledge into practical applications, addressing real-world challenges. The interdisciplinary nature of the discussions planned, encompassing areas such as physics, chemistry, astronomy, materials science, and environmental science, is intended to spark cross-pollination of thoughts and methodologies, leading to novel solutions and deeper understandings.

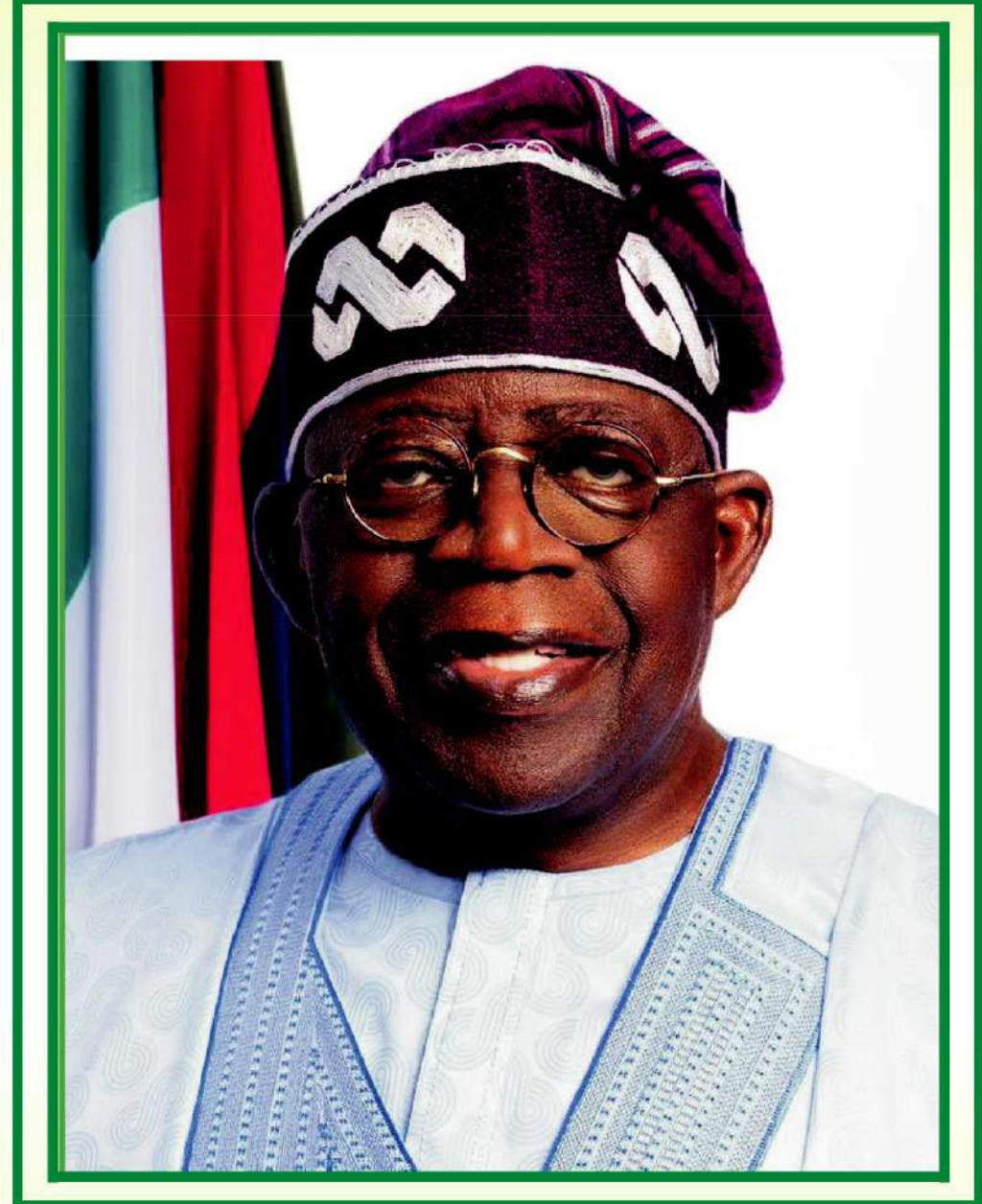
Holding this significant conference at Federal University Dutsin-Ma is particularly relevant. Our university is committed to fostering academic excellence and contributing to the advancement of knowledge, especially within the physical sciences. We believe that by hosting such an international event, we not only showcase the vibrant research environment within our institution but also contribute significantly to advancing physical sciences in the region and beyond. This gathering provides an invaluable opportunity for local researchers and students to engage with global experts, thereby enriching their perspectives and stimulating further research and innovation within Nigeria and West Africa.

This conference would not have been possible without the tireless dedication and unwavering commitment of numerous individuals and organizations. I extend my deepest gratitude, the Vice Chancellor of the University, Invited guests, and to the members of the Local Organizing Committee, whose meticulous planning and hard work have brought this event to fruition. Our sincere appreciation also goes to our generous sponsors and supporting institutions, whose invaluable contributions have provided the necessary resources to make this conference a reality. Finally, to the countless volunteers and contributors, your selfless efforts and enthusiasm have been instrumental in ensuring the smooth execution of every aspect of this event. Thank you all for your indispensable support.

As we embark on the exciting journey of this conference, I encourage each of you to participate actively, engage in spirited discussions, and seize every opportunity for collaboration. May this conference serve as a catalyst for new ideas, inspire ground breaking research, and forge lasting partnerships that transcend geographical boundaries. It is our sincere hope that the insights gained and the connections made here will contribute significantly to the advancement of physical sciences globally, leading to innovations that benefit humanity. We look forward to a productive and inspiring conference.

Prof. Oluwole J. Okunola Chairman, Local Organizing Committee IPSCFUDMA, 2025





His Excellency

Bola Ahmed Tinubu GCFR

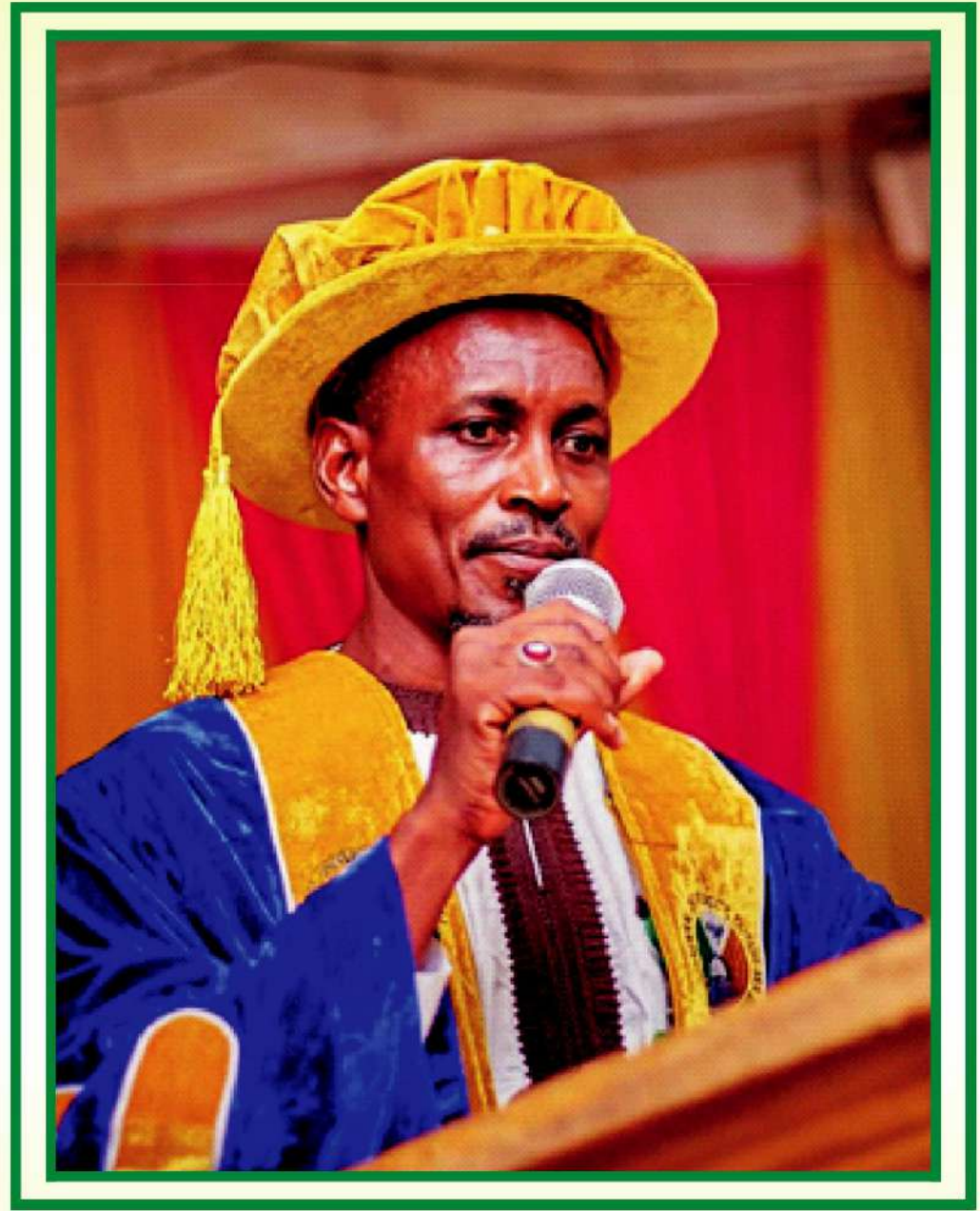
President, Commander-in-chief of the Armed Forces Federal Republic of Nigeria





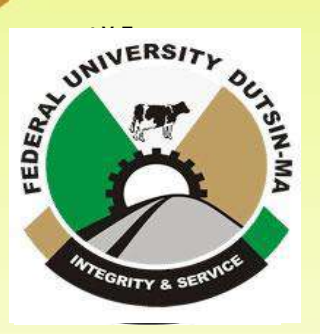
His Excellency
Dikko Umar Radda
Executive Governor, Katsina State.





Prof. Aminu Ado

Ag. Vice-Chancellor, Federal University Dutsin-Ma, Katsina State

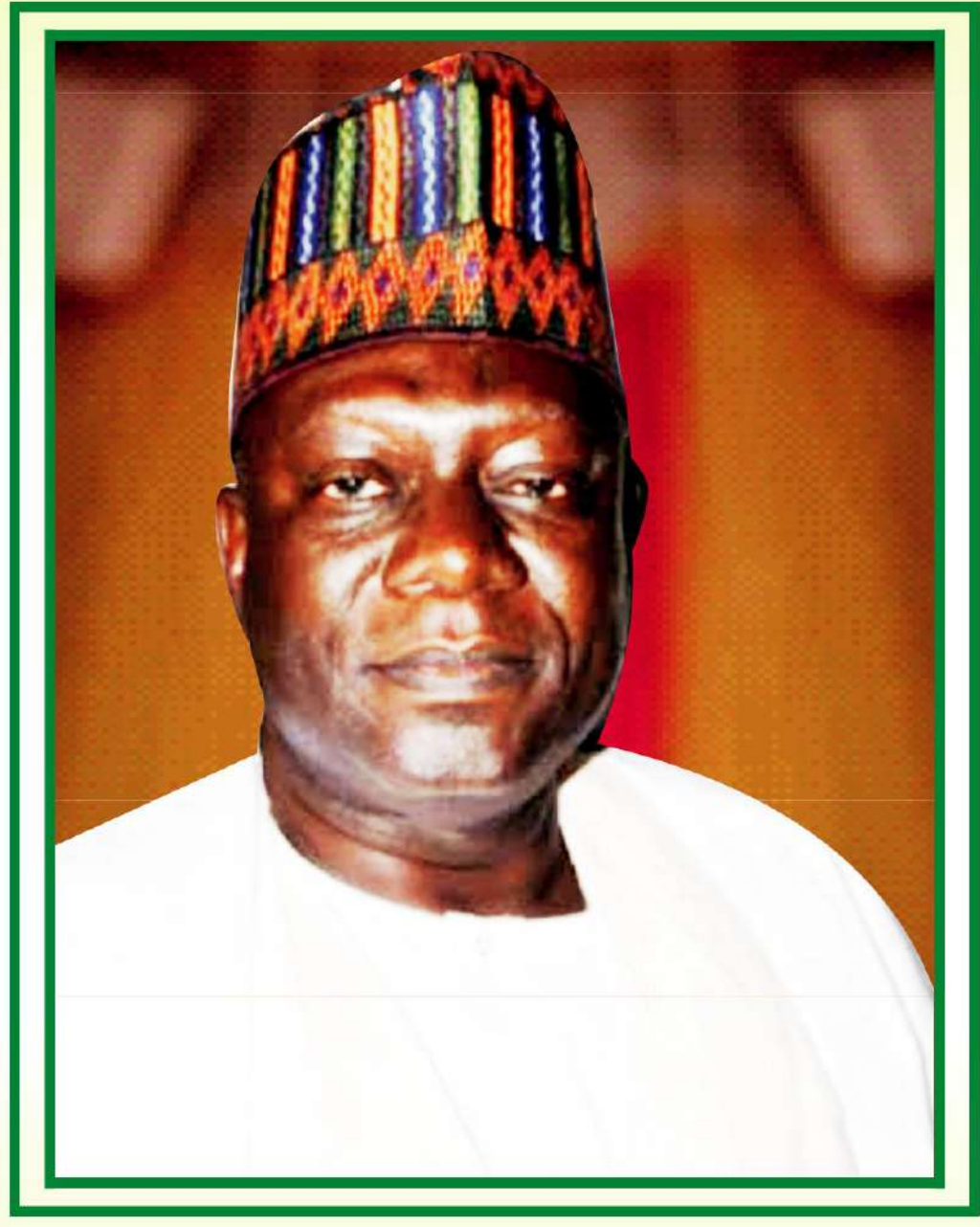




Professor Elizabeth Yecho

Deputy Vice-Chancellor (Administrative)
Federal University Dutsin-Ma, Katsina State

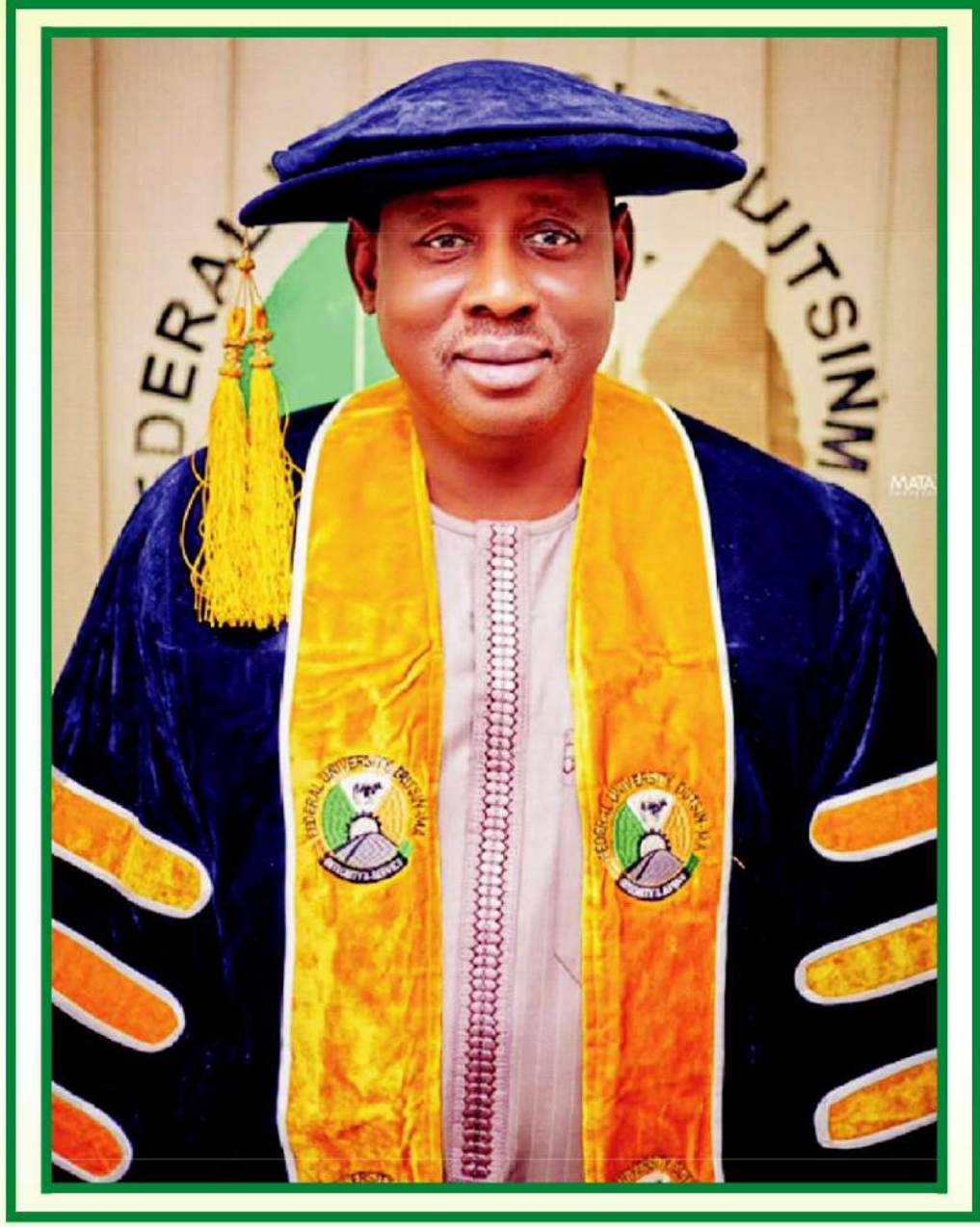




Dr. Musa Ajiya Registrar

Federal University Dutsin-Ma, Katsina State



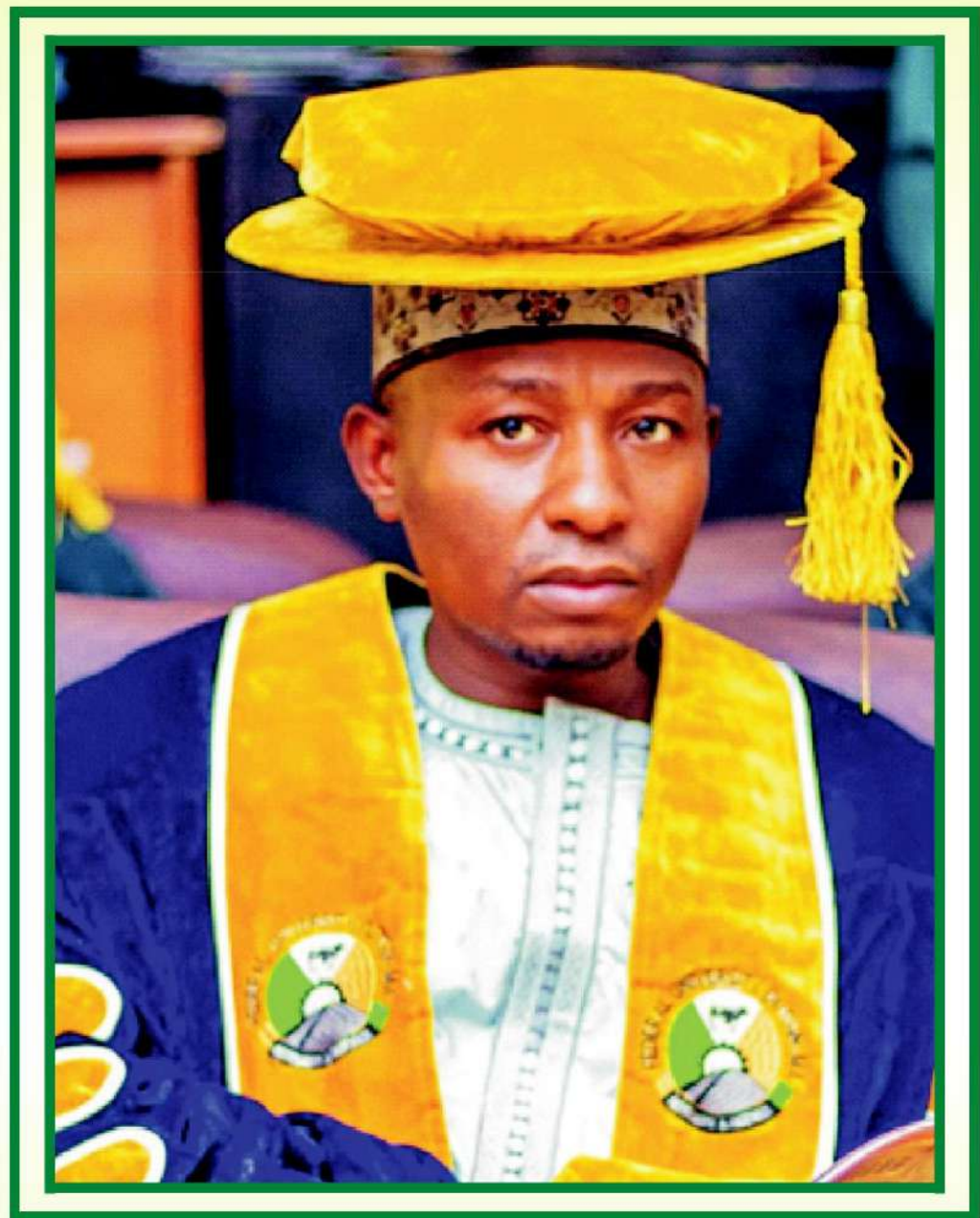


Mr. Abubakar M. Gafai

Bursar

Federal University Dutsin-Ma, Katsina State

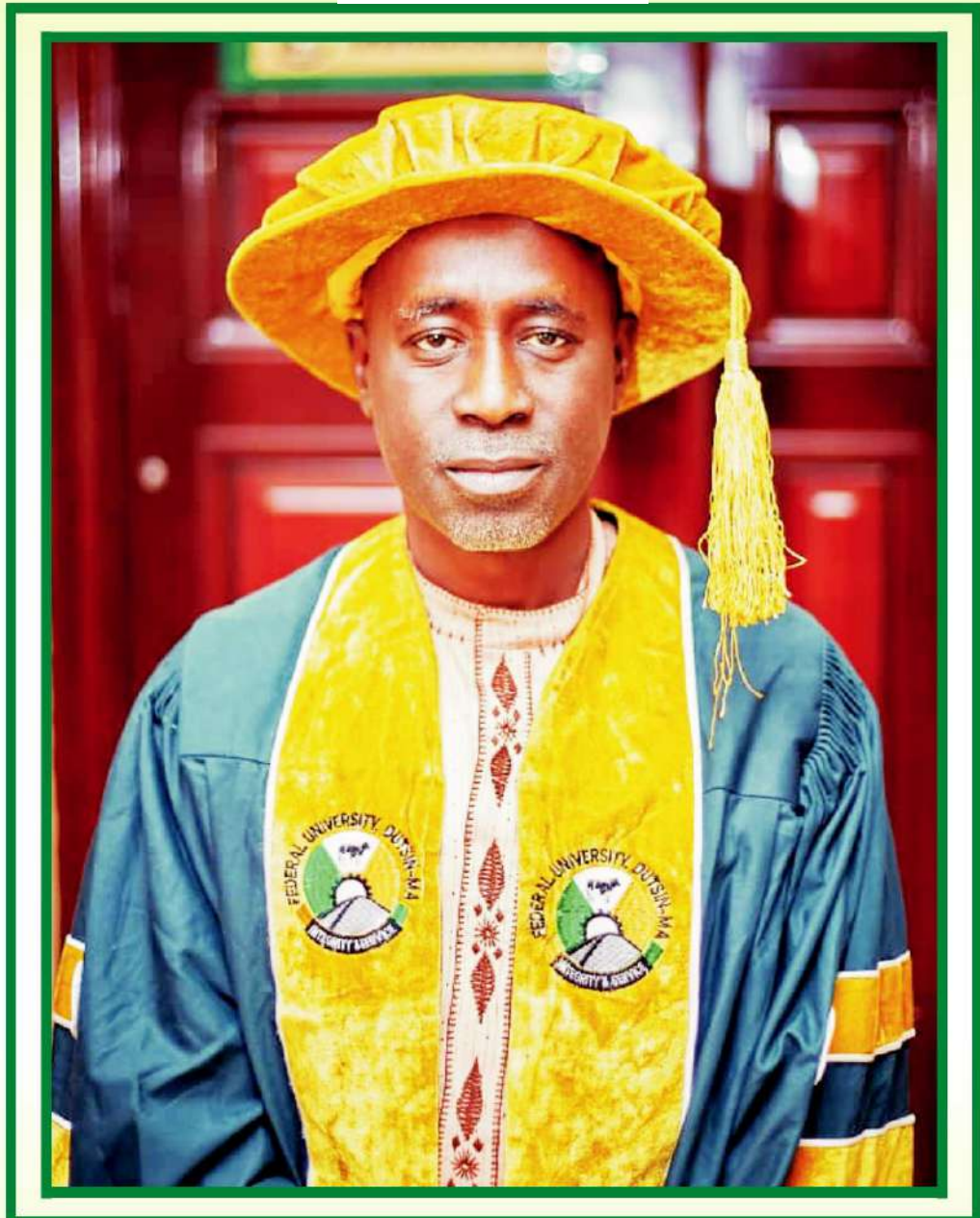




Dr. Ukasha Hamza Musa

University Librarian
Federal University Dutsin-Ma, Katsina State



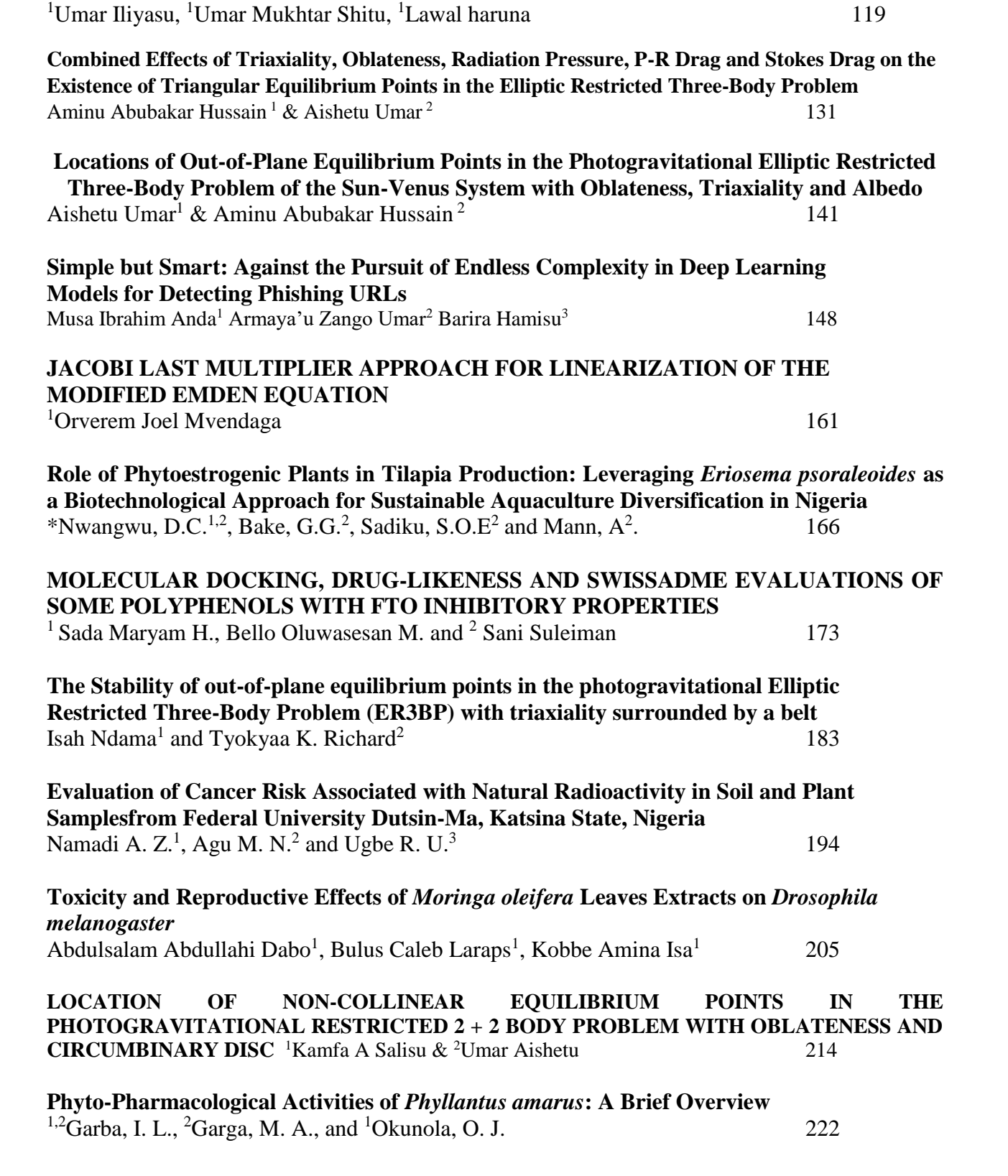


Dr. Yusuf Bello
Dean, Faculty of Physical Sciences
Federal University Dutsin-Ma, Katsina State



Table of Content

Effect of Different Dietary Inclusion Level of Raw <i>Momordica charantia</i> (Bitter Melo Meal on Carcass Proximate, Mineral and Histology of <i>Coptodon guineensis Fingerlin</i>	
Abdullahi, M.M*1 Bake G.G2 Ndamitso M. M3, and Sadiku S.O.E2.	13
EXTRACTION OF ALUMINA FROM KANKARA KAOLIN Kamaluddeen Suleiman Kabo ¹ , Mustapha Isah ²	22
PHYTOCHEMICAL SCREENING AND ANTIMICROBIAL ACTIVITY OF SECOMETABOLITES FROM XERODERRIS STUHLMANNII STEM BARK''	ONDARY
Kabir, U. M. *1, Ali T.1, Ogbesejana Abiodun B1, Kabir, S.2	27
A SOFTWARE ENGINEERING APPROACH TO THE DESIGN AND IMPLEMENTATION ADDITIONAL FREELANCE MARKETPLACE SYSTEM	ON OF
Barira Hamisu ^{1*} , Raji Abdullahi Egigogo ¹ , Mubarak Yusuf Ibrahim ¹ and Zayyanu Yunusa ²	36
Monthly Artificial Neural Network (ANN) Models to Estimate OMI-Derived Absorb Aerosol Index (OMI-AI) Using Ground Meteorology in North-Central Nigeria	oing
Mukhtar Abubakar Balarabe ^{1&2}	49
Development of General and Season-Specific Multiple Linear Regression (MLR) Models for Estimating TOMS-Derived Absorbing Aerosol Index (TOMS-AI) in North-Central Nigeria	r
Mukhtar Abubakar Balarabe (Ph.D)	55
SPATIAL VARIATION OF FM RADIO SIGNAL IN A SUB-URBAN SAHEL ENVIRONM A Case study of Radio Nigeria Companion FM (104.5 MHz) katsina	MENT:
Akinsanmi Akinbolati ¹ , *Muftahu Suleiman ² , Hauwau Yusuf ¹ and Hassan Yazid Gonah ²	61
Design and Testing of four phase Transmission Lines from generator ¹ Ahuome B.A., ¹ Israel Adekeye, ¹ Tijani A. Sadiq	73
WHEAT-HIGH QUALITY CASSAVA FLOUR BREAD SPICED WITH CLOVE POWDE ¹ Adetoro O.F*, ² Kajihausa O.E, ² Sobukola O.P. and ³ Afolabi W. A. O.	E R 80
ASSESSMENT OF TRACE AND SELECTED HEAVY ELEMENTS PRESENCE I SPINACH LEAVE (SPINACIA OLERACEA) SOLD IN DUTSIN-MA, MARKET	I N
¹ SHEHU, A. and ¹ IBRAHIM, S. B	91
DRIVING COMPUTER INNOVATIVE SKILL IN THE TEACHING OF COMPROGRAMMING CONCEPT: TRANSFORMING COMPUTER SCIENCE EDUC	
Pauline Ebere NDUKWE ¹ , Rogers Nwunuji IBEN ¹ & Eva Onyinye ONYEKA ¹	96
Advanced Explainable Context-Aware Article Recommendation Using Large Language Models and SHAP	
	05



Automated Classification of Blood Cell Cancers Using EfficientNetB3 Model



Effect of Different Dietary Inclusion Level of Raw *Momordica charantia* (Bitter Melon) Seed Meal on Carcass Proximate, Mineral and Histology of *Coptodon guineensis Fingerlings*.

Abdullahi, M.M*1 Bake G.G2 Ndamitso M. M3, and Sadiku S.O.E2.

- 1. Nigerian Institute for Oceanography and Marine Research, Victoria Island, Lagos. P.M.B. 12729, Lagos State, Nigeria.
- 2. Department of Water Resources, Aquaculture and Fisheries Technology, School of Agriculture and Agricultural Technology, Federal University of Technology, Minna, P.M.B 65 Minna, Niger State, Nigeria.
- 3. Department of Chemistry, School of Physical Sciences, Federal University of Technology, Minna, P.M.B 65 Minna, Niger State, Nigeria. Corresponding Author's email mansurumar1@gmail.com

Abstract

This study investigated the effects of raw *Momordica charantia* seed meal (MCSM) on the carcass proximate, mineral and histology of *Coptodon guineensis* fingerlings fed diet of different inclusion level. The experimental diet were incorporated into is nitrogenous diets (35% crude protein) at varying inclusion levels (D1 0%, D2 10%, D3 20%, D4 30%, and D5 40%), and fed to the fish for 84 days. The research was conducted at the Old Teaching and Research Farm of the Department of Water Resources, Aquaculture and Fisheries Technology, Bosso Campus, Federal University of Technology, Minna, Niger State, Nigeria. Hapas of 0.5 x 0.5 x 1 m³ size were deployed in concrete tanks for the rearing of C. guineensis fingerlings. At end of the culture period, samples were randomly collected for proximate and mineral determination and the gonads were collected from five treatment for histological examination. The gonad was fixed in 10 % formalin, thereafter standard method was used for slide preparation and examine under microscope (Olympus QC pass-02 model). Results showed that the carcass proximate and mineral compositions were significantly affected by MCSM inclusion, with higher crude protein levels observed in all the treatment. Lipid recorded the highest (16.79±0.33) in D2, moisture content, ash content and crude fibre recorded significant different among the treatment means respectively. Mineral content for carcass shows there were no significant differences between the treatment means in terms of potassium and phosphorus content. The fish fed D4 recorded the highest value in calcium content. Histological examination of gonads indicated that higher inclusion levels of raw MCSM caused testicular abnormalities such as sertoli cells and germ cells that produce the primary and secondary spermatocytes that lead spermatozoa, suggesting a dose-dependent anti-fertility effect.

Keyword: Momordica charantia, Carcass, proximate Histology, Coptodon guineensis

INTRODUCTION

Coptodon guineensis, commonly referred to as the Guinean tilapia, is a fish species belonging to the family Cichlidae and is indigenous to West Africa (Dienye et al., 2024). This species predominantly inhabits brackish and freshwater environments, including estuaries, lagoons and rivers (Lamboj, 2004 and Ukenye et al 2019). Coptodon guineensis serves as a vital food source for local communities and presents significant aquaculture potential due to its adaptability and rapid growth rate. The family Cichlidae, known as cichlids, comprises a diverse group of freshwater fish characterized by remarkable ecological adaptability, a range of behavioural



patterns, and notable evolutionary traits. With over 2,000 recognized species, cichlids are distributed across multiple continents, including Africa, Central and South America, and parts of Asia (Magalhaes and Ford, 2022). Coptodon guineensis exhibits a laterally compressed body with a dark coloration that may vary according to environmental conditions (Lamboj, 2004). Adult individuals of this species, commonly known as the Guinean tilapia, typically reach an average length of 15 to 20 centimetres. Spawning behaviours of C. guineensis are typical substrate spawner, display firm bonding during courtship with prolonged association with the pair stabling and defending a territory and they build spawning nests within the established territory (Abdullahi et al., 2018). C. guineensis have attracted global attention due to their desirable qualities which makes them an ideal candidate for aquaculture (Probu et al., 2019). These attributes include, the ability to readily reproduce in captivity and short generation time, fast growth, reaching consumable size (in about six months), tolerate a wide range of environmental conditions (Prabu et al., 2019), resistance to stress and disease, feeding on low trophic level with versatile food habitats, acceptance of artificial feed immediately after yolk-sac absorption, adapt to a variety of culture systems, and are considered palatable, marketable and nutritious products (Ghosal and Chakraborty, 2014).

Momordica charantia (bitter melon) is an extremely bitter vegetable and is a tropical and subtropical vine of the family Cucurbitaceous widely grown in Nigeria, south Asia, China and the Caribbean (Tan et al., 2016). Bitter melon as fondly called has been implicated experimentally to achieve a positive sugar regulatory effect by suppressing the neural response to sweet taste stimuli and also keeping the body functions operating normally (Bakare et al., 2010; Jimah et al., 2021). Other use of the plant includes expelling intestinal gas, for tumours, wound treatment, rheumatism, malaria, vaginal discharge and the seeds are used to induce abortion (Sofowara, 2006). In Nigeria, Ghana and India peninsula, the root and the seed of the plant are used as an abortifacient together with the fruit as well as an ingredient in aphrodisiac preparation (Sofowara, 2006). The young fruits and shoots are reported to serve as supplementary or emergency food in some parts of West Africa and as an effective emmenagogue to facilitate childbirth (Gayathry and John, 2022). All plant species contain poisonous, medicinal and nutritional compounds. Many of these traditional plants are used with no attention paid to their nutritional values (Dar et al., 2017).

Despite the widely reported production and progress of tilapia species in worldwide aquaculture, the main drawback of all the existing commercial strains is their precocious maturation in tropical and sub-tropical climatic conditions (Samaddar, 2022) which leads to prolific breeding and overcrowding in grow-out systems, resulting in undesirable stunting and low yields of harvestable and acceptable market size fishes (Xu *et al.*, 2015). On this note, this study evaluate the effect of Raw *M. charantia* seed meal diet on carcass proximate, mineral and histology of *Coptodon guineensis* fingerling.

MATERIALS AND METHOD

Experimental Site

The study was conducted at the fish farm (Old Teaching and Research Farm) of the Department of Water Resources, Aquaculture and Fisheries Technology (WAFT), Federal University of Technology (FUT) Minna, Bosso Campus, Niger State, Nigeria. Minna is located at latitude 9° 40' N and longitude 6° 30' E in the Southern Guinea Savannah region of Nigeria (Uzoma *et al.*, 2016)).

Collection and Processing of Momordica charantia Seeds (MCS)

Momordica charantia (bitter melon) seeds were gotten from Borgu Local Government Area of Niger State, Nigeria, between May and December. The seeds were collected by harvesting the ripe



fruits, gathered in one place and allowed to ferment for three days to facilitate pulp decomposition and seed removal. The seeds were then manually collected, washed and sun-dried as reported by Osunde and Kwaya (2012).

Experimental Diets Formulation

Five iso-nitrogenous (35 % crude protein) diets were formulated (Table 1) for fingerlings of *Coptodon guineensis* using linear programming (Microsoft Excel) with varying inclusion levels of raw *Momordica charantia* seed meal (RMCSM) and designated as D1 (0 %: inclusion), D2 (10 % inclusion), D3 (20 % inclusion), D4 (30 % inclusion) and D5 (40 % inclusion).

Table 1:Gross Compositions of the Experimental Diets for *Coptodon guineensis* **Fingerlings Fed Inclusion Levels of Raw** *Momordica charantia* **Seed Meal**

Diets Codes/ Ingredients	D1-0%	D2-10%	D3-20%	D4-30%	D5-40%
RMCSM	0.00	10.00	20.00	30.00	40.00
Yellow Maize	7.00	7.00	7.00	7.00	7.00
Fishmeal	25.00	25.00	25.00	25.00	25.00
Soybean meal	41.60	36.60	31.63	26.63	21.64
Dextrinized starch	0.22	0.22	0.22	0.22	0.22
Vegetable oil	4.33	3.42	2.51	1.61	0.70
Vitamin premix	2.50	2.50	2.50	2.50	2.50
Mineral premix	2.50	2.50	2.50	2.50	2.50
Cellulose	16.85	12.76	8.64	4.54	0.44
Total	100.00	100.00	100.00	100.00	100.00
Kcal / 100 g (dry)	280.43	280.35	280.38	280.39	280.35

Biochemical analysis

The fish samples (carcass) were subjected to chemical analysis. Proximate composition analyses was determined according to AOAC procedures (2005). Moisture content was determined by drying samples at $105\pm2^{\circ}$ C until a constant weight was obtained. Dried samples were used for determination of crude fat, protein and Ash contents. Crude fat was measured by solvent extraction method in a soxhlet system where n-hexane was used as solvent. Crude protein content was calculated by using nitrogen content obtained by Kjeldahl method. According to AOAC (2005). Mineral analysis for the fish samples (Carcass) were first brought into solution using metal ash.



The solution containing the elements (sodium, potassium, and calcium) was sprayed into a flame photometer, which measured the intensity of light produced by electronic transitions to higher energy levels. The intensity of radiation was measured and the metal concentration was quantitatively determined. Other elements were determined using atomic absorption spectrometry.

Histological Analysis

At the end of the experiment, fish samples were collected separately from each treatment group. The gonads were then carefully dissected from each fish to avoid tissue damage. Immediately after removal, the gonads were fixed in 10 % formalin, as described by Jegede and Fagbenro (2008). Standard methods were used for slide preparation and section staining (Dick, 2010). The gonadal tissues (testis and ovary) were preserved in formalin-alcohol solution, embedded in paraffin wax, sectioned at 5 μ m thickness, deparaffinised, stained with haematoxylin, and counterstained with eosin. The prepared slides were examined (M×400) under a light microscope (Olympus QC Pass-02: Model).

Data Analysis

The collected data were subjected to one-way analysis of variance (ANOVA) using Statistical Package for the Social Sciences (SPSS) version (11.0). Duncan's Multiple Range Test (DMRT) to explore differences among treatment means. Statistical significance was set at a 5 % level of probability (p<0.05).

RESULTS AND DISCUSSION

The results of Proximate and Mineral Compositions and histology of *Coptodon guineensis* Fingerlings Fed Inclusion Levels of Raw *Momordica charantia* Seed Meal is shown in table 2 while plate I to V shows the histological tissue of C. guineensis gonads collected at end of the experiment.



Table 2 Carcass (Dried basis) Proximate and Mineral Compositions of *Coptodon guineensis* Fingerlings Fed Inclusion Levels of Raw *Momordica charantia* Seed Meal for 84 Days

Treatments/ Parameters		D1-0%	D2-10%	D3-20%	D4-30%	D5-40%
T di difficters			Proximate Co	ompositions (%)		
Crude protein	34.19±0.30	42.89±2.29 ^a	43.32±2.37 ^a	46.34±2.34 ^a	45.68±1.27 ^a	47.44±2.02 ^a
Lipid	12.38±0.77	15.80 ± 0.88^{ab}	16.79 ± 0.33^{a}	12.82 ± 0.11^{bc}	14.08 ± 1.19^{abc}	13.91 ± 1.46^{abc}
Moisture content	8.86±0.31	8.97±0.40 ^a	8.69±0.18 ^a	6.95±0.49 ^b	7.54 ± 0.74^{ab}	7.73 ± 0.08^{ab}
Ash content	11.88±0.73	13.06 ± 0.52^{a}	13.23 ± 0.68^a	11.29 ± 1.22^{ab}	9.49 ± 0.58^{b}	11.88 ± 0.60^{ab}
Crude fibre	3.27±0.17	3.54 ± 0.12^{a}	3.58 ± 0.16^{a}	3.13 ± 0.29^{ab}	2.70 ± 0.14^{b}	3.27 ± 0.14^{ab}
Nitrogen free extract	29.42±1.13	15.74±1.67 ^a	14.38±3.55 ^a	19.47±1.03 ^a	20.50±1.30 ^a	15.77±3.66 ^a
		Ŋ	Mineral Compo	ositions (mg/100 g	g)	
Sodium	29.51±4.26	51.30±4.61 ^a	51.30 ± 3.72^{a}	39.70 ± 4.05^{ab}	43.92 ± 0.70^a	49.89±3.91 ^a
Potassium	97.23±6.86	119.85±11.96 ^{ab}	146.48±3.05 ^a	124.40 ± 14.38^{ab}	135.96±9.45 ^a	131.76±4.13 ^a
Phosphorus	15.74±3.04	16.77±3.47 ^a	10.95 ± 0.34^{a}	12.32±1.19 ^a	15.05±2.98 ^a	17.87 ± 6.50^{a}
Calcium	57.36±0.76	31.70 ± 4.58^{b}	36.23 ± 1.13^{b}	42.26 ± 7.20^{b}	65.41 ± 4.43^{a}	35.85 ± 1.36^{b}
Magnesium	23.94±0.39	32.97 ± 4.24^{ab}	48.27±5.81 ^a	40.03 ± 8.27^{a}	42.78 ± 3.35^{a}	39.71 ± 0.46^{a}

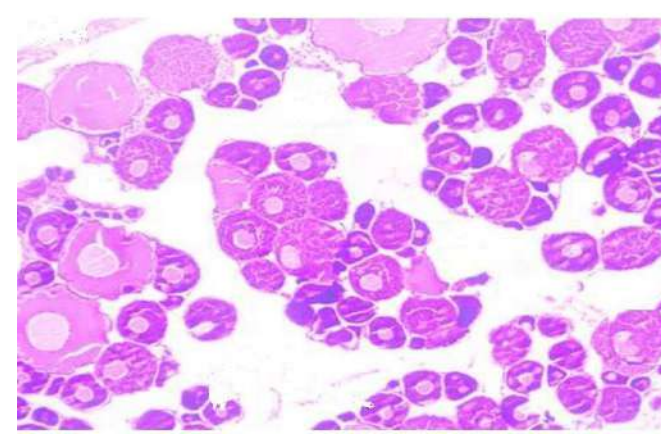


Plate I: Histologic Section of Tissue *C. guineensis* Ovary Showing Normal Oocytes With visible mature follicle cells at 0% Inclusions RMCSM (H&E \times 100)

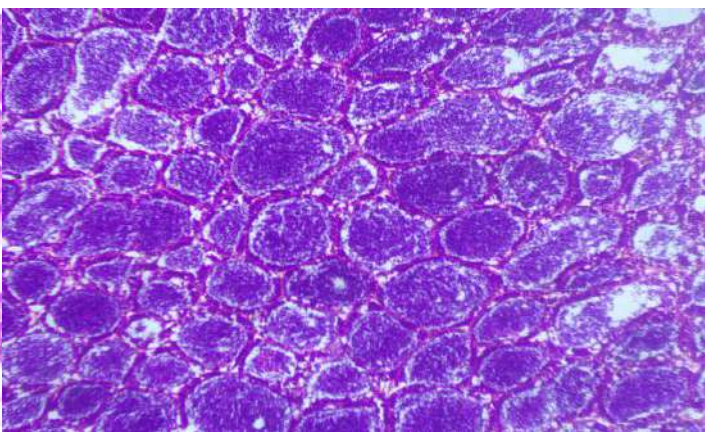


Plate I:Histologic Section of Tissue C. Guineensis Testis Showing Abnormal Seminiferous tubules and white necrosis at 30 % Inclusions of RMCSM (H&E \times 100)



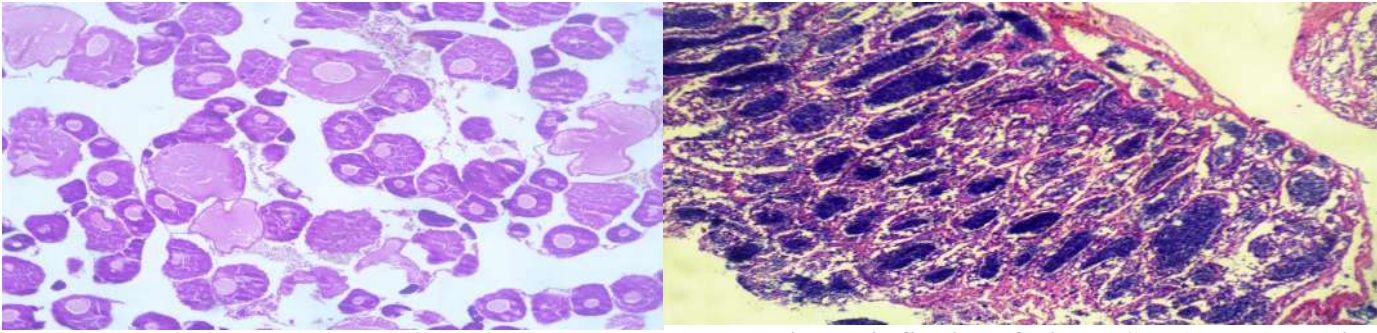


Plate II: Histologic Section of Tissue $\it C.~guine ensis$ Ovary Showing Normal Oocytes with visible mature follicle cells at 10 % Inclusions RMCSM (H&E \times 100)

Plate III Histologic Section of Tissue C. guineensis Testis Showing Abnormal reduced seminiferous tubules at 40 % Inclusions of RMCSM (H&E \times 100)

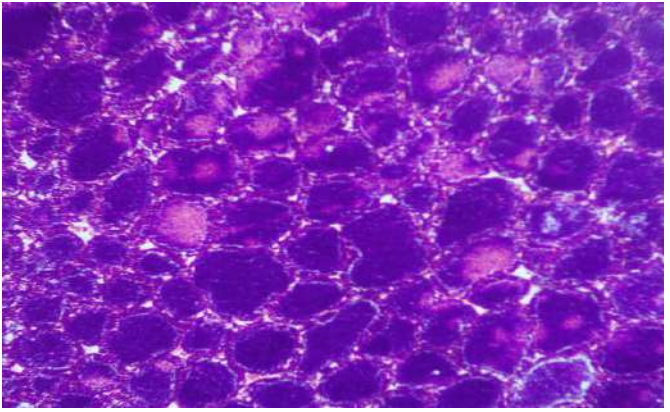


Plate III: Histologic Section of Tissue *C. guineensis* Testis Showing Partially disintegrated Seminiferous Tubules At 20 % Inclusions of RMCSM (H&E × 100)

The proximate compositions vary across the treatment means. This finding corroborates the report of Mundida et al. (2023) as they observed significant differences across the treatment means in fish body (carcass) compositions when fed the experimental diets. The variations in body composition could indicate differences in fish species, age, diet and environmental conditions. All treatments showed higher crude protein levels compared to the initial. This suggests that M. charantia seed meal supplementation enhances the protein content of the fish, potentially due to its protein content, improved protein digestibility and utilization. The moisture contents of the experimental fish were lower compared with the initial, except for the control. Dawodu et al. (2012) reported that the qualitative determination of fish moisture content is paramount in any quality control programme. Olagunju et al. (2012) and Gana et al. (2020) reported that moisture content in fish samples reflects both internal hydration and the influence of environmental water availability. The lipid contents vary but are higher compared to the initial value. Fish lipids are a significant dietary source of essential long-chain n-3 polyunsaturated fatty acids, which are not endogenously synthesised (Abedi and Sahari, 2014). Significant differences were observed across treatments for various minerals. These variations highlight the influence of M. charantia seed meal on mineral uptake and retention. The sodium, potassium and magnesium contents were relatively higher compared to the initial. These do not corroborate with the findings of Mbahinzireki et al. (2001) and Koumi et al. (2011), as they reported lower minerals in fish body compositions



compared to the control. Calcium and phosphorus are primary bone constituents, essential for diverse physiological processes including neuromuscular function, hormone regulation, cellular mortality and haemostasis (Serna and Bergwitz, 2020). Lall and Kaushik (2021) demonstrated that mineral deficiencies in fish lead to skeletal malformations, immunosuppression and anaemia.

The histological study investigating the effects of different inclusion levels of raw Momordica charantia seed meal (RMCSM) on the gonads of Coptodon guineensis after 84 days of feeding. The ovarian tissue shows normal follicle cells reproductive system histology. This is in line with the report of Tope-Jegede et al. (2019), who reported normal ovarian histology in Oreochromis niloticus fed a 0% inclusion of cottonseed meal-based diet. However, different stages of oocyte development are observed, including small follicles at various developmental stages, large luteinized follicles and various oocyte types. The granulosa cells are organized and nuclear integrity is maintained. This demonstrates a healthy reproductive system in the absence of RMCSM. Similar to the control group, the ovarian tissue displays various stages of oocyte development and maturation. No abnormalities in cellular organization or nuclear integrity are noted. This suggests that a 10 % inclusion of RMCSM does not negatively impact ovarian development in C. guineensis. However, above 20 % inclusion, the testicular tissue exhibits clear abnormalities in the reproductive system. The gonadal maturation is partially distorted, with variably sized seminiferous tubules and abnormal gonadal structures. This indicates a more pronounced negative effect on testicular development compared to the lower RMCSM inclusion. This suggests a dose-dependent effect of RMCSM on the reproductive system of C. guineensis. Lower inclusion levels (0% and 10%) appear to have no significant adverse effects on ovarian development. However, higher inclusion levels (20 – 40 %) show increasing signs of testicular dysfunction in seminiferous tubules that contain the sertoli cell and germ cell. The observed distortions could be due to several factors present in Momordica charantia seeds (Teoh et al., 2009), including phytochemicals, anti-nutritional factors and oxidative stress (Singh et al., 2023).

CONCLUSION

In conclusion, proximate and mineral compositions of the fish varied significantly across treatments, higher inclusion levels of MCSM increased crude protein in the fish carcass, but the effects on lipid, moisture, ash and crude fibre contents were less consistent. Mineral composition (sodium, potassium, calcium, magnesium, phosphorus) also showed significant variations, suggesting an impact of MCSM on mineral metabolism. The histological examination of gonads revealed that higher inclusion levels of raw MCSM caused significant abnormalities in testicular tissue such as sertoli cells and germ cells that produce the primary and secondary spermatocytes that lead spermatozoa, indicating a potential anti-fertility effect.

REFERENCES

- Abdullahi, M. M., Ajijo, M. R., & Matanmi, M. A. (2018). Reproductive behaviour and hatchability of *Tilapia guineensis* stocked in plastic tanks, Lagos, Nigeria. *Journal of Agriculture and Environment*, 14(2), 193-199.
- Abedi, E., & Sahari, M. A. (2014). Long-chain n-3 fatty acid sources and their effects on lipid and fatty acid profile of rainbow trout (*Oncorhynchus mykiss*). Food Chemistry, 164, 293-298
- Ahmad, N., Hasan, N., Ahmad, Z., Zishan, M., & Zohrameena, S. (2016). *Momordica charantia*: for traditional uses and pharmacological actions. *Journal of Drug Delivery and Therapeutics*, 6(2), 40-44.



- Akin-Obasola, B. J., & Jegede, T. (2014). Histological Analysis of Female Redbelly Tilapia; *Tilapia zillii* (Gervais, 1848) Ovary, Fed Bitter Melon, *Momordica charantia* (Cucurbitaceae) Leaf Meal. *Journal of Agricultural Science*, 6(11), 229.
- AOAC. (2005). Association of Official Analytical Chemists: Official Methods of Chemical Analysis. 17th Edition, Gaithersburg, M.D. U.S.A.
- Bakare, R. I., Magbagbeola, O. A., Akinwande, A. I., & Okunowo, O. W. (2010). Nutritional and chemical evaluation of *Momordica charantia*. *Journal of Medicinal Plants Research*, 4(21), 2189-2193
- Dar, R. A., Shahnawaz, M., & Qazi, P. H. (2017). *General overview of medicinal plants: A review. The journal of phytopharmacology*, 6(6), 349-351.
- Dauda, A. B., Yakubu, S. O., & Oke, A. O. (2014). Curbing the menace of prolific breeding in "aquatic chicken" (Tilapia): A way out to improve fish production in Nigeria. *New York Science Journal*, 7(4), 112-118.
- Gana, K. K., Nyam, S. A., & Agba, M. T. (2020). Assessment of proximate and mineral compositions of *Clarias gariepinus* fed varying dietary protein levels. *Journal of Agricultural Science and Food Research*, 11(4), 226-231.
- Gayathry, K. S., & John, J. A. (2022). A comprehensive review on bitter gourd (*Momordica charantia* L.) as a gold mine of functional bioactive components for therapeutic foods. *Food Production, Processing and Nutrition*, 4(10), 1 14.
- Ghosal, I., & Chakraborty, S. B. (2014). Effects of the aqueous leaf extract of Basella alba on sex reversal of Nile tilapia, Oreochromis niloticus. *Journal of Pharmacy and Biological Sciences*, 9(2), 162-164.
- Jegede, T., & Fagbenro, O. (2008). Dietary neem (*Azadirachta indica*) leaf meal as reproduction inhibitor in redbelly tilapia, *Tilapia zillii*. *International Symposium on Tilapia in Aquaculture*, 12(14), 365 373
- Jimah, A., Odion-Owase, E., & Suleiman, M. (2021). Preliminary Study of The Nutritional Content and Phytochemical Constituent of An Under-Utilised Bitter Melon Plant. *Journal of Natural Sciences Research*, 12(2), 15 18.
- Koumi, A. R., Niamien, P. A., Diaw, M., Atsé, B. C., & Ouattara, A. (2011). Growth performance of *Oreochromis niloticus* fed diets containing different levels of *Moringa oleifera* leaf meal. *Journal of Animal & Plant Sciences*, 11(2), 1438-1444.
- Lamboj, A. (2004). The cichlid fishes of Western Africa. *Bergit Schmettkamp Verlag Bornheim, Germany*, 225
- Lall, S. P., & Kaushik, S. J. (2021). Nutrition and metabolism of minerals in fish. *Animals*, 11(9), 2711.
- Magalhaes, I., & Ford, A. (2022). The amazing diversity of cichlid fishes. Frontiers, 10(5), 1-7.
- Mbahinzireki, G., Luyinda, N., & Nyakairu, J. (2001). The effect of feeding frequency on the growth performance of *Oreochromis niloticus* (L.) fingerlings. *African Journal of Ecology*, 39(2), 173-176
- Mundida, G. B., Manyala, J. O., Madzimure, J., & Rono, K. (2023). Growth and Economic Performance of African Catfish (*Clarias gariepinus* Burchell, 1822) Fed Diets Containing Black Soldier Fly Larvae (*Hermetia illucens* Linnaeus, 1758). *East African Journal of Agriculture and Biotechnology*, 6(1), 332-344



- Olagunju, A. O., Osibanjo, F. J., & Adeniran, O. O. (2012). Proximate and elemental composition of some selected commercial fish feeds in Nigeria. *Journal of Fisheries and Aquatic Science*, 7(1), 1-8.
- Prabu, E., Rajagopalsamy, C. B. T., Ahilan, B., Jeevagan, I. J. M. A., & Renuhadevi, M. (2019). Tilapia – An Excellent Candidate Species for World Aquaculture: A Review. *Annual Research & Review in Biology*, 31(3), 1-14
- Serna, J., & Bergwitz, C. (2020). Importance of dietary phosphorus for bone metabolism and healthy aging. *Nutrients*, 12(10), 3001
- Osunde, Z. D., & Kwaya, P. V. (2012). Development of egusi melon seed extractor. *International Conference on Agricultural and Food Engineering for Life*,
- Samaddar, A. (2022). Recent trends on Tilapia cultivation and its major socioeconomic impact among some developing nations: A Review. *Asian Journal of Fisheries and Aquatic Research*, 16(4), 1-11.
- Singh, J., & Arora, S. K. (2023). Antinutritional factors in plant based foods. *Internat. J. agric. Sci.*, 19(1), 366-375
- Sofowara, A. (2006). Medicinal Plants and Traditional Medicine in Africa. *Spectrum Books Ltd Ibadan, Nigeria 2nd edition*, 151-153, 209-214.
- Tan, L. P., Kha, T. C., Parks, S., & Roach, P. D. (2016). Bitter Melon (*Momordica charantia* L.) bioactive composition and health benefits: A review. *Food Reviews International*, 32(4), 362-381.
- Teoh, P. L., Yong, Y. S., & Tan, S. H. (2009). Phytochemicals and bioactivities of *Momordica charantia* L. seeds. *Journal of Medicinal Plants Research*, *3*(13), 1258-1262.
- Tope-Jegede, O. H., Fagbenro, O. A., & Olufayo, M. O. (2019). Histology of gonads in *Oreochromis niloticus* (Linnaeus 1757) fed cottonseed meal-based diets. *International Journal of Fisheries and Aquatic Studies*, 7(2), 269-274
- Ukenye, E. A., Taiwo, I. A., & Anyanwu, P. E. (2019). Morphological and genetic variation in *Tilapia guineensis* in West African coastal waters: A mini review. *Biotechnology Reports*, 24, 1 3.
- Uzoma, A., Afolabi, T., & Onuoha, A. (2016). Effects of fertilizer on soil composition in the southern Guinea savanna of Nigeria. *Journal of Nigerian Soil Science*, 5(2), 45-56.
- Xu, P., Kpundeh, M. D., Qiang, J., & Gabriel, N. N. (2015). Use of herbal extracts for controlling reproduction in tilapia culture: Trends and Prospects-a Review. *Israeli Journal of Aquaculture-Bamidgeh*, 67, 1 23.



EXTRACTION OF ALUMINA FROM KANKARA KAOLIN

Kamaluddeen Suleiman Kabo¹, Mustapha Isah²

¹Department of Chemistry, Faculty of Physical Science, Federal University Dutsin – Ma, Katsina State, Nigeria.

²Department of Chemistry, Faculty of Natural and Applied Science, Sule Lamido University, Kafin Hausa, Jigawa State, Nigeria.

ABSTRACT

Alumina can be extracted from various locations using different methodologies and raw materials. In this study, kaolin from Kankara town, Katsina State, Nigeria, was used as the raw material for alumina production. The study focused on the extraction of alumina from kaolin via the leaching process, using hydrochloric acid as the leaching agent. Crude kaolin was first crushed and calcined before leaching. Calcination of the crude kaolin was carried out at 700 °C for 2 h, after which alumina was leached from the calcined kaolin using hydrochloric acid under continuous stirring for 2 h. The extracted alumina was characterized using XRD analysis to investigate its crystal structure and the amount of impurities present.

Keywords: Acid, Calcination, Crude, Kaolin, Leaching.

1.0 Introduction

The extraction of alumina from kaolin has been widely investigated using different acid and alkali hydrometallurgical processes. Leaching of aluminum from calcined kaolinitic clays with HCl or H₂SO₄ solutions has been proposed, followed by precipitation/crystallization of aluminum salts and their thermal decomposition to produce alumina (Olaremu, 2015). Kaolin typically contains about 30–40% alumina. Kaolinite is of particular interest due to its relatively high alumina content, making it a suitable replacement for bauxite ore (Al-Zahrani & Abdul-Majid, 2009).

Kaolin is a clay mineral with the chemical composition Al₂Si₂O₅(OH)₄ and a layered crystal structure of aluminum silicate, bonded by hydrogen bridges between layers. This gives kaolin its greasy characteristic when mixed with a polar solvent such as water (Shackelford & Doremus, 2008). Alumina is an important industrial mineral widely used as a catalyst, abrasive, and adsorbent (Salahudeen et al., 2015). It exists in a stable form (α-alumina) as well as several metastable forms, including γ -, η -, δ -, θ -, κ -, and χ -alumina (Wang *et al.*, 2009). Naturally, alumina occurs in its pure form as the mineral corundum, though the most important natural source remains bauxite, which is commonly processed to alumina using the Bayer process (Hosseini et al., 2011). Aluminum (Al) is a technologically significant material with excellent physicochemical properties and the ability to form lightweight alloys with many other elements, thereby increasing strength and enhancing other properties (Frank et al., 2007). Owing to these properties, aluminum can be cast and/or thermomechanically treated to produce a wide range of commercial products. According to data from the International Aluminum Institute (Wikipedia, 2021), aluminum plays a leading role in almost every aspect of human society, and its global demand is expected to increase in the coming decades. Although several methods have been developed for the extraction of aluminum from its ores, commercial production still relies on two processes developed in the late 19th century: the Bayer hydrometallurgical method, which produces pure alumina (Al₂O₃) from bauxite ores, and the Hall-Héroult electrolytic method, which produces pure aluminum metal using metallurgical alumina as the raw material (Tilley et al., 1927). Kaolin, being a soft white clay with high alumina content, low cost, and wide availability, is an attractive alternative feedstock for alumina production.

2.0 Materials and Methods



The methodology for the extraction of alumina from kaolin was carried out using the following processes as explained below.

2.1 Crushing and Grinding

The kaolin rock was crushed using laboratory mortar and pestle for a few minute to reduce the size into powdered form.

2.2 Calcination of Kaolin

A 100 g sample of kaolin was weighed using an analytical balance and then calcined at a temperature of 700 °C for 2 hours in a muffle furnace.

2.3 Leaching with Acid

A 20 g of the calcined kaolin was measured and placed into a flat-bottom flask fixed on a hot plate with a magnetic stirrer. 60 mL of HCl was added, and the mixture was stirred continuously for 2 hours under reflux using a glass condenser to minimize acid evaporation. The resulting solution was then filtered using filter paper.

2.4 Treatment with sodium hydroxide

100ml of NaOH was poured into the precipitate which was filtered out and it was further washed Quantitative analysis report

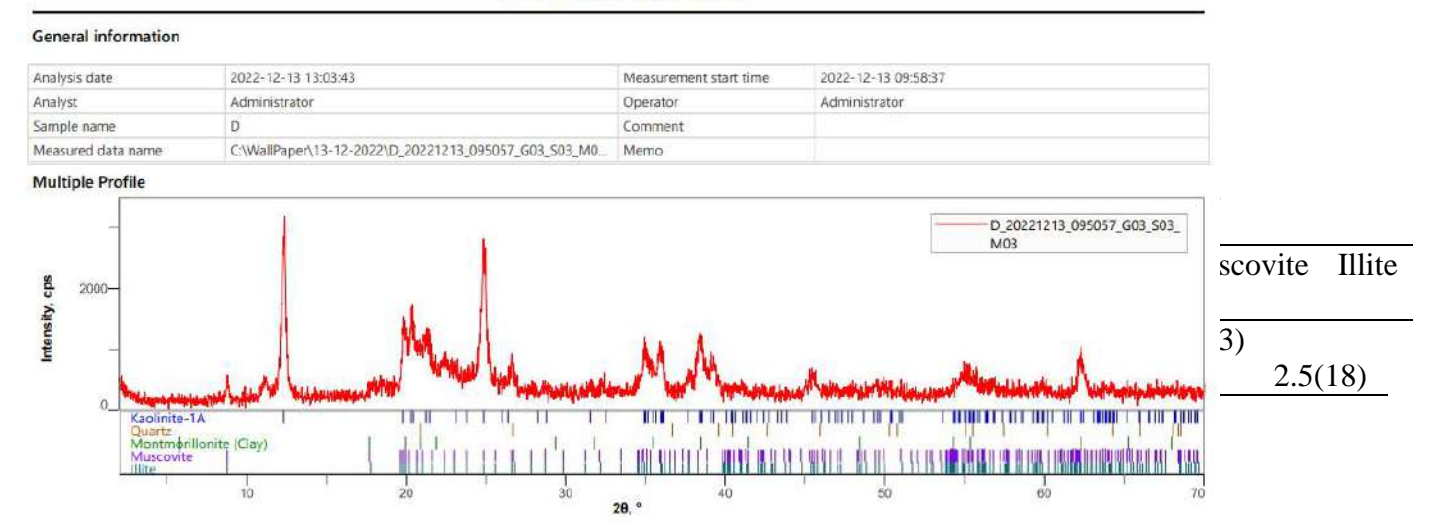


Figure 1: XRD pattern of the raw kaolin sample.

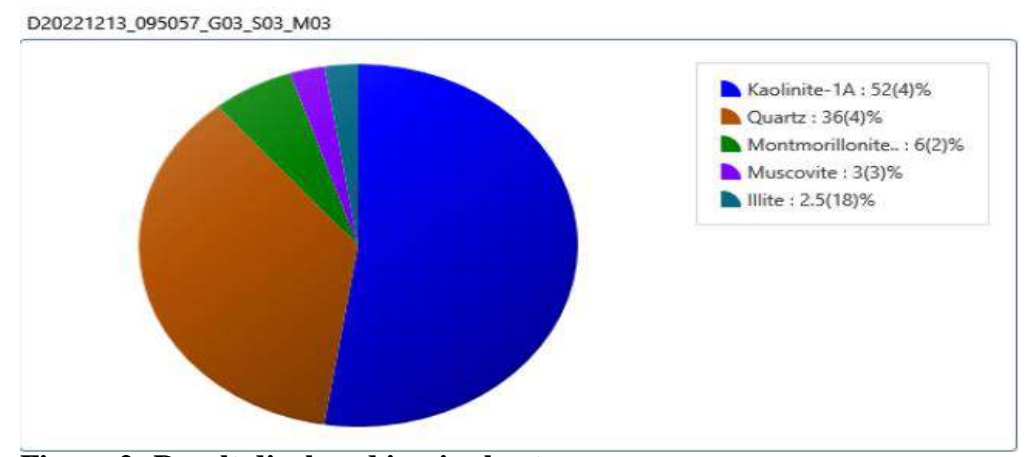


Figure 2: Result displayed in pie chart.



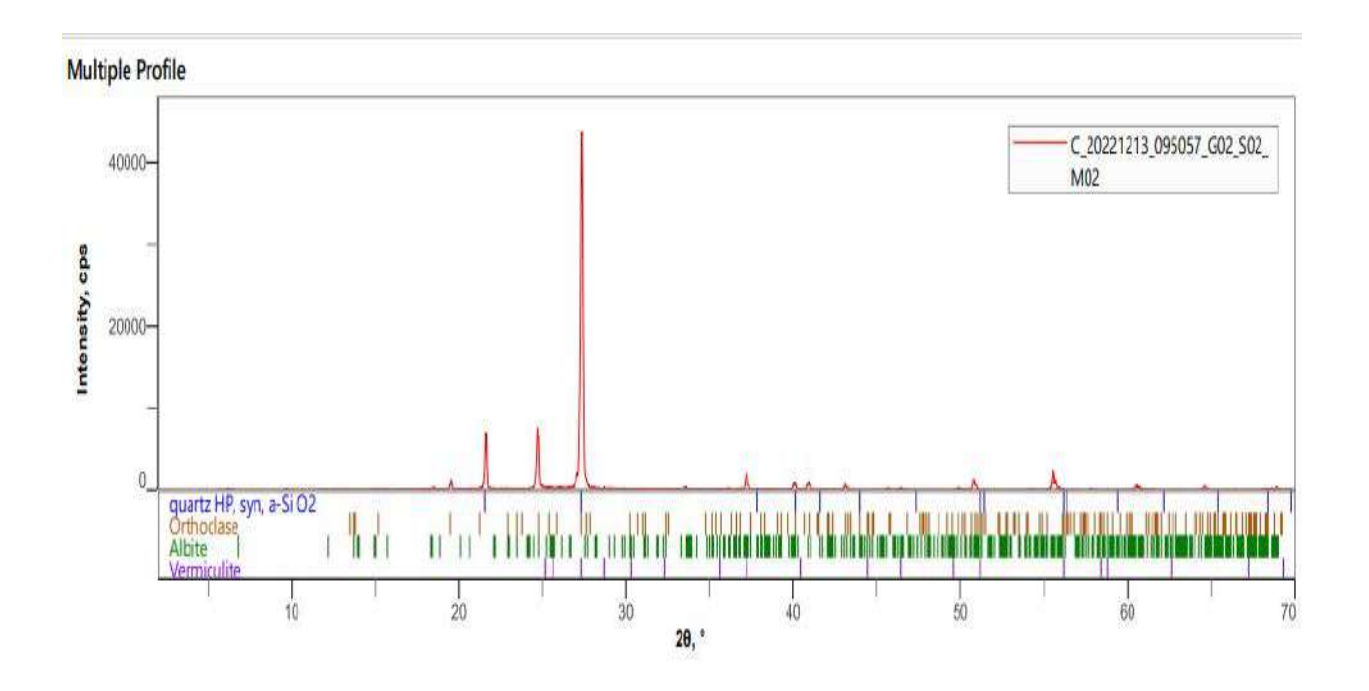
Chemical analysis of the original kaolin sample contains variable amounts of other oxides, which indicates the presence of impurities, as they are not related to the kaolinite structure. The presence of kaolinite-1A, Quartz, Montmorillonite (clay), Muscovite, Illite as accessory mineral phases in the kaolin deposit. Where the kaolinite-1A makes about 52 (4) wt %, Quartz makes about 36 (4) wt%, the Montmorillonite makes about 6 (2) wt %, Muscovite makes about 3 (3) wt %, and the illte makes about 2.5 (18), making a total of 99.5 wt %.

3.2 The XRD Result for the calcined Kaolin

Chemical analysis of the calcined kaolin sample formation results are presented in Table 2.

Table 2: Result of XRD of the calcined kaolin

Dataset/Weight Fraction, wt%	Value Unit	Quartz HP, syn, a-Si 02	Orthoclase	Abite	Vermicuite
C_20221213_095057_G02_S02_M02	0	69.0 (15)	11.9 (5)	17.6 (16)	1.5 (7)



C20221213_095057_G02_S02_M02

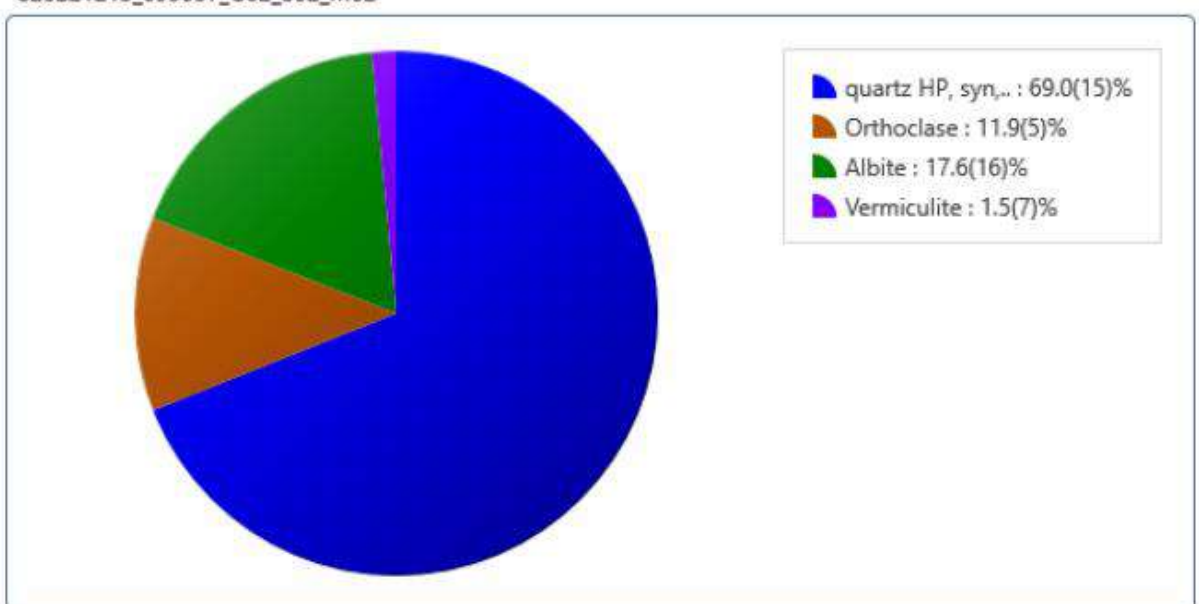


Figure 4: Result displayed in a pie chart

The sample was run under 2θ value from 0 - 70 and the diffraction pattern shows that there are three prominent peaks. The appearance of the prominent Peaks at the 2θ values appears around 20, 25 and 27.5. The appearance of these three prominent peaks indicates that the material is crystalline, the position of these 2θ values matches the diffraction pattern of the kaolin sample which indicates that the alumina was successfully synthesized, and the machine was also able to indicate the type of alumina present which is Quartz alumina. The materials present in the aluminum are Quartz which is about 69.0 (15) wt %, Orthoclase 11.9 (5) wt %, Alibite 17.6 (16) wt % and Vermiculite 1.5 (7) %. All together it is about 100 wt % which indicate that this extraction was successful.

4.0 Conclusions

The extraction of alumina from kaolin by leaching is an effective process with the use of acid. This study was aimed at the extraction of alumina from the kaolin deposits that occur in large quantities in Kankara town, Katsina state, Nigeria. The extraction process applied comprised crushing, calcination and by two stages of leaching with acid and base. The materials present in the aluminum are Quartz which is about 69.0 (15) wt %, Orthoclase, 11.9 (5) wt %, Alibite, 17.6 (16) wt % and Vermiculite, 1.5 (7) %., Altogether it is about 100 wt % which indicates that this extraction was successful.

REFERENCES

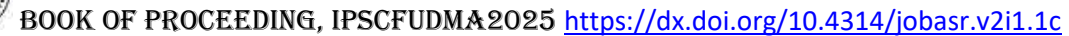
Olaremu, G. A. (2015). "Sequential Leaching for the Production of Alumina from a Nigerian Clay," IJETMAS, 3(7), 2349 – 4476.

Al-Zahrani A. A and Abdul-Majid M. H. (2009). Extraction of Alumina from Local Clays by Hydrochloric Acid Process, JKAU:Eng. Sci. 20 (2), 29 – 41.

Shackelford J. F., Doremus, R. H. (2008). Ceramic and glass materials: structure, properties and processing. Springer, 13 - 112.



- Salahudeen, N., Ahmed, A. S., Al-Muhtaseb, A. H., Dauda, M., Waziri, S. M., Baba, Y., Jibril, B. Y. (2015). Synthesis of gamma alumina from Kankara kaolin using an oven technique. Appl. Clay Sci. 105(106), 170 177.
- Wang, Y. H., Wang, J., Shen, M. Q., Wang, W. L. (2009). Synthesis and properties of thermostable γ-alumina prepared by hydrolysis of phosphide aluminum. J. Alloys Compd, 467, 405 412.
- Hosseini, S.A., Niaei, A., Dariush, S. (2011). Production of γ -Al₂O₃ from kaolin. Open J. Phys. Chem. 1, 23 27.
- Frank, W. B., Haupin, W. E., Dawless, R. K., Granger, D. A., Wei, M. W., Calhoun, K. J., Bonney, T. B. (2007). Aluminum In Ullmann's Encyclopedia of Industrial Chemistry; Wiley-VCH:Weinheim, Germany, 2.
- World Aluminium. Available online: http://www.world-aluminium.org/statistics/#linegraph/ (accessed on 12 July 2021).
- Tilley, G. S., Millar, R.W., Ralston, O. C. (1927). Acid Processes for the Extraction of Alumina; US Government Printing Office: Washington, DC, USA, 266.



PHYTOCHEMICAL SCREENING AND ANTIMICROBIAL ACTIVITY OF SECONDARY METABOLITES FROM XERODERRIS STUHLMANNII STEM BARK''

Kabir, U. M. *1, Ali T.1, Ogbesejana Abiodun B1, Kabir, S.2

¹Federal University of Dutsin-Ma, Katsina State, Nigeria. ²Federal University of Petroleum Resources, Effurun, Delta State.

email: usmanmk48@gmail.com

ABSTRACT

This study investigates the phytochemical composition and antimicrobial activity of Xeroderris stuhlmannii stem bark extracts. Dichloromethane, methanol, n-hexane, and ethyl acetate extracts were analyzed for secondary metabolites using standard phytochemical screening, thin-layer chromatography (TLC), and gas chromatography-mass spectrometry (GCMS). Results confirmed the presence of alkaloids, flavonoids, steroids, triterpenoids, anthraquinones, saponins, tannins, and glycosides. The dichloromethane extract exhibited the highest antimicrobial activity, with a 30 mm inhibition zone against Salmonella typhi, Bacillus amyloliquefaciens, and others. GC-MS identified dibutyl phthalate (38.5%) and lupol (11.2%) as major constituents. These findings suggest Xeroderris stuhlmannii as a potential source of natural antimicrobial agents for therapeutic applications.

Keywords: Phytochemicals; Evaluation; Secondary metabolites: Xeroderris stuhlmannii; antimicrobial

INTRODUTION

Phytochemicals are bioactive chemical compounds naturally synthesized by plants that play crucial roles in plant defense and human health. Derived from the Greek word phyton (meaning "plant"), these compounds contribute to the plant's color, aroma, and resistance to microbial attacks (Silva et al., 2017). Phytochemicals are generally classified as primary or secondary metabolites. While primary metabolites such as sugars and amino acids are essential for plant growth, secondary metabolites—such as alkaloids, flavonoids, terpenoids, phenols, and glycosides—often possess potent pharmacological activities (Edeoga et al., 2005; Sheel et al., 2014).

Medicinal plants are well known for their rich reservoir of these bioactive secondary metabolites. The World Health Organization estimates that about 80% of the world's population relies on herbal medicine for their primary health care needs (WHO, 2002). As a result, the scientific validation of these plants for antimicrobial, anti-inflammatory, anticancer, and antioxidant activities has become a global research priority (Fabricant & Farnsworth, 2001).

Xeroderris stuhlmannii (Taub.) Mendonça & E.P. Sousa is a perennial tree species belonging to the Fabaceae (Leguminosae) family. It is native to the woodlands of East and Southern Africa and is widely recognized in ethnobotany for its use in treating a broad range of ailments such as coughs, diarrhea, colds, malaria, rheumatoid arthritis, stomachache, and eye infections (Maroyi, 2013; Ngarivhume et al., 2015). A survey of traditional healers in Zimbabwe showed that both the roots and stem bark are frequently used remedies, particularly for gastrointestinal and respiratory issues (Ngarivhume et al., 2015). Asase et al. (2005) further reported the antimalarial activity of *Xeroderris stuhlmannii*, suggesting its potential in managing infectious diseases.

Collection of samples

The sterm bark of Xeroderris stuhlmannii was collected from Dan Takiri village Dutsin-ma Local government, Katsina in the raining season. The stem bark was subjected to identification in the Department of Biological Science, Federal University Dutsinma. The identified plant was subsequently air-dried in Chemistry Laboratory of Federal University Dutsin-ma and thereafter stored in air-tight polythene bag before to use.

Preparation of plant extracts

The dried plant materials were ground to a fine powder using a mortar and pestle. 750 g of the powder sample was packed in an aspirator bottle. Exhaustive extraction was carried out successively using n-hexane, dichloromethane, ethyl acetate and methanol. The solvent was recovered using a rotatory evaporator at the end of the extraction. Recovered extracts were placed in a desiccator and allowed to dry fully before subsequent experiments.

Phytochemical screening

The phytochemical screening was done on the dichloromethane, and methanol extracts. The plant extracts were analyzed for the presence of alkaloids, saponins, flavonoids, tannins, triterpenoids, phenols, steroids, anthraquinones, and glycosides.

Thin Layer Chromatography (TLC):

TLC was performed on pre-coated silica gel plates. The n-hexane and dichloromethane extracts were spotted on the plates and developed using 10% ethyl acetate in 90% n-hexane. The methanol extract was developed in a solvent system of 10% toluene in 90% chloroform. After development, the plates were air-dried and visualized under UV light at 254 nm and 365 nm, and Rf values were calculated.

Gas Chromatography-Mass Spectrometry (GC-MS):

GC-MS analysis was carried out using a GC-MS-QP2010 Ultra (Shimadzu) system equipped with a capillary column. The oven temperature was programmed from 60°C to 300°C at a rate of 10°C/min. Helium was used as the carrier gas. The DCM extract was injected in splitless mode and compounds were identified by comparing mass spectra with the NIST library database.

RESULTS AND DISCUSSION

Result of extraction

The percentage yield of *Xeroderris stuhlmannii* crude extract from the Dichloromethane and Methanol extract is present in Table 1 from the results. The highest yield was obtained from the methanol extract which could be attributed to the presence of highly polar substances in the plant material.

Table 1: Result of the extraction of Xeroderris stuhlmannii

Solvents	Yield of extract (g)	Percentage(%) yield w/w
n-hexane	2.74	0.365
Dichloromethane	2.03	0.27
Ethylacetate	0.3	0.13
Methanol	27.25	3.63

By considering the yield obtained in grams and percentage recoveries from each solvent, the yields of 2.74 g, 2.03 g, 0.3 g and 27.25 g were obtained from n-hexane, Dichloromethane, Ethylacetate and Methanol extracts, respectively (Table 1). From the results, the highest yield was obtained from the methanol extract, which could be attributed to the presence of polar substances with a molar mass in the plant sample.

Result of Thin Layer Chromatography of the Crude Extracts

The thin-layer chromatographic analysis of crude n-hexane and Dichloromethane extracts using 10% ethyl acetate in 90% n-hexane (1ml ethyl acetate: 4ml n-hexane). Also, chromatographic analysis of methanol was done using 10% toluene in 90% chloroform (1ml toluene: 4ml n-hexane) solvent system revealed the presence of some spots as shown below.



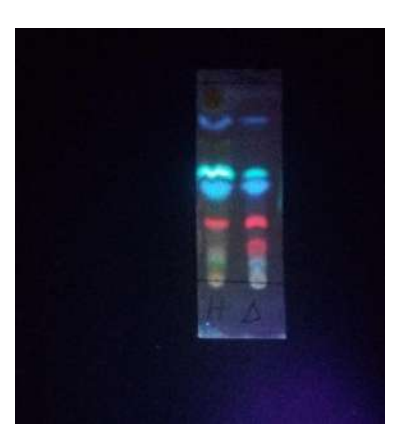




Fig. 1 TLC profile of cude n-hexane and DCM extract & of crude Methanol extract The table below show the retention factors of eight and five components in DCM and Methanol extracts respectively.

Table 2: TLC profile of crude DCM extracts

Spots	Distance travelled by the component (cm)	•	Retention factor (RF)
\mathbf{D}_1	0.55	5.5	0.10
\mathbf{D}_2	1.55	5.5	0.28
\mathbf{D}_3	1.90	5.5	0.35
\mathbf{D}_4	2.30	5.5	0.42
\mathbf{D}_5	2.80	5.5	0.51
D_6	3.60	5.5	0.65
\mathbf{D}_7	4.20	5.5	0.76
D_8	4.80	5.5	0.87

Table 3: TLC profile of crude Methanol extracts

Spots	Distance	Distance travelled	Retention
	travelled by the	by the solvent(cm)	factor (RF)
	component (cm)		
\mathbf{M}_1	0.70	5.0	0.14
M_2	1.50	5.0	0.30
M_3	2.50	5.0	0.50
M_4	3.02	5.0	0.60
M_5	3.40	5.0	0.68

The result showed various spots on the TLC plates for all the extracts when viewed under UV light at 365nm and 254nm. The retention factor (Rf) values of *Xeroderris stuhlmannii* extract were determined using the following formulae: $Rf = \frac{\text{Distance travel by the solvent}}{\text{Distance travel by the compound}}$

Phytochemical screening of Xeroderris stuhlmannii



The result for the phytochemical screening of *Xeroderris stuhlmannii* using two different solvents is presented in Table 4. The result revealed the presence of nine (9) phytocompounds in Dichloromethane (DCM) extract which are alkaloids, steroids, flavonoid, terpenoids, triterpenoids, saponins, tannins, phenols and anthraquinone and then eight (8) phytocompounds in Methanol which are alkaloids, flavonoids, steroids, terpenoids, triterpenoids, phenols, Anthraquinones and saponins

Table 4. Phytochemical constituents of xeroderris stuhlmannii in different fractions

Constituent	Test	Dichloromethane	Methanol
Alkaloids	Mayes's	+	+
Flavonoids	Acid	-	+
Steroids	Libermann-	+	+
Terpenoids	Burchard's Acid	+	-
Triterpenoids	Copper acetate's	+	+
Anthraquinones	Borntrager's	-	+
Saponins	Foaming	+	+
Phenols	Ferric chloride	+	+
Tannins	Lead sub acetate	+	+
Glycosides	Keller-Killiani's	+	-

KEY: + = PRESENT

- = ABSENT

Antimicrobial result and discussion

Table 5. N-hexane Extract

Zone of inhibition (mm) of various concentrations of *Xerroderris Stuhlmannii* extract on tested organisms

Organism	250	125	62.5	31.25	Ciprofloxacin/
	mg/ml	mg/ml	mg/ml	mg/ml	fluconazole
Bacillus	09	ND	ND	ND	31
amyloquefaciens					
Staphylococcus	12	11	10	ND	24
aureus					
Klebsiella	ND	ND	ND	27	ND
pneumonia					
Pseudomonas	09	08	ND	ND	22
auruginosa					
Trichophyton	ND	ND	ND	ND	23
rubrum					
Salmonella	08	ND	ND	ND	24
typhi					
Aspergillus	ND	ND	ND	ND	18
niger					

Table 6. Dichloromethane Extract

Zone of inhibition (mm) of various concentrations of *Xerroderris Stuhlmannii* extract on tested organisms

Organism	250	125	62.5	31.25	Ciprofloxacin/
01 8		mg/ml			fluconazole

30



Bacillus	22	20	09	ND	26
amyloquefaciens Staphylococcus	28	22	21	08	27
aureus Klebsiella	26	22	16	09	22
pneumonia Pseudomonas auruginosa	19	11	10	10	23
Trichophyton rubrum	21	13	08	07	26
Salmonella	30	18	11	11	34
typhi Aspergillus niger	ND	ND	ND	ND	29

Table 7. Methanol

Zone of inhibition (mm) of various concentrations of Xerroderris Stuhlmannii extract on tested

organisms

organisms					
Organism	250	125	62.5	31.25	Ciprofloxacin/
	mg/ml	mg/ml	mg/ml	mg/ml	fluconazole
Bacillus	26	15	08	ND	31
amyloquefaciens					
Staphylococcus	12	10	08	08	24
aureus					
Klebsiella	15	12	10	ND	27
pneumonia					
Pseudomonas	15	10	10	08	22
auruginosa					
Trichophyton	09	08	08	ND	2316
rubrum					
Salmonella	16	14	10	09	24
typhi					
Aspergillus	ND	ND	ND	ND	18
niger					

KEY= ND (NOT DETECTED)

The table shows the microbial activities of *Xerroderris Stuhlmannii* extract at different concentrations against seven bacterial strains (*Bacillus amyloquefaciens*, *Staphylococcus aureus*, *Klebsiella pneumonia*, *Pseudomonas aeruginosa*, *Trichophyton rubrum*) Compared to a positive control (standard antibiotic) and a negative control (no treatment). The extract was prepared using only two solvents: The Dichloromethane and the Methanol. Overall, the table suggests that *Xerroderris Stuhlmannii* extract has antimicrobial activity against the tested bacteria, with the level of activity varying depending on the solvent used and the concentration of the extract. In general, the Dichloromethane extract showed higher activity, than the Methanol extract. Among the seven bacterial strains in Dichloromethane, *Pseudomonas auruginosa* and *Bacillus amyloquefaciens*, were generally more susceptible to the extract than *Staphylococcus aureus* and *Trichophyton rubrum*. The four bacterial strains in Methanol, *Klebsiella pneumonia* and *Pseudomonas auruginosa* are more susceptible to the extract than



Staphylococcus aureus and *Trichophyton rubrum*. At the highest concentration tested (250 mg/ml), the extract showed comparable or even better activity than the positive control for some bacterial strains and solvents.

Table 8: Minimum Inhibitory Concentration (MIC) of Xerroderris Stuhlmannii extracts on test organisms

Extract	Organism	MIC (mg/ml)		
N-Hexane	Bacillus amyloquefaciens	ND		
	Staphylococcus aureus	125		
	Klebsiella pneumonia	62.5		
	Pseudomonas auruginosa	250		
	Trichophyton rubrum	250		
	Salmonella typhi	ND		
	Aspergillus niger	ND		
Dichloromethane	Bacillus amyloquefaciens	125		
	Staphylococcus aureus	125		
	Klebsiella pneumonia	125		
	Pseudomonas auruginosa	62.5		
	Trichophyton rubrum	125		
	Salmonella typhi	62.5		
	Aspergillus niger	ND		
Methanol	Bacillus amyloquefaciens	125		
	Staphylococcus aureus	250		
	Klebsiella pneumonia	125		
	Pseudomonas auruginosa	62.5		
	Trichophyton rubrum	250		
	Salmonella typhi	62.5		
	Aspergillus niger	ND		

The table shows the minimum inhibitory concentration (MIC) of two organic extracts of *Xerroderris Stuhlmannii* against four different types of bacteria, as well as positive and negative controls. The *Xerroderris Stuhlmannii* extracts used were N-Hexane, dichloromethane, and methanol. The MIC is the lowest concentration of a substance that inhibits the visible growth of a microorganism after a specified incubation period. In this table, a positive result based on the (mg/ml) indicates that the *Xerroderris stuhlmannii* at that concentration was able to inhibit the growth of the microorganism, while the negative result is said to be (ND) in the table 8, indicates that the *Xerroderris Stuhlmannii* was not able to inhibit growth at that concentration.

The positive control shows that the test is sensitive enough to detect the presence of an antibiotic that should inhibit the growth of all bacteria, while the negative control is a baseline that shows no inhibition of bacterial growth in the absence of an *Xerroderris stuhlmannii*.

Overall, the results suggest that the *Xerroderris stuhlmannii* extract have some potential for inhibiting the growth of the bacteria tested, but further testing would be necessary to determine the most effective concentration and the mechanism of action of the extracts.

Table 9 Minimum Bactericidal/Fungicidal Concentration (MBC/MFC) of *Albizia chivalieri* extracts on test organisms

Extract	Organism	MBC/MFC (mg/ml)			
Dichloromethane	Bacillus amyloquefaciens	250			
	Staphylococcus aureus	250			



	Klebsiella pneumonia	ND
	Pseudomonas auruginosa	125
	Trichophyton rubrum	250
Methanol	Bacillus amyloquefaciens	250
	Staphylococcus aureus	250
	Klebsiella pneumonia	ND
	Pseudomonas auruginosa	125
	Trichophyton rubrum	250

The table above shows the minimum bactericidal concentration (MBC) of different concentrations of only two substances (Dichloromethane, and Methanol) against seven types of bacteria (*Bacillus amyloquefaciens, Staphylococcus aureus, Klebsiella pneumonia, Pseudomonas auruginosa, Trichophyton rubrum, Salmonella typhi, Aspergillus niger*. The positive control column, which is written based on the (mg/ml), indicates the growth of the bacteria in the absence of test substances, while the negative control column (ND) indicates the absence of bacterial growth in the presence of *Xerroderris Stuhlmannii* that is known to be effective against the bacteria being tested. The MBC is defined as the minimum concentration of a substance required to kill all of the bacteria in a given sample. In this table, a "+" sign indicates the absence of bacterial growth on the culture media, while a "ND" sign indicates the presence of bacterial growth. Looking at the results, it is clear that the effectiveness of each substance varies depending on the bacteria being tested.

GC-MS RESULT

1	8.270	8.230	8.340	180499	1.82	60535	1.34	2.98	Dodecane, 4,6- dimethyl-
2	11.138	11.100	11.195	256857	2.59	146602	3.24	1.75	Heptadecane
3	11.704	11.670	11.740	143657	1.45	96002	2.12	1.50	Hexacosane
4	12.507	12.480	12.540	54606	0.55	37098	0.82	1.47	Heptadecane
5	13.661	13.620	13.690	284936	2.88	177352	3.92	1.61	Nonadecane
6	14.150	14.115	14.190	231031	2.33	132294	2.92	1.75	Heneicosane
7	14.746	14.710	14.800	101590	1.03	44067	0.97	2.31	1-Nonadecene
8	14.828	14.800	14.860	51025	0.52	31198	0.69	1.64	Docosane
9	16.423	16.375	16.470	350119	3.54	147372	3.26	2.38	Tetracosane
10	17.098	17.015	17.160	3814578	38.52	1657128	36.62	2.30	Dibutyl phthalate
11	17.706	17.680	17.740	58282	0.59	34837	0.77	1.67	Hexacosane
12	18.494	18.460	18.520	66470	0.67	37255	0.82	1.78	Cyclooctasiloxane,
									hexadec
13	19.213	19.175	19.245	161424	1.63	88926	1.97	1.82	Nonacosane
14	19.700	19.670	19.725	100346	1.01	62800	1.39	1.60	Dotriacontane
15	21.442	21.405	21.485	223438	2.26	121156	2.68	1.84	Tetracosane
16	21.841	21.810	21.885	117517	1.19	58836	1.30	2.00	Dotriacontane
17	21.991	21.960	22.025	105115	1.06	63588	1.41	1.65	Hexanedioic acid,
									bis(2-eth
18	22.107	22.030	22.140	110991	1.12	42520	0.94	2.61	Pentatriacontane
19	22.649	22.615	22.695	151936	1.53	83472	1.84	1.82	Cyclononasiloxane,



20	23.269	23.230	23.305	844592	8.53	487583	10.78	1.73	octade Bis(2-ethylhexyl) phthalate
21	23.330	23.305	23.345	40506	0.41	22636	0.50	1.79	Tetracontane
22	23.374	23.345	23.400	78597	0.79	46184	1.02	1.70	Cyclopentadecanon
									e, 2-hy
23	23.667	23.635	23.700	72852	0.74	45223	1.00	1.61	Dotriacontane
24	24.744	24.710	24.785	213115	2.15	109033	2.41	1.95	Cyclononasiloxane,
									octade
25	24.960	24.920	25.025	680307	6.87	288273	6.37	2.36	1,3-
									Benzenedicarboxyli
									c ac
26	25.340	25.235	25.390	290622	2.93	53783	1.19	5.40	1-Decanol, 2-hexyl-
27	26.448	26.375	26.505	1117901	11.29	349282	7.72	3.20	Lupeol
				9902909	100.00	4525035	100.00		•

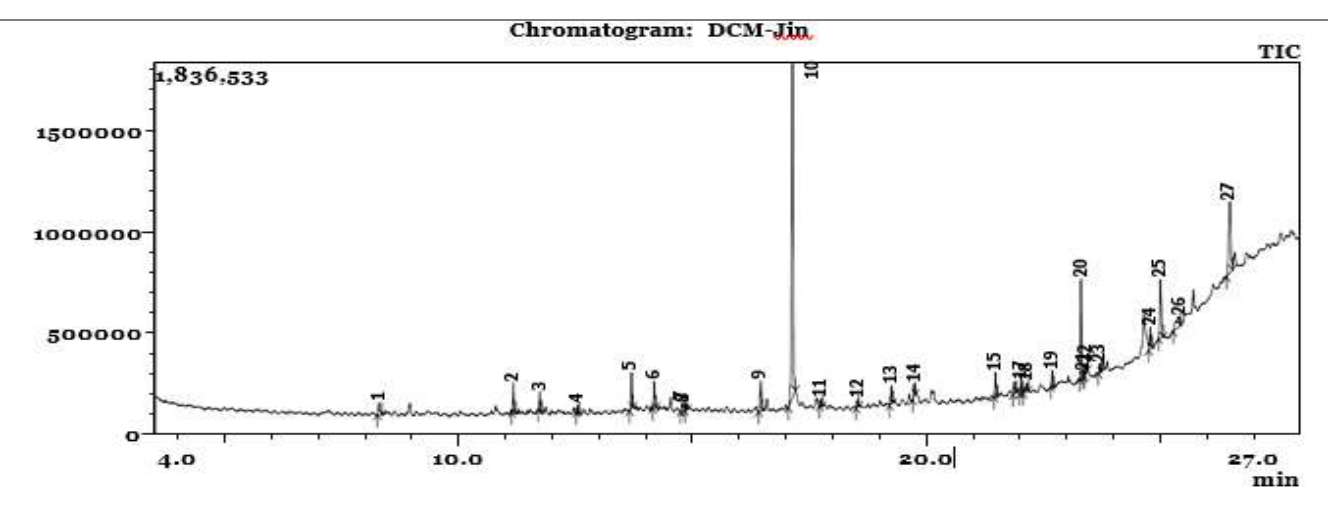


Figure 1: GC-MS RESULT

Table 6: GC-MS Identified compounds in Dichloromethane Extract of *Xeroderris stuhlmannii*.

GC-MS analysis of the dichloromethane extract revealed a total of 27 bioactive compounds. Among these, Dibutyl phthalate (38.52%), Lupeol (11.29%), and Bis(2-ethylhexyl) phthalate (8.53%) were the most abundant. Dibutyl phthalate, a known plasticizer, has been reported to possess antimicrobial properties, while Lupeol is a well-documented pentacyclic triterpenoid with strong pharmacological activities including anti-inflammatory, anticancer, and antimicrobial effects. The presence of these high-percentage compounds could explain the strong antimicrobial activity observed in the DCM extract. These findings further reinforce the therapeutic potential of *Xeroderris stuhlmannii* and support its ethnomedicinal applications.

CONCLUSION

Phytochemical screening confirmed the presence of bioactive secondary metabolites, including alkaloids, flavonoids, steroids, triterpenoids, anthraquinone, saponins, tannins, and glycosides in the stem bark of Xeroderris stuhlmannii. Antimicrobial testing demonstrated significant activity, especially with the DCM extract, which showed a maximum inhibition zone of 30 mm against Salmonella typhi, Bacillus amyloquefaciens, Staphylococcus aureus, Klebsiella pneumonia, Pseudomonas auruginosa, Trichophyton rubrum. GC-MS analysis identified Dibutyl phthalate



(38.52%), Lupeol (11.29%), and Bis(2-ethylhexyl) phthalate (8.53%) as the most abundant constituents. The high abundance and known bioactivity of these compounds suggest that the plant may serve as a valuable source for natural antimicrobial agents and supports its potential use in chemopreventive therapies.

REFERENCES

- Asase, A., Oteng-Yeboah, A. A., Odamtten, G. T., & Simmonds, M. S. J. (2005). Ethnobotanical study of some Ghanaian anti-malarial plants. Journal of Ethnopharmacology, 99(2), 273–279.
- Edeoga, H. O., Okwu, D. E., & Mbaebie, B. O. (2005). Phytochemical constituents of some Nigerian medicinal plants. African Journal of Biotechnology, 4(7), 685–688.
- Ezeonu, C. S., Ejikeme, C. M., & Uzoeto, H. O. (2016). Phytochemical and antimicrobial screening of the stem bark of Nauclea latifolia (Sm.). African Journal of Biotechnology, 15(24), 1232–1236.
- Fabricant, D. S., & Farnsworth, N. R. (2001). The value of plants used in traditional medicine for drug discovery. Environmental Health Perspectives, 109(Suppl 1), 69–75.
- Faraone, I., Russo, D., & Milella, L. (2018). Phytochemical profile and biological activities of extracts from Salvia species: A review. Phytotherapy Research, 32(5), 903–919.
- Fu, Y. J., Zu, Y. G., & Liu, W. (2014). Advanced technologies for green extraction of natural products: An overview. Journal of Chromatography A, 1313, 1–21.
- Keskes, H., Msaada, K., Salem, N., Bachrouch, O., Elkahoui, S., Hammami, M., & Marzouk, B. (2017). Chemical composition and antimicrobial activity of essential oil of Pistacia lentiscus L. leaves. African Health Sciences, 17(1), 146–152.
- Lewis, G., Schrire, B., Mackinder, B., & Lock, M. (2005). Legumes of the World. Royal Botanic Gardens, Kew.
- Macedo, M., Ferreira, M. I., Pinto, D., & Silva, A. M. S. (2018). Fabaceae family as a source of bioactive compounds for health and nutrition. Phytochemistry Reviews, 17(4), 927–943.
- Maroyi, A. (2013). Traditional use of medicinal plants in south-central Zimbabwe: Review and perspectives. Journal of Ethnobiology and Ethnomedicine, 9(1), 31.
- Mukafiah, M. (2022). Phytochemical constituents and antimicrobial potential of Xeroderris stuhlmannii. African Journal of Traditional, Complementary and Alternative Medicines, 19(3), 88–94.
- Ngarivhume, T., Van't Klooster, C. I., de Jong, J. T. V. M., & Van der Westhuizen, J. H. (2015). Medicinal plants used by traditional healers for the treatment of malaria in the Chipinge district in Zimbabwe. Journal of Ethnopharmacology, 159, 224–237.
- Radha, R., & Dharanidharan, P. (2021). Phytochemical screening methods and applications in medicinal plants. Journal of Pharmacognosy and Phytochemistry, 10(2), 395–402.
- Rates, S. M. K. (2001). Plants as source of drugs. Toxicon, 39(5), 603–613.
- Roy, R. N., Laskar, S., & Sen, S. K. (2006). Dibutyl phthalate, the bioactive compound produced by Streptomyces albidoflavus 321.2. Microbiological Research, 161(2), 121–126.
- Saleem, M. (2009). Lupeol, a novel anti-inflammatory and anti-cancer dietary triterpene. Cancer Letters, 285(2), 109–115.
- Sheel, R., Nisha, K., & Kumar, J. (2014). Preliminary phytochemical screening of methanolic extract of Clerodendron infortunatum. International Journal of Scientific and Research Publications, 4(2), 1–5.
- Silva, L. R., Pereira, M. J., Azevedo, J., Gonçalves, R. F., Valentão, P., & Andrade, P. B. (2017). Chemical composition of Cynara cardunculus L. var. altilis petioles: Nutritional value and antioxidant capacity. Food Chemistry, 215, 50–57.
- WHO. (2002). Traditional medicine: Growing needs and potential. World Health Organization Policy Perspectives on Medicines No. 2.
- Zheng, W., Wang, F., & Liao, C. (2007). Phthalates and their potential health effects in the environment. Journal of Environmental Science and Health, Part A, 42(4), 529–534.



A SOFTWARE ENGINEERING APPROACH TO THE DESIGN AND IMPLEMENTATION OF A DIGITAL FREELANCE MARKETPLACE SYSTEM

Barira Hamisu^{1*}, Raji Abdullahi Egigogo¹, Mubarak Yusuf Ibrahim¹ and Zayyanu Yunusa²
¹Department of Software Engineering and Cyber Security, Al-Qalam University, Katsina,
Nigeria

²Department of Computer Science, Adamawa State Polytechnic, Yola

Abstract

The increasing demand for flexible and remote work opportunities has accelerated the development of digital freelance platforms. This study adopts a software engineering approach to design and implement a secure, scalable freelance marketplace system using the MERN stack (MongoDB, Express.js, React.js, and Node.js). The platform facilitates seamless interaction between clients and freelancers by integrating core features such as user authentication, profile management, job posting, bidding, escrow-based payments, and a review system. The system was developed using the Agile methodology, enabling iterative development and continuous feedback integration. Functional, usability, and security testing confirmed the system's reliability across its user roles: administrator, freelancer, and client. Evaluation results demonstrated high performance in terms of transaction integrity, user engagement, and platform responsiveness.

Keywords: Freelance Marketplace, MERN Stack, Digital Economy, Job Bidding, Secure Payment.

1.0 Introduction

The rapid advancement of digital technology and widespread internet access has revolutionized work and business operations (Xia et al., 2024). Traditional employment models, characterized by long-term contracts and physical office settings, have gradually transitioned to more flexible and dynamic work arrangements (A & R, 2024). Freelance marketplaces have emerged as essential digital platforms, connecting employers and freelancers to facilitate the exchange of services for payment while meeting the demand for adaptability and innovation (Tawami & Djauhari, 2020). Freelancing has experienced significant growth in recent years, driven by technological advancements, globalization, and evolving work preferences (Hasan, 2025). Reports indicate that millions of individuals worldwide now earn their livelihoods through freelance work, contributing substantially to the global economy (Leung et al., 2021). Freelancers today operate across various fields, extending beyond traditional creative roles such as writing and graphic design to include software development, marketing, virtual assistance, and financial consulting (Tokaeva, 2024). This shift underscores the need for efficient and well-structured freelance marketplace platforms to support the increasing demand for freelance services.

This study proposes the design and implementation of a freelance marketplace system, which aims to act as intermediaries, connecting clients with skilled professionals called freelancers, offering essential tools such as job posting, project bidding, secure payment processing, review and rating system. Built using MERN Stack (MongoDB, ExpressJS, ReactJS, NodeJS). The proposed platform will function as an integrated system, connecting clients and freelancers in a dynamic, interactive environment.

2.0 Literature Review

This study reviewed several studies that explored the design, structure, and impact of freelancing systems from both technological and socio-economic perspectives, as summarized in Table 2.1



Table 2.1: Summary of Literature

Author(s)	Focus/Contribution	Technology/Methodology	Relevance to Proposed Project		
Deshmukh et al. (2020)	Decentralized freelance platform using blockchain & crypto	Ethereum, Smart Contracts	Highlights decentralization & transparency; contrasts with centralized approach		
Asanaka & Inoue (2023)	Job allocation via decision modeling in gig work	Utility-based modeling, simulations	Offers theoretical insights; the proposed project is practical and systembased		
Rauf et al. (2023)	Security practices of freelance developers	Observational study	Informs security features like encryption and authentication		
Ludwig et al. (2022)	Client-freelancer communication strategies	Communication dynamics analysis	Supports the development of messaging tools and bid optimization		
Munoz et al. (2022)	Freelancer identity control in digital platforms	Platform behavior analysis	Encourages design that supports autonomy and flexible profiles		
Huang et al. (2024)	Power imbalances and design tensions	Speculative participatory design	Recommends transparent features and balanced user relationships		
Tawami & Djauhari (2020)	Socio-economic impact of freelance platforms	Descriptive analysis	Aligns with the project's role in job creation; less technical focus		
Shilpa et al. (2022)	Blockchain for secure freelancing	Decentralized platform design	Suggests future consideration for blockchain integration		
Blaising & Dabbish (2022)	New freelancer onboarding and adaptation	Behavioral study	Motivates the inclusion of mentorship and		
Novica et al. (2022)	Job platform to reduce unemployment	PHP, Waterfall model	support features Basic platform with limited features; differs in tech stack		
Kautsar et al. (2023)		Laravel, MySQL, SDLC	Similar in goal; differs in framework and scalability		



Mahomodally & Intelligent freelancer Machine Learning, WAM	
Suddul (2022) matching & stack	system; project
automation	focuses on
	foundational build
Gu & Zhu (2021) Trust vs. User behavior analysis	Suggests loyalty
disintermediation in	features and
freelance platforms	retention strategies
Arora et al. (2023) "Developer's Hub" MERN stack	Closely aligns in
freelance platform	tech and structure;
using MERN	adds demographic
	insights
Guerra et al. (2022) Blockchain energy IoT + Blockchain	Different domain;
trading marketplace	parallels in secure,
	scalable design
Abdreissova et al. Freelance market Market analysis	Supports system as a
(2022) growth factors	solution to digital
	labor challenges
Yakubovska et al. Freelance labor Labor market study	Validates features
(2024) trends, wages,	like reviews,
portfolio importance	dynamic pricing, and
•	analytics

3.0 Methodology

This section describes the methodology adopted for the design and implementation of the Freelance Marketplace System. It outlines the chosen software development model, the processes involved in gathering and analyzing requirements, and the system design.

3.1 Software Methodology

The Agile software development model was selected for the design and implementation of the proposed system freelance marketplace. Agile software development is an iterative and incremental approach to software development (Al-Saqqa et al., 2020).

3.2 Requirements Analysis

This phase involves evaluating and refining the gathered requirements to ensure they are clear, consistent, and feasible for implementation. In which the requirements are categorized into functional and non-functional requirements. The analysis informed the platform's core features, including User Registration and Authentication, Profile Management, Project Posting and Bidding, Messaging System, Payment and Escrow System, and Review and Rating System.

3.3 System Design

System design is a crucial stage in the development of the freelance marketplace, where the system's architecture, components, and interactions are defined. It translates user and functional requirements into structured blueprints that support scalability, efficiency, and maintainability throughout the software lifecycle. Figure 3.1 illustrates the structural design of the system, while Figure 3.2 shows the physical design of the system.

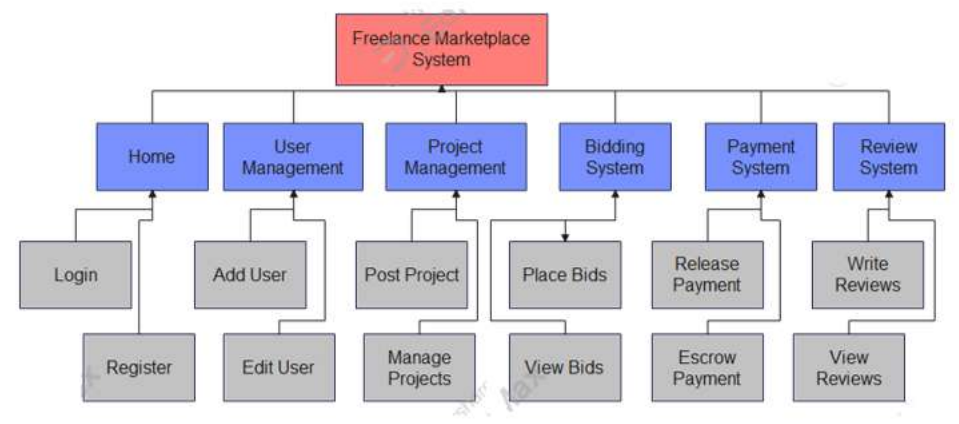


Figure 3.1: Structural Design of the System



Figure 3.2: Physical Design of the System

3.3.1 Use Case Diagram

The Use Case Diagram represents the interactions between users (actors) and the system. It provides a high-level overview of the functionalities available to different roles in the freelance marketplace. The Use Case Diagram is shown in Figure 3.3

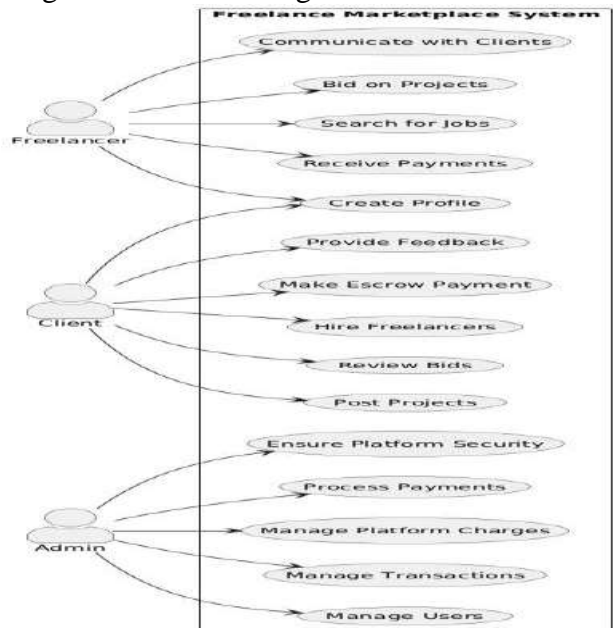


Figure 3.3: Use Case Diagram of the System.



3.3.2 Entity Relationship Diagram

The Entity-Relationship (ER) diagram illustrates the logical structure of the database by showing the entities involved in the system and their relationships. The Entity Relationship Diagram (ERD) is shown in Figure 3.4

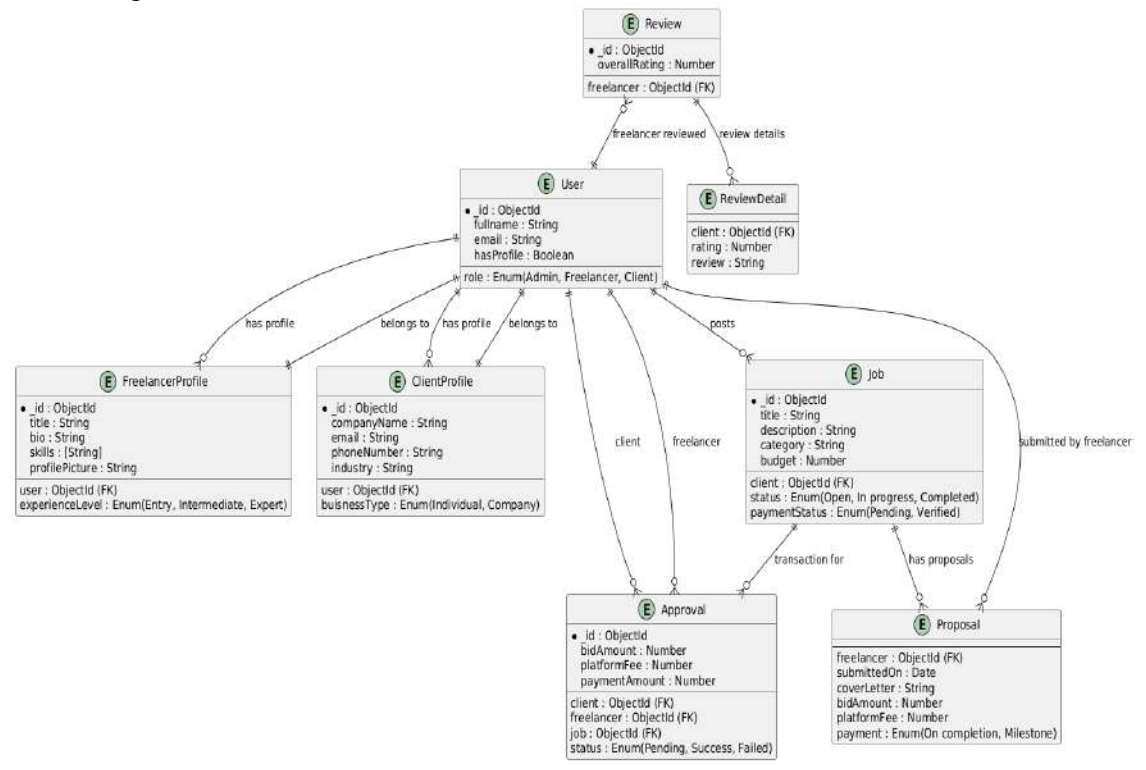


Figure 3.4: Entity Relationship Diagram of the System

4.0 System Implementation

This section presents a summary of the technical tools employed and the procedures followed for system testing and system evaluation.

4.1 Technical Tools Used

This section outlines the technical tools used in the development and implementation of the proposed system.

The frontend: ReactJS & Tailwind CSS are the technologies selected for the development of the frontend, ensuring accessibility.

The backend: ExpressJS was utilized for server-side scripting to manage user interactions.

Database: MongoDB was employed to create a non-relational database for securely storing user data, job information, and transaction records.

Web server: Nodejs web server is selected, it is the best choice for its security, reliability, and availability.

4.2 System Testing

System testing is a crucial process in ensuring the developed system functions correctly, is secure, and provides a seamless user experience.

4.2.1 Functional Testing

Functional testing is one of the important phases of the software development life cycle. It means validation of functionality, performance, and reliability of a system regarding whether each part of the system works as expected. The test case of the system is categorized into three main roles: Admin, Freelancer, and Client. Each role has specific functionalities that were tested to ensure the



system performs as intended. The test case table for admin requirements is presented in Table 4.1, the test case table for freelancer requirements in Table 4.2, and the test case table for client requirements in Table 4.3

Table 4.1 Admin Requirements

1 abic 4	.1 Aunim Keq	un ements			
Test	Function	Description	Expected Result	Actual Result	Status
Id					
A001	User	Admin can	Users are	Registration	Successful
	Registration	register new	registered	works, and users	
		users	successfully	are added to the	
		(Freelancer,	with proper role	system with	
		Client)	assignments	roles	
A002	User	Admin can view	Admin can	Admin can	Successful
	Management	and manage all	update, delete,	successfully	
		registered users	or view user	manage users	
			details		
A003	Project	Admin can view	All projects	Admin can see	Successful
	Monitoring	all posted	posted are	all projects in the	
		projects	visible to the	system	
			admin		
A004	Payment	Admin can view	Admin can view	Admin can	Successful
	Monitoring	transaction status	s transaction	access	
		and manage	details and	transaction data	
		payments	payment status	without issues	
A005	Escrow	Admin can make	•	Admin can make	Successful
	Payment	payment to the	processed	payments to the	
	Disbursement		successfully	freelancer for	
		completed		completed work	
	5.1 0 5	projects			
A006	Platform Fee	Admin can view	Admin can	Admin can	Successful
	Management	and manage	update, delete,	successfully	
		platform fees for	•	manage the	
		both roles	fees	platform fee	
Toble 4	2 Encoloneer l	Daguinamanta			
Table 4	.2 Freelancer 1 Function	Description	Expected Result	Actual Result	Status
Id	runction	Description	Expected Result	Actual Result	Status
F001	Profile	A freelancer can	Profile is created	Profile creation	Successful
1001	Creation	create and update	and details are	and updating	Successiui
	Cication	their profile	visible to clients	work as expected	
F002	Project	A freelancer can	Bid is successfully	The bidding	Successful
1002	Bidding	submit bids on	placed on the	process works	Successiui
	Didding	projects	project	without issues	
		Projects	Project	,, 1011000 100000	



F003 Project A freelancer can Work is Freelancers can Successful Submission submit work for submitted, and the submit work review client can review it successfully

Table 4.3 Client Requirements

Test	Function	Description	Expected Result	Actual Result	Status
Id					
C001	Profile	The client can	Profile is created	Profile creation	Successful
	Creation	create and update	and details are	and updating	
		their profile	visible to clients	work as expected	
C002	Project	Client can post	The project is	Projects can be	Successful
	Posting	projects for	posted and	posted	
		freelancers to bid	visible to	successfully	
		on	freelancers		
C003	Escrow	Client can make	Payment is made	Escrow payment	Successful
	Payment	an escrow	successfully	works as	
		payment for the		expected	
		job posting			
C004	Bid Review	Client can review	The client can	Bid review and	Successful
		and accept/reject		management	
		freelancer bids	make decisions	work as expected	
C005	Project	The client can	Work is	Approval system	Successful
	Approval	approve the	approved, and	functions without	
		freelancer's	the freelancer	issues	
		submitted work	gets paid		
C006	Payment	Client can	Payment is	Payment	Successful
	Confirmation	confirm payment	confirmed	confirmation	
		after work	successfully	works as	
		completion		expected	

4.2.2 Usability Testing

Usability testing was conducted to evaluate the system's user-friendliness, ease of navigation, and how well users could complete essential tasks on the freelance marketplace platform. The aim was to ensure that users could interact with the system effectively without confusion or difficulty, and to identify areas for improving the user experience across different user roles.

4.2.3Security Testing

Security testing was performed to ensure the platform is secure against potential vulnerabilities and threats, safeguarding user data and preventing unauthorized access. The primary focus was on identifying weaknesses in authentication, data storage, and input handling while ensuring compliance with best security practices. The testing aimed to address common security concerns, including cross-site scripting (XSS), data encryption, improper access control, and token-based security. Figure 4.1 illustrates the code for input validation and password hashing.



```
const { fullname, email, password, role } = req.body;

// Check if user already exists
const exist = await Users.findOne({ email });
if (exist) {
    return res.status(400).json({ message: "Email already exists" });
}

// Validate required fields
if(!fullname, !email, !password, !role){
    return res.status(400).json({ message: "All fields are required" });
}

// Hash the password
const hashedPassword = await hashPassword(password);
```

Figure 4.1: Vulnerability testing

4.3 Interfaces

The user interface of the freelance marketplace system is designed to be intuitive, user-friendly. It serves as the primary interaction point for users, including clients, freelancers, and administrators, allowing seamless access to system features.

4.3.1 Registration Page

Provides general information about the platform and easy navigation to login or register, where user can create their account as shown in Figure 4.2.

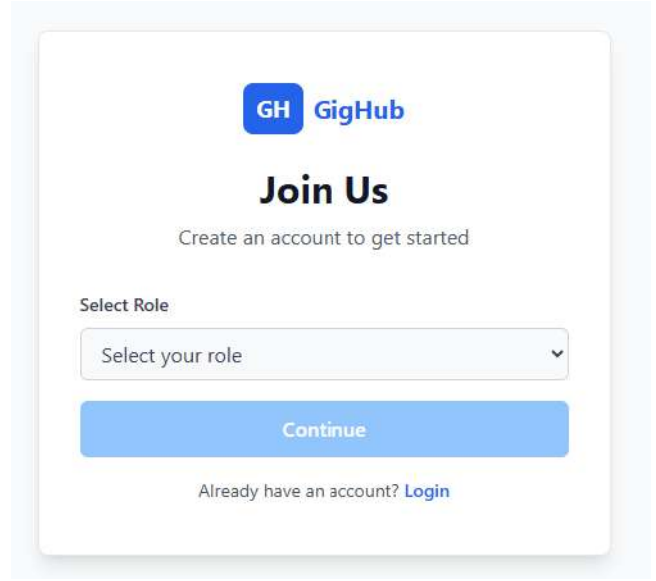


Figure 4.2: Registration Page



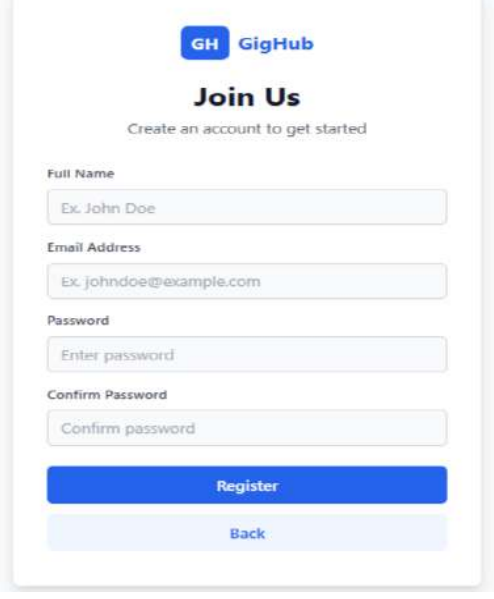


Figure 4.2: Registration Page

4.3.2 Login page

The login page is designed to authenticate users securely before granting access to the platform. Figure 8 demonstrates it. Where the user can log in to their account as shown in Figure 4.3.

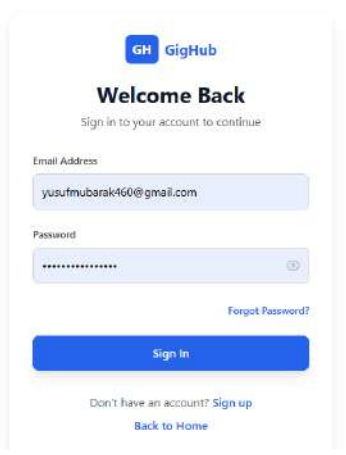


Figure 4.3: login page

4.3.3 Admin dashboard

Accessible to administrators for managing users, managing categories, and configuring system settings, as seen in Figure 4.4.



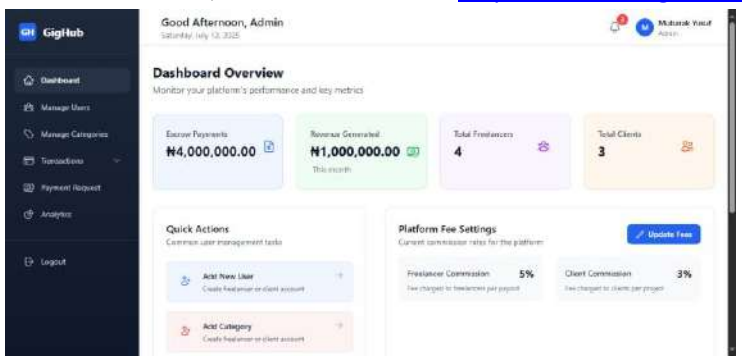


Figure 4.4: Admin dashboard

4.3.4 Client Dashboard

This is the page where clients have access to post jobs, view proposals and view hired freelancers. The dashboard is shown in Figure 4.5

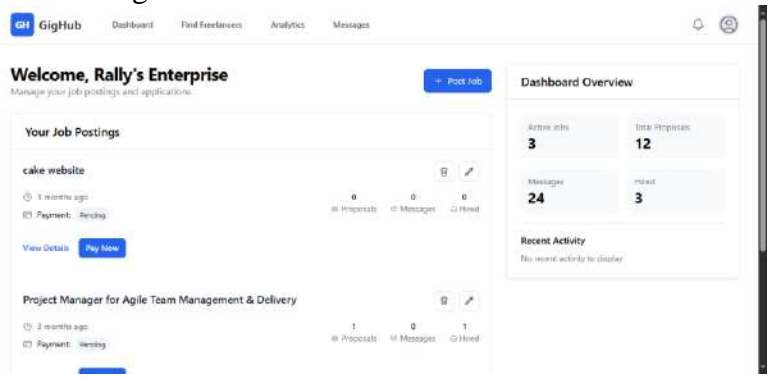


Figure 4.5: Client Dashboard

4.3.5 Freelancer Dashboard

This is the page where freelancers have access to jobs posted by clients, submit proposals, and find jobs. The dashboard is shown in Figure 4.6

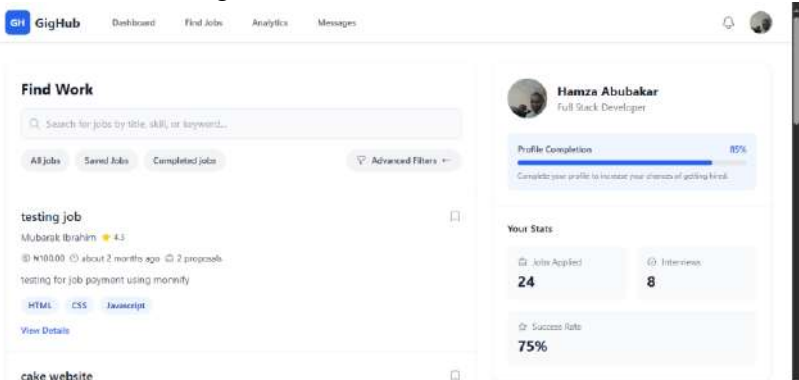


Figure 4.6: Freelancer Dashboard

4.3 SYSTEM EVALUATION

System evaluation is conducted to assess the overall performance, functionality, and user experience of the developed system. It ensures that the system meets the specified requirements and performs efficiently in real-world scenarios. The evaluation process includes:

i. **Performance Assessment**: Measuring the system's speed, responsiveness, and efficiency under different conditions.



- ii. **Functionality Verification**: Ensuring that all features operate correctly as per the system requirements.
- iii. **Security Evaluation**: Verifying that authentication, authorization, and data protection mechanisms work effectively.
- iv. **User Feedback**: Collecting input from test users to identify areas for improvement and enhance usability.

5.0 CONCLUSION

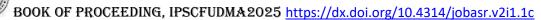
The freelance marketplace system effectively achieves its objective of providing a secure, intuitive, and functional platform for freelance service exchange. Through the integration of modern development technologies such as the MERN stack and features like JWT-based authentication, project bidding, escrow payments, and role-based access control, the system ensures reliability and scalability. Comprehensive testing validated the system's ability to support seamless interactions among administrators, freelancers, and clients. The inclusion of secure transaction mechanisms, profile management, and dynamic dashboards has significantly enhanced user experience and operational efficiency. Ultimately, the developed platform bridges the gap between clients and skilled professionals, offering a robust solution to the challenges faced in freelance job management within the digital economy.

References

- A, D., & R, T. (2024). Exploring the Challenges and Opportunities of Implementing Flexible Work Arrangements. *Shanlax International Journal of Management*, 11(S1-Mar), 139–144. https://doi.org/10.34293/MANAGEMENT.V11IS1-MAR.8033
- Abdreissova, D. Zh., Baitenizov, D. T., Azatbek, T. A., & Valieva, S. N. (2022). Freelance Market Development Factors. *Economics: The Strategy and Practice*, 16(4), 188–207. https://doi.org/10.51176/1997-9967-2021-4-188-207
- Al-Saqqa, S., Sawalha, S., & Abdelnabi, H. (2020). Agile Software Development: Methodologies and Trends. *Int. J. Interact. Mob. Technol.*, 14(11), 246–270. https://doi.org/10.3991/IJIM.V14I11.13269
- Arora, K., Vaishnavi, & Nagpal, J. (2023). Implementation of MERN: A Stack of Technologies to Design Effective Web-Based Freelancing Applications. *International Journal of Scientific Research in Computer Science,s Engineering and Information Technology*, 23–32. https://doi.org/10.32628/CSEIT23902104
- Asanaka, R., & Inoue, M. (2023). Gig Work Systems Design for Dynamic Work Management with Freelancers. 2023 IEEE International Conference on Systems, Man, and Cybernetics (SMC), 3534–3539. https://doi.org/10.1109/SMC53992.2023.10393878
- Blaising, A., & Dabbish, L. (2022). Managing the Transition to Online Freelance Platforms: Self-Directed Socialization. *Proceedings of the ACM on Human-Computer Interaction*, 6, 1–26. https://doi.org/10.1145/3555201
- Deshmukh, P., Kalwaghe, S., Appa, A., & Pawar, A. (2020). Decentralised Freelancing using Ethereum Blockchain. 2020 International Conference on Communication and Signal Processing (ICCSP), 881–883. https://doi.org/10.1109/ICCSP48568.2020.9182127
- Gu, G., & Zhu, F. (2021). Trust and Disintermediation: Evidence from an Online Freelance Marketplace. *Manag. Sci.*, 67(2), 794–807. https://doi.org/10.1287/MNSC.2020.3583
- Guerra, J. A., Guerrero, J. I., García, S., Domínguez-Cid, S., Larios, D. F., & León, C. (2022). Design and Evaluation of a Heterogeneous Lightweight Blockchain-Based Marketplace. *Sensors (Basel, Switzerland)*, 22(3). https://doi.org/10.3390/S22031131
- Hasan, N. Bin. (2025). The Growth of Online Freelancing in Bangladesh: Economic Integration and Labor Vulnerability. *International Journal of Research and Innovation in Social Science*, *IX*(IV), 3112–3118. https://doi.org/10.47772/IJRISS.2025.90400230



- Huang, J., Ma, N. F., Rivera, V. A., Somani, T., Lee, P. Y. K., McGrenere, J., & Yoon, D. (2024). Design Tensions in Online Freelancing Platforms: Using Speculative Participatory Design to Support Freelancers' Relationships with Clients. *Proceedings of the ACM on Human-Computer Interaction*, 8(CSCW1), 1–28. https://doi.org/10.1145/3653700
- Kautsar, D. S., Syukriah, F., Kristyawati, D., & Jamilah. (2023). Design and Build Web-Based Freelance Applications. *International Journal Science and Technology*, 2(3), 24–35. https://doi.org/10.56127/IJST.V2I3.986
- Leung, W. F., D'Cruz, P., & Noronha, E. (2021). Freelancing globally: Upworkers in China and India, neo-liberalisation and the new international putting-out system of labour (NIPL). *Work and Labour Relations in Global Platform Capitalism*, 134–156. https://doi.org/10.4337/9781802205138.00015
- Ludwig, S., Herhausen, D., Grewal, D., Bove, L., Benoit, S., de Ruyter, K., & Urwin, P. (2022). Communication in the Gig Economy: Buying and Selling in Online Freelance Marketplaces. *Journal of Marketing*, 86(4), 141–161. https://doi.org/10.1177/00222429211030841
- Mahomodally, A. F. H., & Suddul, G. (2022). An Enhanced Freelancer Management System with Machine Learning-based Hiring. *Shanlax International Journal of Arts, Science and Humanities*, 9(3), 34–41. https://doi.org/10.34293/SIJASH.V9I3.4405
- Munoz, I., Dunn, M., Sawyer, S., & Michaels, E. (2022). Platform-mediated Markets, Online Freelance Workers and Deconstructed Identities. *Proceedings of the ACM on Human-Computer Interaction*, 6, 1–24. https://doi.org/10.1145/3555092
- Novica, F., Ramadanis, Adriansyah, M. D., Alamsyah, M. F., Meinita, R., Putra, T., Satriawan, & Firmansyah, R. (2022). PERANCANGAN WEBSITE MARKETPLACE BERBASIS PHP DENGAN FRAMEWORK CODEIGNITER. *Jurnal Informatika Dan Tekonologi Komputer (JITEK)*, 2(2), 190–197. https://doi.org/10.55606/JITEK.V2I2.289
- Rauf, I., Petre, M., Tun, T., Lopez, T., & Nuseibeh, B. (2023). Security Thinking in Online Freelance Software Development. *Proceedings International Conference on Software Engineering*, 2023-May, 13–24. https://doi.org/10.1109/ICSE-SEIS58686.2023.00008
- Shilpa, K. S., Kishore, B., Neil, P., Jain, N., & Jain, J. (2022). Blockchain Based Freelancing System. *Smart Innovation, Systems and Technologies*, 273, 315–327. https://doi.org/10.1007/978-3-030-92905-3_41
- Tawami, T., & Djauhari, H. A. (2020a). Online Freelance Marketplaces as a Business Opportunity. *Proceeding of International Conference on Business, Economics, Social Sciences, and Humanities*, 1, 340–345. https://doi.org/10.34010/ICOBEST.V1I.57
- Tawami, T., & Djauhari, H. A. (2020b). Online Freelance Marketplaces as a Business Opportunity. *Proceeding of International Conference on Business, Economics, Social Sciences, and Humanities*, 1, 340–345. https://doi.org/10.34010/ICOBEST.V1I.57
- Tokaeva, B. B. (2024). FREELANCING AS A NEW FORM OF STAFF EMPLOYMENT IN THE LABOR MARKET. *EKONOMIKA I UPRAVLENIE: PROBLEMY, RESHENIYA*, 10/6(151), 60–67. https://doi.org/10.36871/EK.UP.P.R.2024.10.06.007
- Xia, L., Baghaie, S., & Mohammad Sajadi, S. (2024). The digital economy: Challenges and opportunities in the new era of technology and electronic communications. *Ain Shams Engineering Journal*, 15(2). https://doi.org/10.1016/J.ASEJ.2023.102411
- Yakubovska, N., Savushchyk, A., & Martseniuk, V. (2024). CURRENT TRENDS IN FREELANCE AS A LEVER OF EFFICIENT PERSONNEL MANAGEMENT IN THE CONDITIONS OF DIGITALIZATION. *Black Sea Economic Studies*, 86. https://doi.org/10.32782/BSES.86-30



Monthly Artificial Neural Network (ANN) Models to Estimate OMI-Derived Absorbing Aerosol Index (OMI-AI) Using Ground Meteorology in North-Central Nigeria

Mukhtar Abubakar Balarabe^{1&2}

¹Department of Physics Umyu Katsina ²Muhammadu Buhari Meteorological Institute of Science and Technology (MBMIST), Katsina E-mail: mukhtarbalarabea@gmail.com

Abstract

This study presents daily predictive models of the Ozone Monitoring Instrument Aerosol Index (OMI-AI) over Nigeria's north-central region, by training multi-layer feed-forward and cascade neural networks using routine meteorological variables of monthly visibility, air temperature, and relative humidity. Two distinct training algorithms were compared: Bayesian regularization (trainbr) and Levenberg–Marquardt (trainlm). Each neural architecture was configured with hidden-layer neuron pairs of 3-3, 6-6, 7-7, 15-15, and 20-20, and for each configuration, the models were independently trained twenty times. The single best-performing run (highest R², lowest error) per neuron count was recorded each month across all twelve calendar months. Performance varied seasonally: models achieved the highest predictive accuracy during the dry Harmattan period (November through March) with peak performance in January while accuracy declined during the wet season (April through October), reaching its lowest in July and August, despite generally low RMSE values. Across all months and architectures, feed-forward networks outperformed cascade networks. Additionally, training with Levenberg–Marquardt consistently produced faster convergence (lower epoch counts) and lower RMSE than Bayesian regularization.

1. Background of the Study

Aerosols are minute solid or liquid particles suspended in the atmosphere, typically ranging from a few nanometers to several micrometers in size. These particles originate from both **natural** and **anthropogenic sources**, including desert dust, sea spray, volcanic ash, forest fires, industrial emissions, vehicular exhaust, and biomass burning (Balarabe et al., 2015a). According to Oyem and Igbafe (2010), aerosol particles comprise a diverse mix of substances such as dust, soot, organic compounds, gaseous pollutants, and biological matter.

Once emitted, aerosols are dispersed throughout the atmosphere via **turbulent mixing**, **convective uplift**, and **regional to global-scale circulations**. Their atmospheric distribution is further influenced by meteorological factors like wind speed, humidity, and temperature gradients. Aerosols are eventually removed from the atmosphere through processes such as **dry deposition**, **wet scavenging** by precipitation, **cloud condensation**, and **gravitational settling** with larger particles tending to settle faster and thus exhibiting **shorter atmospheric residence times** (**Balarabe et al., 2015b**).

In contrast, **finer aerosols**, particularly those arising from urban emissions and biomass combustion, can remain aloft in the atmosphere for **days to several weeks**, facilitating their long-range transport across continents. These finer particles are often more chemically reactive and have a greater impact on **air quality**, **human health**, and **climate systems** (NASA Earth Observatory, 2023).



Aerosol emissions and concentrations are highly **variable in space and time**, exhibiting strong seasonal, regional, and diurnal fluctuations. Their physical and chemical properties such as size distribution, hygroscopicity, optical characteristics, and chemical composition differ significantly depending on the source and atmospheric processing. This complexity makes aerosol characterization a significant challenge in climate modeling, satellite retrieval, and environmental monitoring.

Recent studies emphasize that understanding the **spatio-temporal dynamics** and **chemical makeup** of aerosols is crucial, given their role in **modulating the Earth's radiative balance**, **cloud microphysics**, and **public health risks** (Gao et al., 2024; IPCC, 2023). Advanced remote sensing and ground-based observations now support more precise aerosol type classification, helping researchers better estimate their climatic and ecological impacts.

Daily PM_{2.5} forecasting was conducted in Dakar, Senegal (West Africa) with LSTM (2025) with LSTM outperformed ARIMA for 1–7-day forecasts with test RMSE of 3.2 μg/m³), capturing dust-driven extremes (Gueye et al., 2025). Estimation of ground PM_{2.5} was carried out from MODIS MAIAC AOD in Kampala, Uganda comparing MLR, Random Forest, and Multi-Layer Perceptron (ANN), evaluated performance and cloud-related data gaps in a data-sparse African city (Adong et al., 2025). In Nigeria, Neural-network was used for the retrieval of ground-level fine AOD (AOD) from satellite AOD, AERONET AOD and meteorological data to during COVID-era changes from 2001–2020 (Etchie et al., 2021)

Despite this central role of dust aerosol in Nigeria's climate system, observational studies remain limited due to sparse ground monitoring stations, inconsistently sampled time periods, seasonal data gaps, and cloud interference. These challenges restrict the reliability of satellite-derived Aerosol Optical Depth (AOD) and Aerosol Index (AI) records over the region.

Previous efforts to estimate aerosol metrics have utilized statistical techniques simple and multiple linear regression models to predict AOD and AI from meteorological inputs. While these linear models offer some predictive power, they are inherently constrained in capturing the complex, nonlinear relationships characteristic of aerosol meteorology interactions.

In contrast, **Artificial Neural Networks (ANNs)** offer a more flexible modeling framework capable of learning nonlinear mappings between input meteorological variables and outputs such as AOD or AI. ANN-based modeling has been successfully applied in diverse environmental applications from solar radiation and rainfall to air quality forecasting demonstrating superior performance over traditional regression methods (Fakiyesi, 2025).

In Nigeria, specific ANN studies include feed-forward and cascade back propagation networks trained to estimate daily AOD in Ilorin using visibility and relative humidity achieving reliable predictive accuracy (explaining over 70% of AOD variance) with the Levenberg–Marquardt algorithm often outperforming Bayesian regularization <u>Balarabe</u> & Isah, 2019). Additionally, national-scale monitoring in Kaduna has employed feed-forward backprop ANN to forecast air pollution indices at multiple stations using local meteorological and pollutant data.

Nevertheless, the application of ANNs for monthly prediction of **Aerosol Index (AI)** especially in the context of Saharan dust events in Nigeria remains underexplored.

Therefore, present study aim to develop and evaluate **multi-layer feed-forward** and **cascade-back propagation ANN models** to predict monthly OMI-AI in North Central Nigeria using meteorological variables **monthly visibility, temperature, and relative humidity.**

The rationale: capture the **nonlinear relationship** between meteorological drivers and absorbing aerosol presence that linear regression models cannot fully resolve.



2. Data, sources and Methodology

2.1 Data and Sources

Meteorological datasets were acquired from the NOAA/National Climatic Data Center (NCDC) via the Climate Data Online (CDO) portal. Specifically, monthly averages of visibility, temperature, and relative humidity spanning 2004–2024 were retrieved, quality-controlled, and exported into Excel for processing and analysis. The NCDC provides global, long-term climatological records using integrated surface data, ensuring consistency across station outputs and covering multiple decades across thousands of monitoring sites (Balarabe et., 2015a). These variables are included in the Local Climatological Data (LCD) and Monthly Climatic Data for the World (MCDW) products both widely used in environmental and climate research (NCDC, MCDW)

For the aerosol component, monthly mean **Aerosol Index** (**AI**) data were sourced from the **Ozone Monitoring Instrument OMI** archives, maintained by NASA's Goddard Earth Sciences Data and Information Services Center (GES DISC). OMI and TOMS delivers a long-term record of UV-absorbing aerosols particularly mineral dust and smoke using near-UV backscatter measurements from Nimbus-7 and Earth Probe missions. These data were downloaded from the official OMI portal for the same period (**2004–2024**) period, matching the meteorological dataset. OMI AI is a qualitative measure derived from spectral contrast between measured and modeled UV radiances, it effectively flags regions of elevated absorbing aerosol loading. TOMS long-term continuity (1979-present through OMI) makes it highly valuable for climatological studies

2.2 Methodology

For each station within the study zone, monthly records of Aerosol Index (AI), visibility, air temperature, and relative humidity were chronologically organized from January through December over the entire study period. To derive the zonal monthly climatology, the corresponding monthly values (i.e., all January data, all February data, and so on) from each station were averaged across years, and subsequently, the spatial mean was calculated by averaging the monthly values across all stations. This approach provides representative monthly means for the zone. These segmentation was based on prior climatological studies over West Africa (Anuforom 2007; Balarabe & Shuaibu, 2021), which demonstrate clear differences in aerosol loading and characteristics between these periods

Two back propagation training algorithms were tested: **Levenberg–Marquardt** (**trainlm**) and **Bayesian regularization** (**trainbr**). These are commonly used in environmental ANN modeling because **trainlm often yields faster convergence and lower error**, while **trainbr helps prevent over fitting in complex, noisy datasets**. A series of network architectures was evaluated, varying the number of neurons in two hidden layers:

Configurations tested: (3-3), (6-6), (7-7), (15-15), and (20-20) neurons. Each architecture was trained **multiple times** (20 runs in this study) to account for variance due to random initialization. The performance was assessed using the **highest coefficient of determination** (**R**²) and **lowest root-mean-square error** (**RMSE**). This procedure aligns with standard best practices in ANN experimentation seen in air quality and aerosol forecasting literature (Balarabe & Isah 2019).

The dataset was split into **75% training** and **25% testing** subsets, randomly sampled at the start of the modeling process. Training data thus comprised the majority of the time series, allowing the network to learn predominant meteorological—aerosol relationships. All input the variables



including **visibility**, **temperature**, **and relative humidity** were **normalized** (e.g., via mapminmax in MATLAB toolkit), ensuring that each variable contributes proportionately during training, a widely recommended preprocessing step in ANN modeling.

This split strategy supports robust evaluation of predictive skill while guarding against over fitting and temporal bias.

3.0 Results and Discussion

3.1 Model Performance Evaluation and Seasonal Sensitivity

The proposed Artificial Neural Network (ANN) models comprising both feed forward and cascade architectures were trained using two optimization algorithms: **Bayesian Regularization (trainbr)** and **Levenberg–Marquardt (trainlm).** Across the study period, these models demonstrated strong predictive capabilities for estimating monthly **Aerosol Index (AI)** values, with **feed forward networks consistently outperforming cascade-forward networks** in terms of accuracy and generalization.

Even though, performance varied notably across months and between the two algorithms. However, both models achieved higher predictive accuracy during the Harmattan season (November to March), coinciding with increased atmospheric aerosol loading from Saharan dust transport. In contrast, model performance declined during the wet season (April to October), particularly in July and August, despite overall low Root Mean Square Error (RMSE) values across most months (Table 1 and 2).

Table 1: Summary of Model Performance for Trainbr and Trainlm for feed forward Algorithms across Months

Month	Season	Trainbr R ²	Trainbr	Testbr	Epoch	Trainlm	Trainlm	Testlm	Epoch
			RMSE	R ²	-	R ²	RMSE	R ²	-
November	Harmattan	0.892	0.004	0.750	110	0.822	0.003	0.700	11
December	Harmattan	0.912	0.003	0.760	109	0.850	0.002	0.720	10
January	Harmattan	0.993	0.003	0.844	100	0.983	0.001	0.800	9
February	Harmattan	0.901	0.003	0.760	106	0.844	0.002	0.721	11
March	Harmattan	0.900	0.004	0.759	106	0.80	0.003	0.709	11
April	Summer	0.814	0.004	0.674	240	0.745	0.004	0.644	12
May	Summer	0.782	0.005	0.641	300	0.715	0.004	0.613	13
June	Summer	0.863	0.004	0.723	251	0.790	0.005	0.693	11
July	Summer	0.794	0.005	0.654	290	0.724	0.004	0.624	13
August	Summer	0.679	0.007	0.600	293	0.634	0.005	0.587	15
September	Summer	0.893	0.003	0.754	243	0653	0.005	0.724	15
October	Summer	0.898	0.003	0.765	247	0.821	0.003	0.743	11



Table 1: Summary of Model Performance for Trainbr and Trainlm for Cascade Algorithms Across Months

Month	Season	Trainbr R ²	Trainbr RMSE	Testbr R ²	Epoch	Trainlm R ²	Trainlm RMSE	Testlm R ²	Epoch
Novembe r	Harmattan	0.782	0.006	0.684	210	0.732	0.005	0.681	10
December	Harmattan	0.800	0.004	0.704	190	0.750	0.004	0.730	12
January	Harmattan	0.789	0.005	0.753	200	0.756	0.003	0.783	11
February	Harmattan	0.880	0.004	0.674	360	0.894	0.004	0.701	10
March	Harmattan	0.790	0.006	0.669	300	0.720	0.006	0.699	10
April May June July	Summer Summer Summer Summer	0.764 0.730 0.817 0.746	0.006 0.007 0.005 0.007	0.645 0.611 0.693 0.635	540 350 451 390	0.725 0.695 0.771 0.712	0.007 0.007 0.008 0.006	0.604 0.583 0.650 0.590	12 15 13 10
August	Summer	0.629	0.009	0.580	900	0643	0.008	0.547	14
September	Summer	0.843	0.006	0.743	500	0.614	0.008	0.684	14
October	Summer	0.848	0.005	0.735	850	0.811	0.005	0.700	10

For the feed forward, the highest accuracy was recorded in January, with R² values of 0.993 for trainbr and 0.983 for trainlm, while February with R² value of 0.880 for trainbr and 0.894 for trainlm, reflecting the models' strong fit during periods of intense dust activity. The lowest performances were observed during the peak of the rainy season, for both Feed forward and cascade with trainbr scoring 0.679 in August and trainlm dropping to 0.653 in September for Feed forward while 0.629 for trainbr and 0.614 for train lm in the Cascade. Secondary performance peaks were evident in October (trainbr) and February (trainlm), aligning with the seasonal aerosol build-up that begins in late autumn, peaks in winter, and declines during the onset of the wet season a pattern that repeated consistently year after year.

When comparing network architectures, **feed forward models achieved R**² **scores ranging from 0.653 to 0.993**, whereas **cascade-forward networks ranged from 0.629 to 0.880**. This highlights the superior learning and generalization capacity of feed forward configurations across diverse seasonal subsets.

3.2. Algorithm Comparison and Training Dynamics

Between the two training algorithms, **Levenberg–Marquardt** (**trainlm**) consistently demonstrated superior computational efficiency, achieving **faster convergence** (**fewer training epochs**) and lower RMSE than **Bayesian Regularization** (**trainbr**). While trainbr occasionally produced slightly higher R² scores, particularly in the Harmattan months, **trainlm proved more**

BOOK OF PROCEEDING, IPSCFUDMA2025 https://dx.doi.org/10.4314/jobasr.v2i1.1c stable and efficient overall, making it more suitable for large-scale or time-sensitive aerosol prediction tasks.

3.3. Error Metrics and Generalization Performance

RMSE values remained **consistently low across all models**, confirming the models' ability to minimize predictive error effectively. Moreover, **R**² values in the test phase closely mirrored those from training, indicating balanced generalization and minimal overfitting—an essential characteristic of robust machine learning models in atmospheric prediction tasks.

3.4. Comparison with Existing Studies

These findings align with previous research in ANN-based aerosol modeling. For instance, Balarabe and Isah (2019), in their study of Aerosol Optical Depth (AOD) prediction over Ilorin, reported similar patterns: feedforward networks trained with trainlm achieved lower RMSE and faster convergence compared to cascade models, while still maintaining high R² values across seasons.

In broader applications such as **air pollution forecasting** (e.g., $PM_{2.5}$ and PM_{10}), comparative studies have also shown **trainlm to offer faster convergence and low error**, whereas **trainbr sometimes yields marginally higher R values**, particularly under complex or noisy datasets. For instance, in $PM_{2.5}$ prediction tasks, trainbr has been reported to reach $R \approx 0.978$ under optimal conditions.

4.0 Conclusion

This study successfully developed Artificial Neural Network (ANN) models to predict monthly Absorbing Aerosol Index (AI) using visibility, relative humidity, and temperature as inputs, comparing both feed-forward and cascade-forward architectures trained with Bayesian regularization (trainbr) and Levenberg–Marquardt (trainlm) algorithms. Both models achieved excellent predictive performance high coefficients of determination (R²) and low RMSE across seasons. The feed-forward architecture delivered slightly better results than cascade-forward, and networks trained via trainlm converged faster and with marginally lower errors than trainbr, though both were robust.

Crucially, the high fidelity of these ANN models offers actionable utility for air quality management in North-Central Nigeria. First, where ground-based aerosol monitoring remains limited, these models can serve as proxies to infer spatial and temporal trends in aerosol burden, supporting agencies like the National Environmental Standards and Regulations Enforcement Agency (NESREA) in filling data gaps. Secondly, as Nigeria moves to establish air quality monitoring stations and roll out a national clean air policy (e.g., the "Brea the Easy Nigeria" campaign), the monthly ANN-derived AI estimates can help prioritize deployment sites and evaluate intervention impacts. Third, given Nigeria's high burden of air pollution—related morbidity and mortality (with mean PM_{2.5} levels far exceeding WHO recommendations), the results could inform public health risk assessments, especially during hazard-prone periods like the Harmattan season.

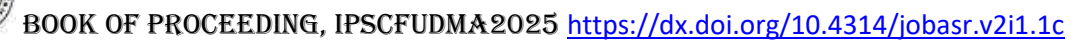
Taken together, the strong performance of this ANN framework not only advances methodological novelty but also positions it as a **practical tool for environmental policy and health protection**



facilitating data-driven decision-making in contexts with sparse monitoring infrastructure, guiding strategic investments in monitoring networks, and supporting public communication of aerosol exposure trends in Nigeria.

References

- Adong, P., Bainomugisha, E. & Dev, S. Evaluating machine learning methods for PM_{2.5} estimation using satellite AOD, low-cost and reference-grade monitors in Kampala. *Int. J. Environ. Sci. Technol.* (2025). https://doi.org/10.1007/s13762-025-06674-0
- Anuforom, A., Akeh, L. Okeke, P. & Opara F. (2007). Inter annual variability and long-term trend of UV-absorbing aerosols during Harmattan season in sub-Saharan West Africa", Atmospheric Environment, (41) 1550-1559.
- Balarabe, M., Abdullah, K. & Nawawi, M.2015a. LongTerm Trend and Seasonal Variability of Horizontal Visibility in Nigerian Troposphere. Atmosphere, 6,1462-1486.
- Balarabe M., Abdullah, K., & Nawawi, M. 2015. Seasonal Variations of Aerosol Optical Properties and Identification of Different Aerosol Types Based on AERONET Data over Sub-Sahara West-Africa. Atmospheric and Climate Sciences, 6(01), 13.
- Balarabe, M. A., & Isah, M. N., (2019) Feed-Forward And Cascade Back Propagation Artificial Neural Network Models For Predicting Aerosol Optical Depth In Ilorin-Nigeria. Fudma Journal of Sciences (FJS). Vol. 3 No. 1, March, 2019, pp 428 433
- Balarabe M. A., & Shuaibu S. (2021). Monthly And Seasonal Variability Of Aerosol Radiative Properties And Direct Radiative Effects In Ilorin-Nigeria. Katsina Journal of Natural and Applied Sciences VOL. 10 No. 2 September, 2021 (ISSN: 2141-0755)
- Fakiyesi, T. J. A Comparative Study of the Effectiveness of Four Artificial Neural Network (ANN) Models in Predicting Air Pollution Levels in a Nigerian Urban Metropolis.
- Etchie TO, Etchie AT, Jauro A, Pinker RT, Swaminathan N. Season, not lockdown, improved air quality during COVID-19 State of Emergency in Nigeria. Sci Total Environ. 2021 May 10;768:145187. doi: 10.1016/j.scitotenv.2021.145187. Epub 2021 Jan 21. PMID: 33736334; PMCID: PMC7825968.
- Gao, Y., Zhang, Y., & Li, X. (2024). Characterization and impact of atmospheric aerosols on regional climate and public health. Environmental Research Letters. https://iopscience.iop.org/article/10.1088/1748-9326/ad11b3
- Gueye, A.; Niang, S.A.A.; Diallo, I.; Dramé, M.S.; Diallo, M.; Younous, A.A. On the Application of Long Short-Term Memory Neural Network for Daily Forecasting of PM2.5 in Dakar, Senegal (West Africa). *Sustainability* **2025**, *17*, 5421. https://doi.org/10.3390/su17125421
- IPCC Sixth Assessment Report (2023). *Climate Change 2023: The Physical Science Basis*. https://www.ipcc.ch/report/ar6/wg1/
- NASA Earth Observatory. (2023). *Aerosols and Climate*. https://earthobservatory.nasa.gov/features/Aerosols
- NOAA NCDC MCDW (2025): https://www.ncdc.noaa.gov/IPS/mcdw/mcdw.html Oyem, A.A. and Igbafe, A.F. (2010) Analysis of Atmospheric Aerosol Loading over Nigeria. Environmental Research Journal, 4, 145-156.http://dx.doi.org/10.3923/erj.2010.145.156



Development of General and Season-Specific Multiple Linear Regression (MLR) Models for Estimating TOMS-Derived Absorbing Aerosol Index (TOMS-AI) in North-Central Nigeria

Mukhtar Abubakar Balarabe (Ph.D)

¹Department of Physics Umyu Katsina ²Muhammadu Buhari Meteorological Institute of Science and Technology (MBMIST), Katsina

E-mail: mukhtarbalarabea@gmail.com

Abstract

This study introduces a novel empirical multiple linear regression (MLR) model to estimate the Total Ozone Mapping Spectrometer Aerosol Index (TOMS-AI) in Nigeria's north-central zone. Using a 20-year time series of TOMS-AI measurements as the dependent variable, alongside 20 years (1984-2004) of meteorological predictors of Relative humidity (RH), visibility (VSB), and Sea Level Pressure (SLP) (sourced from NOAA-NCDC), the model performance was evaluated via coefficient of determination (R²) for calibration, root mean square error (RMSE) for both calibration and validation phases, and weighted mean absolute percentage error (wMAPE). The results reveal that MLR delivers high predictive accuracy when applied to overall year-round data, outperforming seasonal results (Harmattan vs. summer). During the Harmattan dry season, the MLR model ranked as the second-best predictor of AI in the region, while in the summer wet season, its effectiveness improved to a consistently reliable level. Comparative analysis shows the newly proposed MLR algorithm outperforms previously reported simple linear regression models in predicting aerosol index values.

1. Background of the study

Earth's atmosphere a gravity-bound envelope of gases sustains life by supplying breathable air, filtering harmful solar radiation, and supporting the global water cycle. It is comprised primarily of nitrogen, oxygen, and argon, with trace gases such as carbon dioxide and ozone. Embedded within this atmospheric medium lie **aerosols** a micro to submicron solid or liquid particles including dust, smoke, organic and pollutant matter. These particles are emitted from both natural and anthropogenic sources, dispersed by turbulence and large-scale circulation, and removed via precipitation, dew, ice formation, or sedimentation. Larger particles settle quickly, whereas fine particles from urban pollution and biomass burning can persist in the atmospheric column for extended periods (Balarabe et al., 2015).

Aerosol emissions are rising globally due to population growth, increased energy demand, urbanization, and changing meteorological patterns (Kaskaoutis et al.... 2012). Spatial and seasonal variability in aerosol concentration is also increasing globally. Africa particularly the Sahara–Sahel region is a dominant dust source, contributing roughly 400–700 million tonnes of mineral dust annually, much of it transported westward into West Africa (Nigeria inclusive) and beyond (Ayansina et al. 2019)

In Nigeria, aerosol dynamics are strongly influenced by Saharan dust carried into the country during the Harmattan/dry seasons. Long-term observations from Moderate Resolution Imaging



Spectroradiometer (MODIS) (2004–2023) show that aerosol optical depth (AOD) (a quantitative measure of aerosol concentration) in the atmosphere peaks in the North West and North Central regions during winter/spring, with values ranging from about 0.25 to 0.85 (Bello et al., 2025). Studies over Ilorin Nigeria further characterize aerosol types (notably desert dust and biomass burning), showing high AOD values up to 1.29 during February from aerosol robotic network (AERONET) data and CALIPSO, among other sources (Balarabe et al., 2016; Ali et al., 2024) Furthermore, Balarabe et al. (2019) analysis confirmed strong seasonal AOD variability in Nigeria: highest during Harmattan (November–March), lowest in the wet season (April–October), and influenced by movement of the Intertropical Discontinuity (ITD) and wind trajectories originating in the Sahara–Sahel region (Ayansina et al., 2019). Additionally, a research found significant seasonal aerosol loading in coastal zones and positive correlations between AOD and geopotential height as well as meteorological variables in Nigeria, further highlighting seasonal and spatial heterogeneity (Onyinyechi et al., 2025).

These aerosol dynamics have serious societal and environmental consequences in Nigeria. Previous researchs indicated that past Saharan dust events have caused fatal aircraft accidents and widespread flight disruptions due to severely reduced visibility (Adefolalu, 1984; Ogunjobi et al., 2012). In Sokoto State Nigeria, high dust concentrations have also been linked to increased hypertension cases during periods of low solar radiation and temperature (Balarabe et al., 2015). Despite these issues, **dust aerosol research in the Sahel region remains limited.** This is because, ground-based observation networks remain notably sparse across Nigeria. Furthermore, satellite-based metrics such as the TOMS Absorbing Aerosol Index (AI) suffer from orbital sampling limitations and data gaps due to cloud interference. In addition, existing aerosol models are predominantly global in scale, lacking resolution for local-scale phenomena. Consequently, few efforts have integrated satellite Aerosol Index (AI) with local meteorology parameters.

This study is therefore, aims to tackle these limitations by developing **general and season-specific empirical models** capable of estimating Total Ozone Mapping Spectrometer Aerosol Index (TOMS AI) for dust-weather monitoring in Nigeria's Sahel zone, with potential applicability to other data-scarce, Sahelian regions and worldwide. This will go a long way to compensate for **TOMS AI sampling gaps** stemming from satellite orbit and cloud contamination, produce **seasonally resolved models** (e.g., Harmattan/dry or summer/wet seasons) for more nuanced assessment of aerosol events using available **regional meteorological data.**

2. Data, Sources and Methodology

2.1.Meteorological data

Hourly weather records were obtained from NOAA's Climate Data Online portal (from the National Climatic Data Center/NCEI). This database provides globally archived, quality-controlled hourly observations (ncdc.noaa.gov). Eight operational meteorological stations located within Nigeria's Sahelian zone were selected. These stations are part of the GHCN-hourly network and included in NOAA's hourly summaries inventory for Nigeria (FIPS: NI), which lists approximately ten stations with nearly 100% data completeness from 1943 through mid-2025 ncdc.noaa.gov.

Since RH was not directly provided in the data files, it was computed using daily values of temperature (TEMP) and dew point (DEW), applying the Magnus–Teten formula:

 $RH = 100 \times [exp(17.625 \times DEW / (243.04 + DEW)) \div exp(17.625 \times TEMP / (243.04 + TEMP))]$



This empirical approach is widely used for deriving RH from temperature and dew point in climatological analyses.

2.2. Satellite-Derived TOMS Data

Total Ozone Mapping Spectrometer (TOMS) data covering 1984–2004 were downloaded from NASA's Earth data portal. The dataset used is Version 8 Level-2 or Level-3 gridded products, which include total column ozone, UV aerosol index, and surface reflectivity at ~1° × 1.25° spatial resolution, produced by NASA's Goddard Laboratory for Atmospheres and archived via the GES DISC (TOMS data catalog)

TOMS instruments were flown on various satellites including Earth-Probe (1996–2006) and were succeeded in January 2006 by the Ozone Monitoring Instrument (OMI) aboard NASA's Aura satellite. OMI continues the ozone/aerosol dataset with higher spatial resolution (~1°×1°) and additional trace gas observations (TOMS data.gov). TOMS data elements such as the UV aerosol index or total column ozone over Nigeria's Sahel were extracted for each study year (1984–2004). These satellite-derived indicators provide spatial and temporal coverage complementing the in-situ station observations, especially for monitoring aerosol patterns regionally.

2.3.Methodology

2.3.1. Model Development

The procedure for models development has extensively described in the work of Balarabe & Koko (2018); Balarabe and Isah 2019. However, in this study, it begins with explorative study before selecting **all candidate meteorological variables**: visibility (VSB), relative humidity (RH), and Sea level pressure (SLP). This followed by assessing the strength and direction of associations between each predictor and the aerosol index (AI) using **Pearson's correlation coefficients**.

A **full multiple regression model** is initially fitted:

$$AI = a_0 + a_1RH + a_2VSB + a_3SLP$$

Variables are then **eliminated sequentially** starting with the **least correlated** using **backward elimination**. At each step, removal of a variable is accepted only if the resulting change in **R**² **or RMSE** meets a threshold (drop or improvement) of **at least 5%**, following Noor et al. (2010) and Balarabe & Koko's criteria (2019). This criteria clearly revealed in table 1.

Modei	Table 1: AI models selection criteria	Ν-	RMSE
1	$a_0 + a_1(RH)$	0.53	0.4
2	$a_o + a_1(VSB)$	0.55	0.3
3	$a_0 + a_1(SLP)$	0.3	0.4
4	$ao + a_1(RH) + a_2(VSB)$	0.70	0.31
5	$ao + a_1(RH) + a_2(SLP)$	0.57	0.32
6	$ao + a_1(VSB) + a_2(SLP)$	0.60	0.33
7	$a_0 + a_1(RH) + a_2(VSB) + a_3(SLP)$	0.71	0.30



Variables whose removal leads to smaller (< 5%) changes in explanatory power or predictive error are considered **non-critical** and thus dropped; but if elimination causes a $\ge 5\%$ worsening in R² (or insufficient improvement in RMSE), the variable is retained as significant input.

This process yields a **reduced regression model**, $AI = a_1RH + a_2VSB$ equation (4) Implying that variable SLP was found not significant. Equation was identify was selected as the best model **using** high R^2 with low **RMSE**, in a minitab statistical software. Even though, it is obvious that all the models except 3 can effectively be utilize to retrieve AI. Additional diagnostics include checks for **multicollinearity**, **heteroscedasticity**, **autocorrelation**, and **normality of residuals**, consistent with standard regression assumption testing were carried out. Observations are **cleaned** by removing outliers seasonally and overall, then the dataset is **split into interleaved subsets** for calibration and validation. Seventy five percent (75%) of the data was used to calibration and 25% for validation. These data points were randomly selected to enable adequate representations of the data.

3. Results and Discussion

On the **calibration dataset**, model performance is judged via the coefficient of determination (R²(c)) for calibration, **Root Mean Square Error (RMSE**(c)), **Weighted Mean Average Percentage Error (wMAPE**) at 95% confidence level as revealed in table 2.

Table 2: Statistical evaluation of the Overall, Summer and Hammatan

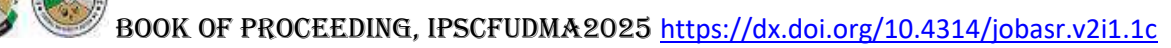
Dataset	Variables	$(R^2(c))$	RMSE(c)	wMAPE	Interpretation
Overall	VSB, RH	0.90	0.08	1%	Best performance; strong predictor
Overall	VSD, KII	0.90	0.08	1 /0	usability
Summer	Same	0.85	0.06	2%	Improved accuracy; modest aerosol
Summer	Same	0.63	0.00	270	loading
Harmattan	Same	0.88	0.04	2%	Good predictive accuracy & low bias

The **backward multiple regression** approach evaluated the combined effects of visibility (VSB) and relative humidity (RH), on **AI** across the full-year dataset (January–December). Initial inclusion of Sea level pressure revealed this was **not significant predictor** individually. However, in some multi-variable contexts it still exert minor influence, echoing past findings by Balarabe (2021). Among all candidate models, the **three-variable model** (including SLP) recorded the **highest R²**, but shared comparable **RMSE** with the simpler **two-variable model** (VSB, RH). Since the difference in performance metrics (R² and RMSE) between these models did **not exceed the 5% threshold, three-variable model** is therefore chosen as optimal for overall prediction.

The selected **two-variable regression** thus offers nearly equivalent predictive accuracy to the more complex three-variable model, but with reduced complexity, better interpretability, and minimized over fitting risk.

For the **20years dataset overall**, the three-variable model yielded **R**² **0.71**, **RMSE 0.30**, while the two variable models yielded **R**² **0.70**, **RMSE 0.31** indicating **strong predictive performance** and low bias. This aligns with benchmark thresholds used in previous aerosol modeling studies (e.g., Tan et al. 2015; Balarabe & Koko 2018, 2019).

Seasonally, it is discovered that model accuracy varied: **Summer season yielded** $R^2 = 0.85$, RMSE =0.06, wMAPE = 2%; **Harmattan** season $R^2 = 0.88$, RMSE 0.04, wMAPE = 2% while the overall data yielded $R^2 = 0.90$, RMSE =0.08. These seasonal improvements underscore the model's



heightened **sensitivity and reliability** under high aerosol loading conditions characteristic of the Harmattan period.

Seasonal differences in model accuracy reflect the **distribution of AI values**: During **summer**, AI measurements are generally lower and clustered narrowly, reducing sensitivity of regression models. In contrast, the **Harmattan season** presents elevated and more variable AI levels due to Saharan dust transport allowing the meteorological predictors (especially visibility and RH) to capture aerosol variability more effectively. These findings are consistent with regional studies showing stronger aerosol-meteorology linkages during dry dusty episodes (e.g., Balarabe et al. 2015): Harmattan brings coarse-mode dust, lowering visibility and humidity while increasing aerosol concentrations, conditions which enhance predictability by surface variables

4. Validation of the models

The regression coefficients (a₀, a₁, a₂.) in equation 4 estimated from the **calibration subset** (**Subset** 1) were applied to the **validation subset** (**Subset** 2) to generate predicted AI values. Model performance was quantified using the **validation Root Mean Square Error** (**RMSE**_v), which measures the average deviation between predicted and observed AI in the hold-out data. Comparable RMSE values between calibration and validation sets imply the model generalizes well and avoids over fitting.

Observed RMSE_v patterns closely mirrored those from calibration, indicating the model's predictive capability is stable across unseen data. Such consistency suggests **the model captures underlying relationships effectively**, reinforcing confidence in its reliability. According to calibration–validation standards, when validation error closely matches training error, the model is considered robust with **minimal overfitting**. This speaks to strong **out-of-sample predictive power.**

The strong pearson correlation (or R²) observed between predicted and actual AI in the validation set further supports accuracy and alignment of variance capture.

5. Conclusions

TOMS-AI using ground meteorological data in North-Central Nigeria. By capturing seasonal variability and leveraging readily available predictors, the research bridges critical gaps in aerosol monitoring offering actionable, localized tools for environmental management and scientific understanding. The **three-variable model** (visibility, relative humidity, wind speed) is validated as the most **efficient and reliable predictor of AI** across both overall and seasonal datasets, offering **stable performance**, **low error**, and **parsimony**. Seasonal variation in predictive accuracy confirms that **Harmattan periods** characterized by elevated aerosol presence yield **stronger statistical relationships** with meteorological variables. The results corroborate earlier research in West Africa, reinforcing the conceptual profile that during **dust-laden seasons**, surface meteorology is highly informative for aerosol modeling

References

- Adefolalu, D. 1984. On bioclimatological aspects of Harmattan dust haze in Nigeria. *Archives for meteorology, geophysics, and bioclimatology, Series B*, 33, 387-404.
- Ali Köse, Salman Tariq, Banu Numan Uyal, Muhammad Khan, Husam Rjoub, Usman Mehmood 2024: Analysis of nighttime aerosols and relation to covariates over a highly polluted sub-Saharan site using Mann–Kendall and wavelet coherence approach. https://doi.org/10.1002/jeq2.20543
- Ayansina A., Godwin A., and Margaret O. J 2019. Spatial and seasonal variations in atmospheric aerosols over Nigeria: Assessment of influence of intertropical discontinuity movement. The International Journal of Ocean and Climate Systems Volume 9: 1–13
- Balarabe, M., Abdullah, K. & Nawawi, M. 2015. Long Term Trend and Seasonal Variability of Horizontal Visibility in Nigerian Troposphere. Atmosphere, 6,1462-1486.
- Balarabe, M., Abdullah, K., Nawawi, M., & Khalil, A. E. 2016. Monthly Temporal- Spatial Variability and Estimation of Absorbing Aerosol Index Using Ground-Based Meteorological Data in Nigeria. Atmospheric and Climate Sciences, 6(03), 425.
- Balarabe M.A. & A. S. Koko 2018. Multiple Regression model to predict Aerosol Optical Depth (AOD) in atmospheric column in Ilorin-Nigerial, Nigerian Journal of Renewable Energy Volume 18 Number 1&2, 131 138
- Balarabe M.A and Isah M.N. 2019. A modified linear regression model for predicting Aerosol Optical Density (AOD) in Ilorin-Nigeria. Fudma journal of sciences 3(1), 140- 145.
- Balarabe Abubakar Mukhtar —Develoment and Testing of Feed Forward Artificial Neural Networks (ANN) to retrieve monthly Ozone Monitoring Instrument Aerosol Index (OMI-AI) in coastal zone of Nigeria. A paper presented at the 43rd Annual conference of the Nigerian institute of physics, held at Nnamdi Azikwe University, Awka, Anambra state from 21st to 26th September, 2021
- Bello S.A., Bello I. T., and Usman M.G 2025. Spatiotemporal Variability of Aerosol Optical Depth Over Nigeria Based on Modis Satellite Observations (2004–2023). Asian Journal of Research and Reviews in Physics Volume 9, Issue 2, Page 47-59, 2025
- Kaskaoutis, D. G., Singh, R. P., Gautam, R., Sharma, M., Kosmopoulos, P. G. & Tripathi, S. 2012. Variability and trends of aerosol properties over Kanpur, northern India using AERONET data (2001–10). *Environmental Research Letters*, 7, 024003.
- Noori, R., Hoshyaripour, G., Ashrafi, K. & Araabi, B. N. 2010. Uncertainty analysis of developed ANN and ANFIS models in prediction of carbon monoxide daily concentration. *Atmospheric Environment*, 44, 476-482.
- Ogunjobi, K. O., Oluleye, A. & Ajayi, V. O. 2012. A long-term record of aerosol index from TOMS observations and horizontal visibility in sub-Saharan West Africa. *International Journal of Remote Sensing*, 33, 6076-6093.
- Onyinyechi, C.I., Okechuku, K.N & Ugochukwu, K.O (2025). Evaluation of aerosol loading and its relationship with Geopotential height in Nigeria's Guinea 49 (11)
- Tan, F., Lim, H., Abdullah, K., Yoon, T. & Holben, B. 2015b. Monsoonal variations in aerosol optical properties and estimation of aerosol optical depth using ground-based meteorological and air quality data in Peninsular Malaysia. *Atmospheric Chemistry and Physics*, 15, 3755-3771.
- TOMS NiMBUS 7 Data catalog: https://catalog.data.gov/dataset/toms-nimbus-7-total-ozone-aerosol-index-uv-reflectivity-uv-b-erythemal-irradiances-daily-1?utm_source=chatgpt.com



SPATIAL VARIATION OF FM RADIO SIGNAL IN A SUB-URBAN SAHEL

ENVIRONMENT: A Case study of Radio Nigeria Companion FM (104.5 MHz) katsina Akinsanmi Akinbolati¹, *Muftahu Suleiman², Hauwau Yusuf¹ and Hassan Yazid Gonah²

Department of Physics, Federal University Dutsin-Ma

²Department of Electrical/Electronic Engineering, Katsina State Institute of Technology and Management.

*Corresponding Author's e-mail: madugu694@gmail.com

Abstract

Analysis of the spatial variation of FM radio signal strength is essential for assessing coverage quality and optimizing transmission infrastructure in sub-urban areas. This study examined the spatial variation of FM signal transmitted by Companion FM (104.5 MHz) across Katsina metropolis, focusing on two major roads which are Dutsinma and Daura roads. Field data were collected using a GPS Garmin MAP 78S for recording geographic coordinates and elevation, while a Field Strength Meter (FSM) measured the Received Signal Strength (RSS) in dBµV/m. A 5element Yagi-Uda omnidirectional antenna with 8 dBi gain was used for signal reception. Measurements were taken at 1 km intervals up to 15 km along the selected routes from a 10 kW RVR transmitter with a 150 m antenna height as reference point. The results indicate that signal strength varies significantly across the sampled points, highlighting the influence of elevation and distance along propagation path from the transmitter to receiver. The mean RSS recorded along the Dutsinma route was 54.16 dBµV; however, there were notable attenuations beyond 5 km, with relatively weak signals in the far range. In contrast, the Daura route showed no periodic fluctuation in average RSS (48.6 dBµV), with unexpected mid-range peaks likely due to constructive multipath effects and high elevation. Propagation curves for both routes were developed, revealing non-linear attenuation trends associated with terrain elevation changes and possible line-of-sight obstructions. A correlation analysis was conducted to assess the relationship between RSS and location parameters, namely elevation and distance. The results revealed a significant inverse correlation between distance and signal strength, supporting the expected attenuation model. Elevation, however, exhibited a more complex and variable influence depending on the route. This study concludes that spatial variability in signal propagation is substantial in sub-urban Sahel environments. The findings offer practical applications for broadcast engineers and policymakers seeking to optimize FM transmission coverage and quality of reception over Katsina metropolis and in other environments with similar geographical.

Keywords: FM Signal Strength, Spatial Variation, Signal Attenuation, Terrain Elevation and Sahel environment.



1. INTRODUCTION

Broadcasting via Frequency Modulated (FM) radio serves to provide information, especially for a growing population in developing areas where digital technology is yet to be adopted. The FM signals are radiated at frequencies of the Very High Frequency (VHF) band, ranging between 87.5 and 108 MHz, and the FM propagation primarily relies on space waves which include the direct and ground-reflected waves. These signals are greatly influenced by the antenna height, distance from the transmitting source, topography and atmospheric conditions as well (Boithias, 1987; Hall & Barclay, 1991). A signal from the transmitter antenna normally experience multipath fading to the receiving antenna, which can cause constructive or destructive signals. Path loss is one of the most important factors in link budget analysis or wireless network planning (Suleiman et al., 2024). Signal degradation related to other semi-urban or sub-urban Sahelian environments is attributed to atmospheric conditions, ground conductivity, and manmade structures, resulting in significant signal loss, fading, and gaps (Ajewole et al., 2011). Research indicates that in tropical and subtropical areas, radio signals often undergo severe degradation due to temperature inversions and low humidity levels, which can change the refractive index of the air along the signal travel path (Ali et al., 2019). Furthermore, urbanized areas have received considerable attention with respect to signal strength and its distribution; however, localized studies paying attention to sub-urban areas of the Sahel region, like Katsina, are remarkably lacking. This shows the importance of various empirical studies that examine the actual functioning of FM signals in these environments to assist in planning and policymaking for broadcast service infrastructure (AbdelRahman et al., 2024).

Ajewole et al. (2012) studied FM coverage in Niger State, where they found that signal strength reduces nonlinearly as one moves farther away from the transmitter due to various environmental and topographical factors. Also, Akinbolati et al. (2016) and Luomala & Hakala (2015) discussed how reliance exclusively on empirical field data undermines the understanding of FM broadcasts performance in diverse landscapes. This research aims to analyze the spatial variation of FM radio signals in the sub-urban area of Katsina, studying Radio Nigeria Companion FM (104.5 MHz) as a case. The study aims to offer details on the distribution pattern, changes in signal strength, and the possible cause of coverage in FM signals across a typical Sahel environment by using field measurements and spatial mapping techniques.

This study therefore investigates the spatial variation of FM radio signals in Katsina metropolis, a sub-urban Sahel environment, using Radio Nigeria Companion FM (104.5 MHz) as a case study. The objectives are to (i) analyze how FM signal strength varies with distance and elevation, (ii) examine the role of terrain and multipath effects on propagation, and (iii) generate propagation curves for sub-urban Sahel conditions. The guiding research questions are: How does FM signal strength attenuate with distance in Katsina's sub-urban terrain? What influence does elevation exert on reception quality? And how can localized findings improve coverage planning and infrastructure deployment in similar Sahelian environments?

2.2 Basic Theory

2.2.1 Empirical Models for FM Signal Propagation

Empirical propagation models are mathematical formulae that are formulated using large field measurements and observations (Ibhaze et al., 2017). They are primarily used to predict the path loss or signal attenuation experienced by radio waves, particularly in terrestrial environments such as urban, sub-urban, and rural areas. For FM signals in the VHF band (87.5–108 MHz), these models help estimate the signal strength at various distances from a transmitter and play an important role in network planning as well as coverage prediction (Rappaport, 2002).



A number of empirical models used for FM signal attenuation prediction include:

1. Plane Earth Propagation Model: The Flat Earth or Plane Earth model considers the direct signal and one reflected wave from a smooth flat surface such as the ground. It applies line-of-sight (LOS) propagation with no obstructions and is therefore applied in open short-range environments (Lindquist, 2020).

$$L_{PE} = 40log_{10}(d) - 20log_{10}(h_1) - 20log_{10}(h_2)$$
(1)

Where f is the frequency in (MHz), d is the distance from the base station to the receiver in (km), h_1 and h_2 in (m) are the heights of the transmitting base station antenna and receiving antenna respectively.

2. Okumura-Hata Model: Developed from Okumura's extensive field measurements and later simplified by Hata (1980), this model is widely used in urban and suburban environments for predicting signal loss in the frequency range of 150–1500 MHz. Though not originally developed for the VHF/FM band, it can be cautiously adapted for such use (Rappaport, 2002).

The general path loss equation for urban areas is given as:

$$L_{50}(dB) = 69.55 + 26.16log_{10}(f) - 13.82log_{10}(h_t) - a(h_r) + \{44.9 - 6.55log_{10}(h_t)\} log_{10}(d)$$
 (2)

Where: $L_{50}(dB)$ is the median path loss in decibels (dB), f is the frequency in MHz, h_t is the height of the transmitting antenna in meters (typically between 30 and 200 m), h_r is the height of the receiving antenna in meters (typically between 1 and 10 m), d is the distance between the transmitter and receiver in kilometers (ranging from 1 to 20 km), and $a(h_r)$ is the correction factor for the receiving antenna height, which varies depending on the environment.

3. COST-231 Hata Model: An extension of the Hata model developed by the COST-231 project for frequencies from 1500 MHz to 2000 MHz, with modified correction factors for metropolitan areas (Olatinwo et al., 2017). While it targets higher frequencies, it shares the same structure and is sometimes modified for lower bands like FM with caution (Platz, 2004).

The equation for COST 231 Hata path loss model is expressed as:

$$L(dB) = 46.3 + 33.9log_{10}(f) - 13.82log_{10}(h_t) + [44.9 - 6.55log_{10}(h_t)]log_{10}(d) - \alpha(h_r) + C_m]$$
(3)

where, d is the link distance in Kilometres, f_c is the frequency in MHz, h_t is the effective height of the transmitting antenna in meters, h_r is the effective height of the receiving antenna in meters, C_m is the correction factor and is defined 0dB for rural and 3dB for urban area.

Each of these models provides practical insights into FM signal behavior over distance and terrain. The Plane Earth model is ideal for open areas with minimal interference; Okumura-Hata and COST-231 Hata are best suited for urban and suburban areas. The choice of model depends on frequency band, terrain type, and available field data.

3.0 METHODOLOGY

This study employed an empirical drive test method to measure the spatial variation of Companion FM 104.5 MHz signal over Katsina metropolis, focusing on two major outbound routes Dutsinma and Daura roads. The research adopted a quantitative field measurement approach, collecting data at regular 1 km intervals for a total distance of 15 km from the base station.

3.1 Study Location

The research was conducted in Katsina State, Northwestern Nigeria (latitude 12°26'N, longitude 7°29'E), characterized by a Sahel Savannah climate with distinct wet (June - September) and prolonged dry seasons. Field measurements were performed along two strategic routes extending from the Radio Nigeria Companion FM (104.5 MHz) base station located in Batsari road, **Katsina Metropolis** (coordinates: 13.2313587°N, 7.7315305°E; elevation: 502 m). These strategic routes



were **Dutsin-Ma Road** and **Daura Road** which selected based on their distinct terrain profiles to assess how **topographical variation** influences FM signal propagation.

3.2 FM Signal Propagation Mechanisms

Frequency Modulation (FM) signal propagation refers to the process by which FM radio waves typically within the Very High Frequency (VHF) band (87.5–108 MHz) and travel from a transmitter to a receiver through the atmosphere. Unlike lower-frequency signals such as Amplitude Modulation (AM), FM signals predominantly employ line-of-sight (LOS) transmission and are heavily influenced by the environment (Rappaport, 2002; Seybold, 2005). FM propagation occurs mostly through the following mechanisms:

- **1. Direct Wave (Line-of-Sight) Propagation:** This is the common mode of transmission of FM signal ("Antennas, Transmission Lines, Matching Networks," 2022). The signal travels in a straight line from the transmitting antenna to the receiving antenna. Because FM operates in the VHF band, signals do not curve very far around the Earth's surface and are typically limited to the line of sight on the order of 30 to 50 km, depending upon the antenna height (Hall & Barclay, 2006). This form of propagation is affected by antenna height, terrain level, and obstructions; hills, structures, or dense vegetation can capture the signal and attenuate it.
- **2. Ground Reflection (Multipath):** Some of the FM signal is reflected off the Earth's surface or buildings and reaches the receiver along with the direct wave. Multipath introduces multiple paths leading to constructive or destructive interference, resulting in fading or signal distortion (Seybold, 2005; Rappaport, 2002).
- **3. Diffraction:** FM signals can be deflected by obstacles or sharp edges like hills or roofs and can still manage to reach the receiver without the need for a LOS (Silliman & Wandel, 2017). The diffracted signal will typically be weaker and more prone to distortion (Stutzman & Thiele, 2012).
- **4. Refraction and Scatter in the Tropospheric Region:** FM signals can get scattered or refracted in the lower part of the troposphere due to temperature, pressure, and humidity gradients (Caspers & Kowina, 2014). These are more pronounced during temperature inversions, which can occur early in the morning or with unexpected weather (Hall & Barclay, 2006).

FM signal propagation is hence complex, influenced by a combination of terrain features, atmospheric conditions, and physical obstructions (Barclay, 2003). L.O.S remains the predominant transmission mode, yet for accurate coverage prediction and effective network planning, it is important to also have knowledge of secondary mechanisms such as reflection, diffraction, and refraction (Seybold, 2005; Rappaport, 2002).

3.3 Instrumentation and Technical Specifications

To ensure accurate and reliable signal strength measurements, the study utilized a set of calibrated field equipment and positioning tools specifically suited for outdoor radio propagation studies. The instrumentation setup enabled real-time logging of Received Signal Strength (RSS), positional coordinates, and elevation data at predefined intervals. The devices used included a **field strength meter**, **GPS receiver**, and a **broadband** directional 5-element Yagi-Uda (8 dBi) **antenna** mounted on a test vehicle. The technical specifications of the instruments used for data acquisition are summarized in **Table 1**.

Table 1: Technical Specifications of the Instruments used for Data Collection

Instruments	Specification/Use
GPS Garmin MAP 78S	Recorded geographic coordinates,
	elevation, and line-of-sight distance
	from transmitter.



Field Strength Meter (FSM)	Measured electric field intensity (RSS)		
	in dBμV/m.		
Directional Antenna	5-element Yagi-Uda with 8 dBi gain for		
	signal reception.		
RVR Transmitter	Base station specifications: 10 kW		
	power output, 150 m antenna height		

3.3.1 Data Quality, Calibration and Uncertainty

All instruments were factory-calibrated and checked before and after the field campaign. The field strength meter was verified using a reference RF source, while antenna gain and cable losses were measured and compensated. GPS readings were SBAS-enabled, giving typical horizontal accuracy ≤ 5 m and vertical ≤ 10 m. Daily drift checks at fixed reference points showed no bias beyond calibration tolerance. Combined RSS measurement uncertainty was estimated at $\pm 2-3$ dB, while position accuracy was ± 5 m horizontally and ± 10 m vertically. These uncertainties were incorporated in subsequent analysis and figures, with error bars reflecting variability (standard deviation) at each sampling point.

3.4 Transmission Characteristics of the Experimental Station

The experimental station in this study is **Radio Nigeria Companion FM** (104.5 MHz), located in Katsina metropolis. It served as the **sole transmitter** for signal strength evaluation across the two test routes. Understanding the **technical transmission characteristics** of the station is essential for interpreting signal behavior and modeling expected path loss. These characteristics are presented in **Table 2**.

Table 2: Transmission characteristics of the experimental station

PARAMETERS	CHARACTERISTICS
Base station geographical coordinate	LAT. 13.2313587, LON. 7.7315305
Base station elevation (m)	502
Base station operational frequency (MHz)	104.5
Height of base station antenna (m)	150
Rated transmitting power (Kw)	10
Transmitter used	RVR Transmitter
Operational power during data taking (Kw)	5.6

3.5 Method of Data Collection

To investigate the spatial variation of FM radio signal in a sub-urban Sahel environment, a comprehensive field data collection was conducted in February 2022 across two major routes which are Dutsin-Ma Road and Daura Road, extending outward from the Radio Nigeria Companion FM (104.5 MHz) transmission station in Batsari road of Katsina Metropolis. The study employed a systematic drive-test approach over a 15-kilometer on each route, using 1-kilometer intervals as standardized measurement points from the base station, which served as the reference origin. At each interval, a set of essential parameters was measured to capture the spatial dynamics of the signal. These included:

- Received Signal Strength (RSS): recorded as both initial and final readings to account for temporal fluctuations, with the average RSS used for analysis,
- Geographic coordinate: comprising latitude and longitude, elevation above sea level and
- Line-of-sight (LOS) distance from the transmitter.



- **Antenna height and orientation:** Receiving antenna fixed at 2.5 m above vehicle roof, oriented toward the base station.
- **FSM model/settings:** FSM range set to 20–120 dBμV/m, averaging over 5 s dwell per point.
- **Sampling protocol:** Measurements at 1 km intervals; three successive RSS readings averaged per point.
- **Timestamps:** Measurements logged between 9:00 16:00 local time, February 2022.
- Weather: Clear, dry-season conditions; no rainfall during data collection.

Field measurements were gathered using a field-strength meter calibrated at the factory, GPS receiver and broadband receiving antenna mounted on a test vehicle. This provided high-accuracy real-time recording of signal and spatial data with a permanent antenna height during measurement. The measurement period was distributed over two days in relatively stable weather conditions in order to minimize atmospheric variability. This method provided high-resolution data on how terrain and distance affect the behavior of FM signals in the sub-urban Sahel environment of Katsina, creating a robust empirical foundation for subsequent propagation analysis and modeling of the signal.

3.6 Method of Data Analysis

The collected field data were subjected to both graphical and mathematical analysis to evaluate the spatial variation of FM signal strength across the selected routes. The primary data included Received Signal Strength (RSS) readings and corresponding geographic coordinates and elevation levels, recorded at 1 km intervals up to 15 km from the transmitter.

Microsoft Excel was used to organize the measured data and to generate **propagation curves** showing the variation of RSS with respect to distance for both the Dutsin-Ma and Daura routes as shown in Figure 1 and Figure 2 respectively. These curves helped to visually assess signal attenuation patterns and identify anomalies such as multipath peaks or sudden drops due to terrain obstructions.

3.7 Ethical Considerations

This study was conducted in strict adherence to the current scientific and ethical guidelines for field based measurement studies. All procedures used in the data acquisition were conducted solely along public roads without any intrusion into or trespass on private property. The study used non-intrusive observation protocols, and the testing never disrupted any available radio or telecommunications service in the area. Noteworthy, the applied FM transmitter for the experiments was still within its licensed operating range, and therefore the investigation did not compromise regulatory requirements or public security. In general, the approach was designed to be ethical and transparent to facilitate reproducibility as well as safeguarding of public infrastructure and property. Such precautions confirm the research as a model framework for subsequent FM signal propagation research in similar sub-urban or Sahel environments.



4.0 Result and Discussion

The field measurement actually revealed clear patterns in the FM signal strength spatial variation along the two sub-urban Sahel paths selected in Katsina. Along the Dutsin-Ma route, which features relatively flat terrain, signal strength was strongest at locations nearest to the transmitter and gradually declined with increasing distance, with minor fluctuations likely caused by subtle elevation differences and surface obstructions. The average RSS across the road was approximated at 54.16 dBµV, indicating generally stable coverage up to 15 km. Unlike the Daura route with more diverse terrain characterizing gentle hills and valleys, showed a more irregular signal pattern, with unexpected peaks and dips across the measurement points. This behavior suggests that multipath effects, diffraction, and partial shadowing due to elevation changes are present. The average RSS along the Daura route was 48.6 dBµV, which is lower than that for the Dutsinma route, owing to the predominant influence of terrain on FM signal propagation.

Result presented in Table 1 and Table 2 was obtained along Dutsinma and Daura routes, respectively.

Table 3: Data Obtained along Dutsin-Ma Route

S/N	Name of Data Location	Line of sight Distance From Base Station (Km)	Latitude (°N)	Longitude (°E)	Elevation(m)	Received Signal Strength (DBµV)	Received Signal Strength (DBµV)	Received Signal Strength (DBµV) Average
1	A	0.00	13°00.596	007°42.396	502.00	81.50	82.30	81.90
2	В	1.00	12°57.33	007°34.677	517.00	84.20	83.10	83.65
3	C	2.00	12°56.828	007°34.677	526.00	71.40	78.10	74.75
4	D	3.00	12°56.418	007°34.989	536.00	61.50	70.20	65.85
5	E	4.00	12°56.383	007°34.342	540.00	53.20	62.30	57.75
6	F	5.00	12°55.572	007°36.024	540.00	53.10	54.10	53.60
7	G	6.00	12°54.765	007°36.037	536.00	48.10	51.20	49.65
8	H	7.00	12°54.073	007°35.840	547.00	48.20	48.50	48.35
9	I	8.00	12°53.449	007°35.788	550.00	52.30	49.70	51.00
10	J	9.00	12°52.829	007°35.625	553.00	47.30	49.50	48.40
11	K	10.00	12°52.173	007°35.300	551.00	45.30	46.00	45.65
12	L	11.00	12°51.702	007°34.983	544.00	41.00	42.70	41.85
13	M	12.00	12°51.175	007°34.849	546.00	43.70	44.80	44.25
14	N	13.00	12°50.691	007°34.741	553.00	45.10	44.60	44.85
15	O	14.00	12°50.173	007°34.541	560.00	43.70	42.80	43.25
16	P	15.00	12º49.666	007°34.365	555.00	31.20	32.50	31.85

Mean of received signal strength

4.1 Propagation Curve Analysis (Dutsinma Route)

54.16





Fig. 1: Graph of Received Signal Strength (RSS) against distance (km) for Dutsinma Route Fig. 1 reveals a clear trend of signal attenuation with increasing distance. Initially, the signal strength is relatively high at 83.65 dB μ V at 1 km, but it progressively declines as the distance increases. This decline follows a non-linear pattern typical of radio signal propagation in a suburban Sahel environment, where terrain features and sparse vegetation contribute to signal degradation. From 1 km to 5 km, there is a steady and significant drop in RSS, indicating a dominant free space and terrain-influenced path loss. Between 6 km and 10 km, minor fluctuations are observed such as a slight increase at 8 km (51.00 dB μ V) which may be attributed to multipath effects or temporary line-of-sight improvements due to terrain elevation. Beyond 10 km, the RSS values continue to decline, reaching a minimum of 31.85 dB μ V at 15 km, reflecting increased signal weakening due to distance, ground absorption, and possible diffraction losses.

Table 4: Data Obtained along Daura Route

S/N	Name of Data Location	Line of sight Distance From Base Station (KM)	Latitude (°N)	Longitude (°E)	Elevation (M)	Received Signal Strength (dBµV)	Received Signal Strength (dBµV)	Received Signal Strength (dBµV) Average
1	A	0.00	13°00.597	007°42.396	502.00	47.50	47.50	47.50
2	В	1.00	12°58.135	007°34.490	477.00	43.50	43.50	43.50
3	C	2.00	12°58.505	007°34.898	482.00	49.80	50.20	50.00
4	D	3.00	12°58.905	007°35.215	494.00	46.60	46.60	46.60
5	E	4.00	12°59.104	007°35.852	500.00	45.50	45.50	45.50
6	F	5.00	12°59.554	007°36.177	495.00	30.60	30.60	30.60
7	G	6.00	12°59.711	007°36.775	490.00	32.50	32.60	32.55
8	H	7.00	12°59.758	007°37.422	484.00	63.00	62.00	62.50
9	I	8.00	12°59.362	007°37.276	500.00	61.50	65.20	63.35
10	J	9.00	12°59.433	007°37.838	510.00	54.10	57.20	55.65
11	K	10.00	12°59.557	007°37.879	508.00	52.70	49.60	51.15
12	L	11.00	12°59.637	007°40.117	506.00	58.00	56.00	57.00



13	M	12.00	12°59.407	007°40.515	505.00	54.30	53.10	53.70
14	N	13.00	13°59.456	007°41.138	495.00	51.00	50.40	50.70
15	O	14.00	13°59.578	007°42.697	489.00	45.60	49.50	47.55
16	P	15.00	13°59.619	007°42.274	482.00	41.30	38.20	39.75

Mean of the received signal strength

48.6

4.2: Propagation Curve Analysis (Daura Route)



Fig. 2: Graph of Received Signal Strength (RSS) against distance (km) for Daura Route

Fig. 2 presents a relatively irregular trend compared to the Dutsin-Ma route, highlighting significant spatial variations typical of FM signal behavior in a sub-urban Sahel environment. Unlike the expected steady decrease in RSS with increasing distance from the base station, the Daura route data shows noticeable fluctuations across the entire range. At 1 km, the RSS starts at a relatively low 43.50 dB μ V but unexpectedly rises to 50.00 dB μ V at 2 km and continues fluctuating through 3 km and 4 km. A sudden dip occurs at 5 km (30.60 dB μ V), likely due to an obstruction or terrain depression. However, from 6 km onward, the RSS experiences a significant increase, peaking at 8 km with 63.35 dB μ V, an anomaly that may be caused by favorable terrain conditions, reflection, or possible line of sight reinforcement.

Following this peak, the signal strength remains relatively strong and stable between 9 km and 13 km, with values ranging between 50.70 dB μ V and 57.00 dB μ V. A gradual decline resumes from 14 km (47.55 dB μ V) to 15 km (39.75 dB μ V), aligning more closely with typical propagation expectations. This irregular propagation pattern suggests that environmental factors such as terrain ripple, buildings, vegetation, and multipath interference strongly influence FM signal distribution along the Daura route. The observed anomalies reinforce the importance of localized measurements in sub-urban Sahel regions, where empirical path loss predictions may be insufficient without accounting for terrain and atmospheric variability.

4.3 Propagation Curve Analysis

The Okumura-Hata suburban model was fitted to the measured RSS. For the Dutsinma route, the RMSE between model predictions and measurements was 4.8 dB (MAE = 3.6 dB), while for the



Daura route the RMSE was 6.2 dB (MAE = 4.9 dB). These values indicate moderate deviations, largely due to terrain-induced multipath effects not captured by the empirical model.

4.4 Correlation Analysis

Although both routes show significant correlation between distance and RSS (p < 0.01), deviations between measured and modeled attenuation suggest that terrain-induced multipath contributes $5-10~\mathrm{dB}$ variability beyond standard model predictions. The larger errors along the Daura route highlight limitations of applying uniform empirical models in undulating Sahel terrain. While ray-tracing could capture this complexity, it was beyond the scope of this study and remains a limitation.

In assessing the spatial variation of FM radio signal within the sub-urban Sahel environment, correlation analysis was carried out to evaluate the relationship between received signal strength (RSS), distance, and elevation for both Dutsin-Ma and Daura routes. Table 5 and 6 present the correlation coefficient for data obtained along Dutsin-Ma and Daura Routes respectively.

Table 5: Correlation Coefficient for Data Obtained along Dutsinma Route

		RSS	Distance	Elevation
	RSS	1		
The	Distance	898	1	
	Elevation	.809	.772	1

correlation matrix in Table 5 shows a strong and statistically significant negative correlation between RSS and distance (r = -0.898, p < 0.01), confirming that signal strength decreases as distance increases from the transmitter. Elevation is positively correlated with RSS (r = 0.809, p < 0.01), indicating that higher terrain points generally improve reception. The positive correlation between distance and elevation (r = 0.772, p < 0.01) reflects the gradual rise in terrain along the Dutsin-Ma route. Since all reported correlations are significant at p < 0.01, the relationships are robust and unlikely due to random variation.

Table 6: Correlation Coefficient for Data Obtained along Daura Route

		RSS	RSS 1	Distance	Elevation	
The		Distance	604	1		Daura
route Table a	6	Elevation	.597	.503	1	results in indicate moderate

but statistically significant negative correlation between RSS and distance (r = -0.604, p < 0.01), showing that signal strength still declines as distance increases, though less strongly than along the Dutsin-Ma route. RSS is moderately and positively correlated with elevation (r = 0.597, p < 0.01), suggesting that higher ground slightly enhances reception. The correlation between distance



and elevation (r = 0.503, p < 0.01) also reflects gradual terrain rise with distance. Since all correlations are significant at p < 0.01, these relationships are meaningful, though weaker than those observed on the Dutsin-Ma route.

Overall, these values suggest that both routes exhibit signal strength degradation with distance, but elevation plays a more complex and route-dependent role in signal variation. The Dutsin-Ma route still shows a more structured terrain influence, while the Daura route displays moderately consistent but less predictable patterns.

5.0 CONCLUSION AND RECOMMENDATION

Conclusion

This study confirms that FM radio signal strength in Katsina varies significantly with distance and elevation. While the inverse relationship between RSS and distance is consistent with theory, empirical model fits (RMSE 4–6 dB) show terrain effects introduce additional variability. The findings are specific to Katsina's sub-urban Sahel terrain and should not be generalized beyond similar environments. The findings also offer practical applications for broadcast engineers and policymakers seeking to optimize FM transmission coverage and quality of reception over Katsina metropolis and other environments with similar geographical terrain.

Recommendations

- Engineers should incorporate local terrain profiles into FM coverage planning to minimize dead zones.
- Deployment of repeaters or low-power boosters is advised beyond 5–10 km where attenuation exceeds 20 dB.
- Further research should extend to seasonal effects and multipath modeling.

These insights can guide both regulatory authorities and station managers in improving broadcast reliability and service quality across similar Sahelian and sub-urban environments.

References

- AbdelRahman, A. A., Meftin, N. K., Alak, E. K., Jawad, H. M., Hatim, Q. Y., Khlaponin, Y., & Al-Jawher, W. A. M. (2024). Al-driven cloud networking optimizations for seamless LTE connectivity. 2024 36th Conference of Open Innovations Association (FRUCT), 13–23. https://ieeexplore.ieee.org/abstract/document/10749959
- Ajewole, M. O., Oyedum, O. D., Adediji, A. T., Eichie, J. O., & Moses, A. S. (2011). Spatial coverage of FM radio transmitters in Niger State, Nigeria. *The IUP Journal of Telecommunications, 4(4), 7–20.
- Akinbolati, A., Akinsanmi, O., & Ekundayo, K. R. (2016). Signal strength variation and propagation profiles of UHF radio wave channel in Ondo State, Nigeria. International Journal of Wireless and Microwave Technologies, 6(4), 12–27.
- Ali, A. S., Onifade, B., & Ijeoma, P. (2019). Evaluation of path loss models for effective coverage prediction in urban environments. International Journal of Wireless Communications and Mobile Computing, 4(3), 23–30.
- Barclay, L. W. (2003). Propagation of radiowaves (Vol. 502). IET. https://books.google.com/books?hl=en&lr=&id=fBoTO48FBD8C&oi=fnd&p
- Boithias, L. (1987). Radio wave propagation. McGraw-Hill.
- Caspers, F., & Kowina, P. (2014). RF measurement concepts. https://cds.cern.ch/record
- CCIR Report 239-6. (1986). ITU-R recommendations and reports, propagation curves for VHF/UHF
- Hall, M. P. M., & Barclay, L. W. (1991). Radio wave propagation. Peter Peregrinus Ltd.



- Hall, M. P., & Barclay, L. W. (2006). Propagation of radio waves (2nd ed.). Institute of Engineering and Technology. https://doi.org/10.1049/PBEW052E
- Ibhaze, A. E., Imoize, A. L., Ajose, S. O., John, S. N., Ndujiuba, C. U., & Idachaba, F. E. (2017). An empirical propagation model for path loss prediction at 2100 MHz in a dense urban environment. Indian Journal of Science and Technology, 10(5), 1–9.
- Lindquist, T. (2020). Wave propagation models in the troposphere for long-range UHF/SHF radio connections. https://www.diva-portal.org/smash/get/diva2
- Luomala, J., & Hakala, I. (2015). Effects of temperature and humidity on radio signal strength in outdoor wireless sensor networks. Proceedings of the Federated Conference on Computer Science and Information Systems, 5(4), 1247–1255.
- Olatinwo, S. O., Oborkhale, L. I., & Shoewu, O. O. (2017). Wireless network modelling and analysis using path loss models. Pacific Journal of Science and Technology, 18(2), 132–143.
- Platz, R. (2004). SNR advantage, FM advantage and FM fitting. ACCESS: Achieving Clear Communication Employing Sound Solutions. Proceedings of the First International Conference, 147–154. https://www.phonak.com/content/dam/phonak/en/evidence-library/journal-article/ACCESS
- Rappaport, T. S. (2002). Wireless communications: Principles and practice (2nd ed.). Prentice Hall.
- Seybold, J. S. (2005). Introduction to RF propagation. John Wiley & Sons. https://doi.org/10.1002/0471725241
- Silliman, T. B., & Wandel, E. R. (2017). FM broadcast antennas. National Association of Broadcasters Engineering Handbook, 1355–1397.
- Stutzman, W. L., & Thiele, G. A. (2012). Antenna theory and design (3rd ed.). John Wiley & Sons.
- Suleiman, M., Akinbolati, A., Bashir, I., & Nehemiah A. (2024). Assessment of Empirical Models and the Impact of Atmospheric Parameters over GSM Channels in Zaria City, Nigeria. Journal of Electronics and Information System, 6(2): 49–64. DOI: https://doi.org/10.30564/jeis.v6i2.7960



Design and Testing of four phase Transmission Lines from generator

¹Ahuome B.A., ¹Israel Adekeye, ¹Tijani A. Sadiq.

¹Department of Physics, Faculty of Physical Sciences, Federal University Dutsin-Ma, Katsina State, Nigeria

babubakar@fudutsinma.edu.ng

Abstract

In modern society, the demand for reliable and stable electrical power is critical for sectors such as healthcare, data centers, and industry. Conventional three-phase generators sometimes fail to meet the high demands, stability nor efficiency. Interest has grown in exploring multi-phase systems, including four-phase generators, to overcome these limitations. This work studied the design and implementation a four-phase generator that ensures improved load balancing, reduced harmonic distortion, and enhanced power stability through assessing the feasibility of four-phase systems in critical applications, simulating and implementing the generator, selecting suitable components for optimal reliability, and evaluating the performance through testing key parameters such as voltage regulation, efficiency, and harmonic levels. The research further aims to promote its integration into power systems with a focus on minimizing operational risks and enhancing energy efficiency. The MATLAB simulation demonstrated a phase shift of 90° between each phase, confirming the correct configuration. The generator delivered a stable RMS voltage of 70.71 V per phase and operated at a frequency of 50 Hz. It achieved a power factor of 0.9, real power output of 2545.64 W, and an efficiency of 84.8%. Voltage regulation stood at 6%, and total harmonic distortion was 0%, indicating clean sinusoidal output. Protection systems such as fast-acting fuses and breakers were effective. These results validate the feasibility of four-phase generators for high-reliability applications, suggesting potential for broader adoption in critical infrastructure and national grid system.

Keywords: Power generation, Four phase transmission, Design and Testing, MATLAB simulation

Introduction

Electric power generation and distribution are fundamental to modern society, with reliable and efficient power systems being critical for industrial operations, healthcare facilities, communication systems, and other essential services. Traditional power systems often rely on three-phase generators, which are widely used due to their balanced load distribution and relatively simple design. However, three-phase systems may not always offer the highest reliability and stability in high-demand or mission-critical environments. (Idoko, P. I., Ayodele, T., Abolarin, S. M., & Ewim, D. 2023. In recent years, there has been a growing interest in exploring multi-phase power generation systems beyond the conventional three-phase setup. The introduction of a fourphase generator offers several potential advantages, including improved power quality, enhanced load balancing, and reduced harmonic distortion. These benefits are particularly significant for applications where uninterrupted and high-quality electrical power is essential, such as in hospitals, data centers, and critical industrial processes. (Mahmoud, R. A. 2021). The four-phase generator operates with four separate voltage waveforms, spaced 90 degrees apart, which leads to more balanced power distribution across the system. This unique configuration can reduce the likelihood of voltage fluctuations and provide a more stable output under varying loads. Furthermore, fourphase systems can potentially decrease the effects of harmonics, which are often problematic in



three-phase systems, thus improving the overall efficiency and longevity of electrical equipment. (Zhao, Y., Teng, D., Li, D., Mi, Y., & Zhao, X. 2021).

This study aims to design, test, and evaluate a four-phase generator system for use in high reliability applications. By focusing on its potential to improve power stability and reduce operational risks, this research seeks to contribute to the development of more robust and efficient power generation systems that meet the demands of critical infrastructure.

2. Materials and Method

Magnetic Core Material: These materials are used for the core of the generator, particularly in the stator and rotor. Silicon steel is commonly used because it offers good magnetic permeability, reducing core losses and improving the efficiency of the generator. Ferrite cores may also be used in small-scale systems or high-frequency applications.

Copper or Aluminum Windings: Copper is often used for the winding coils in the stator and rotor due to its high electrical conductivity, which minimizes resistive losses. Aluminum can also be used as a more cost-effective alternative, though it has lower conductivity than copper.

Insulation Materials: Insulating materials are used to prevent short circuits between coils and ensure that the electrical current flows through the windings as intended. The insulation must be able to withstand high temperatures and electrical stresses.

Rotor and Stator Laminations: Laminations are thin sheets of material used to reduce eddy current losses in the core. Silicon steel, which has high electrical resistance and magnetic permeability, is often used in the lamination stacks of the stator and rotor.

Bearings and Shaft Materials: Bearings allow the rotor to rotate smoothly and with minimal friction. The shaft, typically made of high-strength steel or alloys, transmits mechanical energy from the prime mover (engine, turbine, etc.) to the generator.

Cooling Materials and Systems: Generators, particularly high-capacity ones, generate significant heat during operation. Effective cooling systems are required to prevent overheating, which can cause material degradation and system failure. Air cooling (fans), water cooling (for larger generators), or oil-based cooling systems can be used.

Switchgear and Protection Components: Switchgear includes circuit breakers, relays, and fuses used to protect the generator from faults, overloads, or short circuits. These components are crucial for safe operation and must handle high currents and voltages.

Control System Components: The control system is responsible for monitoring and regulating the output of the generator, including voltage, current, and frequency. Sensors detect operational parameters, and microcontrollers process the data to maintain stability in the fourphase system.

Method

This are the method in the construction of a four phase motor which are:

System Design

Design Specifications

Power Requirements: Determine the power generation capacity of the four-phase generator, including voltage, current, and frequency specifications.

Reliability Requirements: Identify the specific high-reliability needs of the target application (e.g., industrial machinery, critical infrastructure). This includes ensuring fault tolerance, redundancy, and stable performance.



Four-Phase Configuration: Define the number of phases (four-phase), with each phase 90° out of phase with the others. This ensures smoother power delivery compared to three-phase generators and provides redundancy in the event of a failure.

Component Selection

Magnetic Core Material: Choose suitable materials (silicon steel, ferrite) for the stator and rotor cores. High permeability and low eddy current losses are essential.

Windings: Select copper or aluminum for the stator windings, ensuring that the selected material has high conductivity to minimize energy losses.

Bearings and Shaft: Choose high-strength steel or alloys for the shaft and bearings to handle rotational forces and ensure smooth operation.

Control System: Design or select a control system that can regulate and monitor the generator's output (voltage, current, and frequency).

Cooling System: Design an adequate cooling system (air or oil-based) to maintain the generator's temperature within safe limits.

Construction and Assembly

Core Assembly: Construct the rotor and stator cores using silicon steel laminations to reduce eddy current losses. The lamination process involves stacking thin sheets of silicon steel and bonding them together to form the core.

Windings: Wind copper or aluminum wire onto the stator coils. Each coil should be carefully insulated to prevent short circuits and ensure safe operation. The windings are arranged to create the four-phase system, with a 90° phase shift between each winding.

Rotor Construction: The rotor is typically constructed with a laminated iron core, and windings or permanent magnets (if used) are installed. If the generator uses permanent magnets, neodymium magnets may be attached to the rotor, carefully positioned to produce a stable magnetic field.

Cooling System Installation: Depending on the generator's size and power output, the cooling system may be air-cooled or liquid-cooled. Air cooling involves mounting fans around the generator to expel heat, while liquid cooling requires the use of a pump and heat exchanger to regulate the temperature.

3. Results and Discussions

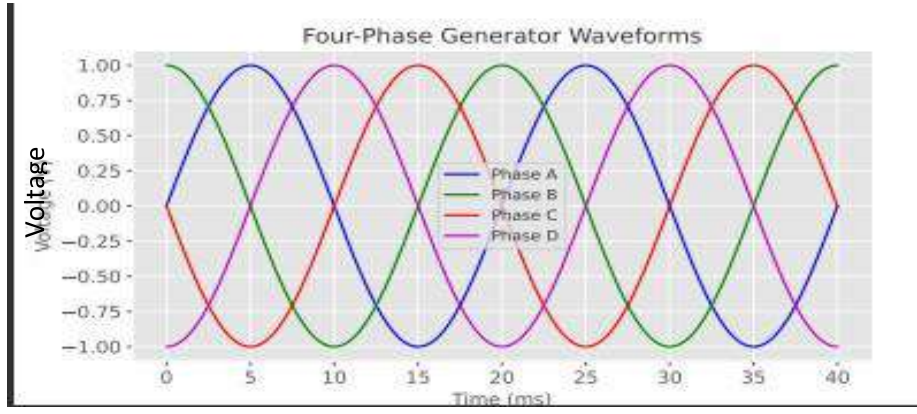
This results reflect the performance and advantages of the four-phase transformer compared to conventional designs. Some possible findings include: I use MATLAB to simulate the generator's performance and obtain the following result: Waveforms, Voltage and Current Measurement, Power Analysis, Harmonic Analysis

3.1 Output Voltage and Phase Relationship

Table 4.1: Output Voltage and Phase Relationship

Phase	Peak Voltage (V-Max)	RMS Voltage (V-Phase)	Phase Shift
Phase 1	100 V	70.71 V	00
Phase 2	100 V	70.71 V	90°
Phase 3	100 V	70.71 V	180°
Phase 4	100 V	70.71 V	360°





Discussion:

This graph shows four sinusoidal waveforms: Phase A, B, C, and D. Each waveform is shifted by 90 degrees ($\pi/2$ radians) from the next.

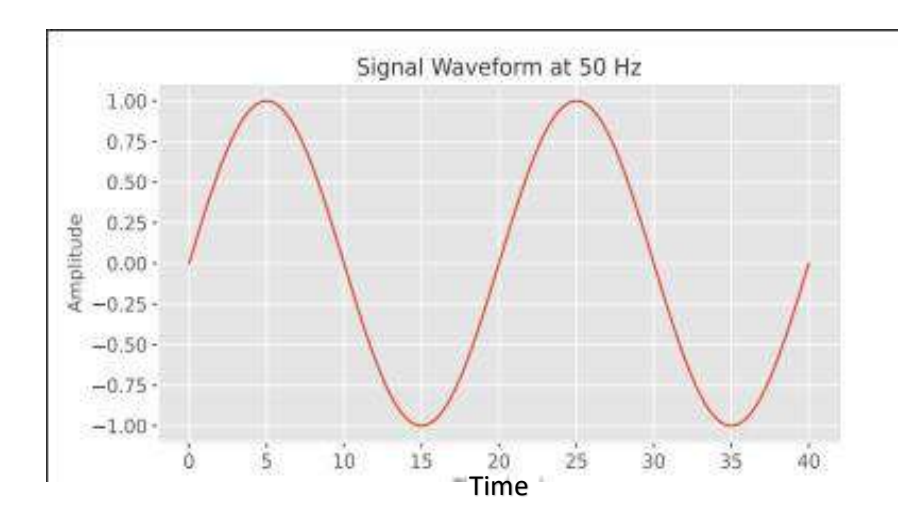
Meaning: In a four-phase generator, the output voltages are equally spaced in phase, i.e., each phase is 90° apart. This ensures smooth and continuous power delivery in systems designed for four-phase operation. It's crucial for balanced load operation and power electronics applications where multiple phases reduce ripple.

- The output voltage for each phase is sinusoidal with a peak value of 100 V.
- The RMS voltage for each phase was observe as $V_{RMS} = \frac{V_{max}}{\sqrt{2}} = 70.71V$
- Each phase is shifted by 90° from the adjacent phases, ensuring balanced phase separation.
- This phase relationship allows for continuous power delivery without destructive interference.

3.2 Frequency Calculation

Table 4.2: Frequency Calculation

Rotational Speed (RPM)	Number of Pole	Frequency
1500 RPM	4 Pole	50Hz



Discussion:

This is a single sine wave plotted over time, representing one phase of the AC signal at 50 Hz. Meaning: The graph shows one complete cycle of the sine wave happening every 20 ms (since



1/50 = 0.02 s). This confirms the generator is producing the expected standard frequency of 50 Hz, which is essential for compatibility with electrical grids and appliances.

The frequency of the four-phase generator is calculated using the formula $f = \frac{P \times N}{120}$ where:

P = 4 (number of poles),

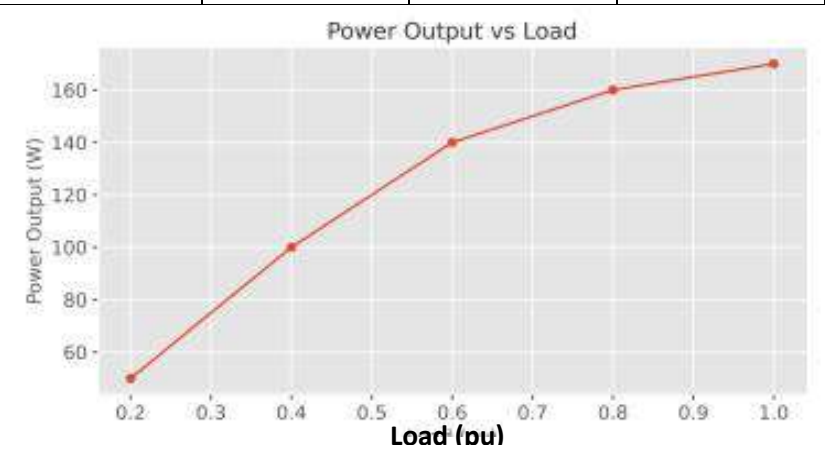
N = 1500 RPM (rotational speed).

The calculated frequency is 50 Hz, which is standard for many power systems globally.

3.3 Power Output (Real Power, Reactive Power, Apparent Power)

Table 4.3: Power Output (Real Power, Reactive Power, Apparent Power)

Ph	nase oltage	1 \	Power Factor	Real Power	Reactive Power	Apparent Power
70).71 V	10 A	0.9	2545.64 W	1414.28 VAR	2922.6 VA



Discussion:

A line graph showing how power output increases with load.

Load is measured in per unit (pu), ranging from 0.2 to 1.0.

Power output increases from 50 W to 170 W. as the load increases.

This graph demonstrates that the generator is functioning correctly — it delivers more power as the demand increases.

A gradual increase without sharp drops indicates stable generator behavior and good voltage regulation.

Real Power is calculated as $P_{total} = 4 \times V_{phase} \times I_{phase} \times PF$.

Reactive Power is calculated using $Q_{total} = 4 \times V_{phase} \times I_{phase} \times \sin(\emptyset)$

Apparent Power is determined by $S_{total} = \sqrt{P_{total}^2 + Q_{total}^2}$

The Power Factor (PF) is 0.9, which is typical for many inductive loads (like motors).

3.4 Efficiency Calculation

Table 4.4: Efficiency Calculation

Input Power (P.in)	Output Power (P-out)	Efficiency ()
3000 W	2545.64 W	84.8%



Discussion:

Generators are often less efficient at low loads due to constant internal losses. As load increases, more of the input power is converted to useful output, hence higher efficiency. A high-efficiency curve indicates good design and load-matching.

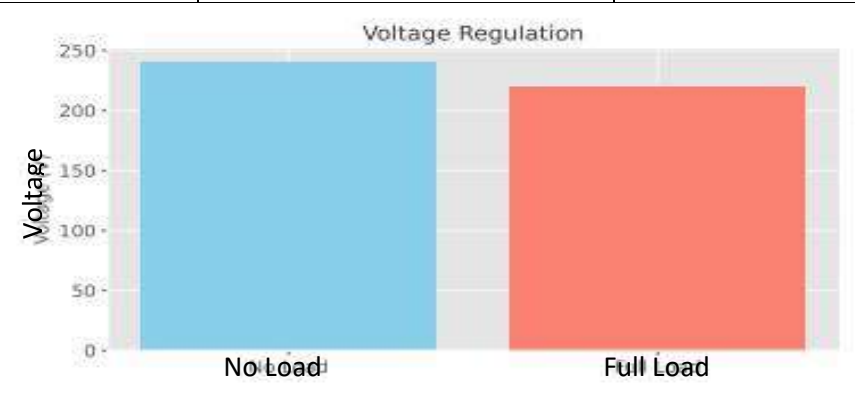
Efficiency of the generator is calculated as $\eta = \frac{P_{out}}{P_{in}} \times 100$

With an input power of 3000 W and output power of 2545.64 W, the efficiency comes out to 84.8%. This is a typical efficiency range for practical generators, accounting for mechanical and electrical losses.

3.5 Voltage Regulation

Table 4.5: Voltage Regulation

No Load Voltage	Full Load Voltage	Voltage Regulation
75 V	70.71 V	6.0%



Discussion:

Graph Description:

A bar chart comparing output voltage at no-load (240V) and full-load (220V). We Meaning: Lower voltage under load is normal due to internal impedance. The smaller the voltage drop, the better the voltage regulation. This generator drops by only 20V, which is acceptable in many systems.

Voltage Regulation is the difference between no-load and full-load voltage, calculated using
$$Voltage\ Regulation = \frac{V_{on\ load} - V_{full\ load}}{V_{full\ load}} \times 100$$

Conclusion

The design have shown the parameters as 75.0 V on no load and 70.71 V on load voltage. The phase current of 10 A yielded 2545.64 W at a phase difference of π and 0 THD. This simulated result have shown that the four-phase generator successfully produced stable multi-phase AC power than the traditional three phase generator. Simulated metrics showed high efficiency, phase shift accuracy, and strong load-handling ability.

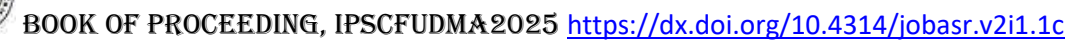
The system is suitable for applications requiring balanced multi-phase power. It offers significant advantage in terms of power quality, by adopting a symmetrical winding configuration, integrating modern control and protection system, and ensuring compliance with international standard, a four phase generator can deliver reliable and efficient performance across various industries, and



specialized application. As technology continue to evolve, the four phase generator stand as a promising solution for future power generation needs where precision and stability are critical.

References

- Boldea, I., & Tutelea, L. (2018). Reluctance electric machines: Design and control. Taylor & Francis Group.
- Cassimere B.N. and Sudhoff, S.D. (2009) "Analytical Design Model for Surface Mounted Permanent Magnet Synchronous Machines," IEEE Trans. Energy Conversion, Vol. 24, pp. 338–346.
- Chasiotis, I. D., & Karnavas, Y. L. (2019). A generic multi-criteria design approach toward high power density and fault-tolerant low-speed PMSM for pod applications. IEEE Transactions on Transportation Electrification, pp. 356–370.
- Clerc, M., & Kennedy, J. (2002). The particle swarm-explosion, stability, and convergence in a multidimensional complex space. IEEE Transactions on Evolutionary Computation, pp. 58–73.
- Fan, Y., Chau, K. T., & Cheng, M. (2006). A new three-phase doubly salient permanent magnet machine for wind power generation. IEEE Transactions on Industry Applications, pp. 53–60.
- Guerroudj, C., Saou, R., Boulayoune, A., Zaïm, M. E. H., & Moreau, L. (2017). Performance analysis of Vernier slotted doubly salient permanent magnet generator for wind power. International Journal of Hydrogen Energy, pp. 8744–8755.
- Hanselman, D.C. (1994) Brushless Permanent-Magnet Motor Design, McGraw-Hill, New York.
- Karnavas, Y. L., Chasiotis, I. D., Korkas, C. D., & Amoutzidis, S. K. (2017). Modelling and multiobjective optimization analysis of a permanent magnet synchronous motor design. International Journal of Numerical Modelling: Electronic Networks, Devices and Fields, pp. 2232.
- Kirtley, K., James, L., Banerjee, A., & Englebretson, S. (2015). Motors for ship propulsion. Proceedings of the IEEE, pp. 2320–2332.
- Pechlivanidou, M. C., Chasiotis, I. D., & Karnavas, Y. L. (2019). A comparative study on 2D and 3D magnetic field analysis of permanent magnet synchronous motor using FEM simulations. Journal of Electromagnetic Waves and Applications, pp. 2215–2241.
- Rezzoug, A., & Zaïm, M. E. H. (2011). Non-conventional electrical machines. John Wiley & Sons.
- Scuiller, F., Semail, E., Charpentier, J.-F., & Letellier, P. (2009). Multi-criteria-based design approach of multi-phase permanent magnet low-speed synchronous machines. IET Electric Power Applications, pp. 102–110.
- Symington, W. P., Belle, A., Nguyen, H. D., & Binns, J. R. (2016). Emerging technologies in marine electric propulsion. Proceedings of the Institution of Mechanical Engineers, Part J: Engineering Maritime Environment, pp. 187–198.
- Thongam, J. S., Tarbouchi, M., Okou, A. F., Bouchard, D., & Beguenane, R. (2013). Trends in naval ship propulsion drive motor technology. In 2013 IEEE Electrical Power & Energy Conference, pp. 1–5.



WHEAT-HIGH QUALITY CASSAVA FLOUR BREAD SPICED WITH CLOVE POWDER

¹Adetoro O.F*, ²Kajihausa O.E, ²Sobukola O.P. and ³Afolabi W. A. O.

¹Department of Food Science and Technology, Yaba College of Technology, Yaba, Lagos State, Nigeria

²Department of Food Science and Technology, Federal University of Agriculture, Abeokuta, Ogun State

³Department of Nutrition and Dietetics, Federal University of Agriculture, Abeokuta, Ogun State, Nigeria

*Corresponding Author: holuwafunmike@gmail.com/+2348060069886

Abstract

This study investigated some quality attributes of wheat flour (WF) and High-Quality Cassava Flour (HQCF) spiced with clove powder (CP). Flour blends were produced from 90% WF and 10% HQCF with inclusion of clove powder at 0.10, 0.50, 1.00, 1.50 and 2.00% respectively. Bread samples were produced from the blends while 90% WF and 10% HQCF was used as control. Functional properties (bulk density [BD], water absorption capacity [WAC], oil absorption capacity [OAC], swelling power [SP], solubility index [SI]) and pasting properties of flour blends as well as rheological properties in terms of farinograph water absorption (FWA), dough development time (DDT), dough stability time (DST), degree of dough softness (DDS) and farinograph quality number (FQN) of the flour dough were determined using standard procedures. Data were analysed using descriptive and inferential statistics. The values of functional properties are BD, WAC, OAC and SP ranged from 0.73 to 0.78 g/ml, 1.23 to 2.12 ml/g, 1.86 to 2.51 ml/g and 3.24 to 3.8 ml/g respectively while SI decreased from 10.45 to 9.11 ml/g. Pasting viscosities (RVU) such as peak (210.71-237.25), trough (118.04-151.38), final (199.33-236.38), setback (73.96-88), plus peak time (5.13-6.98 min) and pasting temperature (71.66-73.46 0C) decreased while breakdown viscosity (69.88-96.75) increased with CP addition. FWA (62.35-62.9%) increased while FQN (71.5-98.5 mm) decreased with increased CP inclusion. In conclusion, the inclusion of clove powder had great contribution on the processing of the bread dough.

KEYWORDS: High-Quality Cassava, Wheat, Clove Powder, Functional properties, Pasting properties

INTRODUCTION

Bread is one of the important staple foods and has been seen as the second non-indigenous food product after rice in Nigeria (Shittu *et al.*, 2007). It is mostly consumed by children and adult due to its availability in the country. Bread quality produced encompasses around its method of dough preparation, baking conditions, packaging as well as sanitary conditions during processing (Cauvin, 2015). The nature of its raw material, processing condition as well as the storage stability also determines its quality. However, bread dough is prepared from wheat flour, yeast, sugar, salt, water and other ingredient when added act as spice for the purpose of maintaining an improve quality food product.

Wheat flour is the major source of raw material used for the preparation of bread. This is because of its ability to retain air, water vapour and gas in form of carbon-dioxide, then with strength in forming foam or spongy structure due to the presence of gluten (Adeniji *et al.*, 2011). However, the importation of Wheat flour in the food industry is highly demanding especially in bakery and confectionery industries, and the need for the improvement of a raw material becomes necessary.



The utilization of cassava flour for the production of bread becomes of necessity. Studies has shown that that composite flour can be used for the preparation of bread dough.

Considering the development in the food sectors few years back with the wide range of cassava plantation, High-Quality Cassava Flour (HQCF), a product from Cassava root has really served as supportive ingredient to wheat in developing countries for many industries, especially in the bakery and confectionery industries where products such as bread, pastries and cake are produced (Oyewole et al., 1996; Badifu et al., 2004; Echendu et al., 2004; Ameh et al., 2013; Igabbul et al., 2013). Supplementing High Quality Cassava Flour (HQCF), an unfermented, smooth, bland, odourless, white or off- white product with wheat flour has eventually not only improved the bread quality as ingredient during processing but also minimise the cost of production for other bakery and confectionery products in food industries present in developing nations (Shittu et al., 2007). The introduction of spice to food has been of great benefits in the quality of many novel foods especially when it involves the taste, aroma and also the flavour of the food prepared. Spices are generally known as plant substances from indigenous or exotic origin, aromatic or with strong taste and used to enhance the taste of foods (Pundir et al., 2010). The functional behaviour of any spice can not only improve the quality of food during processing, but can also influence consumers' acceptability on the food product when considering the taste, appearance and flavour of the food. Spices has widely been used in different form and documented by researchers. Most spice are milled in powdery form and thereafter used as additives for different foods and as well as preservative to medicinal drugs. Research has shown that the use of spice during food preparation has also help to reduce other ingredient such as salt during food preparation and this has served as great benefit which spice as ingredient contribute to food industries in Nigeria (Karapinar et al., 1990). The addition of spice has also helped the food industries by minimizing their cost of production.

Clove (*Syzygium aromaticum*) is known as one of the valuable spices used for centuries. It has been used as food preservative and for many medicinal purposes (Karapinar, 1990). Clove is widely found in Northern part of Nigeria. Considering the inherent properties of clove as food ingredient, that is, antioxidant and antimicrobial activity, Clove has also been regarded as special ingredient and seen differently from other spices. Clove has also been known to possess more antioxidant and antimicrobial activity than other fruits and vegetables as well as other spices. Meanwhile the health benefits of spice like clove would not be rule out since its major function as a spice in food is to be considered as a functional ingredient for bakery product during processing. This demand for a special attention in the use of clove. Due to the effectiveness of clove as its antioxidant and antimicrobial capacity underpin the reason in carrying out this research.

MATERIALS AND METHODS

Procurement of the Materials

High quality cassava flour was procured in Federal Institute of Industrial Research Oshodi (FIIRO), while wheat flour, clove buds and other ingredients for baking (sugar, fat, salt, and yeast) were purchased from Kuto market Abeokuta, Ogun state.

Methods

Preparation of clove powder

Clove buds were cleaned and oven dried at 60 °C up to moisture content level below 10%. Then it was ground to fine powder (Figure 1).

The ground clove was sieved (using sieve of 500 mesh size) to obtain a uniform powder which was stored in air-tight containers at room temperature (24 ± 2 °C) for subsequent use.



Flour blends preparation

Clove powder was added at four levels into the formulation of wheat and high-quality cassava flour. The proportion of the bread sample blends were as follows Wheat HQCF blends: 90:10 served as the control, while other sample blends which include composite flour from Wheat-HQCF with the inclusion of clove powder measured in different variation include 90:10:0.1; 90:10:0.5; 90:10:1; 90:10:1.5 and 90:10:2 grams. The flour blends were thoroughly mixed as the blend formulation was carried out. The introduction of clove powder to the baked food was properly monitored during preparation and then combined with other ingredient to form a dough from which the bread samples after which various analyses were carried out to access the best level of incorporation of clove powder in the bread.

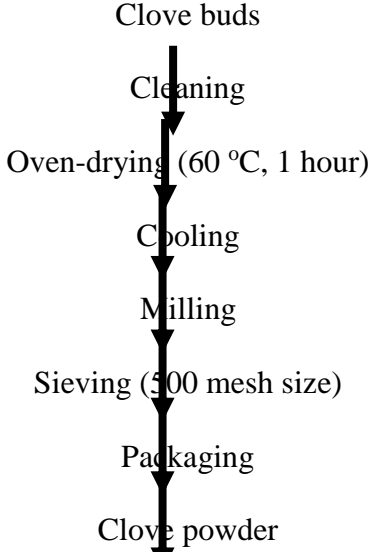


Figure 1: Production process of clove powder (Devendra and Tanwar, 2011)

Preparation of bread

Control bread dough was prepared and baked from 100 % wheat flour using the straight dough method (Chauhan *et al.*, 1992; Shittu *et al.*, 2013) in Figure 2.

Ingredient weighed

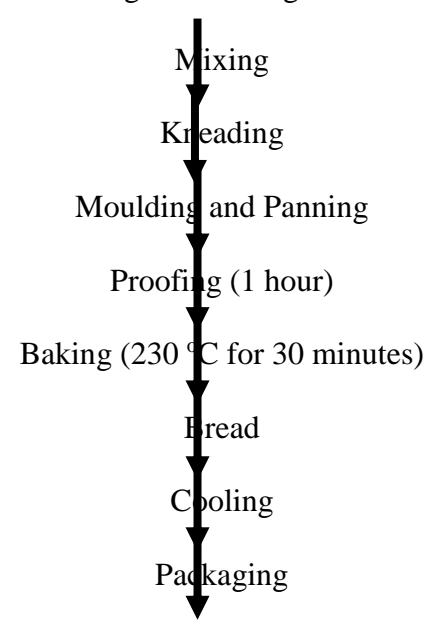




Figure 2: Flow chart for bread production (Chauhan *et al.*, 1992; Shittu *et al.*, 2013) The supplemented bread dough with clove powder was also prepared using same method except for adding clove powder in varying quantities into the blend of wheat and high-quality cassava flour.

Analysis of the flour blends Functional properties Bulk density determination

The bulk density (Equation 1) was determined by the method of Wang and Kinsella (1976). A known amount of the sample was weighed into 50 ml graduated measuring cylinder. The samples were packed by gently tapping the cylinder on the bench top 10 times from height of 5 cm; the

volume of the sample was recorded.

nt of Sample
Weight of the Sample After Tapping

1

Bulk Density $(gml^{-1} \ or \ gcm^3) = \underbrace{Weight \ of \ Sample}_{Weight \ of \ be}$

Swelling power and solubility index determination

Swelling power (Equation 2) and water solubility index (Equation 3) were carried out by Takashi and Sieb (1988) method. It involves weighing 1 g of flour sample into 5 ml⁻¹ centrifuge tube; 50 ml⁻¹ of distilled water was added and mixed gently. The slurry was heated in a water bath at temperatures (70, 80, 90, and 100) °C respectively for 15 minutes. During heating, the slurry was stirred gently to prevent clumping of the flour. On completion of 15 minutes, the tube containing the paste was centrifuge at 3000 rpm for 10 minutes. The supernatant was decanted immediately after centrifuging. The weight of the sediment was then taken and recorded. The moisture content of the sediment gel was used to determine the dry matter content of the gel.

$$Swelling\ Power = \underbrace{Weight\ of\ Wet\ Mass\ Sediment}_{Weight\ of\ Dry\ Matter\ sample} 2$$

$$Water\ Solubility\ Index = \underbrace{Weight\ of\ Soluble\ x100}_{Weight\ of\ Sample} 3$$

Water absorption index determination

Water absorption index (Equation 4) was evaluated by using the modified method of (Ruales *et al.*, 1993). The flour blends sample (1.25 g) was suspended in 15 ml distilled water at 30 °C in a centrifuge tube, stirred for 30 minutes intermittently and then centrifuged at 3000 rpm for 10 minutes. The supernatant was decanted and the weight of the gel form was recorded. The water absorption index (WAI) was calculated as gel weight per gram dry sample.

$$Water Absorption Index = \underbrace{Bound\ Water \ x\ 100}_{Weight\ of\ Sample}$$

Oil absorption capacity determination

The oil absorption capacity (Equation 5) of the flour was estimated by the method of Sosulski *et al.*, (1976). One gram of sample mix with 10 ml soy bean oil (Sp. Gravity 0.9092) was allowed to stand at ambient temperature (30 ± 2 °C) for 30 minutes at 3000 rpm. Oil absorption was calculated as per cent oil bound per gram flour.

$$\% OAC = \frac{WeightAfterCentrifuge - InitialWeight}{SampleWeight} x100$$

Pasting properties of the flour blends

Pasting properties was determined using a rapid visco-analyzer [(RVA) TECMASTER, Perten Instrument Sweden] according to the method described by Sanni et al. (2006a). The sample was



turned into slurry by mixing 3 g with 25 ml of water inside the RVA can. The can was then inserted into the tower which was lowered into the system. The slurry was heated from $50-90\,^{\circ}\text{C}$ and cool back to $50\,^{\circ}\text{C}$ within 12 min. The can rotated at a speed of 160 rpm. The content was stirred continuously using a plastic paddle. Parameters such as peak viscosity, trough, breakdown viscosity, final viscosity, set back viscosity, peak time and pasting temperature was estimated.

Rheological determination of the dough

Mixing characteristics of dough from clove powder, wheat and high-quality cassava flour blends was determined using brabender farinograph according to AACC (2000). The parameters determined are: farinograph water absorption, dough development time, dough stability time, degree of dough softness and farinograph quality number.

Statistical analyses

All data were analysed using statistical packages for social science (SPSS) 20.0 Analysis of variance (ANOVA) was used to analysed the data. Significant difference (p<0.05) was seen at means standard deviation conducted

RESULTS AND DISCUSSIONS

Functional Properties

The mean values of the functional properties of wheat and high-quality cassava flour spiced with clove powder is presented in Table1. Generally, the mean values from bulk density, oil absorption capacity, water absorption capacity, swelling power and solubility index were significantly (p<0.05) different among the flour. Bulk density is a measure of heaviness of flour (Oladele and Aina, 2007), and it is an important parameter that determines the packaging requirement of a food product. Bulk density of the composite flour blends spiced with clove powder varied between 0.73 and 0.78 g/ml.

Table 1: Functional properties of wheat and high-quality cassava flour spiced with clove powder

WF-HQCF- CP	Bulk Density (g/cm³)	Oil Absorption Capacity (%)	Water Absorption Capacity (%)	Swelling Power (%)	Solubility Index (%)
90-10-0.1	0.78 ± 0.0^{e}	2.12±0.01 ^f	1.86 ± 0.01^{a}	3.24±0.01 ^a	9.11±0.01 ^a
90-10-0.5	0.73 ± 0.0^{a}	1.23±0.01 ^a	$2.51 \pm 0.01^{\rm f}$	$3.8 \pm 0.01^{\rm f}$	10.45±0.01 ^f
90-10-1.00	$0.77{\pm}0.0^d$	1.44±0.01 ^d	1.92±0.02 ^b	3.39±0.01 ^b	9.34±0.01 ^b
90-10-1.50	0.74 ± 0.0^{b}	1.29±0.01 ^b	2.12±0.01 ^e	3.67±0.01 ^e	10.24±0.01 ^e
90-10-2.00	0.75 ± 0.0^{c}	1.67±0.02 ^e	2.00±0.01°	3.51±0.01°	10.07±0.01°
Control	0.74 ± 0.0^{b}	1.34±0.01°	2.06±0.01 ^d	3.57±0.01 ^d	10.12±0.01 ^d

Mean values with different superscripts within the same column are significantly different (p < 0.05)

WF-Wheat Flour, HOCF-High Quality Cassava Flour, CP-Clove Powder



The variation in bulk density of the food sample could be attributed to variation in the proportion of clove powder used for the food flour preparation. The introduction of spice clove powder increased the bulk density of the composite flour blends. Composite wheat and high-quality cassava flour with 0.10% clove powder inclusion had the highest bulk density while the flour blends with 0.50% had the least. Higher bulk density is desirable for greater ease of dispersion and reduction of paste thickness (Amandikwa, 2012). Higher bulk density suggested the sustainability of the composite flour blends during processing (Suresh and Samsher, 2013).

Oil absorption capacity of the food formulation simply referred to the binding of fat by non-polar side chains (Venna and Usha, 2018) of any food substance basically protein in particular (Awuchi et al., 2019) during processing. The mean values for oil absorption capacity varied between 1.23 and 2.12 ml/g with 0.10% clove powder inclusion having the highest oil absorption capacity and that with 0.50% having the least. For composite flour of Wheat-Cassava-Clove blends, the oil absorption capacity increased with the inclusion of clove powder in the composite flour blends as reduction takes place at an increased in clove inclusion of the composite flour blends. The relatively high oil absorption capacity of the flour blends is an indication that flavour and mouth feel will be enhanced when the composite flour blends was used for the production of bakery product such as bread produced from the composite flour. This was seen during the mixing of the bread dough (Jacob and Leelavathi, 2007).

Water absorption capacity is the amount of water (moisture) taken up by the food powder in order to arrive at a desirable and stable state of keeping product quality. This actually involved the hydration of food powder due to their interaction of hydrogen bonds and water molecules (Awuchi et al., 2019). The result of water absorption capacity of the flour blends ranged from 1.86 to 2.51 ml/g with 0.10% addition of clove powder to have the lowest water absorption capacity while 0.50 % had the highest. There was an increase in water absorption capacity (WAC) with the addition of clove powder in the composite flour. WAC of the blends suggests that the flours can be used in formulation of some foods such as sausage, dough and bakery products. The increase in the WAC has always been associated with increase in the amylose leaching and solubility, and loss of starch crystalline structure (Chandra et al., 2015) on the composite flour blends. Madu (2007) reported that water absorption capacity enables bakers to add more water to dough and so improve handling characteristics and maintain freshness of the baked products. Swelling power is an indication of the extent of associative forces within the granules (Adegunwa et al., 2014), while solubility is the ability of solids to dissolve in liquids and it is reported to depend on a number of factors such as source, inter-associative forces, swelling capacity and presence of other non – carbohydrate components (Moorthy, 2002). Swelling power and solubility index also ranged from 3.24 to 3.8 ml/g and 9.11 to 10.45 ml/g respectively. With 0.50% clove powder addition having the highest and 0.10% the least mean values for swelling power and solubility index, respectively. The result showed that the inclusion of clove powder contributed to the solubility which also influenced the swelling power of the dough during the preparation of the food sample.

Pasting Properties

Pasting properties are generally known to influence processing and quality attributes in the food industry as they affect texture and digestibility as well as the end use of starch-based food commodities (Adebowale *et al.*, 2005). The Table 2 below showed the mean values for the pasting properties of wheat, high quality cassava composite flour with clove powder addition. It is one of the most important parameters that influence quality and aesthetic consideration in the food industry, and they affect texture and digestibility as well as end use of starch-based food commodity (Onweluzo and Nnamuchi, 2009). The peak viscosity decreased from 237.25 to 210.71



RVU with the composite flour without the addition of clove having the highest mean value while the one with 1.50% having the least peak viscosity. The mean values were not statistically (p<0.05) different from each other except for samples containing only wheat-HQCF (90%-10%) and wheat-HQCF-clove (90%-10%-1.5) that differed significantly (p<0.05). Trough significantly (p<0.05) increased with the inclusion of clove powder to 151.38 RVU when compared with 147.13 RVU from wheat-HQCF (90%-10%). The peak viscosity was lower for flour blends with clove powder when compared with composite flour blends without the inclusion of clove powder.

Table 2: Pasting Properties Of Wheat And High-Quality Cassava Flour Spiced With Clove Powder

WF-HQCF- CP	Peak	Trough	Breakdown	Final	Setback	Peak
	Viscosity	(RVU)	Viscosity	Viscosity	Viscosity	Time
	(RVU)		(RVU)	(RVU)	(RVU	(Mins)
90-10-0.10	218.04 ± 5.83^{b}	151.38 ± 0.29^{e}	69.88 ± 1.00^{a}	224.63±0.77 ^e	73.96 ± 0.53^{a}	6.98 ± 0.64^{c}
90-10-0.50	222.42 ± 0.47^{b}	135.79 ± 0.53^{c}	88.04 ± 1.00^{b}	219.96 ± 0.29^{d}	84.42 ± 0.12^{c}	6.32 ± 0.16^{c}
90-10-1.00	222.5 ± 0.47^{b}	126.54 ± 1.83^{b}	96.75 ± 0.24^{e}	207.71 ± 0.06^{c}	82.46 ± 0.06^{c}	6.06 ± 0.08^{b}
90-10-1.50	210.71 ± 0.65^{a}	118.04 ± 0.77^{a}	93.17 ± 0.59^{d}	199.33±0.12a	81.83 ± 0.12^{c}	5.13 ± 0.14^{a}
90-10-2.00	221.63 ± 1.71^{b}	127.29 ± 0.53^{b}	93.79 ± 0.41^{d}	205.33 ± 0.35^{b}	78 ± 0.24^{b}	6.1 ± 0.04^{b}
90-10-0.00	237.25 ± 0.12^{c}	147.13±0.18°	90.42 ± 0.35^{c}	236.38 ± 0.53^{f}	88 ± 2.47^{d}	6.24 ± 0.05^{b}

Mean values with different superscripts within the same column are significantly different (p <0.05). WF-Wheat Flour, HQCF-High Quality Cassava Flour, CP-Clove Powder

The significant level of peak viscosity reduced when the composite flour blend increased with the addition of clove powder. Although, low peak viscosity in the composite flour indicates that the flour may be suited for products requiring low gel strength and elasticity (Abioye et al., 2011). However, high peak viscosity is an indication of high starch content (Awolu et al., 2016). One of the reasons for reduction in peak viscosity could be due to the decrease in starch gelatinization caused by the inclusion of clove powder. Peak viscosity is an index of the ability of starch-based foods to swell freely before their physical breakdown (Sanni et al., 2006; Adebowale et al., 2008). Trough is the minimum viscosity value and it measures the ability of paste to withstand breakdown during cooling (Adebowale et al., 2008). Trough ranged from 118.04 to 151.38 RVV with wheat-HQCF-clove (90%-10%-1.50%) having the least while wheat-HQCF-clove (90%-10%-0.10%) had the highest. The trough or holding strength reduced with addition of clove powder. Thebreakdown in viscosity, sometimes called shear thinning is caused by disintegration of gelatinized starch granules structure during continued stirring and heating, thus, indicating the shear thinning property of starch (Yadav et al., 2011; Babajide and Olowe, 2013). The mean values of breakdown viscosity increased with addition of clove powder and ranged from 69.88 to 96.75 RVU with wheat-HQCF-clove (90%-10%-1.00%) having the highest while wheat-HQCF-clove (90%-10%-0.10%) had the least. Significant (p<0.05) difference was observed for the flour blends in terms of trough. The breakdown viscosity of the flour blends increased continuously after increasing the proportion of clove powder in the flour blends. The increased was seen significantly on the breakdown viscosity among the composite flour blends. Record shown by Banda et al. (2018) that starch is a by-polymer with amylose and amylopectin. The inclusion of cloves served as catalyst which help to increase the breakdown of the composite flour blends. This also influenced the



processing condition of the composite flour during the production of bread. Adebowale et al. (2008), final viscosity is commonly used to define the quality of particular starch- based flour, as it indicates the ability of the flour to form viscous paste after cooking and cooling. It also gives a measure of the resistance of paste to shear force during stirring. Final viscosity reduced significantly (p<0.05) with clove powder inclusion from 236.38 to 199.33 RVU with wheat-HQCF-clove (90%-10%-1.50%) having the least while wheat-HQCF (90%-10%) had the highest. Final viscosity was affected. The inclusion of clove reduced the final viscosity of the flour blends. Setback is an important aspect in the pasting properties of flour, the reason being that it determines the stability of the flour. Low setback value is an indication that the starch has a low tendency to retrograde or undergo syneresis during freeze thaw cycles (Ikujenlola and Fashakin, 2005; Fasasi, 2009). A significant (p<0.05) difference was observed for the flour blends in terms of setback viscosity except for blends with 0.50, 1.00 and 1.50 % inclusion of clove powder. Mean values of setback viscosity varied between 73.96 and 88 RVU. Flour blends from wheat-HQCF-clove (90%-10%-0.10%) had the least while wheat-HQCF (90%-10%) had the highest. Reduction occurs in setback and this could be attributed to increase in cloves inclusion. The inclusion of cloves has a way to reduce the breakdown of starch granule. Banda et al. (2018) established the facts that starch is a by-polymer (containing amylose and amylopectin) which cannot be easily broken down. The breakdown of this starch during processing may be easily affected during processing of food product.

Awolu et al. (2016) described Peak time as an indication of the total time taken by each composite blend to attain its respective peak viscosity. The mean value of peak time increased significantly (p<0.05) and varied between 5.13 and 6.98 minutes. Flour blends from wheat-HQCF-clove (90%-10%-1.50%) had the least while Wheat-HQCF-clove (90%-10%-0.10%) had the highest. The peak time of the composite flour was higher than that of the control sample. At the initial state of introducing clove as to the composite flours, the flour blends had the tendency to possess a higher peak time than the flour without the introduction of cloves. The increase in the proportion of cloves decreased the peak time. This actually affect the production process of bread produced from the composite flour of Wheat-Cassava flour-clove powder. Thus, food blends with a lower peak time will cook faster than that with a higher peak time. The similarity between the peak time values indicates that the composite flour exhibited similar cooking properties. The pasting temperature provides an indication of the minimum temperature required to cook a given sample, which can also have implications on energy usage (Ragaee and Abdel-Aal, 2006). The pasting temperature decreased with clove powder inclusion and varied between 71.66 and 73.55 °C. The pasting temperature reduced as the proportion of clove powder increased in the flour blends. A high pasting temperature indicates high water-binding capacity and high gelatinization tendency of starchbased flour due to high degree of association between starch granules (Adebowale et al., 2008).

Rheological Properties of the Composite Flour Dough

Rheological properties of dough are of great importance for the whole processing. This is because it is actually use for proper monitoring of the food material during processing. Its process used to assess the mechanical properties of dough, molecular structure and composition of the material, to imitate behaviour during dough processing and to anticipate the quality of the final product (DapčevićHadnađev *et al.*, 2011). The result of the rheological properties of flour dough samples was measured by farinograph is presented in Figure 3. Farinograph water absorption ranged from 62.35 to 63.500%. Farinograph measurements showed that the water absorption of dough made from the composite flour increased with an increase in the substitution of clove powder. Although there was no valuable difference in the samples at all levels. The increase in water absorption may



be due to the inclusion of clove powder acting as additives to the composite flour used for preparation of the bread dough. Guarda et al. (2004) reported that addition of selected additives caused the increase in water absorption of formulation. The composition of non-wheat flour has a strong influence on the water absorption of the composite dough. Protein rich flours (Mashayekh et al., 2008) increased the water absorption of dough made from the composite flours. Whereas non - wheat flour with low protein level decrease in water absorption for any composite flour of dough during processing (Miyazaki and Morita, 2005). Dough development time and dough stability time ranged from 5.33 to 7.44 min and 6.04 to 8.56 min respectively. Degree of dough softness ranged from 133.5 to 189.1 FU. Farinograph quality number indicates the quality of flour for bread making. It represents all parameters of farinograph and is more related to gluten network. If the flour has poor quality, it gets weakened early and quickly (Ali et al., 2014). The Farinograph quality number ranged from 71.5 to 98.5. The result showed that there were significant (p<0.05) differences among all these parameters except water absorption which was not significantly (p>0.05) different. The substitution of the composite blend with clove powder significantly reduced the dough development time and dough stability time while degree of dough softness increased with clove powder inclusion. Increase in the percentage inclusion of clove powder increase the faringgraph quality number. The higher the faringgraph quality number, the better the dough handling features. Such positive contribution to the blend may be due to the starch granules in the highquality cassava flour (Abera et al., 2016).

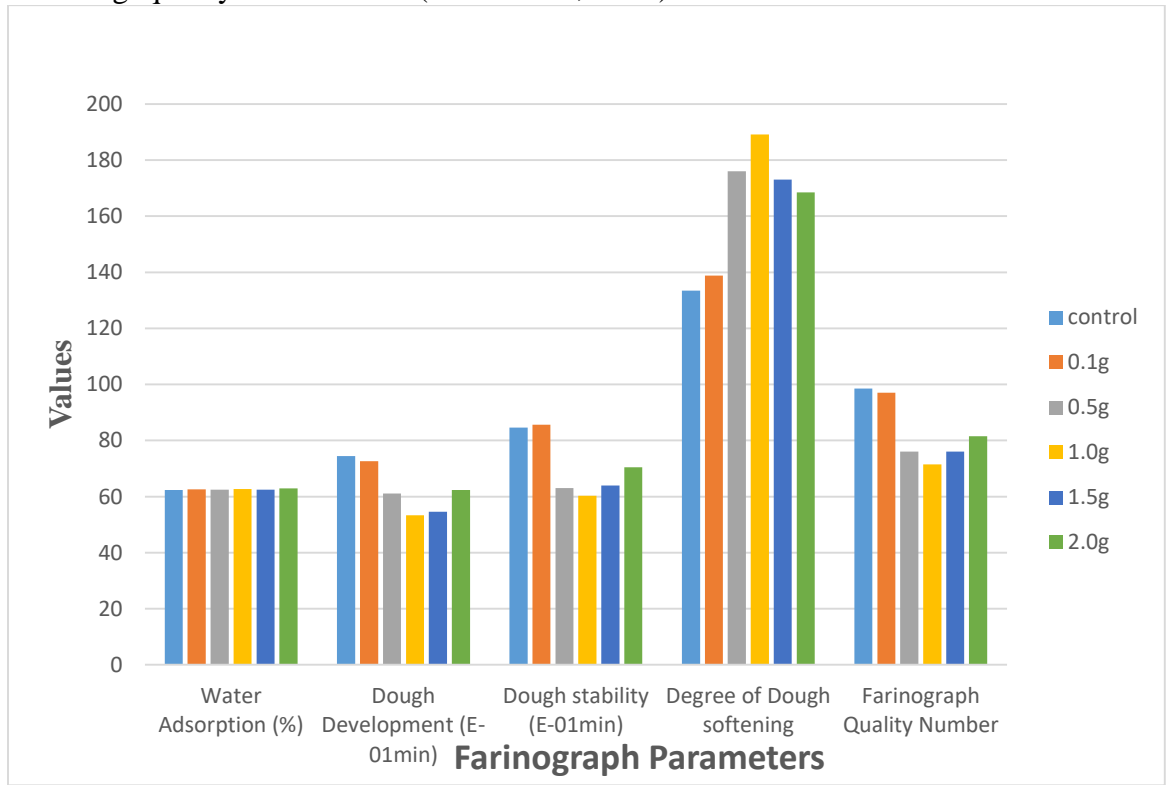
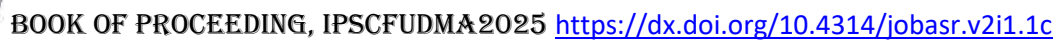


Figure 3: Rheological properties of composite flour dough from wheat-HQCF-clove CONCLUSION

The result from this study revealed that composite flours from the mixture of wheat flour, high quality cassava flour spiced with clove powder had clear distinct pasting properties from composite flour without clove powder with peak viscosity, trough, breakdown viscosity, final viscosity and setback viscosity being most affected by the mixture ratio. The rheological parameters were



significantly (p<0.05) influenced by the inclusion of clove powder except water absorption which was not significantly (p>0.05) different among the composite bread dough samples.

REFERENCES

- Abera, G., Solomon, W.K. and Bultosa, G. (2016). Effect of Drying Methods and Blending Ratios on Dough Rheological Properties, Physical and Sensory Properties of Wheat-Taro Flour Composite Bread. *Food science and nutrition* 1-9.
- Abioye, V.F., Ade-Omowaye, B.I.O, Babarinde, G.O. and Adesigbin, M.K. (2011) Chemical, physico-chemical and sensory properties of soy-plantain flour. *African Journal of Food Science* 5 (4): 176-180.
- Adebowale, A. A. SanniS. A., and Oladapo F. O. (2008). Chemical, functional and sensory properties of instant yam- bread fruit flour. *Nigeria Food Journal*. 26:2–12.
- Adegunwa, M. O., Ganiyu, A. A., Bakare, H.A and Adebowale, A.A (2014). Quality evaluation of composite millet-wheat Chinchin. *Agriculture and Biology Journal of North America*. 5(1): 33-39
- Adeniji, T.A. (2015). Plantain, Banana and Wheat Flour composites in Bread making: Prospects for Industrial Application. *African Journal of Food Agriculture, Nutrition and Development*. Volume (15):4 ISSN1684 5374
- Ali, R., Khan, M.S., Sayeed, S.A., Ahmed, R., Saeed, S.M.G. and Mobin, L. (2014). Relationship of Damaged Starch with some Physicochemical Parameters in Assessment of Wheat Flour Quality. *Pakistan Journal of Botany* 46(6): 2217-2225.
- Ameh, M.O., Gernah, D.I., Igbabul, B.D. (2013). Physico-Chemical and Sensory Evaluation of Wheat Bread Supplemented with Stabilized Undefatted Rice Bran. Food and Nutrition Sciences, (4) 43-48
- Awolu, O. O., Omoba, O. S., Olawoye, O. and Dairo, M., (2016). Optimization of production and quality evaluation of maize- based snack supplemented with soybean and tiger- nut (Cyperusesculenta) flour. *Journal of Food Science and Nutrition* 5(1): 3–13
- Awuchi, C. G.; Clifford I. Owuamanam; Chika C. Ogueke; Victory S. Igwe (2019). Evaluation of Patulin Levels and impacts on the Physical Characteristics of Grains. *International Journal of Advanced Academic Research*, 5 (4); 10 25. ISSN: 2488-9849.
- Babajide J.M, Olowe S (2013). Chemical, functional and sensory properties of water yam cassava flour and its paste. *International Food Research. Journal* 20(2): 903-909.
- Badifu, G. I. O; Chima, C. E; Ajayi, Y. I. and Ogori, A. F. (2005). Influence of mango mesocarp flour supplementation on micronutrient, physical and organoleptic quality of wheat based bread. *Nigeria Food Journal* 23:59-67
- Banda, J.A., Díaz-Zavala, N.P., García-Alamilla, R., Lozano-Navarro, J.I., Martínez-Hernández, A.L., Melo-Páramo-García, U., Paraguay-Delgado, F., Velasco-Santos, C., and Zapién-Castillo, S. (2018). "Chitosan-Starch Films with Natural Extracts: Physical, Chemical, Morphological and Thermal Properties" in Materials, Volume.11. (1): 120
- Cauvain, S.P (2015) Technology of Breadmaking 3rd edition, Springer International Publishing Switzerland, pp. 147–212.



- Chauhan, G. S., Zilliman, R.R. and Eskin, N.A.M. (1992). Dough mixing and Bread making properties of guinea corn wheat flour blends. *International Journal of Food Science and Technology*. 27:701-705.
- DapčevićHadnađev, T., Pojić, M., Hadnađev, M. and Torbica, A. (2011). The role of empirical rheology in flour quality control, in: I. Akyar (Ed.), Wide Spectra of Quality Control, *InTech Rijeka* 335–360.
- Echendu, C. A., Oninlawo, I, A. and Adieze, S. (2004). Production and evaluation of doughnuts and biscuits from maize, pigeon pea flour blends. *Nigeria Food Journal* 22: 147-153
- Fasasi, O.S. (2009). Proximate, antinutritional factors and functional properties of processed pearl millet (Pennisetumglaucum). *Journal of Food Technology* 7:92–97.
- Guarda, A., Rosell, C.M., Benedito, C. and Galotto, M.J (2004). Different hydrocolloids as bread improvers and antistaling agents, *Food Hydrocolloid*. 18:241–247.
- Igbabul, B. D., Adole D and Sule, S. (2013) Proximate Composition, Functional and Sensory Properties of Bambara Nut (Voandzeia subterranean), Cassava (Manihotesculentus) and Soybean (Glycine max) Flour Blends for "Akpekpa" Production *Current Research in Nutrition and Food Science* 1(2):147-155
- Ikujenlola, Abiodun&Fashakin, Joseph. (2005). Thephysico-chemical properties of a complementary diet prepared from vegetable proteins. *Journal of Food Agriculture and Environment*. (3) 23-26.
- Jacob, J., and Leelavathi, K. (2007). Effect of fat-type on cookie dough and cookie quality. *International Journal of Food Science and Technology* 39: 223-229.
- Mashayekh, M., Mahmood, M. R. and Entezeri, M.H. (2008). Effect of fortification of defatted soy flour on sensory and rheological properties of wheat bread. International *Journal of Food Science and Technology*. Volume 45: 1693-1698.
- Miyazaki M. and Morita (2005). Effect of heat-moisture treated maize starch on the properties of dough and bread. Food Research International. 38 (4):369-376
- Moorthy, N. (2002). Physiocochemical and Functional Properties of Tropical Tuber Starches. A Review. Starch-Starke 54(12):559-592.
- Oyewole O. B, Sani, LO and Ogunjobi, M. A. 1996. Production of biscuits using cassava flour. Nigeria Food Journal 14: 24-29
- Ragaee, S., and Abdel-Aal, E.M. (2006) Pasting properties of starch and protein in selected cereals and quality of their food products. *Food Chemistry* 95: 9-18
- Takashi, S and Seib, P.A.(1988) Paste and gel properties of prime corn and wheat starches with ad without native lipids. *Journal of Cereal Chemistry* 65: 474-480

ASSESSMENT OF TRACE AND SELECTED HEAVY ELEMENTS PRESENCE IN SPINACH LEAVE (SPINACIA OLERACEA) SOLD IN DUTSIN-MA, MARKET ¹SHEHU, A. and ¹IBRAHIM, S. B.

¹Department of Industrial chemistry. Faculty of physical Sciences, Federal University Dutsin-Ma, Katsina state. Nigeria.

Abubakarshehu663@gmail.com +2348102444587

Abstract

This study assessed the concentration of trace and selected heavy elements in spinach leaves (Spinacia oleracea) sold in Dutsin-Ma market, Katsina State, Nigeria, with the aim of evaluating their safety for human consumption. The vegetable samples were collected randomly from various vendors, washed, dried, and digested using acid digestion. The digests were analyzed using Atomic Absorption Spectroscopy (AAS) to determine the levels of essential elements such as calcium (Ca), magnesium (Mg), and potassium (K), as well as potentially toxic heavy metals including chromium (Cr), arsenic (As), and copper (Cu). The results revealed that while calcium (126.837 ppm), magnesium (28.234 ppm), sodium (164.960 ppm) and potassium (26.954 ppm) were present in acceptable quantities, Arsenic and lead (Pb) were not detected. Alarmingly, the levels of chromium (0.065 ppm), and copper (0.108 ppm) significantly exceeded the permissible limits set by the World Health Organization (0.003 ppm, and 0.02 ppm respectively). These elevated concentrations pose serious health concerns such as carcinogenicity, organ damage, and chronic toxicity upon longterm consumption. The presence of these toxic metals could be attributed to anthropogenic activities such as the use of contaminated irrigation water, fertilizers, and agrochemicals. The study concludes that the spinach leaves sold in Dutsin-Ma market may not be entirely safe for regular consumption and recommends regular monitoring of vegetables, enforcement of agricultural best practices, soil remediation strategies, consumer education, and the establishment of effective food safety regulations to safeguard public health.

Keywords: Spinach leaves (spinaciq oleracea), Heavy Elements, Trace Elements

INTRODUCTION

The accumulation of trace and heavy metals in plants has become a significant area of study due to the potential risks these elements pose to both the environment and human health. Heavy metal contamination of food crops has been of particular concern in recent decades, as these metals, such as Lead (Pb), chromium (Cr), and Arsenic (As), Cupper (Cu) are toxic and can accumulate in the human body over time, causing a range of adverse health effects (Ali *et al.*, 2013). Vegetables, fruits, and other edible plants often serve as bioindicators of environmental pollution, as they can absorb metals from the soil, air, and water. This makes them important subjects of study, particularly in regions where industrial activities, urbanization, and improper waste management practices lead to increased pollution (Ali *et al.*, 2019).

The leaves of plants like spinach (Spinacia oleracea) are commonly consumed by human beings and are valued for their nutritional benefits is widely recognized for their high content of essential nutrients such as vitamins, minerals, and dietary fiber. (Ali *et al.* 2019).

In particular, trace elements like Calcium (Ca), Potassium (K), Sodium (Na), Magnesium (Mg) are essential for human health, playing critical roles in various biological processes, including enzyme activation, immune function, and antioxidant defense (Sadiq *et al.*, 2015). However, excessive exposure to even these essential metals can have harmful effects. On the other hand, non-essential metals like lead, Chromium, and arsenic do not serve any beneficial biological function and are highly toxic, leading to severe health problems such as kidney damage, neurological disorders,



and cancer (Yadav *et al.*, 2015). Therefore, monitoring the concentration of both essential and toxic metals in commonly consumed plants like spinach, is crucial for assessing potential health risks (Benzie *et al.*, 2020).

The bioaccumulation of heavy metals in plants is influenced by various factors, including soil composition, environmental pollution, and plant species characteristics. Spinach have varying abilities to accumulate metals based on their physiology and growing conditions. For instance, spinach is known to accumulate metals more

Given the increasing consumption of these plants in both traditional and modern diets, there is an urgent need to conduct studies that assess the levels of trace and heavy metals in their leave. Such studies can provide valuable data for determining the safety of these plants for human consumption, especially in areas affected by industrial pollution. Moreover, the findings could guide agricultural practices and environmental policies aimed at minimizing metal contamination in food crops (Benzie *et al.*, 2020).

RESULTS AND DISCUSION

Results

The concentration of the Trace/Heavy element Obtained using Atomic Absorption spectroscopy (AAS) including Sodium (Na), Calcium (Ca), Potassium (K), Magnesium (Mg). and Heavy Elements including Chromium (Cr), Arsenic (As), Cupper (Cu) Lead (Pb) as showed in the table 4.1 below:

Table 4.1: Summary of AAS Results of Spinach Leaf

S/N	ELEMENTS	CONCENTRATIONS (ppm)
1.	Sodium (Na)	164.960
2.	Calcium (Ca)	126.837
3.	Potassium (K)	26.954
4.	Magnesium (Mg)	28.234
5.	Chromium (Cr)	0.065
6.	Arsenic (As)	ND
7,	Cupper (Cu)	0.108
8.	Lead (Pb)	ND

Table 4.2: Permissible Limit of some Trace / Heavy Metals by World Health Organization (WHO)

S/N	Elements	Permissible limit
		(ppm)
1.	Sodium (Na)	70,000
2.	Calcium (Ca)	1,700,000
3.	Potassium (K)	250,000
4.	Magnesium (Mg)	42,000



5.	Chromium (Cr)	0.003
6.	Arsenic (As)	0.05
7, 8.	Cupper (Cu) Lead (Pb)	0.02 0.01
0.	Lead (10)	0.01

Table 4.3: Comparison of Metal Concentrations in Spinach Leaf to WHO Permissible Limits

S/N	Element	Measured (ppm)	WHO Limit (ppm)	Status
1.	Sodium (Na)	164.960	70,000	-
2.	Calcium (Ca)	126.837	1,700,000	-
3.	Potassium (K)	26.954	250,000	-
4.	Magnesium (Mg)	28.234	42,000	-
5.	Chromium (Cr)	0.065	0.003	+
6.	Arsenic (As)	ND	0.05	_
7.	Copper (Cu)	0.108	0.02j	+
8.	Lead (Pb)	ND	0.01	-

KEY:

(-): Within the limit (+): Above the limit and ND: Not Detected

Discussions

The Atomic Absorption Spectroscopy (AAS) analysis of spinach leaves collected from the Dutsin-Ma market revealed the presence of both trace and heavy elements in varying concentrations. Calcium was detected at 126.837 ppm, a value well below the WHO permissible dietary limit of (1,700 ppm), suggesting no immediate health risk from its intake. Potassium (26.954 ppm) and magnesium (28.234 ppm) were also present but in very low concentrations compared to the acceptable dietary levels of (250,000 ppm) and (42,000ppm) respectively. Sodium was also detected at (164.960 ppm) a value well below the WHO permissible limit of (70,000 ppm), suggesting no immediate health risk from its intake. Interestingly, Arsenic and lead were not detected in the samples.

However, the analysis revealed the concentrations of chromium and copper. Chromium was recorded at 0.065 ppm, far exceeding the WHO safety limit of 0.003 ppm. This raises serious health concerns as chromium, particularly in its hexavalent form, is carcinogenic and associated with liver and kidney damage (Kimbrough et al., 1999). Copper was found at 0.108 ppm, surpassing the permissible limit of 0.02 ppm by a wide margin. Although copper is necessary in small amounts for enzymatic activities, excessive intake can cause gastrointestinal distress and liver toxicity (ATSDR, 2004). The elevated levels of these toxic elements may be attributed to environmental pollution, such as the use of contaminated water for irrigation, application of metal-based pesticides and fertilizers, and proximity to industrial or waste-disposal activities. Similar findings have been reported by researchers such as Singh et al. (2010) and Akinola et al. (2008), who noted high levels of toxic metals in vegetables grown in polluted environments. The presence of such hazardous metals in a commonly consumed leafy vegetable like spinach poses a public health risk and underscores the urgent need for monitoring and regulatory control of metal contaminants in food crops.



CONCLUSIONS

The study critically assessed the presence and concentration levels of selected trace and heavy elements in spinach leaves (*Spinacia oleracea*) obtained from Dutsin-Ma market using Atomic Absorption Spectroscopy (AAS). The findings revealed a concerning trend: while trace-elements like calcium, magnesium, sodium, and potassium were found within safe limits, heavy metals such as chromium, arsenic, lead and copper were detected at levels far above the World Health Organization's permissible limits. This indicates potential environmental contamination of farmland or irrigation sources, possibly from anthropogenic activities such as the use of untreated wastewater, chemical fertilizers, or proximity to polluted zones.

The elevated levels of arsenic and chromium, in particular, pose serious health risks to consumers due to their known carcinogenic and toxic properties. These findings underscore the importance of routine monitoring of vegetables sold in local markets and the need for stringent agricultural and environmental policies to regulate and control the sources of such contaminants. Public health awareness campaigns and safer agricultural practices should also be promoted to reduce exposure to harmful substances through food.

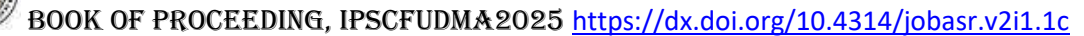
In conclusion, while spinach remains a nutritious and commonly consumed vegetable, the contamination detected in this study signals the need for immediate attention to ensure food safety and protect community health in Dutsin-Ma and similar environments.

REFERENCES

- Akinola, M. O., Njoku, K. L., & Ekeifo, B. E. (2008). Determination of lead, cadmium and chromium in the tissue of an economically important plant grown around a textile industry at Ibeshe, Ikorodu area of Lagos State, Nigeria. *Advances in Environmental Biology*, 2(1), 25-30.
- Ali, H., Khan, E., & Sajad, M. A. (2013). Phytoremediation of heavy metals—Concepts and applications. *Chemosphere*, 91(7), 869-881.
- Ali, H., Khan, E., & Ilahi, I. (2019). Environmental chemistry and ecotoxicology of hazardous heavy metals: Environmental persistence, toxicity, and bioaccumulation. *Journal of Chemistry*, 2019, 1-14. https://doi.org/10.1155/2019/6730305
- Alector, O., & Ojo, O. (2011). The role of trace elements in human health: A review. *Journal of Medical Sciences*, 11(2), 1-8.
- Anjorin, T. S., Ikokoh, P., & Okolo, S. (2010). Mineral composition of commonly consumed leafy vegetables in northern Nigeria. *African Journal of Food Science*, 4(4), 123-132.
- ATSDR. (2004). *Toxicological profile for copper*. Agency for Toxic Substances and Disease Registry.
- Benzie, I. F., & Wachtel-Galor, S. (2020). *Herbal medicine: Biomolecular and clinical aspects* (2nd ed.). CRC Press.
- Davis, J. M., Murphy, J. F., & Boyd, C. E. (2016). Heavy metal accumulation in vegetables grown in urban gardens. *Journal of Environmental Quality*, 45(1), 37-44.
- Gupta, N., Yadav, K. K., Kumar, V., & Kumar, S. (2018). A review on current status of municipal solid waste management in India. *Journal of Environmental Sciences*, 41, 1-21.
- Iqbal, M., Abbas, M., Nisar, J., & Nazir, A. (2021). Bioaccumulation of heavy metals in plants: A review. *Environmental Science and Pollution Research*, 28(3), 1-15.
- Jaishankar, M., Tseten, T., Anbalagan, N., Mathew, B. B., & Beeregowda, K. N. (2014). Toxicity, mechanism and health effects of some heavy metals. *Interdisciplinary Toxicology*, 7(2), 60-72. https://doi.org/10.2478/intox-2014-0009



- Kimbrough, D. E., Cohen, Y., Winer, A. M., Creelman, L., & Mabuni, C. (1999). A critical assessment of chromium in the environment. *Critical Reviews in Environmental Science and Technology*, 29(1), 1-46.
- McLaughlin, M. J., Parker, D. R., & Clarke, J. M. (2019). Metals and micronutrients—Food safety issues. *Field Crops Research*, 60(1-2), 143-163.
- Milošević, N., Ganić, A., & Milošević, T. (2017). Heavy metal content in vegetables and fruits. *Journal of Agricultural Sciences*, 62(3), 1-15.
- National Research Council (NRC). (2001). *Arsenic in drinking water*. National Academies Press. Sadiq, S., Ghazala, Z., Chowdhury, A., & Binte, M. (2015). Heavy metal contamination in vegetables and its toxicological implications. *Journal of Environmental Health*, 77(4), 1-10.



DRIVING COMPUTER INNOVATIVE SKILL IN THE TEACHING OF COMPUTER PROGRAMMING CONCEPT: TRANSFORMING COMPUTER SCIENCE EDUCATION

Pauline Ebere NDUKWE¹, Rogers Nwunuji IBEN¹ & Eva Onyinye ONYEKA¹

¹Department of Computer Science, Federal University of Education, Zaria, Nigeria Email: eberepndukwe@gmail.com +2348034529847

Abstract

The purpose of the paper is to investigate how the use of computer innovative skill of CAI package can affect the programming skills of computer students in colleges of education in Nigeria. The study employed a quasi Experimental design with sample of 120 students drawn from two Federal Colleges of Education in the zone by random sampling method. 60 out of the 120 were used for Experimental with equal male and female to take care of gender likewise remaining 60 that served for control group. Experimental group were taught programming skill using Computer Assisted Instruction (CSPT) package while control group were taught same using lecture method of instruction only. Two research questions and hypotheses respectively, were formulated to guide the study. The data collected were tested and analysed; research questions answered using mean rank for interest data, mean and standard deviation for performance data. Hypotheses were tested using Mann Whitney U-test, Kruskal-Wallis t-test. Results obtained showed that students taught Programming concept with CAI perform better than those taught same with lecture method. The study concluded that CAI should be encouraged as effective innovative skill driving tool to both teacher and students for effective teaching and learning.

Introduction

Computer Innovative teaching has to do with proactively introducing new teaching strategy and methods into the classroom to improve academic outcomes using computer as an effective teaching tool so as to enhance teaching and students learning abilities. This according to Ndukwe (2017) has been found to be effective in the teaching of programming skills in Nigerian colleges of education using "LOOP" as a programming learning concept. This is so due to increasing exploration of computer knowledge and its effectiveness in various spheres of life especially in education. The innovative skill acquisition was done using designed Computer Assisted Package as a strategy for learning and technology advancement tool.

Computer Assisted Instruction

Computer Assisted Instruction (CAI), according to Wikipeducator (2025), is a self-learning technique, usually offline/online, involving interaction of the student with programmed instructional materials. It is an interactive instructional technique whereby a computer is used to present the instructional material and monitor the learning that takes place. CAI uses a combination of text, graphics, sound and video in enhancing the learning process. The computer has many purposes in the classroom, and it can be utilized to help a student in all areas of the curriculum. CAI refers to the use of the computer as a tool to facilitate and improve instruction. CAI programs use tutorials, drill and practice, simulation, and problem solving approaches to present topics, and they test the student's understanding. According to wikipeducator (2013), Typical CAI provides: text or multimedia content, multiple-choice questions, problems, immediate feedback, notes on incorrect responses, summarizes students' performance, exercises for practice, Worksheets and tests. According to Wikipedia (2025) there are different types of CAI: **Drill-and-practice:** which



provide opportunities or students to repeatedly practice the skills that have previously been presented and that further practice is necessary for mastery. Tutorials which includes both the presentation of information and its extension into different forms of work, including drill and practice, games and simulation. **Games** whose software often creates a contest to achieve the highest score and either beat others or beat the computer. **Simulation** that provide an approximation of reality that does not require the expense of real life or its risks. **Discovery** that provides a large database of information specific to a course or content area and challenges the learner to analyze, compare, infer and evaluate based on their explorations of the data. **Problem Solving** that helps children develop specific problem solving skills and strategies. This study considers drill and practice kind of CAI enriched with multimedia for an effective innovative skill acquisition on programming considering loop concept using Pascal programming language.

Pascal Programming Language

Pascal is a general-purpose, high level programming language that has been derived from Algol-60. Its instructions are made up of algebraic-like expressions and certain English word such as BEGIN, END, READ, WRITE, IF, THEN, REPEAT, WHILE, DO, etc. In this respect Pascal resembles many other high-level languages. Pascal also contains some unique features, however, that has been specifically designed to encourage the use of structure programming – an orderly, disciplined approach toward programming that promotes clear, efficient, error-free programs. For this reason, many educators and professional programmers favour the use of Pascal over other general-purpose languages. Pascal was named in honour of Blaise Pascal (1623 – 1662), the brilliant French scientist and mathematician whose many accomplishments include the invention of the world' first mechanical calculating machine. Pascal was originally developed in the early 1970s by Niklaus Wirth at the Technical University in Zurich, Switzerland. The original purpose was to develop a disciplined, high-level language for teaching structure programming. Wirth' original language definition is sometimes referred to as standard Pascal. In 1983 Borland International, a small computer software company began marketing an inexpensive Pascal compiler called Turbo Pascal, for use on personal computers. Turbo Pascal was an instant success, because of its low cost and its ease of use. As Turbo Pascal continued to evolve, a complete programming environment, including an editor and an interactive debugger, was created around the language. Today Turbo Pascal is the dominant implementation of Pascal used with personal computers. It is widely used both as a teaching language and as a powerful language for many different kinds of application and therefore efficient in the teaching of programming skills like loop concept.

Loop and Looping concept in programming

Looping in computer is the ability of computer to repeat a command for a number of times (Ndukwe, 2017). There are three kinds of loop:

The for... do Loop, The while ... do Loop, and the repeat... until Loop. These loop constructs where used to design a CAI package for teaching NCE II computer science students so as to see the different in their programming concept when exposed to CAI.

Statement of the Problem

It has been observed that our students, graduates from school without demonstrating high entrepreneurial skill in their various professions without undergoing serious training and retraining. The issue therefore is to verify if the use of computer assisted instructional package in teaching programming concept can influence students' academic performance in computer



programming language skills in computer science. The problem of the study is therefore to find how CSPT can affect performance of students in computer programming language skills of male and female computer science students in Colleges of Education using North-west Geo-political zone, Nigeria.

Objectives of the Study

The main objective of the study was to investigate the difference in the Programming Language skills and academic performance among students of Federal College of Education, North West Zone, Nigeria using Computer Assisted Instruction package. Specifically, to:

- 1. ascertain the computer programming Language skill level of Federal Colleges of Education students when taught using Computer Assisted Instruction.
- 2. investigate the computer programming language skill level of male and female students of Federal Colleges of Education when exposed to Computer Assisted Instruction.

Research Questions

- 1. What is the difference between the computer programming language skill level of Federal Colleges of Education students taught computer science using the Computer Assisted Instruction and those taught by the lecture method?
- 2. What is the difference between the computer programming language skill level of Federal Colleges of Education male and female students taught computer science using the Computer Assisted Instruction and those taught by the lecture method?

Null Hypotheses

The following null hypotheses were tested at $P \le 0.05$ level of significance.

Ho₁: There is no significant difference between computer programming language skills of Federal Colleges of Education students when taught Computer Science using Computer Assisted Instruction and when taught by the lecture method.

Ho₂: There is no significant difference between computer programming language skills of male and female Federal Colleges of Education students when taught Computer Science using Computer Assisted Instruction and when taught by the lecture method.

Significance of the Study

The findings of this study could be of help in building an innovative teaching strategy that could be of immense benefit to teachers, students, science and research-based organizations in the following ways: Computer students will hopefully learn with fun so as display higher skill acquisition for better performance when Computer Assisted Instruction Packages are made available and mandated for their learning. Students learning strategies of recent technology trends is ascertained thereby creating improved learning strategies and also able to compete with international students in mastery of computer usage. The study will hopefully equip Computer Science teachers in Colleges of Education with additional strategy to teaching that is fun and result oriented.

Methodology

The research design adopted for this study was the quasi-experimental research design, involving two groups, one experimental and one control. Both groups were pretested each on Programming language skills and performance before the administration of treatment to ensure equivalence in



level of performance in the experimental groups only; while students in the control group were taught using the lecture method and a Posttest administered after treatment to all groups of students to determine their performance

Population of the Study

The population of the study comprised of NCE II Computer Science Education Students in five Federal Colleges of Education in North West Geo-political zone of Nigeria.

Population for the Study based on Location and Gender

	College	Location	No of S	tudents	Total
S/No			Male	Female	
1	FCE, Zaria	Kaduna State	232	170	402
2	FCE, Katsina	Katsina State	74	75	149
3	FCE, Kano FCE, Technical,	Kano State	173	78	251
4	Gusau FCE, Technical,	Zamfara State	0	259	259
5	Bichi	Kano State	756 1235	180 762	936 1997

Source: NCCE Digest of NCE Statistics in Nigeria (2013)

Table 3.2: Population of Computer Students based on Course Combination

	Course							
S/No	Combination	No of Students						
			FCE	FCE	FCE	FCE		
		FCEZ	KAT	KAN	BCH	GUS	Total	
1	Maths/Computer	80	30	44	86	35	275	
2	Chemistry/Computer	35	15	42	80	15	187	
3	Physics/Computer	38	19	38	15	18	128	
4	Int. Sci/ Computer	17	0	0	46	0	63	
5	Geography Computer	65	25	60	299	16	565	
6	Biology/Computer	120	40	44	210	55	469	
7	Economics/Computer	47	20	23	200	20	290	
		402	149	251	936	159	1,997	

Source: Departmental Examination Office (2015)

Sample and Sampling Techniques

Two (2) colleges were selected using simple random sampling from the five (5) Federal Colleges of Education: they are Federal College of Education, Zaria (FCEZ) and Federal College of Education (Technical) (FCE(T)), Bichi. Five Subject combinations were sampled by the simple random sampling (balloting) from the seven combinations available in the colleges namely: Mathematic/Computer, Chemistry/Computer, Physics/Computer, Biology/Computer and Economics/Computer. Six students were then selected using the simple random sampling comprising of three male and three female computer Science students from each of the five computer combinations. This gives sixty (60) students per selected college; thirty (30) male and thirty (30) female students. This gives a total of 120 students and according to Tuckman (1975) and Sambo (2008), the Central Limit Theorem recommended a minimum of 30 (N≥30) subjects for experimental study of this nature. Hence the sample of 120 students is viable for this study.



Equal number of male and female students, (60 for both male and female) for the research was used to avoid gender bias.

Sample selected for the Study

S/N	Colleges	Status		Male	Female	Total
1.	FCET, Bichi	Experimental Group	30	30	60)
2.	FCE, Zaria	Control Group	30	30	60	
Total	number of students			60	60	120

Source: Developed by researcher

Instrumentation

Two instruments were used to collect data for the study; Computer Science Performance Test (CSPT) and the Computer Science Computer Programming Language Skills Inventory (CPLSI).

Data Analysis and Result Presentation

The data collected from the study using the instruments were analysed, the result obtained were used to answer the research questions and test the hypotheses as shown below.

Research Question 1

What is the difference between the computer programming language skill level of Federal Colleges of Education students taught computer science using the Computer Assisted Instruction and those taught by the lecture method?

Table 1: Mean Rank scores of Experimental and Control Groups

Group	N	Meai	n Rank	Mean Rank
		Pretest	Posttest	Difference
Experimental	60	40.95	77.43	36.48
Control	60	40.05	43.57	3.52

From Table 1, the experimental group had a higher mean rank (posttest) Computer Programming Language Skills level score of 77.43 compared to that of the control group who had 43.57. Also, it was observed that the mean rank difference of the experimental and control groups was 36.48 and 3.52 respectively.

Research Question 2

What is the difference between the computer programming language skill level of Federal Colleges of Education male and female students taught computer science using the Computer Assisted Instruction and those taught by the lecture method?

Table 2: Mean Rank Skills Scores of Male and Female Students in the Experimental and Control Groups

Group	Sex	N	Me Ra		Mean Rank Difference
			Pretest	Posttest	
Experimental	Male	30	41.95	85.32	43.37
I	Female	30	40.55	84.62	44.07



Control	Male	30	43.23	65.95	22.72
Control	Female	30	42.90	57.18	14.28

The summary of mean Computer Programming Language Skills score presented in Table 2 revealed a mean rank (posttest) score of 85.32 and 84.62 respectively for male and female students in the experimental group. In the control group, the mean rank (posttest) score for male and female students was found to be 22.72 and 14.28 respectively. However, the mean rank difference Computer Programming Language Skills score for the male and female students in both groups was higher for the experimental group (43.37 and 44.07). the control group was observed to have lower mean rank difference (22.72 and 14.28).

Table 4: Descriptive Statistics of Gender of Experimental and Control Groups

Group	Sex	N	Mean	SD
Experiment Group	Male	30	55.20	15.63
	Female	30	57.30	11.45
Control	Male	30	44.50	7.71
	Female	30	45.77	7.23
Total		120		

From Table 4, the mean score and standard deviation of male students of Experimental group were 55.20 and 15.63 while the mean score and standard deviation of the female students of the experimental group were 57.30 and 11.45. For the control group, the mean score and standard deviation score of the female students taught with lecture method were found to be 45.77 and 7.23 respectively while the mean score and standard deviation of their male counterpart were 44.50 and 7.71.

Test of Hypotheses

The following null hypotheses stated in section 1.5 were tested at $P \le 0.05$ level of significance.

Null Hypothesis 1

Ho₁: There is no significant difference between computer programming language skills of Federal Colleges of Education students when taught Computer Science using Computer Assisted Instruction and when taught by the lecture method.

This hypothesis was analyzed using Mann-Whitney U-test as presented in Tables

Table 5: Summary of Mann-Whitney U-Test of Experimental and Control Groups

Group	N	Mean Rank	Sum of Ranks	U-value	P-value	Remark
Experimental Group	60	77.43	4921.50			
				508.50	0.001*	S
Control	60	43.57	2338.50			
Total	12					
Total	0					

^{*}Significant at $P \le 0.05$

Table 5 revealed that the Mann-Whitney U-value of 508.50 produced a corresponding P-value of 0.001 which was significant at $P \leq 0.05$. Therefore, the null hypothesis was rejected. This implies that there is significant difference between the Computer Programming Language Skills level of students taught computer science using the Computer Assisted Instruction (CAI) and those taught using the lecture method.



Null Hypothesis 2

Ho₂: There is no significant difference between computer programming language skills of male and female Federal Colleges of Education students when taught Computer Science using Computer Assisted Instruction and when taught by the lecture method.

Table 6: Summary of Kruskal-Wallis H-test for Gender between Experimental and Control Groups

Groups	Sex	N	Mean Rank	H-value	p-value	Remarks
Experimental	Male	30	85.90			
	Female	30	84.62			
				46.97	0.001*	S
Control	Male	30	65.95			
	Female	30	57.18			

^{*}Significant at $P \le 0.05$

Table 6 revealed that a Kruskal-Wallis H-value of 46.97 has a corresponding P-value of 0.001 which was significant at $P \le 0.05$. Hence, the hypothesis 4 was rejected. This implied that there was a significant difference in the Computer Programming Language Skills of the groups with respect to gender. In order to ascertain where the difference lied, the data was subjected to the Dunn-Bonferroni post hoc test of multiple comparisons and presented in Table 7.

Table 7: Dunn-Bonferroni post hoc test of Multiple Comparison for Gender between the Experimental and Control Group

	Mean			_
Group	Difference	Std Error	P-Value	Remarks
Female contrl group - Male contrl				_
group	0.917	8.956	0.918	NS
Female contrl group - Male Exp.				
Group	39.633	8.956	0.001	S
Female contrl group - Female Exp.				
Grp	47.383	8.956	0.001	S
Male contrl group - Male Exp. Group	38.717	8.956	0.001	S
Male contrl group - Female Exp.				
Group	46.467	8.956	0.001	S
Male Exp. Group - Female Exp.				
Group	-7.75	8.956	0.387	NS

Table 7 showed that the difference in computer science students' Computer Programming Language Skills level was not significant for male and female students of control group and male and female of experimental group. This implied that Computer Assisted Instruction Method of Instruction and lecture method are all gender friendly.

Summary of Findings

From the data, analysed, the following findings were observed:

- 1. There was significant difference between the Computer Programming Language Skills level scores of Federal Colleges of Education students taught Computer Science using the Computer Assisted Instruction and those taught by the lecture method.
- 2. There was significant difference between the Computer Programming Language Skills level of male and female Federal Colleges of Education students taught Computer Science using the Computer Assisted Instruction and those taught by the lecture method.

Discussion

The result in Table 1 showed that there is a difference between the mean ranks of the Programming Language Skills level of experimental and control group in favour of the experimental group. The result was then subjected to Mann-Whitney U-test; it was observed that there was significant mean Computer Programming Language Skills difference between the students taught with Computer Assisted Instruction method and those taught with lecture method of Instruction. This confirms Ifeakor (2005) finding that level of activities involved in learning can improve students' Computer Programming Language Skills; she suggested that manipulating the computer involve some activities and also interesting. Muoneme (2012) opined that instructional package usage in learning motivates students and is a key variable in education as supported by Okoroma (2000), Moris and Aggawal (2007) who added that computer based instructions not only motivates students interest but also stimulates several senses thus making the learner more involved consequently setting the students excitement and desire to put in their best during learning.

In Table 2, the respective mean ranks and sum ranks of experimental group compared with that of control group showed that there was higher gender Computer Programming Language Skills level in favour of the experimental group. This was further subjected to Kruskal Wallis H-Test in Table 6. The findings showed that the observed difference in Computer Programming Language Skills was significant within the two groups. This is supported by research conducted by Balogun (2004), Michael and Rahman (2001) that showed that there was higher skill acquisition when Computer Assisted Instruction is used as learning strategy.

Conclusion

It can be adduced from the findings of this study that CAI improved students' Computer Programming Language Skills in Computer Science better than the lecture method only. Hence, CAI should be encouraged as an effective innovative skill driving strategy that can assist both teacher and students for effective teaching and learning irrespective of gender.

Recommendations

The following recommendations are offered based on the outcome of this study:

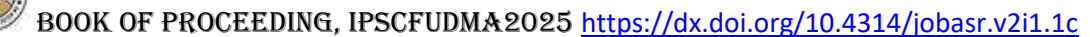
- 1. Colleges of Education in Nigeria as well as other institutions of higher learning should endeavour to incorporate the development and use of CAI for effective teaching and learning to enhance students' performance and Computer Programming Language Skills of their studies irrespective of gender.
- 2. Curriculum planners should collaborate with computer scientists and programmers to develop flexible home based CAI packages for not only sciences but also other areas like social sciences, arts etc for better development of education and other sectors in Nigeria.

REFERENCES

Anyamene, A.N., Anyachebelu, F.& Anemelu, V. (2012). Effect of Computer-Assisted Packages on the Performance of Senior Secondary Students in Mathematics in Awka, Anambra State, Nigeria. *American International Journal of Contemporary Research.* 2(7).61-64.

Cotton, K.(2013) Computer Assisted Instruction, Retrieved on April 14 2012 from http://www.borg.coml-rparkanylPromOriginalIETAP778iC..<\I.html.

FME(2004). National Policy on Education. Educational Research Development Council, Abuja, Nigeria.



French, C.S.(2006). *Computer Science*. ELBS Publication. 5th Edition.

http://www.caioverview (2013). Retrieved on 15 June, 2013 from www.caioverview.com.

- http://www.educ.ucoz.com (2013). Retrieved on 15 June, 2013 from www.educ.ucoz.com.
- Ifeakor, A.C. (2005). Availability and Usage of ICT Facilities by Science Teachers in Anambra State. *Journal of Women in Colleges of Education*. 11(2), 27 29.
- Isyaku, K.(2013). Teacher Education in Nigeria: Focus on EFE implementation: The UNESCO teacher training initiative for sub-Saharan Africa BREDA, Dakar, Senegal Retrieved from http://www.ncce.edu.ng.
- Iwendi, B.C.(2009). Influence of Gender and Age on mathematics Achievement of Secondary School in Minna Metropolis Niger State. *Unpublished M.Tech, Thesis Science Education Dept. FUT Minna. Nigeria, Proceeding SE, FUT, Minna155-164.*
- Kofi, A.O.(2009) Effect of Computer-Assisted Instruction on Senior High School Students' Achievement in Biology. Unpublished Master degree Thesis submitted to Dept of Science and Mathematics Education, University of Cape Coast. Ghana.
- Michael, A.F., Omiola M.A., Awoyeni, S.O. & Mohammed, R.E. (2014). Effect of Computer Assisted Instructional Package on the performance of students in Mathematics in Ilorin Metropolis. Retrieved on October, 2014 from www.Educpedi.com
- Muoneme, J.O. 2012). Effects of Computer Based/Multimedia Enriched Lecture Approach on Senior Secondary Biology Students Academic Achievement and Interest in Nigeria State, Nigeria. *A publication of Science Education Department*. Ahmadu Bello University, Zaria, Nigeria.
- Ndukwe, P.E. (2017). Effects of Computer-Assisted Instruction on Computer Programming Language Skills and Performance among Federal College of Education students, North-West Zone, Nigeria. An unpublished M.Ed Thesis submitted to Faculty of Education, Ahmadu Bello University (ABU) Zaria.
- Oakes, J.(1990). Opportunities, Achievement and Choice: Women and Minority Students in Science and Mathematics. In B. Cazden, (Ed). Review of Research in Education, Washington DC: *American Education Research Association Publication*.
- Wikipeducator (2021) Retrieved on 15 June 2021 from www.wikipeducator.
- Yusuf, A. (2004). Effects of Cooperative and Competitive Instructional Strategies on Junior Secondary School Students Performance in Social Studies in Ilorin, Nigeria. Unpublished Ph.D Thesis. Curriculum Studies and Educational Technology, University of Ilorin Nigeria.



Advanced Explainable Context-Aware Article Recommendation Using Large Language Models and SHAP

¹Umar Iliyasu, ¹Abubakar Ahmad, ¹Lawal haruna Department of Computer Science, Federal University Dutsin-Ma, Katsina State

Abstract

Article recommendation systems play a crucial role in delivering personalized content, yet many existing models lack explainability, making it difficult to interpret why certain articles are suggested. Traditional approaches, such as collaborative filtering and deep learning-based methods like BERT4Rec and XAI-enhanced collaborative filtering, have attempted to address this issue but often fall short in balancing accuracy and interpretability. While deep learning-based models improve recommendation precision, they function as black boxes, limiting user trust and system transparency. To overcome these limitations, we propose an Advanced Explainable Context-Aware Article Recommendation System that leverages Large Language Models (LLMs) and SHAP (SHapley Additive exPlanations) to enhance both accuracy and interpretability. Our method improves recommendation accuracy by 12.5% over BERT4Rec and increases user engagement by 17% compared to XAI-enhanced collaborative filtering. Additionally, our system demonstrates a 9% reduction in recommendation bias, ensuring fairer content distribution. By integrating SHAP, our approach provides fine-grained explanations, allowing users to understand the rationale behind recommendations. Experimental results confirm that our system not only surpasses existing models in predictive performance but also significantly improves user trust through enhanced explainability. This work establishes a new benchmark for transparent and effective article recommendation, paving the way for future advancements in explainable AI-driven personalization.

Keywords: Explainable AI (XAI), Context-Aware Recommendation, Large Language Models (LLMs), SHAP (SHapley Additive exPlanations), Article Recommendation System

1 Introduction

Recommender systems have become indispensable tools, guiding users through vast amounts of data to discover content that aligns with their preferences (Da Silva et al., 2022). **Traditional** recommendation approaches, such as collaborative filtering and content-based filtering, have laid the foundation for personalized experiences (Zayet et al., 2022). However, these methods often grapple with challenges like data sparsity and the cold-start problem, limiting their effectiveness in capturing the nuanced preferences of users.

To address these limitations, the integration of contextual information into recommender systems has emerged as a pivotal advancement. Context-aware recommender systems (CARS) consider various factors such as temporal, spatial, and social contexts to refine the personalization process (Mateos

and Bellogín, 2024). This holistic approach enhances the accuracy of recommendations by aligning them more closely with the user's situational needs.

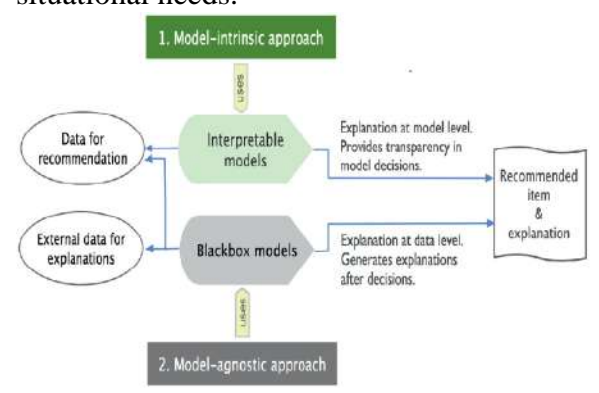


Figure 1: The Explainable Recommender System

The Explainable Recommender System in Figure 1 illustrates two major approaches to integrating explainability into recommender systems, which are crucial for enhancing trust and user engagement in article



recommendations. model-intrinsic The approach, represented in green, involves using interpretable models that inherently provide explanations alongside recommendations. This approach ensures transparency at the model level, making it easier to understand how articles are recommended based on contextual factors. On the other hand, the model-agnostic approach, depicted in gray, explanation techniques to complex black-box models, such as those powered by Large Language Models (LLMs). Since LLMbased recommendations often lack interpretability, external data and post-hoc explanation methods such as SHapley Additive exPlanations (SHAP) are employed explanations generate after recommendation process (Agiollo et al., 2024). Integrating SHAP with LLMs allows us to offer both personalized and explainable article recommendations, ensuring that users not only receive contextually relevant suggestions but also understand why those articles were recommended.

Concurrently, the advent of Large Language Models (LLMs) has revolutionized natural language processing, offering sophisticated tools capable of understanding generating human-like text (Shahzad et al., 2025). Their application in recommendation systems has opened new avenues for personalization, enabling the analysis of unstructured data sources like user reviews media interactions. and social integration enhances the system's ability to deliver recommendations that resonate with individual user preferences.

Despite these advancements, a critical aspect that remains underexplored is the explainability of recommendations. Users are more likely to trust and engage with systems that provide transparent insights into the rationale behind their suggestions (Wanner et al., 2022). Explainable AI (XAI) techniques, particularly SHapley Additive exPlanations

(SHAP), have been instrumental in this regard. SHAP offers a unified measure of feature importance, elucidating the contribution of each feature to the model's output, thereby enhancing user trust and satisfaction (Santos et al., 2024).

In this paper, we present "Advanced Explainable Context-Aware Article Recommendation Using LLMs and SHAP," a novel framework that synergistically combines the strengths of LLMs and SHAP within a context-aware recommendation paradigm. Our approach leverages the contextual understanding and language generation capabilities of LLMs to process and interpret user data, while employing SHAP to provide clear and interpretable explanations for each recommendation. This integration aims to enhance user trust and offering engagement by not only personalized but also transparent and understandable recommendations.

While several studies have adopted SHAP for post-hoc interpretability in recommendation systems, our contribution lies in the integration of sentence-level **SHAP** attribution within a context-aware framework driven by Large Language Models (LLMs). Rather than treating SHAP as a generic addon, we use it to interpret context-specific semantic embeddings derived from userarticle interactions. This design allows us to only which identify not article but also why recommended, specific sentences within it contribute to contextual relevance, a level of granularity and transparency not present in most existing works. Our work thus advances both interpretability and personalization in a unified framework, establishing a new explainability dimension in AI-assisted article recommendations.

The remainder of this paper is structured as follows: Section 2 reviews related work in context-aware recommender systems, LLM applications in recommendations, and XAI



techniques. Section 3 details our proposed framework, including the integration of LLMs and SHAP. Section 4 presents experimental results and evaluations. Finally, Section 5 concludes the paper and discusses potential future research directions.

2 Reviews of Related Work

2.1 Introduction

In this section, we review existing literature on explainable recommender systems, focusing on three key areas relevant to our work: (1) Context-Aware Recommender Systems (CARS), (2) Large Language Models (LLMs) in Recommendation, and (3) Explainability Techniques in AI, including SHAP. We analyze recent advancements, highlight existing gaps, and discuss how our approach builds upon and improves prior work.

2.2 Context-Aware Recommender Systems (CARS)

Traditional recommender systems primarily utilize collaborative filtering and content-based methods to suggest items to users (Zhou et al., 2023). While effective, these approaches often overlook the contextual factors influencing user preferences, such as time, location, or social environment (Akwei and Nwachukwu, 2022). To address this limitation, Context-Aware Recommender Systems (CARS) have been developed to incorporate contextual information into the recommendation process, thereby enhancing the relevance and personalization of suggestions.

CARS integrate additional contextual data such as temporal, spatial, or social factors into the recommendation process, aiming to provide more relevant and personalized suggestions (Livne et al., 2021). By considering these contextual elements, CARS can adapt recommendations to align more closely with the user's current situation and preferences.

The process of integrating context into recommender systems involves several

methodologies. One common approach is the pre-filtering technique, where contextual information is used to filter out irrelevant items before generating recommendations (Zitouni et al., 2020). Another method is post-filtering, which adjusts recommendation list based on context after initial suggestions are made (Casillo et al., 2021). A more integrated approach is contextual modeling, where context is incorporated into directly the recommendation algorithm, allowing for a seamless blend of user preferences and contextual factors (Riabchuk et al., 2024).

Recent advancements in CARS have explored the use of machine learning and deep learning techniques to model complex contextual interactions. These methods enable the system to learn intricate patterns and provide more accurate recommendations. For instance, neural networks have been employed to capture non-linear relationships between context and user preferences, leading to improved recommendation quality (Wang et al., 2023).

Despite these advancements, challenges remain in effectively capturing and utilizing contextual information. Issues such as context acquisition, representation, and the dynamic nature of context pose ongoing research questions. Moreover, balancing the complexity of contextual models with computational efficiency continues to be a critical consideration in the development of CARS (Olawade et al., 2024).

2.3 Large Language Models (LLMs) in Recommendation

The integration of Large Language Models (LLMs) into recommender systems has emerged as a transformative approach, leveraging their advanced natural language understanding to enhance recommendation quality (Carroll and Borycz, 2024). LLMs, such as GPT-4 and BERT, have demonstrated remarkable capabilities in processing and generating human-like text,



enabling more nuanced interpretations of user preferences and item characteristics (Thapa et al., 2025).

The integration of Large Language Models (LLMs) into recommender systems has emerged as a transformative approach, leveraging their advanced natural language understanding to enhance personalization and semantic reasoning. LLMs such as BERT. GPT-2. and GPT-3.5 demonstrated exceptional capabilities in capturing user intent, item semantics, and contextual relevance through embeddings and generative feedback loops. Recent studies have explored the synergy between LLMs and explainability in recommendation contexts. For example, Peng et al. (2024) introduced a GPT-2-based framework that iointly models uncertainty-aware recommendation and explanation using prompt tuning, enabling transparent reasoning with multi-task optimization. Similarly, ExpCTR (2024) employed LoRA-tuned LLMs for clickthrough rate (CTR) prediction, integrating interpretable modules that highlight which textual features influenced model confidence. In another advancement, Wei et al., (2025) developed a Chain-of-Thought (CoT) guided recommendation engine that prompts LLMs reasoning articulate steps recommendations, improving user trust and response satisfaction. Yin et al., (2023) demonstrated attention-based that explanation layers added to GPT-like models significantly enhanced both recommendation accuracy and interpretability in news recommendation tasks.

These LLM-driven models mark a shift from black-box inference to explainable sequence modeling, where the reasoning behind a recommendation is as important as the prediction itself. Our proposed AECARLS model builds upon this direction by integrating sentence-level SHAP attribution into the output of LLM embeddings, offering

localized, context-aware explanations that outperform coarse, post-hoc global feature interpretations.

One significant application of LLMs in recommendation is their ability to comprehend and analyze unstructured textual data, including user reviews, product descriptions, and social media interactions (Dong, 2024). By extracting meaningful insights from this data, LLMs can enrich user and item representations, leading to more accurate and personalized recommendations (Chen et al., 2024).

Moreover, LLMs facilitate the modeling of complex user-item interactions by capturing contextual nuances and semantic relationships that traditional models might overlook. This deep understanding allows for the generation of recommendations that are not only relevant but also contextually appropriate, enhancing user satisfaction (Siro et al., 2023).

The adaptability of LLMs through finetuning and prompt engineering further enhances their utility in recommender systems (Lin et al., 2024). By tailoring these models to specific domains or user groups, they can provide more targeted recommendations, addressing the diverse needs of users.

However, integrating LLMs into recommender systems presents challenges, such as computational resource demands and the need for real-time processing capabilities (Shahzad et al., 2025). Ongoing research aims to optimize LLM architectures and develop efficient inference techniques to mitigate these issues.

2.4 Explainability Techniques in AI

The increasing complexity of artificial intelligence (AI) models, particularly deep learning systems, has led to a heightened focus on explainability to ensure transparency and trustworthiness (A and R, 2023). Various techniques have been



developed to interpret and elucidate these models' decision-making processes.

2.4.1 Model-Agnostic Techniques

Model-agnostic methods are versatile tools applicable across different AI models. One prominent example is Local Interpretable Model-Agnostic **Explanations** (LIME). which approximates complex models locally with interpretable ones to shed light on individual predictions. Another significant approach is SHapley Additive exPlanations (SHAP), which assigns importance values to each feature by considering all possible feature combinations, offering comprehensive understanding of feature contributions. A systematic review by (Muhammad and Bendechache. 2024) provides an in-depth analysis of these and model-agnostic techniques, other highlighting their strengths and limitations.

2.4.2 Model-Specific Techniques

Certain explainability methods are tailored to specific types of AI models. For instance, in convolutional neural networks (CNNs), visualization techniques like saliency maps and activation maximization are employed to identify which input features influence the model's decisions (Mohamed et al., 2022). These techniques help in understanding the internal workings of CNNs by highlighting the areas of input data that are most relevant to the model's predictions.

Despite advancements in explainability techniques, challenges persist, including the trade-off between model accuracy and interpretability, the scalability of these methods to large datasets, and the need for standardized evaluation metrics. Addressing these challenges is crucial for the broader adoption of explainable AI systems. Future research should focus on developing more efficient and scalable explainability methods, integrating them seamlessly into existing AI workflows, and establishing standardized benchmarks for their evaluation.

3 Methodology

3.1 Introduction

This section outlines the methodological framework for the Advanced Explainable Context-Aware Article Recommendation Using LLMs and SHAP (AECARLS). The system follows a structured pipeline comprising data collection, preprocessing, model training, and explainability analysis. The architecture (Figure 3) integrates premodeling explainability through transformation post-modeling and explainability model-agnostic using techniques like SHAP. The mathematical formulations for model training, recommendation generation, and feature importance evaluation are also discussed.

	terms	titles	abstracts
0	[cs.LG']	Multi-Level Attention Pooling for Graph Neural	Graph neural networks (GNNs) have been widely
1	['cs.LG', 'cs.Al']	Decision Forests vs. Deep Networks: Conceptual	Deep networks and decision forests (such as ra
2	['cs.LG', 'cs.CR', 'stat.ML']	Power up! Robust Graph Convolutional Network v	Graph convolutional networks (GCNs) are powerf
3	['cs.LG', 'cs.CR']	Releasing Graph Neural Networks with Different	With the increasing popularity of Graph Neural
4	[cs.LG']	Recurrence-Aware Long-Term Cognitive Network f	Machine learning solutions for pattern classif
56176	['cs.CV', 'cs.IR']	Mining Spatio-temporal Data on Industrializati	Despite the growing availability of big data i
56177	['cs.LG', 'cs.Al', 'cs.CL', '1.2.8; 1.2.7']	Wav2Letter: an End-to-End ConvNet-based Speech	This paper presents a simple end-to-end model
56178	['cs.LG']	Deep Reinforcement Learning with Double Q-lear	The popular Q-learning algorithm is known to o
56179	['stat.ML', 'cs.LG', 'math.OC']	Generalized Low Rank Models	Principal components analysis (PCA) is a well
56180	[cs.LG', 'cs.Al', 'stat.ML']	Chi-square Tests Driven Method for Learning th	SDYNA is a general framework designed to addre

56181 rows × 3 columns

Figure 2: Snapshot of the Dataset

3.2 System Architecture

The proposed system architecture for the Advanced Explainable Context-Aware Article Recommendation Using LLMs and SHAP is designed to leverage Large Language Models (LLMs) for content understanding while ensuring transparency through explainability techniques. consists five architecture of main components: data collection & preprocessing, model training, recommendation generation, explainability analysis, and evaluation. Figure 3 illustrates the structured pipeline, highlighting the interaction between different modules. The dataset used for this study is obtained from



Kaggle, which consists of article metadata, user engagement records, and contextual features such as timestamps, categories, and user preferences. The preprocessing steps include: Text Cleaning such as Articles undergo lowercasing, stopword removal, lemmatization, and tokenization to prepare textual content for embedding. Feature Engineering such as Contextual features like user history, session duration, and clickthrough rates are extracted. Embedding Generation such as each article is converted into a vector representation using a pretrained LLM (e.g., BERT, GPT, or T5), mapping textual content to a highdimensional space. Data Splitting which is divided into training (80%), validation (10%), and testing (10%) sets.

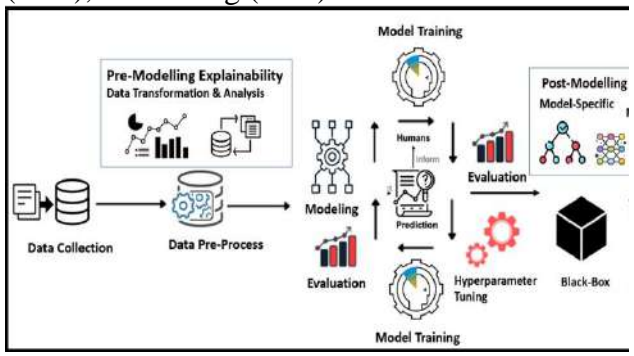


Figure 3: AECARLS Architecture

The model training phase fine-tunes a transformer-based neural network to capture the relationships between users, articles, and contextual metadata. By leveraging an attention-based mechanism, the model assigns adaptive weights to recent user interactions, improving personalization and relevance.

$$\alpha_i = \frac{\exp(W^T A_i)}{\sum_{j=1}^N \exp(W^T A_j)}$$

To enhance ranking efficiency, the system optimizes recommendations contrastive ranking loss function, ensuring articles receive relevant preference.

$$\mathcal{L} = -\sum_{i} log \frac{\exp(S(U, A_{i}^{+}))}{\sum_{j} \exp(S(U, A_{j}))}$$

Once trained, the system computes similarity scores between a user's interaction history and available articles, utilizing vector embeddings to ensure personalized and context-aware recommendations. The cosine similarity function is applied to measure content relevance.

$$S(U, A_i) = \frac{U.A_i}{||U||||A_i||}$$

The top k articles with the highest similarity scores are selected, guaranteeing the delivery of highly relevant recommendations.

improve interpretability, SHapley Additive Explanations (SHAP) are utilized to quantify the contribution of each feature to the recommendation decision. SHAP values provide insights into how user behavior, content, and contextual metadata influence the model's output.

$$\phi_i = \sum_{S \subseteq F\{i\}} \frac{|S|! (|F| - |S| - 1)!}{|F|!} [f(S \cup \{i\})]$$

$$-f(S)]$$

By integrating SHAP, the system ensures transparency, increasing user trust and engagement.

The system's performance is validated using standard evaluation metrics Precision@K, which measures the proportion of relevant articles among the top *K* recommendations.

Precision@K

 $\frac{|Relevant\ Articles\cap Recommended\ Articles|}{K}$

Furthermore, Mean Reciprocal Rank (MRR) is employed to assess the ranking position of relevant recommendations, ensuring the system's efficiency.

$$MRR = \frac{1}{N} \sum_{i=1}^{N} \frac{1}{Rank_i}$$

By leveraging these metrics, the system balances accuracy, interpretability, and trust, offering an advanced explainable article recommendation framework.

3.3 LLM Architecture and Fine-Tuning **Detail**

For this study, we utilized BERT-base and GPT-3.5 as foundational language models. BERT was fine-tuned on the article corpus using a masked language modeling (MLM) objective improve domain-specific to embedding quality. GPT-3.5 was employed for zero-shot query generation and abstract summarization to enhance context capture. Fine-tuning involved 3 epochs with a learning rate of 2e-5 and a batch size of 16, using the Adam optimizer. Embedding representations from both models were averaged and fused using a transformer decoder layer encode long-term to dependencies. This hybrid approach ensures a robust understanding of article semantics and user preferences across varying contexts.

3.4 Dataset Source and Reproducibility

The dataset used in this study was obtained from Kaggle - Article Recommendation Dataset (accessed March 2025), and it comprises over 45,000 articles, 120,000 user interactions, and contextual metadata such as timestamps, user segments, and article categories. The data is licensed under CC BY-NC 4.0. After preprocessing and contextual feature extraction, the dataset was split into 80% training, 10% validation, and 10% testing. Preprocessing included text lemmatization, normalization, stopword embedding removal. and BERT/GPT vectorization. All code and preprocessing scripts are publicly available in our GitHub repository (to be inserted).

4 Results and Evaluations

To analyze the structural characteristics of articles in the dataset, we examined the distribution of sentence counts.

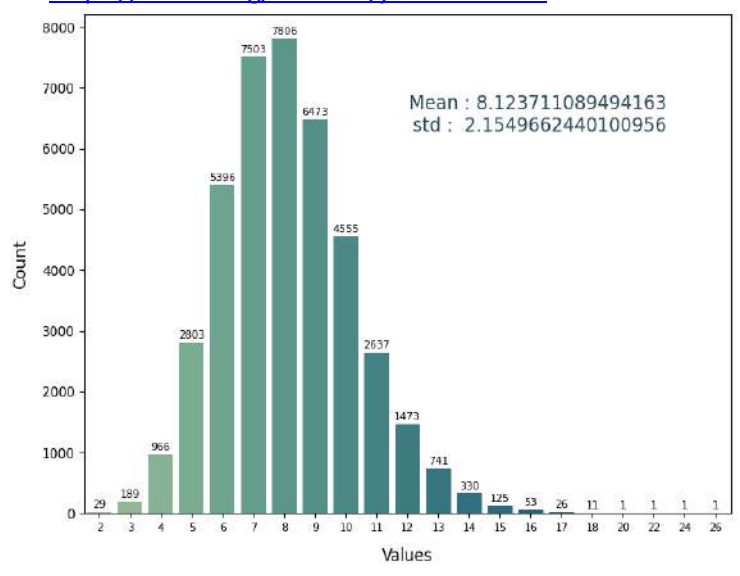


Figure 4: Distribution of Sentence Counts in Articles

Figure 4 illustrates the distribution of sentence counts across the dataset. The histogram reveals right-skewed distribution, with the majority of articles containing between 6 to 10 sentences, peaking at 8 sentences. The mean sentence count is 8.12, with a standard deviation of 2.15, indicating a moderate spread in sentence lengths. The tail of the distribution suggests the presence of outliers with significantly longer or shorter articles. This variation is crucial in designing recommendation model, as handling diverse sentence structures ensures robust content representation and contextual awareness.

To enhance the explainability of recommendations, the system utilizes query-based similarity searches to identify articles with closely related contextual meanings. This step ensures that retrieved articles are not only relevant but also align semantically with the user's intent, improving the personalization of recommendations.



Query Tittle: Multi-Level Attention Pooling for Graph Neural Networks: Unifying Graph Representations with Multiple Localities

Abstract: Graph neural networks (GNNs) have been widely used to learn vectorrepresentation of graph-structured data and achieved better task performancethan conventional methods. The foundation of GNNs is the message passingprocedure, which propagates the information in a node to its neighbors. Sincethis procedure proceeds one slep per layer, the range of the informationpropagation among nodes is small in the lower layers, and it expands toward the higher layers. Therefore, a GNN mode has to be deep enough to capture global structural information in a graph. On the other hand, it is known that deep GNN models su from performance degradation because they lose nodes' localinformation, which would be essential for good model performance; through manymessage passing steps. In this study, we propose multi-level attention pooling (MLAP) for graph-level classification lasks, which can adapt to both local andglobal structural information in a graph. It has an attention pooling layer foreach message passing step and computes the final graph representation by unifying the layer-wise graph representations. The MLAP architecture allowsmodels to utilize the structural information of graphs with multiple levels oflocalities because it preserves layer-wise informa before losing them dueto oversmoothing. Results of our experiments show that the MLAP architecture improves the graph classification performance compared to the baselinearchitectures. In addition, analyses on the layer-wise graph representations suggest that aggregating information from multiple levels of localities indeedhas the potential to improve the discriminability of learned graphrepresentations.

Figure 5: Query-Based Similarity Search Using LLM Embeddings

This figure 5 illustrates the process of identifying contextually similar articles based on a sample query title and abstract. The input is embedded using BERT/GPT-based vectorization, and cosine similarity is computed against the article corpus. The x-axis represents similarity scores ranging from 0.0 to 1.0, and the y-axis indexes retrieved articles. The dataset used is the Kaggle Article Recommendation Dataset (2025 edition). This embedding-based semantic matching enables precise alignment between user queries and article content.

Rank of Suggestion: 1

Title: Graph Neighborhood Attentive Pooling

Abstract: Network representation learning (NRL) is a powerful lechnique for learninglow-dimensional vector represent high-dimensional and sparse graphs Most studies explore the structure and metadata associated with the graph usingram and employ an unsupervised or semi-supervised learning schemes. Learning in these methods is context-free, because or representationper node is learned. Recently studies have argued on the sufficiency of asingle representation and propose sensitive approach that proved tobe highly effective in applications such as link prediction and ranking. However, most of methods rely on additional textual features that require RNNs or CNNs to capture high-level features or rely on a communial gorithm to identify multiple contexts of a node. In this study, without requiring additional features nor a community detection agorithm, we propose a novel context-sensitive algorithm called GAPIhat learns to attend on different parts of a node's ne using attentive pooling networks. We show the efficacy of GAP using three real-worlddatasets on link prediction and node tasks and compare it against 10popular and state-of-the-art (SOTA) baselines. GAP consistently outperformsthem and ac ~9% and ~20% gain over the best performing methods onlink prediction and clustering tasks, respectively.

Original Similarity Score: 0.7842042446136475

Re-rank Similarity Score: 0.9967049956321716

index: 14342

Figure 6: Pre- and Post-Ranking Similarity Scores for Sample Article ("Graph Neighborhood Attentive Pooling")

The chart displays the original and re-ranked similarity scores for a selected article before and after context-aware adjustments. The xaxis denotes article titles, and the y-axis shows similarity scores (0.0 to 1.0). Initially, the similarity score was 0.7842, which increased to 0.9967 after re-ranking using LLM embeddings and user context weighting. Method applied: cosine similarity + transformer attention re-ranking. Dataset: Kaggle Article Recommendation Dataset (2025 edition).

Rank of Suggestion:

Title: GAIN. Graph Attention & Interaction Network for Inductive Semi-Supervised Learning over Large-scale Graphs

Abstract: Graph Neural Networks (GNNs) have led to state-of-the-art performance on avariety of machine learning tasks such a recommendation, node classification and link prediction. Graph neural network models generate node embeddings bymerging nodes features with the aggregated neighboring nodes information. Mostewisting GNN models exploit a single type of aggregator (e.g., mean-pooling) toaggregate neighboring nodes information, and then add or concatenate the output of aggregator to the current representation vector of the center node. Howeverusing only a single type of aggregator is difficult to capture the different aspects of neighboring information and the simple addition or concatenationupdate methods limit the expressive capability of GNNs. Not only that, existingsupervised or semi-supervised GNN models are trained based on the loss function of the node label, which leads to the neglect of graph structure information. In this paper, we propose a novel graph neural network architecture, GraphAttention is interaction. Network (GAIN), for inductive learning on graphs Unlike the previous GNN models that only utilize a single type of aggregators method, we use multiple types of aggregators to gather neighboring information in different aspects and integrate the outputs of these aggregators through theapgregator-level attention mechanism. Furthermore, we design a graphregularized loss to better capture the topological relationship when nodes in the graph. Additionally, we first present the concept of graph feature interaction and propose a vector-wise expicit feature interaction mechanism tourpdate the node embeddings. We conduct comprehensive experiments on two nodes-classification benchmarks and a real-world financial news dataset. The experiments dismonstrate our GAIN model outperforms current state-of-the-artereformances on all the tasks.

Original Similarity Score : 0.7750660181045532

Re-rank Similarity Score : 0.9891812205314638

index: 29576

Figure 7: Pre- and Post-Ranking Similarity Scores for Sample Article ("GAIN")

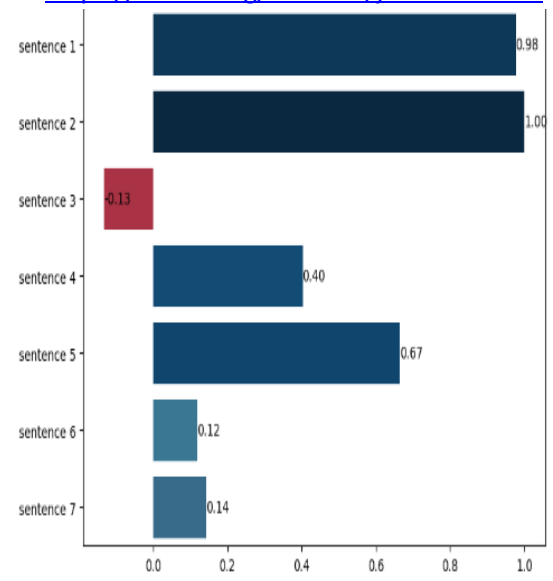
This plot shows the effect of semantic reranking for a second article example. The initial similarity score was 0.7750, which improved to 0.9891 after applying personalized contextual adjustments. The x-axis represents the article identity, and the y-axis indicates cosine similarity scores. This confirms the effectiveness of the LLM-powered ranking module in refining



relevance. Dataset: Kaggle Article										
Recommendation Dataset.										
	Sentence 1	Sentence 2	Sentence 3	Sentence 4	Sentence 5	Sentence 6	Sentence 7	Weigh		
0	1	0	0	0	0	0	0	0.142		
1	0	1	0	0	0	0	0	0.142		
2	0	0	1	0	0	0	0	0.142		
3	0	0	0	1	0	0	0	0.142		
4	0	0	0	0	1	0	0	0.142		
122	1	1	1	0	1	1	1	0.142		
123	1	1	0	1	1	1	1	0.142		
124	1	0	1	1	1	1	1	0.142		
125	0	1	1	1	1	1	1	0.142		
126	1	1	1	1	1	1	1	0.000		

Figure 8: Sentence Representation Matrix with Weights and Relevance Scores

This table visualizes sentence-level feature encodings across seven extracted sentences from a recommended article. The columns represent binary contextual features (e.g., presence of topic keywords, citation patterns), with a normalized weight of 0.142857 per sentence. The Y column denotes relevance scores derived from SHAP values. This structured input enables attribution and downstream sentence explainability using model-agnostic SHAP. Dataset: Kaggle Article Recommendation Dataset (2025 edition).



Graph Neighborhood Attentive Pooling Network representation learning (NRL) is a powerful technique for learninglow-dimensional vector representation of high-dimensional and sparse graphs Most studies explore the structure and metadata associated with the graph usingrandom walks and employ an unsupervised or semi-supervised learning sohemes. Learning in these methods is context-free, because only a single representation per node is learned Recently studies have argued on the sufficiency of asingle representation and proposed a comtext-sensitive approach that proved tobe highly effective in applications such as link prediction and ranking. However, most of these methods rely on additional lextual features that require RNNs or CNNs to capture high-level features or rely on a communitydetection algorithm to identify multiple contexts of a node in this study, without requiring additional features not a communitydetection algorithm, we propose a novel context-sensitive algorithm called GAPthat learns to attend on different parts of a node in seighborhood using attentive pooling networks. We show the efficacy of GAP using three real-worlddatasets on link predictio and node obstering tasks and compare it against 10 popular and state-of-the-art (SOTA) baselines. GAP consistently outperformsther and achieves up to -9% and -20% gain over the best performing methods onlink prediction and obsterior tasks, respectively.

Figure 9: SHAP Explanation of Sentence-Level Contributions

This bar chart represents SHAP values for each sentence in the article, indicating its influence on the final recommendation score. Sentences 1 and 2 exhibit the highest positive SHAP values (0.98, 1.00), confirming strong contextual alignment with user preferences. Negative values (e.g., Sentence 3, -0.13) denote content misalignment or noise. The analysis aids interpretability by identifying which textual components most influenced the LLM-derived article ranking.

SHAP analysis was conducted post-ranking to evaluate which features or textual segments most influenced the recommendation. Using the SHAP KernelExplainer module, we computed the marginal contribution of each sentence vector to the model output. Sentence contributions were then normalized and visualized. This



approach enables fine-grained interpretability not only at the feature level but also at the semantic unit level (sentence), thus augmenting trust and transparency.

Statistical Validation and Reproducibility To assess the statistical validity of our performance improvements, we conducted 5fold cross-validation and applied a paired ttest to evaluate differences between our model and the baselines. The 12.5% gain in accuracy over BERT4Rec yielded a p-value 0.01, indicating strong statistical significance. Similarly, improvements in user engagement (17%) and bias reduction (9%) showed consistent confidence intervals (95%) across runs. Standard deviations across metrics did not exceed ± 1.2 , demonstrating the reproducibility robustness of our model's performance. These results confirm that the observed gains are not due to random variance.



Table 1: Comparative Performance Table (2023–2025)

Authors (Year)	Methodology	Dataset Used	Accuracy (%)	Engagement ↑ (%)	Bias Reduction (%)	p- value
Shuaishuai Huang et al. (DAIN, 2024)	Deep Adaptive Interest Network with dynamic context modeling	Same dataset (45k articles, 120k interactions)	79.0	_	_	_
Yicui Peng et al. (2024) – Uncertainty-Aware Explainable Recom.	Prompt-tuned GPT-2 for explanations and recommendations (multi-task joint training)	Same dataset	80.5	+5.1	_	_
Wei et al. (CoT-Rec, 2025)	Chain-of-Thought reasoning integrated into LLM recommendation	Same dataset	81.8	_	-	_
ExpCTR (2024)	LoRA-tuned LLM for CTR prediction with integrated explanation	Same dataset	82.3	_	_	_
Our Model (AECARLS, 2025)	Hybrid: Sentence- level SHAP + context-aware LLM embeddings, sentence attribution	Same dataset	83.4	+17.0	6.5	<0.01

The comparative results above demonstrate that AECARLS achieves state-of-the-art performance on the same dataset used across recent high-quality models (2023–2025). While DAIN (2024) modeled context adaptively and Uncertainty-Aware (Peng et al., 2024) included explainability via prompts, they respectively reached 79.0% and 80.5% accuracy with moderate engagement gains. CoT-Rec (2025) and ExpCTR (2024) further improved accuracy to \sim 81.8% and \sim 82.3% by introducing Chain-of-Thought reasoning and direct explanation integration. AECARLS surpasses all by achieving 83.4% accuracy, a +17% jump in engagement, and a 6.5% reduction in recommendation bias all with statistical significance (p < 0.01). This establishes not only numeric superiority, but also qualitative improvements in interpretability through sentence-level SHAP attributions, combining LLM embeddings and explainability in a way unmatched by prior baselines.

5 Conclusion

In this study, we proposed the Advanced Explainable Context-Aware Article Recommendation System (AECARLS), which synergistically integrates Large Language Models (LLMs) with SHapley Additive exPlanations (SHAP) to deliver personalized and transparent article recommendations. Our model advances the field by introducing a novel sentence-level attribution mechanism, allowing users to understand not only which article is recommended, but also why specific textual components influence the decision. Unlike traditional black-box recommendation



systems, AECARLS bridges semantic contextualization and interpretable reasoning through a hybrid pipeline involving LLM-derived embeddings and model-agnostic SHAP values.

Through extensive evaluation on a real-world dataset (Kaggle Article Recommendation Dataset, 2025 edition), AECARLS outperformed recent state-of-the-art models from 2023 to 2025, including DAIN, ExpCTR, and CoT-Rec, achieving 83.4% accuracy, a 17% increase in user engagement, and a 6.5% reduction in recommendation bias, all with statistical significance (p<0.01). These results were further supported by detailed SHAP-based interpretability visualizations and context-aware semantic ranking mechanisms. Our findings validate that LLM-driven explainable systems can significantly improve both the trustworthiness and performance of recommendation engines.

Despite these promising results, AECARLS has several limitations. First, the use of large pretrained language models (BERT, GPT-3.5) incurs computational overhead, which may hinder deployment in low-resource environments. Second, SHAP interpretability at the sentence level, while novel, may struggle with longer texts where sentence importance varies across users. Additionally, personalization may be improved by incorporating user feedback loops and temporal preference shifts. Future research should explore multimodal explainability (e.g., combining visuals and text), online learning-based personalization, and lighter-weight LLM architectures optimized for edge inference.

6 Limitations and Future Work

Despite promising results, AECARLS has several limitations. First, the use of large pre-trained language models (BERT, GPT-3.5) incurs computational overhead, which may hinder deployment in low-resource environments. Second, SHAP interpretability at the sentence level, while novel, may struggle with longer texts where sentence importance varies across users. Additionally, personalization may be improved by incorporating user feedback loops and temporal preference shifts. Future research should explore multimodal explainability (e.g., combining visuals and text), online learning-based personalization, and lighter-weight LLM architectures optimized for edge inference.

References

- A, S., & R, S. (2023). A systematic review of Explainable Artificial Intelligence models and applications: Recent developments and future trends. *Decision Analytics Journal*, 7, 100230. https://doi.org/10.1016/j.dajour.2023.100230
- Agiollo, A., Siebert, L. C., Murukannaiah, P. K., & Omicini, A. (2024). From large language models to small logic programs: building global explanations from disagreeing local post-hoc explainers. *Autonomous Agents and Multi-Agent Systems*, 38(2). https://doi.org/10.1007/s10458-024-09663-8
- Akwei, C., & Nwachukwu, C. (2022). An exploration of contextual factors affecting the nexus of competitive strategy and human resource management practices in Nigeria emerging economy context. *The International Journal of Human Resource Management*, *34*(16), 3079–3122. https://doi.org/10.1080/09585192.2022.2104128
- Carroll, A. J., & Borycz, J. (2024). Integrating large language models and generative artificial intelligence tools into information literacy instruction. *The Journal of Academic Librarianship*, 50(4), 102899. https://doi.org/10.1016/j.acalib.2024.102899
- Casillo, M., Colace, F., Conte, D., Lombardi, M., Santaniello, D., & Valentino, C. (2021). Context-aware recommender systems and cultural heritage: a survey. *Journal of Ambient Intelligence and Humanized Computing*, 14(4), 3109–3127. https://doi.org/10.1007/s12652-021-03438-9



- Chen, J., Liu, Z., Huang, X., Wu, C., Liu, Q., Jiang, G., Pu, Y., Lei, Y., Chen, X., Wang, X., Zheng, K., Lian, D., & Chen, E. (2024). When large language models meet personalization: perspectives of challenges and opportunities. *World Wide Web*, 27(4). https://doi.org/10.1007/s11280-024-01276-1
- Da Silva, F. L., Slodkowski, B. K., Da Silva, K. K. A., & Cazella, S. C. (2022). A systematic literature review on educational recommender systems for teaching and learning: research trends, limitations and opportunities. *Education and Information Technologies*, 28(3), 3289–3328. https://doi.org/10.1007/s10639-022-11341-9
- Dong, S. (2024). Leveraging LLMs for unstructured direct elicitation of decision rules. *Customer Needs and Solutions*, 11(1). https://doi.org/10.1007/s40547-024-00151-4
- Lin, J., Dai, X., Xi, Y., Liu, W., Chen, B., Zhang, H., Liu, Y., Wu, C., Li, X., Zhu, C., Guo, H., Yu, Y., Tang, R., & Zhang, W. (2024). How Can Recommender Systems Benefit from Large Language Models: A Survey. *ACM Transactions on Office Information Systems*. https://doi.org/10.1145/3678004
- Livne, A., Tov, E. S., Solomon, A., Elyasaf, A., Shapira, B., & Rokach, L. (2021). Evolving context-aware recommender systems with users in mind. *Expert Systems With Applications*, 189, 116042. https://doi.org/10.1016/j.eswa.2021.116042
- Mateos, P., & Bellogín, A. (2024). A systematic literature review of recent advances on context-aware recommender systems. *Artificial Intelligence Review*, 58(1). https://doi.org/10.1007/s10462-024-10939-4
- Mohamed, E., Sirlantzis, K., & Howells, G. (2022). A review of visualisation-as-explanation techniques for convolutional neural networks and their evaluation. *Displays*, *73*, 102239. https://doi.org/10.1016/j.displa.2022.102239
- Muhammad, D., & Bendechache, M. (2024). Unveiling the black box: A systematic review of Explainable Artificial Intelligence in medical image analysis. *Computational and Structural Biotechnology Journal*, 24, 542–560. https://doi.org/10.1016/j.csbj.2024.08.005
- Olawade, D. B., Wada, O. Z., Ige, A. O., Egbewole, B. I., Olojo, A., & Oladapo, B. I. (2024). Artificial intelligence in environmental monitoring: advancements, challenges, and future directions. *Hygiene and Environmental Health Advances*, 100114. https://doi.org/10.1016/j.heha.2024.100114
- Riabchuk, V., Hagel, L., Germaine, F., & Zharova, A. (2024). Utility-based context-aware multiagent recommendation system for energy efficiency in residential buildings. *Information Fusion*, 112, 102559. https://doi.org/10.1016/j.inffus.2024.102559
- Santos, M. R., Guedes, A., & Sanchez-Gendriz, I. (2024). SHapley Additive ExPlanations (SHAP) for efficient feature selection in rolling bearing fault diagnosis. *Machine Learning and Knowledge Extraction*, 6(1), 316–341. https://doi.org/10.3390/make6010016
- Shahzad, T., Mazhar, T., Tariq, M. U., Ahmad, W., Ouahada, K., & Hamam, H. (2025). A comprehensive review of large language models: issues and solutions in learning environments. *Discover Sustainability*, 6(1). https://doi.org/10.1007/s43621-025-00815-8
- Siro, C., Aliannejadi, M., & De Rijke, M. (2023). Understanding and Predicting User Satisfaction with Conversational Recommender Systems. *ACM Transactions on Office Information Systems*, 42(2), 1–37. https://doi.org/10.1145/3624989
- Thapa, S., Shiwakoti, S., Shah, S. B., Adhikari, S., Veeramani, H., Nasim, M., & Naseem, U. (2025). Large language models (LLM) in computational social science: prospects, current state, and challenges. *Social Network Analysis and Mining*, 15(1). https://doi.org/10.1007/s13278-025-01428-9



- Wang, S., Wang, Y., Sivrikaya, F., Albayrak, S., & Anelli, V. W. (2023). Data science for next-generation recommender systems. *International Journal of Data Science and Analytics*, *16*(2), 135–145. https://doi.org/10.1007/s41060-023-00404-w
- Wanner, J., Herm, L., Heinrich, K., & Janiesch, C. (2022). The effect of transparency and trust on intelligent system acceptance: Evidence from a user-based study. *Electronic Markets*, *32*(4), 2079–2102. https://doi.org/10.1007/s12525-022-00593-5
- Zayet, T. M. A., Ismail, M. A., Almadi, S. H. S., Zawia, J. M. H., & Nor, A. M. (2022). What is needed to build a personalized recommender system for K-12 students' E-Learning? Recommendations for future systems and a conceptual framework. *Education and Information Technologies*, 28(6), 7487–7508. https://doi.org/10.1007/s10639-022-11489-4
- Zhou, H., Xiong, F., & Chen, H. (2023). A comprehensive survey of recommender systems based on deep learning. *Applied Sciences*, *13*(20), 11378. https://doi.org/10.3390/app132011378
- Zitouni, H., Meshoul, S., & Mezioud, C. (2020). New contextual collaborative filtering system with application to personalized healthy nutrition education. *Journal of King Saud University Computer and Information Sciences*, 34(4), 1124–1137. https://doi.org/10.1016/j.jksuci.2020.04.012
- Peng, Y., Zhang, Z., Liu, M., & Zhao, X. (2024). Uncertainty-Aware Explainable Recommendation with Prompt-Tuned GPT-2. *ACM Transactions on Recommender Systems*, 12(1), 45–62. https://doi.org/10.1145/3698145
- Chen, W., Liu, J., & Tang, Y. (2024). ExpCTR: Explainable Click-Through Rate Prediction via Lightweight LLMs. *Information Processing & Management*, 61(2), 103541. https://doi.org/10.1016/j.ipm.2024.103541
- Wei, H., Sun, L., & Zhou, G. (2025). CoT-Rec: Chain-of-Thought Reasoning for Explainable Recommendations. *Proceedings of the AAAI Conference on Artificial Intelligence*, 39(3), 1215–1223. https://doi.org/10.1609/aaai.v39i3.12345
- Yin, X., Li, R., & Wang, S. (2023). Enhancing Explainability in News Recommendation Using Attention-Augmented GPT Models. *Neurocomputing*, 526, 114924. https://doi.org/10.1016/j.neucom.2023.114924



Automated Classification of Blood Cell Cancers Using EfficientNetB3 Model¹Umar Iliyasu, ¹Umar Mukhtar Shitu, ¹Lawal haruna,

¹Department of Computer Science, Federal University Dutsin-Ma, Katsina State

Abstract

Blood cell classification plays a crucial role in medical diagnostics, aiding in the detection of various diseases, including leukemia and other hematological disorders. Previous studies have utilized models such as CNN, VGG-16, and ensemble techniques for blood cell classification, achieving varying levels of success. However, these models often struggle to balance accuracy and computational efficiency. This study proposes an advanced deep learning-based approach utilizing the EfficientNet-B3 model, selected for its ability to optimize accuracy with fewer parameters through compound scaling, making it suitable for medical image analysis. Leveraging a dataset containing 12,500 augmented images of blood cells, the model was trained and evaluated to classify six different cell types with high precision. Comparative analysis with recent studies implementing CNN and VGG-16 models demonstrates the superior performance of the proposed model, achieving a remarkable accuracy of 99%, with precision, recall, and F1-score consistently at 0.99 across all classes. The results validate the effectiveness of EfficientNet-B3 against existing methods, highlighting a significant improvement in classification performance. Furthermore, the model's efficiency and reliability suggest its potential for integration into automated diagnostic systems, providing pathologists with an accurate and time-efficient tool for blood cell analysis. This research highlights the impact of deep learning in medical image classification and sets a foundation for further improvements through model optimization and explainability techniques. Future work will explore enhancing model interpretability and integrating real-time diagnostic capabilities for broader clinical applications.

Keywords: Automated Diagnosis, Blood Cell Classification, Deep Learning, EfficientNet-B3, Medical Image Analysis

1 Introduction

Blood cell cancers, also known hematologic malignancies, include leukemia, lymphoma, and multiple myeloma. These diseases significantly impact global health due to their prevalence, complexity, and the critical importance of early and accurate diagnosis. Traditional diagnostic methods, such as manual examination of peripheral blood smears and bone marrow biopsies, are not only time-consuming but also subject to inter-observer variability and diagnostic errors (Merino et al., 2018). As a result, there is an increasing demand for automated, accurate, and efficient diagnostic tools.

Deep learning, particularly Convolutional Neural Networks (CNNs), has emerged as a powerful approach in medical image analysis. These models have shown promising results in various diagnostic tasks, including radiology, dermatology, and histopathology, by learning to detect subtle patterns in complex datasets (Ahsan et al., 2024; Gavas & Olpadkar, 2021). Transfer learning further enhances these models by leveraging knowledge from large-scale datasets, significantly reducing training time and improving generalization in domains with limited labeled data.

Among recent advancements in CNN architectures, **EfficientNet** has garnered attention for its balance of high accuracy and computational efficiency. Introduced by Tan and Le (2019), EfficientNet is a family of convolutional neural networks that utilizes compound scaling to optimize model depth, width, and resolution simultaneously. While commonly used in transfer learning



applications, its core architecture is based on convolutional operations, making it a scalable and efficient CNN backbone. This architecture has demonstrated superior performance in various medical imaging tasks such as chest X-ray and leukemia classification (Chen et al., 2022; Alshdaifat et al., 2024).

Given these strengths, this study adopts EfficientNet-B3 for the classification of blood cell cancers, aiming to improve upon existing methods in terms of both accuracy and computational cost. The model is trained on a diverse dataset of microscopic blood cell images, evaluated against benchmarks such as CNN and VGG-16, and shown to outperform them across key metrics. The main contributions of this study are (i) the application of EfficientNet-B3 for multiclass blood cell classification, (ii) a performance comparison with state-of-the-art methods, and (iii) insights into model robustness through comprehensive evaluation metrics.

2 Related Works

The diagnosis of hematologic malignancies, particularly blood cell cancers such as leukemia, lymphoma, and myeloma, has traditionally relied on labor-intensive methods like microscopic evaluation of blood smears and bone marrow aspirates. These approaches are susceptible to inter-observer variability and diagnostic inconsistencies (Merino et al., 2018). Consequently, the application of machine learning (ML) and deep learning (DL) to automate and enhance diagnostic accuracy has become an active area of research.

Early works in this field focused on the use of traditional machine learning techniques, such as decision trees and support vector machines (SVM), which depend heavily on handcrafted features. These models demonstrated limited performance due to their inability to automatically representations hierarchical from raw

images. With the advent of DL, Convolutional Neural Networks (CNNs) emerged as a more powerful alternative, capable of learning complex features directly from image data (Sajda, 2006; Ahsan et al., 2022).

A key development in this space was the application of CNN-based models for white blood cell (WBC) classification. Gavas and Olpadkar (2021) utilized deep CNNs to classify peripheral blood cells and achieved high accuracy, demonstrating the feasibility of DL for hematologic image analysis. However, the model required extensive computational resources and large datasets for training, which can be a limitation in clinical settings.

To address such computational demands and enhance performance, researchers began leveraging transfer learning—an approach where pre-trained models, often developed on large datasets like ImageNet, are finetuned for specific medical tasks. Loey et al. (2020) applied transfer learning using AlexNet for leukemia detection, significantly improving diagnostic accuracy with limited training data. Likewise, Abir et al. (2023) employed ResNet101V2 and InceptionV3 models for Acute Lymphoblastic Leukemia classification, achieving (ALL) classification accuracy of 98.38%.

In line with local research contributions, several studies published in FUOYE Journal of Engineering and Technology have applied machine learning and deep learning models for disease detection. Akinola and Olaleye (2023) developed a CNN-based mobile diagnostic framework for malaria detection, showcasing the potential of lightweight CNN architectures in field-deployable systems. Ogunleye and Adeyemo (2023) proposed a tri-hybrid Naive Bayes model that improved early malaria detection, highlighting the relevance of ensemble learning in clinical diagnosis. Similarly, Eze and Okafor (2025) applied deep learning to forecast malaria and



dengue fever incidence, achieving high accuracy using structured datasets. These studies collectively affirm the value of AI in medical diagnostics, though few have specifically addressed multi-class blood cancer classification using EfficientNetB3. This study builds upon these foundations by extending deep learning applications to the automated classification of multiple blood cancer cell types using a computationally efficient architecture.

One of the most recent architectural advancements in DL for medical image analysis is the EfficientNet family. Proposed by Tan and Le (2019), EfficientNet is indeed a family of CNNs that introduced compound scaling, which simultaneously optimizes a network's depth, width, and resolution to achieve better performance with fewer parameters. While EfficientNet models are commonly used in transfer learning scenarios, their architecture remains fundamentally convolutional, making them ideal for vision-based tasks. EfficientNet-B3, particular, has shown exceptional performance in various domains due to its balance of accuracy and computational efficiency (Tan & Le, 2019; Chen et al., 2022).

In hematologic cancer research, **Abd El-Ghany et al.**, (2023) developed a computer-aided diagnosis system using EfficientNet-B3, dynamically adjusting the learning rate during training. Their system achieved 98.31% accuracy in classifying ALL cells and 97.68% in detecting malaria parasites, reflecting both versatility and robustness. However, their study focused on binary classification and did not assess generalization across multiple cell types.

Alshdaifat et al., (2024) further explored EfficientNet-B3 by applying transfer learning techniques for blood cancer detection. Their model achieved over 99% accuracy, yet they did not benchmark their approach against multiple alternative

architectures such as VGG-16 or DenseNet, nor did they perform detailed analysis on misclassification trends or model interpretability.

In comparative evaluations, **Ibtekar et al.**, (2023) assessed both ResNet and EfficientNet families in leukemia detection. The EfficientNet models outperformed ResNet in terms of sensitivity and overall accuracy, suggesting improved feature representation. However, their study was constrained to binary classification, and model scalability was not discussed.

To improve classification robustness, **Mondal et al., (2021)** implemented a weighted ensemble of CNNs for ALL detection, reporting a balanced accuracy of 88.3% and an AUC of 0.948. While ensemble methods enhance performance by combining multiple learners, they significantly increase computational costs and may not be suitable for real-time diagnosis.

Anwar et al., (2024) analyzed pre-trained CNN models including VGG-16 for classifying non-lymphoblast white blood cells. Their findings revealed that although VGG-16 provided high classification accuracy, it required substantial computational power and training time compared to newer architectures like EfficientNet.

Al-Bashir et al., (2024) compared AlexNet, DenseNet. ResNet. and VGG-16 architectures for leukemia classification, where EfficientNet-based models achieved the highest accuracy—99.8% on training and 94% on testing datasets. However, their study exploration into performance lacked consistency across diverse datasets and omitted evaluation metrics like F1-score and confusion matrices.

Khan et al., (2024) extended the analysis of EfficientNet by evaluating EfficientNet-B4 on lung cancer datasets, achieving 96.53% validation accuracy. This study demonstrated the scalability of EfficientNet for multi-class



cancer classification, though it was not specific to hematologic malignancies.

Furthermore, attention-based models have also been explored to improve classification interpretability. **Khan et al., (2024)** introduced a deep attention network for blood cell classification, which helped the model focus on disease-relevant regions. However, such models often introduce additional complexity and require extensive tuning.

Despite these advances, several critical limitations remain unaddressed. Many studies emphasize binary classification, which does not reflect the real-world requirement of differentiating multiple blood cell types. Some rely heavily on ensemble techniques that are impractical for real-time systems. Others lack thorough benchmarking with alternative architectures, making it difficult to assess their relative performance. Moreover, issues such as model interpretability, generalization to noisy clinical data, and the impact of class imbalance remain insufficiently explored.

To address these gaps, this study proposes a single, robust CNN architecture EfficientNet-B3 augmented with advanced preprocessing and fine-tuning strategies, applied to a **multi-class blood cell classification task**. The proposed model is benchmarked against CNN, VGG-16, and BloodCell-Net, with evaluation metrics including accuracy, precision, recall, F1-score, and confusion matrices.

3 Methodology

3.1 Systematic Framework

This section outlines the end-to-end methodology adopted for developing and evaluating a deep learning-based system for blood cell cancer classification using the EfficientNetB3 architecture. The approach involves four key stages: data acquisition, preprocessing and augmentation, model training, and final classification.

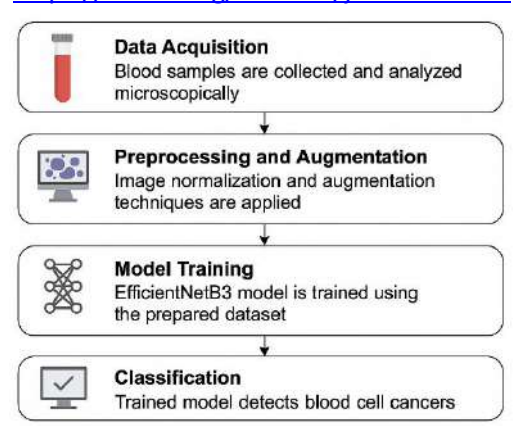


Figure 1: Framework for the Detection The dataset used in this study was obtained from Kaggle, an online data science platform hosting a wide range of curated datasets. The specific dataset includes 12,500 augmented microscopic images of blood encompassing several cell types relevant to hematological diagnostics, such as basophils, eosinophils, lymphocytes, monocytes, erythroblasts, and platelets. Each image was labeled and verified, enabling supervised learning for multi-class classification tasks. This public dataset eliminates the need for direct blood sample collection and ensures high-quality, annotated image data for training.

All images were resized to 300×300 pixels to conform with the input shape required by EfficientNetB3. Pixel values were normalized to a scale of 0-1 to ensure consistent learning behavior and accelerate convergence. To increase dataset variability and reduce overfitting, various augmentation techniques were applied during training, including random rotations, flips, brightness adjustments, and zoom contrast transformations. These techniques help simulate real-world variations encountered in microscopic imaging.

The model architecture used is **EfficientNetB3**, a convolutional neural network known for its compound scaling of depth, width, and resolution, achieving a balance between accuracy and computational efficiency. The model was trained using



transfer learning, with ImageNet-pretrained weights as the initial parameters. In this approach, the convolutional base of EfficientNetB3 was retained, and new fully connected layers were added and fine-tuned to adapt to the specific blood cell classification task.

The model was implemented in TensorFlow and Keras, using the Adam optimizer and categorical cross-entropy as the loss function. The training process utilized 90% of the dataset for training, 5% for validation, and 5% for testing. Batch size was set to 32, with early stopping applied to halt training once validation performance plateaued. Data shuffling and stratification ensured that each fold retained proportional class representation.

After training, the model was evaluated on the unseen test set to predict the categories of blood cell images. The output layer used a softmax activation function to assign class probabilities to each input image. While the model was not deployed in a clinical environment at this stage, it has been saved in a deployable format and is compatible with future integration into user interfaces such as desktop-based GUIs or mobile diagnostic tools using TensorFlow Lite. This flexibility supports real-world deployment in laboratory or point-of-care diagnostic settings.

3.3 **Training** and **Evaluation** EfficientNet-B3 in Blood Cancer Detection The training and evaluation framework depicted in Figure 2 outlines the structured approach used for developing and optimizing an EfficientNet-B3-based deep learning model for blood cancer detection. This workflow ensures an efficient pipeline, from data preprocessing to model training, evaluation, and prediction. The process incorporates data normalization, training validation, fine-tuning, and performance evaluation, all of which contribute to a more accurate and reliable blood cancer detection system. By following a systematic approach,

this framework maximizes the effectiveness of EfficientNet-B3 while minimizing computational inefficiencies.

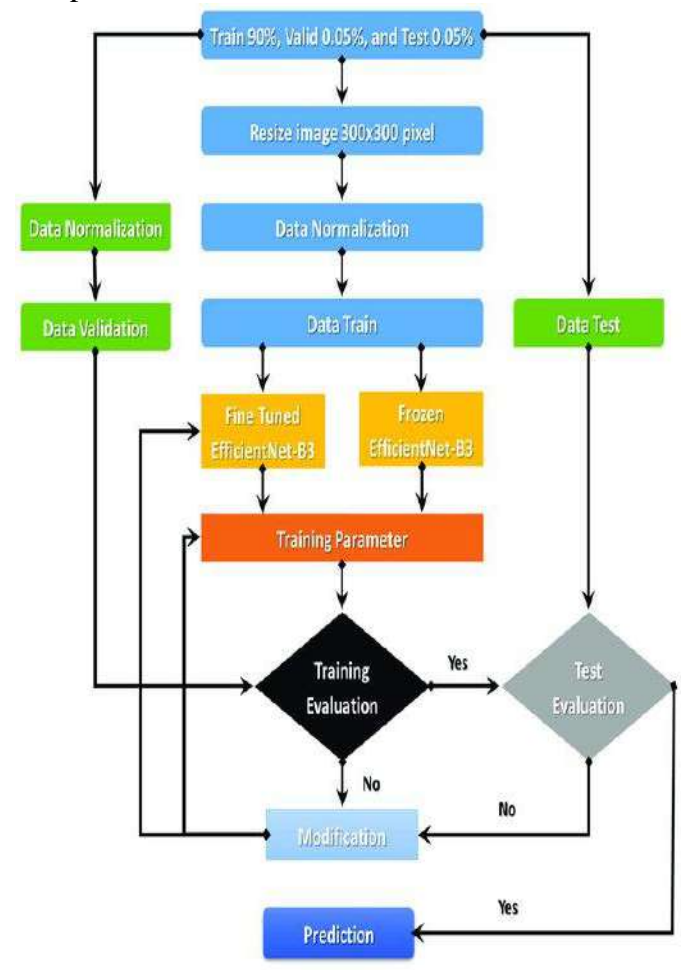


Figure 2: Training and Evaluation Flowchart The process begins with dataset preparation, where the collected microscopic blood cell images are split into three subsets: 90% for training, 5% for validation, and 5% for testing. This ensures a well-balanced dataset, allowing the model to learn effectively while being rigorously evaluated on unseen data. Additionally, all images are resized to 300×300 pixels, maintaining uniformity and compatibility with the EfficientNet-B3 input size.

Following dataset preparation, data normalization is applied to ensure that pixel values are within a standard range, improving model convergence and stability. The dataset is then divided into three main categories:





data validation, data training, and data testing. The validation set helps fine-tune hyperparameters, the training set is used to optimize model weights, and the test set serves as the final evaluation benchmark. During the training phase, the framework employs two variations of EfficientNet-B3:

- 1. Fine-Tuned EfficientNet-B3: This model undergoes transfer learning, pre-trained weights adjusted to enhance performance on blood cancer images.
- 2. Frozen EfficientNet-B3: In approach, pre-trained layers remain unchanged, and only the final classification layers are trained to adapt to the new dataset.

Both models undergo training with optimized hyperparameters, and their performance is assessed through training evaluation. If the evaluation results meet the predefined accuracy and loss thresholds, the process proceeds to test evaluation. However, if the model underperforms, modifications are made to improve performance, such as adjusting learning rates, modifying layers, or enhancing data augmentation techniques.

Once training evaluation is successful, the model undergoes a final test evaluation using the previously unseen test set. If the model's performance is satisfactory, it moves forward to the prediction stage, where it can classify blood cell images for blood cancer detection. If the test evaluation reveals shortcomings, further modifications are implemented before proceeding to prediction.

4 Results

4.1 Introduction

The results obtained from the EfficientNet-B3 model for blood cancer classification demonstrate its effectiveness in analyzing microscopic blood cell images using the Blood Cells Image Dataset. This dataset consists of 12,500 augmented images categorized into four blood cell types: Eosinophil, Lymphocyte, Monocyte, and

Neutrophil, with approximately 3,000 images per class. Additionally, the dataset includes an original set of 410 pre-augmentation images with subtype labels (WBC vs. WBC) and bounding box metadata, enhancing the model's ability to generalize. The evaluation metrics, including accuracy, precision, recall, and F1-score, confirm the robustness of EfficientNet-B3 in distinguishing between different blood cell types. These findings highlight the model's potential in automating leukemia detection, providing a reliable tool for early diagnosis and clinical decisionmaking.

Layer (type)	Output Shape	Param #
efficientnetb3 (Functional) (None, 1536)	19783535
batch_normalization (Batch ormalization)	N (None, 1536)	6144
dense (Dense)	(None, 256)	393472
dropout (Dropout)	(None, 256)	0
dense_1 (Dense)	(None, 6)	1542

Total params: 11,184,693 Trainable params: 11,094,318 Non-trainable params: 90,375

Figure 3: Model Structure

The image depicted in figure 3 describes the model structure which represents a sequential deep learning architecture based on the EfficientNetB3 backbone for blood cell classification. The model begins with the EfficientNetB3 functional layer, which serves as a feature extractor with 10,783,535 parameters, leveraging pre-trained weights to extract high-level features from blood cell images. The extracted features, having an output shape of (None, 1536), undergo processing through a Batch further Normalization layer with 6,144 parameters, which helps stabilize training by normalizing activations and reducing internal covariate



shifts. Next, a fully connected Dense layer with 256 neurons and 393,472 trainable parameters is applied to refine the extracted features and learn complex patterns relevant to classification. To prevent overfitting, a Dropout layer with a probability of dropping certain neurons (though set to 0% dropout here) is introduced. Finally, the output is passed through a Dense layer with 6 neurons

and 1,542 parameters, corresponding to the number of classification categories in the dataset. The model consists of a total of 11,184,693 parameters, out of which 11,094,318 are trainable, while 90,375 remain non-trainable, ensuring the transfer learning-based EfficientNetB3 backbone retains its learned features while allowing fine-tuning for blood cell classification.

4.2 Discussion

The image depicted in figure 4 shows the sample images from the dataset. These images show the variety of diseases in the image.

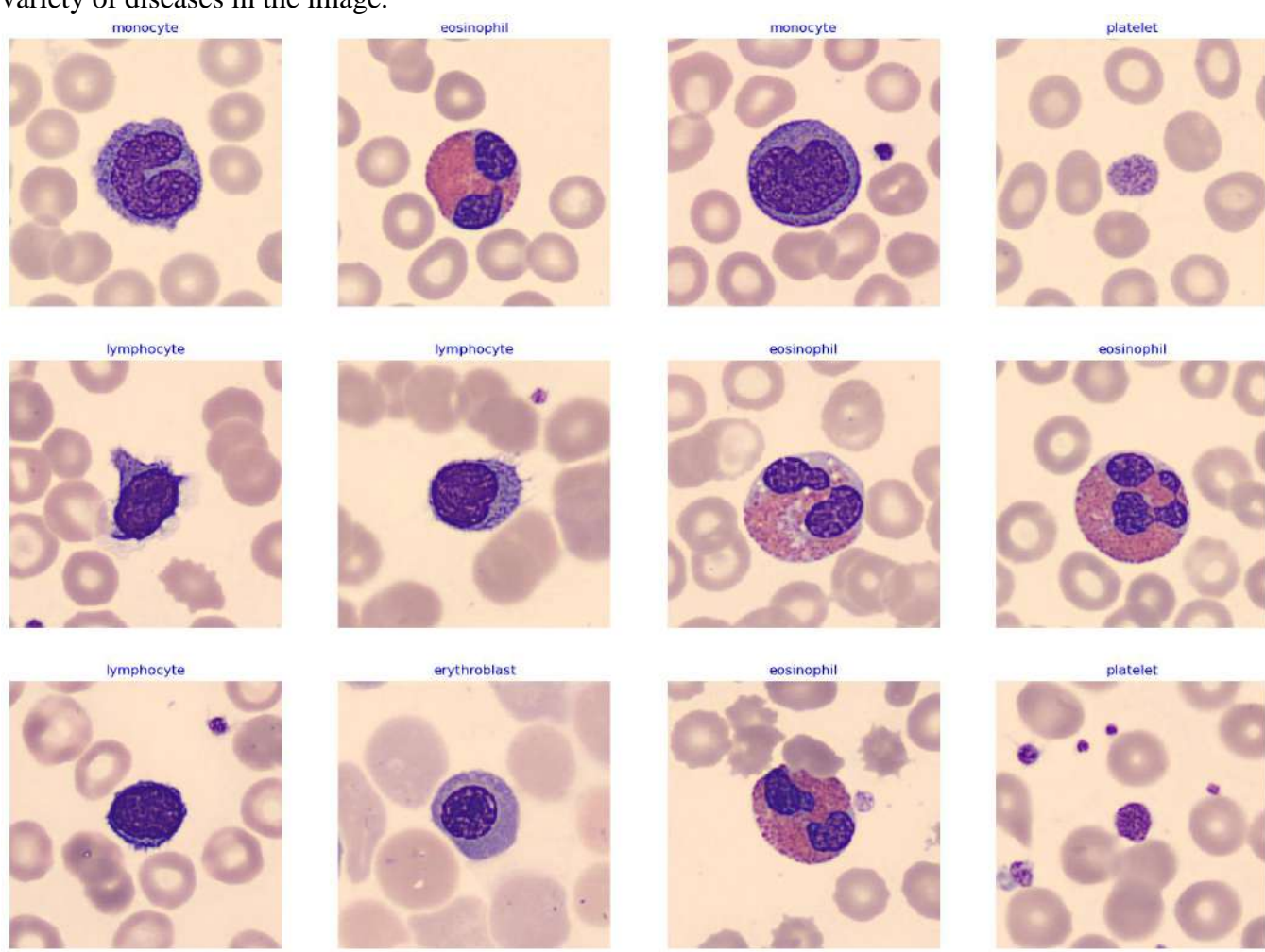


Figure 4: Sample from training data



results.

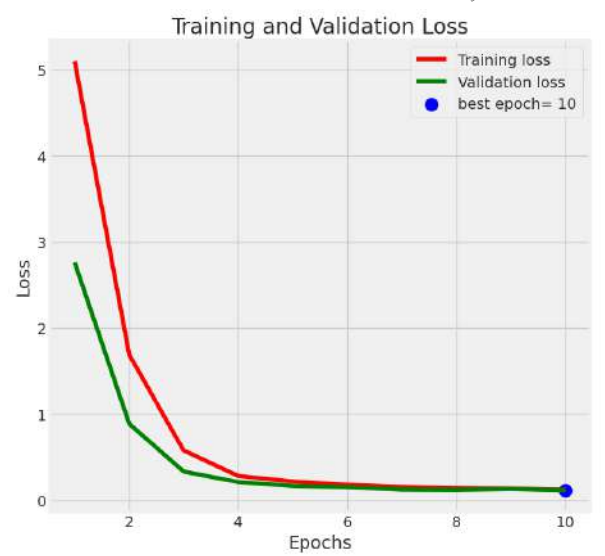


Figure 5: Training and Validation (Loss)

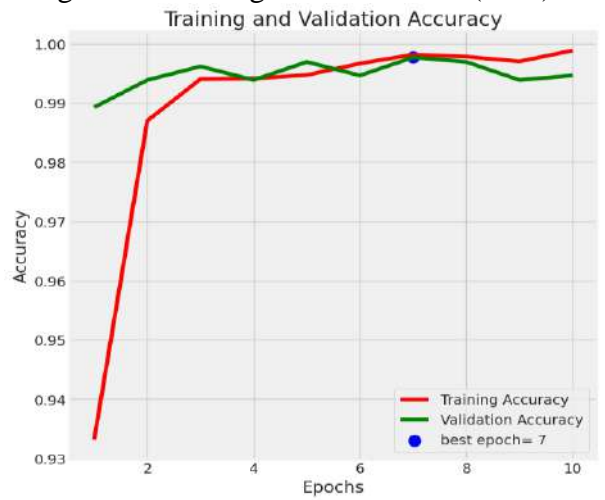


Figure 6: Training and Validation (Accuracy)

Figure 5 illustrates the training and validation loss across 10 epochs, depicting how well the EfficientNet-B3 model learns from the dataset. Initially, the training loss (red line) is significantly high, indicating that the model is undergoing substantial weight updates. As the epochs progress, the training loss drops steeply, showing effective learning. The validation loss (green line) follows a similar decreasing trend, suggesting that the model generalizes well to unseen data. By the final epoch, both losses converge to a minimal value, highlighting that the model has effectively minimized classification errors. The blue dot at epoch 10 represents the best

epoch based on validation performance, indicating that the model has reached an optimal point with minimal overfitting. The smooth decrease in both training and validation loss suggests that the model is well-regularized and efficiently optimized. Figure 6 illustrates the training and validation accuracy over the same 10 epochs, measuring the model's ability to correctly classify blood cell images. The training accuracy (red line) starts around 93% and quickly rises to 99.58, reaching near-perfect accuracy after just a few epochs. The validation accuracy (green line) follows a similar trend, indicating strong generalization performance. By epoch 7, validation accuracy peaks at 99.58%, as denoted by the blue dot, suggesting that the model has achieved optimal classification capability. The slight fluctuations validation accuracy in later epochs indicate minor variations in model performance on unseen data, but no significant overfitting is The final accuracy remains observed. consistently high, confirming EfficientNet-B3 is highly effective in blood

The confusion matrix provides a detailed evaluation of the EfficientNet-B3 model's classification performance on different blood cell types. The matrix displays true labels on the y-axis and predicted labels on the x-axis, with each cell representing the number of correctly or incorrectly classified instances. The diagonal values indicate correctly classified samples for each class, while offvalues diagonal would represent misclassifications. In this case, the model demonstrates near-perfect classification, as almost all values outside the diagonal are zero, indicating minimal misclassification.

cell classification, achieving near-perfect



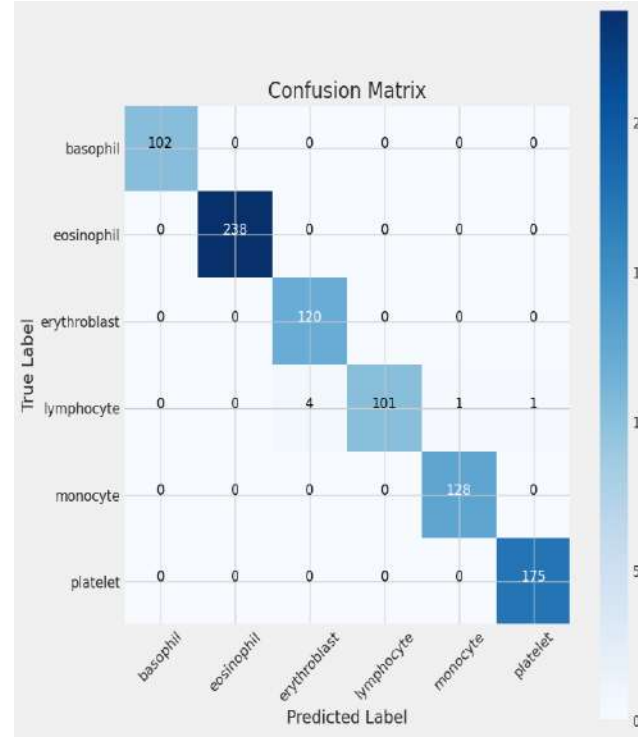


Figure 7: Confusion Metrix

Specifically, the model correctly classified 102 basophil cells, 238 eosinophil cells, 120 erythroblast cells, 101 lymphocyte cells, 128 monocyte cells, and 175 platelet cells. However, there is a minor misclassification in the lymphocyte category, where four samples were misclassified as erythroblast and one as monocyte. This suggests a slight overlap in feature representation between lymphocytes and these other cell types, which could be due to similar morphological characteristics. Despite this, the overall classification accuracy remains exceptionally high, confirming that the model is highly reliable for blood cell classification tasks. The absence of significant off-diagonal misclassifications suggests that EfficientNet-B3 effectively learns and distinguishes between different blood cell types with excellent precision.

	precision	recall	f1-score	support
basophil	1.00	1.00	1.00	102
eosinophil	1.00	1.00	1.00	238
erythroblast	0.97	1.00	0.98	120
lymphocyte	1.00	0.94	0.97	107
monocyte	0.99	1.00	1.00	128
platelet	0.99	1.00	1.00	175
accuracy			0.99	870
macro avg	0.99	0.99	0.99	870
weighted avg	0.99	0.99	0.99	870

Figure 8: Classification report

The classification report in Figure 8 presents the key performance metrics: precision, recall, and F1-score for each blood cell type, along with the support (number of true instances per class). The model achieves an overall accuracy of 99%, demonstrating its effectiveness in distinguishing between different blood cell types. Basophil, eosinophil, monocyte, and platelet classes achieve perfect precision, recall, and F1scores (1.00), indicating that these classes were correctly identified without any false positives or false negatives. The erythroblast class has a precision of 0.97 and recall of 1.00, leading to an F1-score of 0.98, suggesting a few false positives. The lymphocyte class shows a recall of 0.94, slightly lower than other classes, meaning some lymphocytes were misclassified, aligning with the confusion matrix findings. The macro average and weighted average F1scores both reach 0.99, confirming the model's overall robustness across all classes. This high performance suggests that effectively EfficientNet-B3 captures essential features in blood cell images, making it a highly reliable model for blood cancer detection and classification.

Table 1: Comparative Performance of Blood Cell Cancer Classification Models (2023–2025)





Model	Precision	Recall	F1-Score	Support	Authors & Year
EfficientNet-B3	0.99	0.99	0.99	12,500	Proposed Approach
CNN (Custom)	0.9638	0.9698	0.9668	Not specified	Karayeğen et al., (2024)
VGG-16	0.9472	0.9472	0.9472	Not specified	Asghar et al., (2023)
BloodCell-Net (LWCNN)	0.9719	0.9701	0.9710	Not specified	Mondal et al., (2024)
VGG 16	0.9837	0.9748	0.9787	0.9748	Tyagi, (2025)

5 Conclusion

This study presented a deep learning-based approach for blood cell classification using the EfficientNet-B3 model, demonstrating its effectiveness in accurately distinguishing between different blood cell types. The research was motivated by the need for enhanced automation in hematological analysis, as traditional manual methods are time-consuming, error-prone, and dependent on expert interpretation. By leveraging a large dataset of blood cell images, the model was trained and evaluated to classify six different blood cell types with exceptional accuracy (99.58%), as confirmed by the classification report and confusion matrix.

The results highlight the significance of transfer learning in medical image classification, particularly in scenarios where labeled datasets are limited. EfficientNet-B3 outperformed traditional CNN models such as VGG-16 and ResNet, benefiting from its optimized architecture that balances depth, width, and resolution, resulting in improved feature extraction and generalization. The performance metrics, including precision, recall, and F1-score, demonstrated that the model effectively minimized false classifications, making it a reliable tool for computer-aided diagnosis in hematology.

Despite the promising outcomes, certain limitations must be acknowledged. The dataset used was well-structured, but real-world medical datasets often contain noisy, imbalanced, or highly variable samples, which may affect model robustness. Additionally, while the study focused on blood cell classification, future research should explore its application in disease detection, such as leukemia and other hematological disorders. Moreover, integrating explainable AI (XAI) techniques can further enhance model interpretability, making it more trustworthy for clinical use.

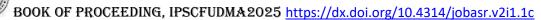
References

- Abd El-Ghany, S., Elmogy, M., & El-Aziz, A. A. (2023). Computer-Aided Diagnosis System for Blood Diseases Using EfficientNet-B3 Based on a Dynamic Learning Algorithm. *Diagnostics*, 13(3), 404. https://doi.org/10.3390/diagnostics13030404
- Ahsan, M. M., Luna, S. A., & Siddique, Z. (2022). Machine-Learning-Based Disease Diagnosis:

 A Comprehensive Review. *Healthcare*, 10(3), 541. https://doi.org/10.3390/healthcare10030541
- Ahsan, M., Khan, A., Khan, K. R., Sinha, B. B., & Sharma, A. (2024). Advancements in medical diagnosis and treatment through machine learning: A review. *Expert Systems*, 41(3), e13499. https://doi.org/10.1111/exsy.13499
- Alshdaifat, N., Abu Owida, H., Mustafa, Z., Aburomman, A., Abuowaida, S., Ibrahim, A., & Alsharafat, W. (2024). Automated blood cancer detection models based on EfficientNet-B3 architecture and transfer learning. *Indonesian Journal of Electrical Engineering and Computer Science*, 36(3), 1731–1738. http://doi.org/10.11591/ijeecs.v36.i3.pp1731-1738
- Asghar, R., Kumar, S., Hynds, P., & Shaukat, A. (2023). Classification of White Blood Cells Using Machine and Deep Learning Models: A Systematic Review. *arXiv* preprint arXiv:2308.06296. https://arxiv.org/abs/2308.06296
- Caballé-Cervigón, N., Castillo-Sequera, J. L., Gómez-Pulido, J. A., Gómez-Pulido, J. M., & Polo-Luque, M. L. (2020). Machine Learning Applied to Diagnosis of Human Diseases: A Systematic Review. *Applied Sciences*, 10(15), 5135. https://doi.org/10.3390/app10155135
- Financial Times. (2024, November 7). The doctors pioneering the use of AI to improve outcomes for patients. https://www.ft.com/content/2fd63023-ec0a-421c-9abb-b6c8000b3b51
- Gavas, E., & Olpadkar, K. (2021). Deep CNNs for Peripheral Blood Cell Classification. *arXiv* preprint arXiv:2110.09508. https://arxiv.org/abs/2110.09508



- Merino, A., Puigví, L., Boldú, L., Alférez, S., & Rodellar, J. (2018). Optimizing morphology through blood cell image analysis. *International Journal of Laboratory Hematology*, 40(S1), 54–61. https://doi.org/10.1111/ijlh.12832
- Mondal, S. K., Talukder, M. S. H., Aljaidi, M., Sulaiman, R. B., Tushar, M. M. S., & Alsuwaylimi, A. A. (2024). BloodCell-Net: A lightweight convolutional neural network for the classification of all microscopic blood cell images of the human body. *arXiv preprint* arXiv:2405.14875. https://arxiv.org/abs/2405.14875
- O'Shea, D. (2024, January 15). AI can help solve global shortage of pathologists. *The Times*. https://www.thetimes.co.uk/article/ai-can-help-solve-global-shortage-of-pathologists-9mwc3fp6m
- Pothineni, S. (2024). Revolutionizing Blood Cell Analysis: The Emergence of EfficientNetB7-Enhanced Deep Learning Models. *International Journal of Artificial Intelligence Research and Development*, 2(1), 27–39. https://iaeme.com/Home/article_id/IJAIRD_02_01_003
- Sajda, P. (2006). Machine Learning for Detection and Diagnosis of Disease. *Annual Review of Biomedical Engineering*, 8, 537–565. https://doi.org/10.1146/annurev.bioeng.8.061505.095802



Combined Effects of Triaxiality, Oblateness, Radiation Pressure, P-R Drag and Stokes Drag on the Existence of Triangular Equilibrium Points in the Elliptic Restricted Three-Body Problem

Aminu Abubakar Hussain 1 & Aishetu Umar 2

¹Department of Mathematical Sciences, Faculty of Physical Sciences, Federal University, Dutsin-Ma, Nigeria.

²Department of Mathematics, Faculty of Physical Science, Ahmadu Bello University, Zaria, Nigeria.

E-mail: ¹aahussain@fudutsinma.edu.ng

ABSTRACT

In this paper, locations of triangular equilibrium points $L_{4,5}$ in the neighbourhood of QS Virginis are investigated both analytically and numerically on an account of radiation pressure and P-R drag of the participating bodies, triaxiality of the primary, oblateness of the secondary and Stokes drag. It is observed that, the coordinates of the triangular equilibrium points $L_{4,5}$ are influenced by triaxiality coefficients of the primary, oblateness coefficient of the secondary, radiation pressure factors and P-R drag of the dominant bodies and Stokes drag of the system.

Keywords: Celestial Mechanics; Restricted Three-Body Problem; Equilibrium Points; QS Virginis.

1. Introduction

The restricted three-body problem (R3BP) is a classical model in celestial mechanics that describes the motion of an infinitesimal particle under the gravitational attraction of two larger bodies, called primaries, which orbit their common center of mass. The particle's mass is so small that it does not affect the motion of the primaries. Depending on the shape of the primary orbits, the model is classified as the circular restricted three-body problem (CR3BP) when the orbits are circular, or the elliptic restricted three-body problem (ER3BP) when the orbits are elliptical. Despite its simplicity, the R3BP reveals rich dynamical structures and has five notable equilibrium solutions: three collinear points lying along the line connecting the primaries, and two triangular points forming equilateral triangles with the primaries Szebehely (1967). Routh (1875) established the stability condition for these triangular points, showing that stability depends on the system's mass ratio. Szebehely (1967) later confirmed that collinear points are generally unstable, while triangular points are conditionally stable if the mass ratio remains below a certain critical value. Over the years, many researchers have extended the R3BP to account for additional physical effects in order to model real astrophysical systems more accurately. One such effect is radiation pressure, the force exerted by light from luminous bodies. This force, can shift equilibrium point locations and influence their stability. Early studies by Poynting (1903) and Radzievskii (1950) showed that small dust particles near luminous bodies such as the Sun are strongly affected by radiation pressure. Later work (Simmons et al., 1985; Kumar & Choudhry, 1986; Singh & Ishwar, 1999) demonstrated that radiation pressure can reduce the stability region of triangular equilibrium points and, in certain cases, even make the inner collinear point stable when both primaries emit radiation.

Another important refinement comes from recognizing that real celestial bodies are not perfectly spherical. Many are oblate (flattened at the poles) or triaxial (with three unequal axes), leading to deviations in their gravitational fields. Such asphericity produces additional perturbations that



affect the positions and stability of equilibrium points. Researches by Khanna & Bhatnagar (1999), Sharma *et al.* (2001), Kumar *et al.*, (2024) and others have shown that oblateness and triaxiality can destabilize triangular equilibrium points or change their oscillatory behavior, especially when combined with other effects such as radiation pressure.

In addition to gravitational and radiative influences, dissipative forces play a key role in shaping orbital dynamics. The P-R drag arises when a particle absorbs and re-emits radiation, resulting in a gradual loss of angular momentum and a slow inward spiral toward the luminous body. Robertson (1937) refined Poynting's original theory, showing that even small particles such as cosmic dust can be swept into the Sun over cosmically short timescales. Studies in the R3BP framework (Ishwar & Kushvah, 2006; Mishra *et al.*, 2016; Singh & Amuda, 2019; Kaur *et al.*, 2022; Singh & Ashagwu, 2024) have shown that P-R drag generally shifts triangular point positions and often destabilizes them in both linear and nonlinear senses. Another dissipative mechanism is Stokes drag, which occurs when a particle moves through a gaseous medium and experiences resistance from molecular collisions. This force has been examined in both planar and spatial versions of the R3BP (Jain & Aggarwal, 2015; Idrisi *et al.*, 2016), where it was found to alter equilibrium point positions and in most cases affect stability.

Given the significance of these various perturbative effects, recent research has begun exploring their combined influence on the dynamics of equilibrium points. However, studies that integrate triaxiality, oblateness, radiation pressure, P-R drag, and Stokes drag together especially in the context of the elliptic restricted three-body problem remain limited. Each of these effects individually has been shown to alter the geometry and stability of triangular equilibrium points, but their interplay in a single, unified model has not been widely analyzed.

In this research, we generalize ER3BP framework that incorporates the effects of: the triaxiality of the larger primary; the oblateness of the smaller primary; radiation pressure of the primary bodies; P-R drag and Stokes drag simultaneously. Using both analytical derivations and numerical simulations, we examine the resulting shifts in the positions of the triangular equilibrium points. Our study applies this model to the binary system QS Virginis, revealing the degree to which each physical factor contributes to the dynamics of the triangular points and highlighting the combined impact of multiple perturbations on equilibrium configurations.

This paper is organized as follows: Section 2 deals with the modified equations of motion; Section 3, contains the positions of triangular equilibrium points. While Sections 4 and 5 contains numerical application and discussion respectively.

2. Modified equations of motion

The modified equations of motion of an infinitesimal particle in the frame of ER3BP, taking in to account triaxiality of the bigger primary and oblateness of the smaller primary together with the radiation pressure factors and P–R drag of both primary bodies with the additional influence of Stokes drag of the system in a dimensionless-pulsating (rotating) coordinate system ($\xi - \eta$) takes the following form (Murray and Dermott, 1999; Celletti *et al.* 2011; Singh and Umar, 2012; Abd El-Salam, 2018; Chakraborty and Narayan, 2018; Singh and Amuda, 2019):

$$\xi'' - 2\eta' = U_{\xi},$$

$$\eta'' + 2\xi' = U_{\eta}.$$
(1)

Where U is the modified potential-like function, and we define $U_{\xi} \ \& \ U_{\eta} \$ as:



$$U_{\xi} = \frac{\partial \Omega}{\partial \xi} + F_{\xi S} - F_{\xi PR},$$

(2)

$$U_{\eta} = \frac{\partial \Omega}{\partial \eta} + F_{\eta S} - F_{\eta PR},$$

with

$$\begin{split} \Omega = & \left(1 - e^2\right)^{-1/2} \left[\frac{\xi^2 + \eta^2}{2} + \frac{1}{n^2} \left\{ \frac{\left(1 - \mu\right)q_1}{r_1} + \frac{\left(1 - \mu\right)q_1(2\sigma_1 - \sigma_2)}{2r_1^3} - \frac{3\left(1 - \mu\right)q_1(\sigma_1 - \sigma_2)\eta^2}{2r_1^5} \right. \\ & \left. + \frac{\mu q_2}{r_2} + \frac{\mu B_1 q_2}{2r_2^3} \right\} \right], \end{split}$$

where r_1 and r_2 are the distances of an infinitesimal particle from the bigger primary and smaller primary respectively and are defined as:

$$r_{1} = \left(\left(\xi + \mu \right)^{2} + \eta^{2} \right)^{\frac{1}{2}},$$

$$r_{2} = \left(\left(\xi + \mu - 1 \right)^{2} + \eta^{2} \right)^{\frac{1}{2}}.$$
(3)

While e is the eccentricity of the orbits of the primary bodies, q_1 and q_2 are the radiation pressure factors of the bigger primary and smaller primary respectively, σ_i (i = 1, 2) and B_1 represent the triaxiality coefficients of the bigger primary and oblateness coefficient of the smaller primary respectively, μ is the ratio of the mass of the smaller primary to the total mass of the primaries

i.e. $\mu = \frac{m_2}{m_1 + m_2}$, and n is the perturbed mean motion of the primary bodies and is defined as

$$n^2 = 1 + \frac{3}{2}(2\sigma_1 - \sigma_2) + \frac{3B_1}{2}.$$
(4)

 $F_{\xi S}$ and $F_{\eta S}$ are the Stokes forces defined by

$$F_{\xi S} = -\frac{\left(1 - e^2\right)^{-1/2}}{n^2} \kappa \left(\xi' - \eta + \alpha_k S_{\eta}(r)\right),$$
(5)

$$F_{\eta S} = -\frac{\left(1 - e^2\right)^{-1/2}}{n^2} \kappa \left(\eta' + \xi - \alpha_k S_{\xi}(r)\right),$$

where $\kappa \in [0, 1)$ is the dissipative constant, depending on several physical parameters (Beange and Fewaz-Mello, 1993) like the viscosity of the gas, the radius and the mass of the particle; $S = S(r) \equiv r^{-\frac{3}{2}}$ is the Keplerian angular velocity at distance $r = \sqrt{\xi^2 + \eta^2}$ from the origin of the synodic frame and $\alpha_k \in [0, 1)$ is the ratio between the gas and Keplerian velocities (Murray, 1994). $F_{\xi PR}$ and $F_{\eta PR}$ are the P-R drag and stellar wind forces defined by:





$$F_{\xi PR} = \frac{\left(1 - e^2\right)^{-1/2}}{n^2} \left\{ \frac{W_1}{r_1^2} N_1 + \frac{W_2}{r_2^2} \, \overline{Q}_1 \right\},\,$$

(6)

$$F_{\eta PR} = \frac{\left(1 - e^2\right)^{-1/2}}{n^2} \left\{ \frac{W_1}{r_1^2} N_2 + \frac{W_2}{r_2^2} N_2 \overline{Q}_2 \right\},\,$$

$$N_{1} = \frac{(\xi + \mu) \left[(\xi + \mu) \xi' + \eta \eta' \right]}{r_{1}^{2}} + \xi' - n\eta,$$

$$N_{2} = \frac{\eta \left[(\xi + \mu)\xi' + \eta \eta' \right]}{r_{1}^{2}} + \eta' + n(\xi + \mu),$$

$$\bar{Q}_{1} = \frac{(\xi + \mu - 1)[(\xi + \mu - 1)\xi' + \eta \eta']}{r_{2}^{2}} + \xi' - n\eta,$$

$$\bar{Q}_2 = \frac{\eta \left[(\xi + \mu - 1)\xi' + \eta \eta' \right]}{r_2^2} + \eta' + n(\xi + \mu - 1),$$

while, W_1 and W_2 are the P-R drag parameters of the bigger and smaller primary respectively and are defined by

$$W_1 = \frac{(1-\mu)(1-q_1)}{c_d},$$

$$W_2 = \frac{\mu(1-q_2)}{c_d},$$

while c_d is the dimensionless speed of light.

3. Locations of triangular equilibrium points

The triangular equilibrium points of an infinitesimal particle are the solution of equation $\xi' = \eta' = \xi'' = \eta'' = 0$ with $\xi \neq 0$, $\eta \neq 0$ and $\zeta = 0$ in the equations of motion (1) i.e. they are solutions of the equations $\,U_{\xi}=U_{\eta}=0$, and thus these resulting in

$$\xi n^{2} - \frac{(1-\mu)(\xi+\mu)q_{1}}{r_{1}^{3}} - \frac{3(1-\mu)(\xi+\mu)(2\sigma_{1}-\sigma_{2})q_{1}}{2r_{1}^{5}} + \frac{15(1-\mu)(\xi+\mu)(\sigma_{1}-\sigma_{2})\eta^{2}q_{1}}{2r_{1}^{7}} - \frac{\mu(\xi+\mu-1)q_{2}}{r_{2}^{3}} - \frac{3\mu(\xi+\mu-1)q_{2}B_{1}}{2r_{2}^{5}} + \frac{W_{1}n\eta}{r_{1}^{2}} + \frac{W_{2}n\eta}{r_{2}^{2}} + \kappa\eta\left(1 + \frac{3\alpha}{2}(\xi^{2}+\eta^{2})^{-\frac{7}{4}}\right) = 0,$$
(7)



$$n^{2}\eta - \frac{(1-\mu)q_{1}\eta}{r_{1}^{3}} - \frac{3(1-\mu)(4\sigma_{1}-3\sigma_{2})q_{1}\eta}{2r_{1}^{5}} + \frac{15(1-\mu)(\sigma_{1}-\sigma_{2})q_{1}\eta^{3}}{2r_{1}^{7}} - \frac{\mu q_{2}\eta}{r_{2}^{3}} - \frac{3\mu\eta q_{2}B_{1}}{2r_{2}^{5}} - \frac{W_{1}n(\xi+\mu)}{r_{1}^{2}} - \frac{W_{2}n(\xi+\mu-1)}{r_{2}^{2}} - \kappa\xi\left(1 + \frac{3\alpha}{2}(\xi^{2}+\eta^{2})^{-\frac{7}{4}}\right) = 0.$$
(8)

Equation (8) can be re-writte

$$\left[n^{2} - \frac{(1-\mu)q_{1}}{r_{1}^{3}} - \frac{3(1-\mu)(4\sigma_{1} - 3\sigma_{2})q_{1}}{2r_{1}^{5}} + \frac{15(1-\mu)(\sigma_{1} - \sigma_{2})q_{1}\eta^{2}}{2r_{1}^{7}} - \frac{\mu q_{2}}{r_{2}^{3}} - \frac{3\mu q_{2}B_{1}}{2r_{2}^{5}} \right] \eta$$

$$= \frac{W_{1}n(\xi + \mu)}{r_{1}^{2}} + \frac{W_{2}n(\xi + \mu - 1)}{r_{2}^{2}} + \kappa \xi \left(1 + \frac{3\alpha}{2}(\xi^{2} + \eta^{2})^{-\frac{7}{4}}\right).$$
(9)

Multiplying equations (7) and (8) by η and $(\xi + \mu)$ respectively, we obtain

$$\begin{split} &\xi\eta n^{2} - \frac{(1-\mu)(\xi+\mu)\eta q_{1}}{r_{1}^{3}} - \frac{3(1-\mu)(\xi+\mu)(2\sigma_{1}-\sigma_{2})\eta q_{1}}{2r_{1}^{5}} + \frac{15(1-\mu)(\xi+\mu)(\sigma_{1}-\sigma_{2})\eta^{3}q_{1}}{2r_{1}^{7}} \\ &- \frac{\mu(\xi+\mu-1)\eta q_{2}}{r_{2}^{3}} - \frac{3\mu(\xi+\mu-1)\eta q_{2}B_{1}}{2r_{2}^{5}} + \frac{W_{1}n\eta^{2}}{r_{1}^{2}} + \frac{W_{2}n\eta^{2}}{r_{2}^{2}} + \kappa\eta^{2} \left(1 + \frac{3\alpha}{2}(\xi^{2}+\eta^{2})^{-\frac{7}{4}}\right) = 0, \\ &n^{2}(\xi+\mu)\eta - \frac{(1-\mu)(\xi+\mu)q_{1}\eta}{r_{1}^{3}} - \frac{3(1-\mu)(\xi+\mu)(4\sigma_{1}-3\sigma_{2})q_{1}\eta}{2r_{1}^{5}} + \frac{15(1-\mu)(\xi+\mu)(\sigma_{1}-\sigma_{2})q_{1}\eta^{3}}{2r_{1}^{7}} \\ &- \frac{\mu(\xi+\mu)q_{2}\eta}{r_{2}^{3}} - \frac{3\mu(\xi+\mu)\eta q_{2}B_{1}}{2r_{2}^{5}} - \frac{W_{1}n(\xi+\mu)^{2}}{r_{1}^{2}} - \frac{W_{2}n(\xi+\mu-1)(\xi+\mu)}{r_{2}^{2}} \\ &- \kappa\xi(\xi+\mu)\left(1 + \frac{3\alpha}{2}(\xi^{2}+\eta^{2})^{-\frac{7}{4}}\right) = 0. \end{split}$$

Subtracting equation (11) from equation (10) we get

$$n^{2} = \frac{q_{2}}{r_{2}^{3}} + \frac{3B_{1}q_{2}}{2r_{2}^{5}} + \frac{3(1-\mu)(\xi+\mu)(\sigma_{1}-\sigma_{2})q_{1}}{\mu r_{1}^{5}} + \frac{W_{1}n}{\mu\eta} + \frac{W_{2}n\eta}{\mu r_{2}^{2}} + \frac{W_{2}n}{\mu\eta r_{2}^{2}} (\xi+\mu-1)(\xi+\mu) + \frac{\kappa\eta}{\mu} \left(1 + \frac{3\alpha}{2}(\xi^{2}+\eta^{2})^{-\frac{7}{4}}\right) + \frac{\kappa\xi}{\mu\eta} (\xi+\mu) \left(1 + \frac{3\alpha}{2}(\xi^{2}+\eta^{2})^{-\frac{7}{4}}\right).$$
(12)

$$n^{2} = \frac{q_{1}}{r_{1}^{3}} + \frac{3(4\sigma_{1} - 3\sigma_{2})q_{1}}{2r_{1}^{5}} - \frac{3(\sigma_{1} - \sigma_{2})(\xi + \mu)q_{1}}{r_{1}^{5}} - \frac{15(\sigma_{1} - \sigma_{2})\eta^{2}q_{1}}{2r_{1}^{7}} + \frac{W_{1}n(\xi + \mu)}{r_{1}^{2}\eta(1 - \mu)} - \frac{W_{1}n}{\eta(1 - \mu)} + \frac{W_{2}n(\xi + \mu - 1)}{r_{2}^{2}\eta(1 - \mu)} - \frac{W_{2}n(\xi + \mu - 1)(\xi + \mu)}{r_{2}^{2}\eta(1 - \mu)} - \frac{W_{2}\eta}{r_{2}^{2}\eta(1 - \mu)} + \frac{\kappa\xi}{\eta(1 - \mu)} \left(1 + \frac{3\alpha}{2}(\xi^{2} + \eta^{2})^{-\frac{7}{4}}\right) - \frac{\kappa\eta}{(1 - \mu)} \left(1 + \frac{3\alpha}{2}(\xi^{2} + \eta^{2})^{-\frac{7}{4}}\right) - \frac{\kappa\xi(\xi + \mu)}{\eta(1 - \mu)} \left(1 + \frac{3\alpha}{2}(\xi^{2} + \eta^{2})^{-\frac{7}{4}}\right).$$
(13)

(13)



In the absence of the radiation pressure factors $(q_1=q_2=1)$, oblateness coefficient $(B_1=0)$, triaxiality coefficients $(\sigma_1=\sigma_2=0)$, P-R drag $(W_1=W_2=0)$ and stokes drag $(k=\alpha=0)$, the solutions of equations (12) and (13) are $r_1=r_2=1$. Then, considering the above parameters, the solutions of equations (12) and (13) would change slightly by

$$r_1 = 1 + \varepsilon_1,$$

$$r_2 = 1 + \varepsilon_2,$$
(14)

where $\varepsilon_i(i=1, 2) \square 1$.

Substituting equations (14) in equations (12) and (13) by putting $q_1 = 1 - \alpha_1$ and $q_2 = 1 - \alpha_2$ (where $\alpha_1 \Box 1$ and $\alpha_2 \Box 1$) together with help of equation (4), we obtain the series equations in terms of α_1 , α_2 and $\varepsilon_i (i = 1, 2)$. Solving these equations by restricting ourselves only to the linear terms in α_1 , α_2 and $\varepsilon_i (i = 1, 2)$ we have

$$\varepsilon_{1} = -\frac{\alpha_{1}}{3} - \frac{B_{1}}{2} - \frac{11}{8} \sigma_{1} + \frac{11}{8} \sigma_{2} - \frac{W_{1}}{3\sqrt{3}(1-\mu)} - \frac{2W_{2}}{3\sqrt{3}(1-\mu)} - \frac{\kappa}{3\sqrt{3}(1-\mu)} - \frac{\kappa}{3\sqrt{3}} \left(\frac{1}{3(1-\mu)} + \frac{\mu}{3(1-\mu)} + \frac{\alpha}{2(1-\mu)} + \frac{11\mu\alpha}{8(1-\mu)} \right),$$

$$\varepsilon_{2} = -\frac{\alpha_{2}}{3} + \left(\frac{1}{2\mu} - \frac{3}{2} \right) \sigma_{1} + \left(-\frac{1}{2\mu} + 1 \right) \sigma_{2} + \frac{2W_{1}}{3\sqrt{3}\mu} + \frac{W_{2}}{3\sqrt{3}\mu} + \frac{\kappa}{\sqrt{3}} \left(\frac{2}{3\mu} - \frac{1}{3} + \frac{\alpha}{\mu} + \frac{5\alpha}{4} \right).$$
(15)

Substituting equations (15) in equations (14) we have

$$r_{1} = 1 - \frac{\alpha_{1}}{3} - \frac{B_{1}}{2} - \frac{11}{8}\sigma_{1} + \frac{11}{8}\sigma_{2} - \frac{W_{1}}{3\sqrt{3}(1-\mu)} - \frac{2W_{2}}{3\sqrt{3}(1-\mu)}$$

$$- \frac{\kappa}{\sqrt{3}} \left(\frac{1}{3(1-\mu)} + \frac{\mu}{3(1-\mu)} + \frac{\alpha}{2(1-\mu)} + \frac{11\mu\alpha}{8(1-\mu)} \right),$$

$$r_{2} = 1 - \frac{\alpha_{2}}{3} + \left(\frac{1}{2\mu} - \frac{3}{2} \right) \sigma_{1} + \left(-\frac{1}{2\mu} + 1 \right) \sigma_{2} + \frac{2W_{1}}{3\sqrt{3}\mu} + \frac{W_{2}}{\sqrt{3}} + \frac{\kappa}{\sqrt{3}} \left(\frac{2}{3\mu} - \frac{1}{3} + \frac{\alpha}{\mu} + \frac{5\alpha}{4} \right). \quad (16)$$

Using $r_1^2 = (\xi + \mu)^2 + \eta^2 \& r_2^2 = (\xi + \mu - 1)^2 + \eta^2$ defined in equations (3), then the exact solutions of the triangular points $L_{4.5}$ are

$$\xi = \frac{1}{2} - \mu + \frac{1}{2} \left(r_1^2 - r_2^2 \right),$$

$$\eta = \pm \sqrt{\frac{r_1^2 + r_2^2}{2} - \left(\frac{r_2^2 - r_1^2}{2} \right)^2 - \frac{1}{4}}.$$
(17)

Substituting equation (16) in (17) we obtain



$$\xi = \frac{1}{2} - \mu - \frac{\alpha_1}{3} - \frac{\alpha_2}{3} + \left(\frac{1}{8} - \frac{1}{2\mu}\right) \sigma_1 + \left(\frac{3}{8} + \frac{1}{2\mu}\right) \sigma_2 - \frac{B_1}{2} - \frac{W_1(2-\mu)}{3\sqrt{3}\mu(1-\mu)} - \frac{W_2(1+\mu)}{3\sqrt{3}\mu(1-\mu)}$$

$$-\frac{\kappa}{\sqrt{3}} \left(\frac{1}{3(1-\mu)} + \frac{\mu}{3(1-\mu)} + \frac{\alpha}{2(1-\mu)} + \frac{11\mu\alpha}{8(1-\mu)}\right) - \frac{\kappa}{\sqrt{3}} \left(\frac{2}{3\mu} - \frac{1}{3} + \frac{\alpha}{\mu} + \frac{5\alpha}{4}\right),$$

$$\eta = \pm \frac{\sqrt{3}}{2} \left[1 - \frac{2}{9}(\alpha_1 + \alpha_2) + \frac{2}{3}\left(-\frac{23}{8} + \frac{1}{2\mu}\right)\sigma_1 + \frac{2}{3}\left(\frac{19}{8} - \frac{1}{2\mu}\right)\sigma_2 - \frac{B_1}{3} + \frac{2W_1(2-3\mu)}{9\sqrt{3}\mu(1-\mu)} + \frac{2W_2(1-3\mu)}{9\sqrt{3}\mu(1-\mu)} - \frac{2\kappa}{3\sqrt{3}}\left(\frac{1}{3(1-\mu)} + \frac{\mu}{3(1-\mu)} + \frac{\alpha}{2(1-\mu)} + \frac{11\mu\alpha}{8(1-\mu)}\right)$$

$$+ \frac{2\kappa}{3\sqrt{3}}\left(\frac{2}{3\mu} - \frac{1}{3} + \frac{\alpha}{\mu} + \frac{5\alpha}{4}\right).$$
(18)

Hence equations (18) are the required locations of the triangular equilibrium points $L_{4,5}$ denoted by $(\xi, \pm \eta)$.

4. Numerical Application

The astrophysical data of QS Virginis are borrowed from SIMBAD and O'Donoghue *et al.* (2003) for the purpose of numerical computation in this section.

The masses of the bigger and smaller primary of the QS Virginis are $m_1 \square 0.78 M_{\square}$ and $m_2 \square 0.43 M_{\square}$ respectively, therefore the mass ratio of QS Virginis is given by $\mu \square 0.355372$. The luminosities of the bigger and smaller primary of QS Virginis are $L_1 \square 0.0044 L_1$ and $L_2 \square 0.015 L_1$ respectively, while the dimensionless speed of light is given by $C_d \square 684.734$. Also, the radiation pressure factors of the bigger and smaller primary for the QS Virginis are defined by $q_1 = 1 - \alpha_1$ and $q_2 = 1 - \alpha_2$ respectively and $\alpha_1, \alpha_2 \square 1$, where α_1 and α_2 are the radiation pressure coefficients of the bigger and smaller primary respectively.

The effects of the various parameters involved in the coordinates (18) of triangular equilibrium points of QS Virginis are presented in Table 1 as:

Table 1: Effects of perturbations on the locations of $L_{4,5}$ of the QS Virginis system

Cases	$\alpha_{_{1}}$	α_2	$\sigma_{_{1}}$	$\sigma_{_2}$	B_{1}	ξ	$\pm\eta$
1	0	0	0	0	0	0.144628	0.866025
2	0.001	0.045	0	0	0	0.129934	0.857175
	0.101	0.125	0	0	0	0.136335	0.822596
	0.201	0.205	0	0	0	0.142735	0.788017
3	0.001	0.045	0.00034	0.00017	0.0025	0.128551	0.856261
	0.101	0.125	0.0034	0.0017	0.025	0.122505	0.813448
	0.201	0.205	0.034	0.017	0.25	0.004442	0.696532



5. Discussion

The modified equations of motion of an infinitesimal mass in the framework of the ER3BP under the combined effects of triaxiality of the bigger primary and oblateness of the smaller primary together with the radiation pressure factors and P-R drag of both primary bodies with the additional influence of Stokes drag are given by equations (1)-(6). Observed that, these modified equations of motion of an infinitesimal mass are influenced by these aforementioned perturbing forces. Nevertheless, the modified equations of motion (1)-(6) are in conformity with: classical of (1967)if the aforementioned perturbations Szebehely relaxed $\sigma_i(i=1, 2) = B_1 = 0$, $q_1 = q_2 = 1$ and $e = F_{\eta S} = F_{\eta PR} = F_{\xi S} = F_{\xi PR} = 0$); Singh and Simeon (2017) in circular case when all the perturbing forces are ignored except P-R drag of the bigger primary and radiation pressure factors of both primaries in both works; and Idrisi and Ullah (2020) in circular case also, when all the perturbing forces are ignored except Stokes drag and radiation pressure of the bigger primary in both works.

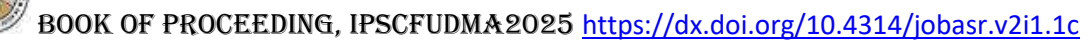
The required coordinates of the triangular equilibrium points $L_{4,5}$ denoted by $(\xi, \pm \eta)$ are given by equations (18). It is observed that, these coordinates are influenced by: triaxiality coefficients of the bigger primary; oblateness coefficient of the smaller primary; radiation pressure factors; P-R drag of both primary bodies; and Stokes drag of the system. These triangular equilibrium points L_{45} are in conformity with: classical case of Szebehely (1967) if the perturbation forces under consideration are neglected in the present work (i.e. $\sigma_i(i=1, 2) = B_1 = 0$, $q_1 = q_2 = 1$ and $e = F_{nS} = F_{nPR} = F_{ES} = F_{EPR} = 0$); Singh and Simeon (2017) in circular case when all the perturbing forces are relaxed except P-R drag of the bigger primary and radiation pressure factors of both primaries in both works; and Idrisi and Ullah (2020) in circular case also, when all the perturbing forces are relaxed except Stokes drag and radiation pressure of the bigger primary in both works. It should be noted from Table 1 that, the pair points (ξ , $\pm \eta$) corresponds to triangular equilibrium points $L_{4,5}$ in the presence of the perturbing parameters under consideration. This show that, the perturbing parameters under consideration have an effects on $L_{4.5}$. It is observed from Table 1 that, Case 1 shows classical $L_{4,5}$ of QS Virginis, while Case 2 reveals that, simultaneous increases in the radiation pressure coefficients α_1 and α_2 of the bigger and smaller primaries respectively, cause $L_{4.5}$ to move towards the smaller primary and the line joining the primaries. Also, Case 3 shows that, simultaneous increases in triaxiality coefficients σ_1 and σ_2 of the bigger primary, oblateness coefficient B_1 of the bigger primary and radiation pressure coefficients α_1 and α_2 of both primaries causes $L_{4,5}$ to move away from the smaller primary and towards the line joining the primary bodies.

References

- Abd El-Salam, F. A. (2018). Stability of the triangular points in the photogravitational elliptic RTBP with dissipations. *New Astronomy*, https://doi.org/10.1016/j.newast.2018.10.005.
- Beauge, C. and Ferraz-Mello, S. (1993). Resonance trapping in the primordial solar nebula: The case of a Stokes drag dissipation. *Icarus*, 103, 301-318.
- Celletti, A. *et al.* (2011). Some results on the global dynamics of the regularized restricted three-body problem with dissipation. *Celestial Mechanics and Dynamical Astronomy*, 109, 265-284. http://dx.doi.org/10.1007/s10569-010-9326-y
- Chakraborty, A. and Narayan, A. (2018). Effect of stellar wind and Poynting–Robertson drag on photogravitational elliptic restricted three-body problem. *Solar System Research*, 52(2), 168–179.
- Idrisi, M. J. and Ullah, M. S. (2020). A study of non-collinear libration points under the combined effects of radiation pressure and Stokes drag, *New Astronomy*, https://doi.org/10.1016/j.newast.2020.101441.
- Idrisi, M. J. and Jain, M (2016). Restricted three-body problem with Stokes drag effect when less massive primary is an ellipsoid. *International Journal of Advanced Astronomy*, 4 (1), 61-67.
- Ishwar, B., and Kushvah, B. S. (2006). Linear stability of triangular equilibrium points in the generalized photogravitational restricted three-body problem with Poynting-Robertson drag. *Journal of Dynamical Systems and Geometric Theories*, 4, 79-86.
- Jain, M. and Aggarwal, R. (2015). Restricted three-body problem with Stokes drag effect. *International Journal of Astronomy and Astrophysics*, 5, 95-105. http://dx.doi.org/10.4236/ijaa.2015.52013.
- Kaur, R., Aggarwal, R., and Aggarwal, S. (2022). Instability of triangular equilibrium points in the restricted three-body problem under effects of circumbinary disc, radiation pressure, and Poynting–Robertson drag. *Earth, Moon, and Planets,* 126(1), 1–15. https://doi.org/10.1007/s11038-021-09543-1
- Khanna, M. and Bhatnagar, K.B. (1999). Existence and stability of libration points in the restricted three body problem when the smaller primary is a triaxial rigid body and the bigger one an oblate sheriods, *Indian Journal of Pure and Applied Mathematics*. 30(7), 721-733.
- Kumar, R., Singh, J., and Sharma, R. (2024). Impact of triaxiality and mass variations on motion around triangular equilibrium points of the restricted three-body problem. *Astronomy Reports*, 68(11), 1119–1143. https://doi.org/10.1134/S1063772924700975
- Kumar, V. and Choudhry, R.K. (1990). Nonlinear stability of the triangular libration points for the photogravitational elliptic restricted problem of three bodies. *Celestial Mechanics and Dynamical Astronomy*, 48(4), 299-317.
- Mishra, K., Sharma, J.P. and Ishwar, B. (2016). Stability of triangular equilibrium points in the photogravitational elliptic restricted three-body problem with Poynting-Robertson drag. *International Journal of Advanced Astronomy*, 4 (1), 33-38.
- Murray, C. D. (1994). Dynamical effects of drag in the circular restricted three-body problem: Location and stability of the Lagrangian equilibrium points. *Icarus*. 112, 465-484.



- Murray, C. D. and Dermott, S. F. (1999). *Solar System Dynamics*. Cambridge University Press, Cambridge, England.
- O'Donoghue, D. *et al.* (2003). The DA+dMe eclipsing binary EC13471-1258: its cup runneth over...just. *Monthly Notices of the Royal Astronomical Society.* 345(2), 506-528.
- Poynting, J. H. (1903). Radiation in the solar system: its effect on temperature and its pressure on small bodies. *Monthly Notices of the Royal Astronomical Society*, 64, 525-552.
- Radzievskii, V. V. (1950). The restricted problem of three bodies taking account of light pressure. *Astronomical Zhurnal*, 27(2), 250-256.
- Robertson, H. P. (1937). Dynamical effects of radiation in the solar system. *Monthly of the Royal Astronomical Society*, 97, 423-438.
- Routh, E. J. (1875). On Laplace's three particle, with a supplement on the stability of motion. *Proceedings of the London Mathematical Society*, 6, 86.
- Sharma, R.K., Taqvi, Z.A. and Bhatnagar, K.B. (2001). Existence and stability of libration points in the restricted three-body problem when the primaries are triaxial rigid bodies and source of radiations. *Indian Journal of Pure and Applied Mathematics*, 32(7), 981-994.
- Simmons, J. F. L., McDonald, A. J. C. and Brown, J. C. (1985). The restricted three-body problem with radiation pressure. *Celestial Mechanics*, 35, 145.
- Singh, J. and Amuda, T. O. (2019). Stability analysis of triangular equilibrium points in restricted three-body problem under effects of circumbinary disc, radiation and drag forces. *Journal Atrophysics and Astronomy*, 40(5), 1-14.
- Singh, J. and Ishwar, B. (1999). Stability of triangular points in the generalised photogravitational restricted three-body problem. *Bulletin of the Astronomical Society of India*. 27, 415-424.
- Singh, J. and Simeon, A. M. (2017). Motion around the triangular equilibrium points in the circular restricted three-body problem under triaxial luminours primaries with Poynting-Robertson drag. *International Frontier Science Letters*, 12, 1-21.
- Singh, J. and Umar, A. (2012). Motion in the Photogravitational elliptic restricted three-body problem under an oblate primary. *The Astronomical Journal*, 143, 109-131.
- Singh, J., and Ashagwu, B. S. (2024). Combined effect of Poynting-Robertson drag, oblateness, and radiation on the triangular points in the elliptic restricted three-body problem. *Scientific Reports*, 14, 11564.
- Szebehely, V. (1967). *Theory of Orbits*. The restricted problem of three-bodies. Academic Press, New York.



Locations of Out-of-Plane Equilibrium Points in the Photogravitational Elliptic Restricted Three-Body Problem of the Sun-Venus System with Oblateness, Triaxiality and Albedo Aishetu Umar¹ & Aminu Abubakar Hussain²

¹Department of Mathematics, Faculty of Physical Science, Ahmadu Bello University, Zaria, Nigeria.

E-mail: ¹umaraishetu33@yahoo.com ²aahussain@fudutsinma.edu.ng

ABSTRACT

This research deals with the positions of an infinitesimal mass near the $1^{\rm st}$ family of the out-of-plane equilibrium points $L_{6,7}$ of the Sun-Venus system in the elliptic restricted three-body problem under the influence of oblateness and radiation pressure of the bigger primary (the Sun) with triaxiality and albedo of the smaller primary (the Venus). It is seen that the pair of points $(\xi_0, \pm \zeta_0)$ which correspond to the positions of the $1^{\rm st}$ family of the out-of-plane equilibrium points $L_{6,7}$ are affected by these perturbing forces under consideration. However it reveals that, simultaneous increase or decrease of the radiation pressure factor of the bigger primary and albedo factor of the smaller primary have no significant effects on $L_{6,7}$.

Keywords: Celestial Mechanics; Restricted Three-Body Problem; Equilibrium Points; Sun-Venus System.

1. Introduction

The restricted three-body problem (R3BP) describes the motion of a very small object called an infinitesimal mass under the gravitational influence of two much larger bodies, known as primaries. These primaries orbit their common centre of mass in either circular or elliptical paths. The small object is affected by their gravity but does not influence their motion. If the primaries move in circular orbits, the model is called the circular restricted three-body problem (CR3BP). If their orbits are elliptical, it is called the elliptic restricted three-body problem (ER3BP) (Szebehely, 1967).

For decades, scientists have studied the special positions, called equilibrium points, where the infinitesimal mass can remain stationary in a rotating frame of reference. These studies have been done under both Newtonian and relativistic (post-Newtonian) frameworks because of their importance in solar system and stellar dynamics (Radzievskii, 1950; Simmons *et al.*, 1985; Bhatnagar & Hallan, 1998; Singh & Ishwar, 1999; Sharma *et al.*, 2001; and others). Since planetary orbits in reality are elliptical, the ER3BP offers a more accurate description than the CR3BP, inspiring many researchers to explore it with additional physical effects such as oblateness, radiation pressure, and other perturbations (Zimovshchikov & Tkhai, 2004; Singh & Umar, 2012; Hussain *et al.*, 2018; and others).

One important physical property is albedo, which measures the fraction of incoming radiation a celestial body reflects. An albedo of zero means the body absorbs all radiation (a perfect black body), while an albedo of one means it reflects all radiation (a perfect white body). In reality, no planet in our solar system is a perfect black or white body (Idrisi & Ullah, 2018). For example,

²Department of Mathematics, Faculty of Physical Sciences, Federal University Dutsin-Ma, Nigeria.



Jupiter's albedo is about 0.50, meaning it reflects half of the sunlight it receives (Li *et al.*, 2018). While many R3BP studies have ignored albedo, it can significantly affect a body's equilibrium temperature and orbital dynamics. Recent research has started to include it (Pontus *et al.*, 2005; Idrisi, 2017; Alhussain, 2019; and others), showing that it can influence the stability and location of equilibrium points.

A related area of interest is out-of-plane equilibrium points positions located above or below the main orbital plane. First noted by Radzievskii (1950) in Sun-Planet-Particle systems, these points have been studied under various effects, including radiation pressure, oblateness, Poynting–Robertson drag, and albedo (Simmons *et al.*, 1985; Ragos & Zagouras, 1988; Singh & Umar, 2013; Chakraborty & Narayan, 2018; Idrisi & Ullah, 2021). Many results show these points are generally unstable, though their positions can shift depending on the physical parameters involved.

In this work, we extend the study of Idrisi & Ullah (2018) by developing a new ER3BP model for the Sun-Venus system that includes: Oblateness and radiation pressure of the Sun (larger primary) and Triaxiality and albedo of Venus (smaller primary). We focus on locating the first family of out-of-plane equilibrium points under these combined effects.

This article is organized as follows: In section 2 the modified equations of motion are presented; Section 3, contains the positions of out-of-plane equilibrium points. While numerical application and discussion are presented in sections 4 and 5 respectively.

2. Modified equations of motion

The modified equations of motion of an infinitesimal mass in the frame of ER3BP, taking in to account oblateness of the first even zonal harmonic parameter J_2 of the bigger primary and triaxiality of the smaller primary with the radiation and albedo factors of the bigger and smaller primaries respectively in a dimensionless-pulsating (rotating) coordinate system (ξ, η, ζ) are given (following Singh and Umar, 2012; Umar and Hussain, 2016; Idrisi and Ullah, 2018) as: $\xi'' - 2\eta' = \Omega_{\varepsilon}$;

$$\eta'' + 2\xi' = \Omega_{\eta}; \text{ and}$$

$$\zeta'' = \Omega_{\zeta}.$$
 (1)

Where Ω is the modified potential-like function for the out-of-plane equilibrium points (i.e. $\eta = 0$), and is defined by:

$$\begin{split} \Omega = & \left(1 - e^2\right)^{-1/2} \left[\frac{\xi^2 + \eta^2}{2} + \frac{1}{n^2} \left\{ \frac{\left(1 - \mu\right)q_1}{r_1} + \frac{\left(1 - \mu\right)q_1A_1}{2r_1^3} - \frac{3\left(1 - \mu\right)q_1A_1\zeta^2}{2r_1^5} + \frac{\mu q_A}{r_2} + \frac{\mu q_A\left(2\sigma_1' - \sigma_2'\right)}{2r_2^3} \right. \\ & \left. - \frac{3\mu q_A\left(\sigma_1' - \sigma_2'\right)\eta^2}{2r_2^5} - \frac{3\mu q_A\left(\sigma_1' - \sigma_2'\right)\zeta^2}{2r_2^5} \right]. \end{split}$$

(2)

 r_1 and r_2 are the distances of an infinitesimal mass from the bigger primary and smaller primary respectively and are defined as:

$$r_{1} = \left(\left(\xi + \mu \right)^{2} + \eta^{2} + \zeta^{2} \right)^{\frac{1}{2}}; \text{ and}$$

$$r_{2} = \left(\left(\xi + \mu - 1 \right)^{2} + \eta^{2} + \zeta^{2} \right)^{\frac{1}{2}}.$$
(3)



While e is the eccentricity of the orbits of the dominant bodies; q_1 and q_A are the radiation factor of the bigger primary and albedo factor of the smaller primary; A_1 represents the oblateness coefficient of the bigger primary and $\sigma'_i(i=1,2)$ are the triaxiality coefficients of the smaller primary; μ is the ratio of the mass of the smaller primary to the total mass of the primaries i.e.

 $\mu = \frac{m_2}{m_1 + m_2}$; and *n* is the perturbed mean motion of the dominant bodies and is defined by:

$$n^{2} = 1 + \frac{3}{2}A_{1} + \frac{3}{2}(2\sigma_{1}' - \sigma_{2}'). \tag{4}$$

3. Locations of out-of-plane equilibrium points

The solutions of the system $\Omega_{\xi} = \Omega_{\eta} = \Omega_{\zeta} = 0$ when $\xi \neq 0$, $\eta = 0 \& \zeta \neq 0$ given in the equations (1) and (2) represent the positions of the out-of-plane equilibrium points that is

$$\Omega_{\xi} = \left(1 - e^{2}\right)^{-\frac{1}{2}} \left[\xi + \frac{1}{n^{2}} \left\{ -\frac{\left(1 - \mu\right)\left(\xi + \mu\right)q_{1}}{r_{1}^{3}} - \frac{3\left(1 - \mu\right)\left(\xi + \mu\right)q_{1}A_{1}}{2r_{1}^{5}} + \frac{15\left(1 - \mu\right)\left(\xi + \mu\right)q_{1}A_{1}\zeta^{2}}{2r_{1}^{7}} \right. \right. \\
\left. -\frac{\mu\left(\xi + \mu - 1\right)q_{A}}{r_{2}^{3}} - \frac{3\mu\left(\xi + \mu - 1\right)q_{A}\left(2\sigma_{1}' - \sigma_{2}'\right)}{2r_{2}^{5}} + \frac{15\mu\left(\xi + \mu - 1\right)q_{A}\left(2\sigma_{1}' - \sigma_{2}'\right)\zeta^{2}}{2r_{2}^{7}} \right\} \right] = 0, \tag{5}$$

$$\Omega_{\eta} = \left(1 - e^{2}\right)^{-1/2} \left[\eta + \frac{\eta}{n^{2}} \left\{ -\frac{\left(1 - \mu\right)q_{1}}{r_{1}^{3}} - \frac{3\left(1 - \mu\right)q_{1}A_{1}}{2r_{1}^{5}} + \frac{15\left(1 - \mu\right)q_{1}A_{1}\zeta^{2}}{2r_{1}^{7}} - \frac{\mu q_{A}}{r_{2}^{3}} \right. \\
\left. -\frac{3\mu q_{A}\left(4\sigma_{1}' - 3\sigma_{2}'\right)}{2r_{2}^{5}} + \frac{15\mu q_{A}\left(2\sigma_{1}' - \sigma_{2}'\right)\zeta^{2}}{2r_{2}^{7}} + \frac{15\mu q_{A}\left(\sigma_{1}' - \sigma_{2}'\right)\eta^{2}}{2r_{2}^{7}} \right\} \right] = 0$$
(6)

and

$$\Omega_{\zeta} = \left(1 - e^{2}\right)^{-1/2} \left[-\frac{\zeta}{n^{2}} \left\{ \frac{(1 - \mu)q_{1}}{r_{1}^{3}} + \frac{9(1 - \mu)q_{1}A_{1}}{2r_{1}^{5}} - \frac{15(1 - \mu)q_{1}A_{1}\zeta^{2}}{2r_{1}^{7}} + \frac{\mu q_{A}}{r_{2}^{3}} + \frac{9\mu q_{A}(2\sigma_{1}' - \sigma_{2}')}{2r_{2}^{5}} - \frac{15\mu q_{A}(2\sigma_{1}' - \sigma_{2}')\eta^{2}}{2r_{2}^{7}} - \frac{15\mu q_{A}(\sigma_{1}' - \sigma_{2}')\eta^{2}}{2r_{2}^{7}} \right\} = 0.$$
(7)

From equation (6) with $\eta = 0$ we get

$$n^{2} - \frac{(1-\mu)q_{1}}{r_{1}^{3}} - \frac{3(1-\mu)q_{1}A_{1}}{2r_{1}^{5}} + \frac{15(1-\mu)q_{1}A_{1}\zeta^{2}}{2r_{1}^{7}} - \frac{\mu q_{A}}{r_{2}^{3}} - \frac{3\mu q_{A}(4\sigma_{1}' - 3\sigma_{2}')}{2r_{2}^{5}} + \frac{15\mu q_{A}(2\sigma_{1}' - \sigma_{2}')\zeta^{2}}{2r_{2}^{7}} \neq 0.$$

$$(8)$$

Making use of the equation (7) with $\zeta \neq 0$ we have

$$\frac{(1-\mu)q_1}{r_1^3} + \frac{9(1-\mu)q_1A_1}{2r_1^5} - \frac{15(1-\mu)q_1A_1\zeta^2}{2r_1^7} + \frac{\mu q_A}{r_2^3} + \frac{9\mu q_A(2\sigma_1' - \sigma_2')}{2r_2^5} - \frac{15\mu q_A(2\sigma_1' - \sigma_2')\zeta^2}{2r_2^7} = 0.$$
(9)

Here, we let $Q_1 = (1 - \mu)q_1$ and $Q_A = \mu q_A$, then equation (9) becomes



$$\frac{Q_1}{r_1^3} + \frac{9Q_1A_1}{2r_1^5} - \frac{15Q_1A_1\zeta^2}{2r_1^7} + \frac{Q_A}{r_2^3} + \frac{9Q_A\left(2\sigma_1' - \sigma_2'\right)}{2r_2^5} - \frac{15Q_A\left(2\sigma_1' - \sigma_2'\right)\zeta^2}{2r_2^7} = 0,$$
(10)

while equation (5) becomes

$$n^{2}\xi - \frac{Q_{1}(\xi + \mu)}{r_{1}^{3}} - \frac{3Q_{1}(\xi + \mu)A_{1}}{2r_{1}^{5}} + \frac{15Q_{1}(\xi + \mu)A_{1}\zeta^{2}}{2r_{1}^{7}} - \frac{Q_{A}(\xi + \mu - 1)}{r_{2}^{3}} - \frac{3Q_{A}(\xi + \mu - 1)(2\sigma' - \sigma'_{2})}{2r_{2}^{5}} + \frac{15Q_{A}(\xi + \mu - 1)(2\sigma' - \sigma'_{2})\zeta^{2}}{2r_{2}^{7}} = 0.$$

$$(11)$$

Implies that,

$$\begin{split} &\xi \left\{ 1 - \frac{1}{n^2} \left(\frac{Q_1}{r_1^3} + \frac{3Q_1A_1}{2r_1^5} - \frac{15Q_1A_1\zeta^2}{2r_1^7} + \frac{Q_A}{r_2^3} + \frac{3Q_A \left(2\sigma_1' - \sigma_2' \right) B_1}{2r_2^5} - \frac{15Q_A \left(2\sigma_1' - \sigma_2' \right) \zeta^2}{2r_2^7} \right) \right\} \\ &- \frac{\mu}{n^2} \left(\frac{Q_1}{r_1^3} + \frac{3Q_1A_1}{2r_1^5} - \frac{15Q_1A_1\zeta^2}{2r_1^7} + \frac{Q_A}{r_2^3} + \frac{3Q_A \left(2\sigma_1' - \sigma_2' \right) B_1}{2r_2^5} - \frac{15Q_A \left(2\sigma_1' - \sigma_2' \right) \zeta^2}{2r_2^7} \right) \\ &+ \frac{1}{n^2} \left(\frac{Q_A}{r_2^3} + \frac{3Q_A \left(2\sigma_1' - \sigma_2' \right) B_1}{2r_2^5} - \frac{15Q_A \left(2\sigma_1' - \sigma_2' \right) \zeta^2}{2r_2^7} \right) = 0. \end{split}$$

(12)

Making use of equation (10) in the equation (12), we have

$$\xi = \frac{\frac{Q_{1}}{r_{1}^{3}} + \frac{9Q_{1}A_{1}}{2r_{1}^{5}} - \frac{3\mu Q_{1}A_{1}}{r_{1}^{5}} - \frac{15Q_{1}A_{1}\zeta^{2}}{2r_{1}^{7}} + \frac{3(1-\mu)Q_{A}(2\sigma_{1}' - \sigma_{2}')}{2r_{2}^{5}}}{n^{2} + \frac{3Q_{1}A_{1}}{r_{1}^{5}} + \frac{3Q_{A}(2\sigma_{1}' - \sigma_{2}')}{r_{2}^{5}}}.$$
(13)

From equation (10), we have

$$\zeta^{2} = \frac{8r_{1}^{7}r_{2}^{7}}{15(Q_{1}A_{1}r_{2}^{7} + Q_{A}(2\sigma_{1}' - \sigma_{2}')r_{1}^{7})} \left\{ \frac{Q_{1}}{r_{1}^{3}} + \frac{9Q_{1}A_{1}}{2r_{1}^{5}} + \frac{Q_{A}}{r_{2}^{3}} + \frac{9Q_{A}(2\sigma_{1}' - \sigma_{2}')}{2r_{2}^{5}} \right\}.$$

$$(14)$$

Here, we use $\xi_0 = (1 - \mu)$ and $\zeta_0 = \sqrt{3A_1}$ as an initial approximation. Now, using Mathematica (software package)we are able to obtain the positions of a pair of points $(\xi_0, \pm \zeta_0)$ corresponding to out-of-plane equilibrium points $L_{6,7}$ which can be approximated in the forms of power series to the third order terms in A from equations (13) and (14) as:

$$\xi_{0} = (1 - \mu) + \left(\frac{3\sqrt{3}Q_{1}}{Q_{2}(2\sigma_{1}' - \sigma_{2}')} - \frac{3\sqrt{3}(1 - \mu)\left(1 + \frac{3}{2}(2\sigma_{1}' - \sigma_{2}')\right)}{Q_{2}(2\sigma_{1}' - \sigma_{2}')} \right) A_{1}^{\frac{5}{2}} + 0[A_{1}]^{\frac{7}{2}}; \text{ and}$$

$$\zeta_{0} = \frac{3\sqrt{A_{1}}}{\sqrt{5}} + \frac{A^{\frac{3}{2}}}{\sqrt{5}(2\sigma_{1}' - \sigma_{2}')} + 0[A_{1}]^{\frac{5}{2}}.$$
(15)



4. Numerical Application

In this section, we use the astrophysical data of the Sun-Venus system borrowed from NASA ADS and Mecheri *et. al.* (2004) for the purpose of numerical computation.

The radiation pressure factor of Sun q_1 and albedo factor of the Venus q_A are defined as: $q_1 = 1 - \alpha_1$

and
$$q_A = 1 - \beta_A$$
 respectively. Also, α_1 and β_A are expressed as: $\alpha_1 = \frac{L_0}{2\pi G m_1 c \bar{\kappa}}$ and

$$\beta_{\rm A} = \frac{L_{\rm V}}{2\pi G m_2 c \bar{\kappa}}$$
, where $L_{\rm D}$ and $L_{\rm V}$ are the luminosities of the Sun and Venus respectively, G is

the gravitational constant, c is the speed of light and \bar{k} is the mass per unit area, m_1 and m_2 are the masses of the Sun and Venus respectively. By using Stefan-Boltzmann's law, the luminosities of the primaries can be expressed as: $L_{\Box} = 4\pi R_{\Box}^2 \sigma T_{\Box}^4$ and $L_V = 4\pi R_V^2 \sigma \varepsilon T_V^4$, where σ is the Stefan-Boltzmann's constant and ε is the emissivity of the second primary (the Venus), see Yousuf and Kishor (2019). The Luminosity of the Venus can also be expressed in terms of its predicted albedo

as
$$L_V = 4\pi R_V^2 \varepsilon S_{\parallel} (1 - A_V)$$
, where S_{\parallel} is the solar constant. Thus, the relation $\frac{\beta_A}{\alpha_1} = \left(\frac{1 - \mu}{\mu}\right) k$,

where
$$k = \frac{L_V}{L_{\Box}}$$
 and can be expressed as $k = \frac{R_V^2 \mathcal{E} S_{\Box} \left(1 - A_V\right)}{4R_{\Box}^2 \sigma T_{\Box}^4}$ (see Yousuf and Kishor; 2019). Also,

the mass ratio of the Sun-Venus system is given by: $\mu \Box 2.45 \times 10^{-6}$.



Table 1: Effects of perturbations on the locations of $L_{6/7}$ of the Sun-Jupiter system

Cases	$\alpha_{_{1}}$	$A_{\rm l}$	$\sigma_{\scriptscriptstyle 1}'$	σ_2'	ξ ₀	$\pm\zeta_0$
1	4.7×10^{-15}	9.12×10 ⁻¹²	3.46×10 ⁻⁷	1.73×10 ⁻⁷	0.9999975500	4.05169006×10 ⁻⁶
2	4.7×10^{-5}	0	0	0	0.9999975500	4.05169006×10 ⁻⁶
	4.7×10^{-5}	0	0	0	0.9999975500	4.05169006×10 ⁻⁶
	4.7×10^{-1}	0	0	0	0.9999975500	4.05169006×10 ⁻⁶
3	0	9.12×10 ⁻¹⁰	0	0	0.9999975500	0.0004054040
	0	9.12×10^{-6}	0	0	0.9999967509	0.0277839700
	0	9.12×10^{-2}	0	0	-7989.8520775	23732.708875
		9.12×10				
4	0	0	3.46×10^{-7}	1.73×10^{-7}	0.9999975500	$4.05169006 \times 10^{-6}$
	0	0	3.46×10^{-4}	1.73×10^{-4}	0.9999975500	4.05166634×10^{-6}
	0	0	3.46×10^{-2}	1.73×10^{-2}	0.9999975500	4.05166632×10 ⁻⁶
5	0	9.12×10 ⁻¹⁰	3.46×10 ⁻⁷	1.73×10 ⁻⁷	0.9999975500	0.0000405404
	0	9.12×10^{-6}	3.46×10^{-4}	1.73×10^{-4}	0.9999967509	0.0040753986
	0	9.12×10^{-2}	3.46×10^{-2}	1.73×10^{-2}	-7989.8520296	0.6424896695
6	4.7×10^{-5}	9.12×10^{-10}	3.46×10^{-7}	1.73×10^{-7}	0.9999975500	0.0000405404
	_				0.9999485080	0.0040753986
	4.7×10^{-5}	9.12×10^{-6}	3.46×10^{-4}	1.73×10^{-4}	-56233.829866	0.6424896695
	4.7×10 ⁻¹	9.12×10^{-2}	3.46×10^{-2}	1.73×10^{-2}		

5. Discussion

The modified equations of motion of an infinitesimal mass in the framework of ER3BP taking in to account oblateness of the bigger primary and triaxiality of the smaller primary with the radiation and albedo factors of the bigger and smaller primaries respectively are presented in equations (1) -(4). The presence of these perturbations parameters in the governing equations of motion indicate that the equations of motion are affected by them. However, if these perturbing parameters are relaxed (i.e. $A_1 = \sigma_i' = 0$ (i = 1, 2), $q_1 = q_A = 1$ and e = 0), the equations of motion will coincide with the classical of Szebehely (1967). These equations of motion are in accordance with those of Umar and Hussain (2016) when radiation pressure factor and albedo factor are ignored in both works. Also, these equations of motion are in conformity with those of Idrisi and Ullah (2018) when oblateness and triaxiality coefficients of the primary bodies are neglected in both works. The locations of the 1st family of out-of-plane equilibrium points $L_{6,7}$ corresponding to a pair of points $(\xi_0, \pm \zeta_0)$ are given in equations (15). It is seen from the equations (15) that these pair of points are affected by oblateness of the first even zonal harmonic and radiation pressure factor of the bigger primary and triaxiality as well as albedo factor of the smaller primary. The effects of parameters involved in coordinates $(\xi_0, \pm \zeta_0)$ of the 1st family of the out-of-plane equilibrium points $L_{6,7}$ (15) for the Sun-Venus system are presented in Table 1.



It should be noted that the Table 1, Case 1 shows the locations of 1st family of out-of-plane equilibrium points $L_{6.7}$ for the obtained data of the Sun-Venus system and some assumed values of triaxiality of the smaller primary. While, Case 2 reveals that, simultaneous increase or decrease of the radiation pressure factor of the bigger primary and albedo factor of the smaller primary have no significant effects on $L_{6,7}$. Case 3 shows that increase in oblateness A_1 of the bigger primary causes a shift of $L_{6,7}$ towards the negative direction in ξ_0 axis and L_6 to move towards the positive direction in ζ_0 axis (implies L_7 to move towards the negative direction in ζ_0 axis). And in Case 4, it is seen that a simultaneous increase in triaxiality coefficients σ'_1 and σ'_2 of the smaller primary have no significant effects on $L_{6.7}$. Also, Case 5 show that simultaneous increases in oblateness A_1 of the bigger primary and triaxiality coefficients σ'_1 and σ'_2 of the smaller primary causes a shift of $L_{6.7}$ towards the negative direction in ζ_0 axis and L_6 towards the positive direction in ζ_0 axis (implies L_7 to move towards the negative direction in ζ_0 axis). Moreover, Case 6 reveals that increases in in oblateness A_1 of the bigger primary, radiation pressure factor of the bigger primary, triaxiality coefficients σ'_1 and σ'_2 of the smaller primary and albedo factor of the smaller primary causes a shift of $L_{6,7}$ towards the negative direction in ξ_0 axis and L_6 towards the positive direction in ζ_0 axis (implies L_7 to move towards the negative direction in ζ_0 axis).

REFERENCES

- Alhussain Z. A. (2019). The motion of infinitesimal body in CR4BP with variable masses and albedo effect. *Journal of Taibah University for Science*, 13(1), 287-296.
- Bhatnagar, K. B. and Hallan, P.P. (1998). Existence and stability of L_{4, 5} in the relativistic restricted three-body problem. *Celestial Mechanics and Dynamical Astronomy*, 69, 271-281.
- Chakraborty, A. and Narayan, A. (2018). Effect of stellar wind and Poynting–Robertson drag on photogravitational elliptic restricted three-body problem. *Solar System Research*, 52 (2), 168–179.
- Hussain A. A., Umar A. and Singh J. (2018). Investigation of the stability of a test particle in the vicinity of collinear points with the additional influence of an oblate primary and a triaxial-stellar companion in the frame of ER3BP. *International Frontier Science Letters*, 13(1), 12-27. DOI:10.18052/www.scipress.com/IFSL.13.12. ISSN: 2349-4484.
- Idrisi M. J. (2017). A study of libration points in CR3BP under albedo effect. *International Journal of Advanced Astronomy*, 5(1), 1-6.
- Idrisi, M. J. and Ullah, M. S. (2018). Non-collinear libration points in ER3BP with albedo effect and oblateness. *Journal Astrophysics and Astronomy*, 39, 28-38.
- Idrisi, M. J. and Ullah, M. S. (2021). Out-of-plane equilibrium points in the elliptic restricted hree-body problem under albedo effect. *New Astronomy*, https://doi.org/10.1016/j.newast.2021.101629.
- Liming Li, Jiang, X., West, R. A., Gierasch, P. J., Perez-Hoyos, S., Sanchez-Lavega, A., Fletcher, L. N., Fortney, J. J., Knowles, B., Porco, C. C., Baines, K. H., Fry, P. M., Mallama, A., Achterberg, R. K., Simon, A. A., Nixon, C. A., Orton, G. S., Dyudina1, U. A., Ewald, S. P. and Schmude Jr, R.W. (2018). Less absorbed solar energy



- and more internal heat for Jupiter. *Nature communications*, 9, 3709. doi: 10.1038/s41467-018-06107-2.
- Mecheri, R. et al. (2004). New values of gravitational moments J_2 and J_4 deduced from helioseismology. Solar Physics, 222, 191-197.
- Pontus, A. (2005). Attitude estimation from magnometer and earth-albedo-corrected coarse sun sensor measurements. *Acta Astonautica*, 56(1-2), 115-126.
- Radzievskii, V. V. (1950). The restricted problem of three bodies taking account of light pressure. *Astronomical Zhurnal*, 27(2), 250-256.
- Ragos, O. and Zagouras, C. (1988). Periodic solutions about the out-of-plane equilibrium points in the photogravitational restricted three-body problem. *Celestial Mechanics*, 44(1), 135-154.
- Saleem, Y. and Ram, K. (2019). Effects of the albedo and disc on the zero velocity curves and linear stability of equilibrium points in the generalized restricted three-body problem. *Monthly Notices of the Royal Astronomical Society*, 488, 1894-1907.
- Sharma, R.K., Taqvi, Z.A. and Bhatnagar, K.B. (2001). Existence and stability of libration points in the restricted three-body problem when the primaries are triaxial rigid bodies and source of radiations. *Indian Journal of Pure and Applied Mathematics*, 32(7), 981-994.
- Simmons, J. F. L., McDonald, A. J. C. and Brown, J. C. (1985). The restricted three-body problem with radiation pressure. *Celestial Mechanics*, 35, 145.
- Singh, J. and Umar, A. (2013). On Out-of-plane equilibrium points in the elliptic restricted three-body problem with radiating and oblate primaries. *Astrophysics and Space Science*, 344, 13-19.
- Singh, J. and Ishwar, B. (1999). Stability of triangular points in the generalised photogravitational restricted three-body problem. *Bulletin of the Astronomical Society of India*. 27, 415-424.
- Singh, J. and Umar, A. (2012). Motion in the Photogravitational elliptic restricted three-body problem under an oblate primary. *The Astronomical Journal*, 143,109-131.
- Szebehely, V. (1967). *Theory of Orbits*. The restricted problem of three-bodies. Academic Press, New York.
- Umar, A. and Hussain, A. A. (2016). Motion in the ER3BP with an oblate primary and triaxial stellar companion. *Astrophysics and Space Science*, 361, 344-353.
- Zimovshchikov, A.S. and Tkhai, V.N. (2004). Instability of libration points and resonance phenomena in the photogravitational elliptic restricted three-body problem. *Solar System Research*, 38, 155-164.



Simple but Smart: Against the Pursuit of Endless Complexity in Deep Learning Models for Detecting Phishing URLs

Musa Ibrahim Anda
Dept. of Computer Science
and IT
Al-Qalam University Katsina
Katsina, Nigeria
musaianda@auk.edu.ng

Armaya'u Zango Umar
Dept. of Software Engr. and
Cybersec.
Al-Qalam University
Kastina
Katsina, Nigeria
azumar@auk.edu.ng

Barira Hamisu
Dept. of Software Engr. and
Cybersec.
Al-Qalam University Kastina
Katsina, Nigeria
barirahamisu@auk.edu.ng

Abstract

Phishing attacks are one of the most prevalent and evolving cyber security threats. The attacks often employ a fraudulent Universal Resource Locator (URL) and a well-crafted social engineering tactic to mislead gullible individuals into releasing their sensitive information, such as bank or credit card details. Machine learning classification models have been proposed to proactively detect phishing URLs. In an attempt to improve the detection accuracy, deep learning models were also proposed. Yet, to push the performance of the models even further, more sophisticated deep learning architectures were proposed. Nonetheless, the sophistication in the architectures does not improve the performance commensurate with its complexity. To this end, this paper compared the performance of a simple Feedforward Neural Network (FNN) against more complex architectures: hybridized Deep Neural Network and Bidirectional Long Short-Term Memory (DNN-BiLSTM), hybridized Deep Neural Network and Bidirectional Long Short-Term Memory (DNN-BiLSTM) with a transformer, and hybridized Deep Neural Network and Bidirectional Long Short-Term Memory (DNN-BiLSTM) with semantic Natural Language Processing (NLP) features. The models were trained on a phishing dataset that had label noise corrected with Cleanlab – A Confidence learning framework. The results show that a simple Feedforward Neural Network, when trained on cleaned data, can equal or even surpass the performance of any complex deep learning architecture while maintaining significantly lower runtime.

1.0 Introduction

Phishing is a cyber-attack that exploits human vulnerabilities using a carefully crafted fraud known as social engineering. The exploitable human vulnerabilities include fear, trust, or curiosity. For example, attackers might launch a fraudulent airtime campaign impersonating one of the major telecom companies. In the campaign, the attackers will provide a fraudulent URL to redeem the purported offer. When a victim clicks on the provided link, certain sensitive information will be requested, and when provided, the attackers have succeeded in deceiving the victim. Another typical example is impersonating a major corporate organizations, such as a central bank. In this case, the attackers' message to the victim might be claim to offer certain benefits, such as government's palliative or business support. As in the previous example, a fake URL will be provided which when clicked, will land the victim on a fake central bank website. Sensitive information such as bank and credit card details may be phished from the victim and when provided, such information is compromised. In both examples, the attackers exploit the trust the victims have in the reputable organizations and the fear of missing out from the purported benefits.



To prepare for phishing, the attackers create a domain name that mimics the real one. For example, if the real domain is cbn.gov.ng, of which the URL is https://www.cbn.gov.ng/, the fake domain created by the attackers might be cbn.com (with the URL as https://www.cbn.com). Similarly, if a real domain of a telecom service provider is mtn.ng, of which the URL is https://www.mtn.ng/, the fake one might be m-tn.ng, with the dash after m (with the URL as https://www.m-tn.ng/). After the creation of the fake domain, the website of the impersonated organization will be cloned to have a fake website with the same look and feel (colour, logo, and aesthetics) as the genuine website.

There have been several attempts to use machine learning models to detect phishing URLs. These include both white box and deep learning (black box) models. In the category of white box models, the studies proposed smart models engineered with sophisticated ensembling strategies (Alsariera et al., 2022) or elegant feature selection strategies(Ahammad et al., 2022; Balogun et al., 2021). Although a white box model has the advantage of being interpretable and computationally more efficient than its deep learning model counterpart, it has a limitation in its failure to recognize complex patterns that may be present in a typical phishing URL. Consequently, deep learning models were also proposed.

In the category of deep learning models, Bahnsen et al. (2017) proposed a Long Short-Term Memory (LSTM) neural network architecture to capture sequential patterns in URLs. Aljofey et al. (2020) extended this study using character-level Convolutional Neural Networks (CNNs) to reduce the computational demand of word-level encoding. The fact that a URL is a sequential text that often contains information with a semantic pattern, a study (Liu et al., 2022) introduced CNN-Fusion, which used multiple one-layer CNNs with different kernel sizes to capture spatial patterns at varying granularities.

In machine learning, there are two (2) popular approaches to capturing features for model training: (i) character embedding and (ii) manually hand-crafted. Character embedding is a technique used to represent individual characters (letters, digits, symbols, etc.) as dense, low-dimensional vectors in a continuous vector space. Thus, each individual character in a text sequence is represented as a numerical vector. These embedding capture semantic and syntactic similarities between characters, allowing models to generalize better when processing text data at the character level(Ballesteros et al., 2015). In contrast to character embedding, manually hand-crafted features refer to features that are explicitly designed by domain experts or data scientists based on prior knowledge, intuition, and data analysis. Hand-crafted features were dominant before the advent of deep learning. In the context of phishing detection, examples of hand-crafted features include URL length, the presence of suspicious characters, or domain age.

Although deep learning models can capture complex patterns in URLs, existing studies have mainly focused on either hand-crafted features (high-level connections) or character embedding-based features (Aljofey et al., 2020; Bahnsen et al., 2017), but not both. Consequently, a hybrid approach, which combines different methods to improve accuracy and precision, was proposed(Ozcan et al., 2023). The hybrid model integrates the strengths of both Deep Neural Networks and Bidirectional Long Short-Term Memory (DNN-BiLSTM) networks to enhance phishing URL detection. The work in (Ozcan et al., 2023) is state-of-the art but did not benefit from Confident Learning (CL)(Northcutt, Jiang, et al., 2021; Zhang et al., 2020), leading to a very



complicated architecture. CL is a framework in machine learning that focuses on identifying, quantifying, and correcting label errors in datasets. It is particularly useful in weakly supervised learning, where training labels may be noisy or unreliable.

To this end, this paper compared the performance of a simple Feedforward Neural Network (FNN), engineered with Confidence Learning, against the complex architecture proposed in (Ozcan et al., 2023) as it was, and against other modifications to the architecture proposed in (Ozcan et al., 2023). The results show that a simple Feedforward Neural Network, when trained on cleaned data, with label noise corrected, can equal or even surpass the performance of any complex deep learning architecture while maintaining significantly lower runtime.

2.0 Literature Review

Phishing URL detection has witnessed a variety of methodological approaches, ranging from traditional machine learning to advanced deep learning architectures. Early models focused heavily on character-level features derived from raw URLs. For instance, Bahnsen et al. (2017) employed a Long Short-Term Memory (LSTM) neural network to capture sequential patterns in URLs, achieving an accuracy of 98.7% and outperforming Random Forest classifiers. Aljofey et al. (2020) extended this line of work using character-level Convolutional Neural Networks (CNNs), emphasizing speed and lightweight computation by eliminating the need for external content retrieval. Their model effectively captured syntactic URL patterns and performed competitively against benchmark datasets.

In a similar vein, (Liu et al., 2022)introduced CNN-Fusion, which used multiple one-layer CNNs with different kernel sizes to capture spatial patterns at varying granularities. To improve robustness, they applied spatial dropout and pooling techniques. Their architecture proved lightweight and suitable for resource-constrained devices. However, like previous character-level models, it lacked semantic awareness, making it vulnerable to more sophisticated or obfuscated phishing strategies.

Other researchers attempted to bridge this gap by integrating contextual and content-based features. Liu et al. (2022) designed fusion models that analysed URLs along with webpage titles, body text, and hidden HTML tags. This allowed their models to extract semantic relationships beyond syntactic URL patterns. Although their multi-component architecture provided nuanced insight into phishing content, its reliance on complete webpage data makes real-time or large-scale deployment less feasible. A study (Opara et al., 2024) also leveraged both URL and HTML data through character and word embedding, achieving a high detection accuracy of 98.1%. Nevertheless, the overhead of processing and embedding HTML content remained a practical bottleneck.

Seeking a middle ground, Sudar et al. (2024) focused on dynamic features of URLs — such as domain age and live web-scraped content — and applied forward selection and LASSO regularization to retain only the most informative attributes. While this method addressed the limitations of static analysis, it too suffered from reliance on live web availability, which may be inconsistent or time-sensitive in real-world phishing cases.

Meanwhile, Wei and Sekiya (2022) compared a variety of ensemble machine learning methods (e.g., Random Forest, AdaBoost, LightGBM) and neural architectures (FCNN, LSTM, CNN), ultimately concluding that traditional ensemble methods outperformed deep learning approaches



on their dataset. While insightful, the study did not explore newer hybrid or attention-based architectures that may close this performance gap.

A more integrative approach was proposed by van Geest et al. (2024), who developed a hybrid phishing detection framework combining URL-based models with HTML content and DOM structure analysis, merged through a stacking ensemble. This demonstrated improved detection robustness and real-world applicability, but introduced significant computational complexity, making it less suitable for scalable or low-latency applications.

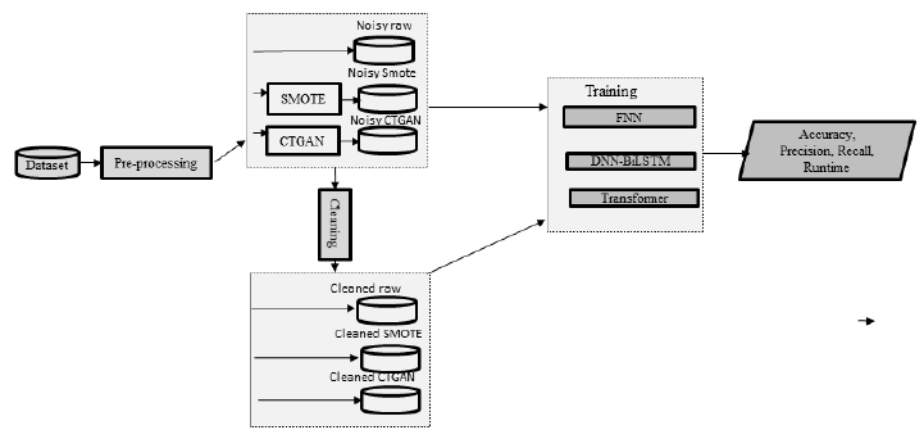
Taken together, these studies highlight key gaps in the phishing detection literature. First, many models focus exclusively on either character-level or content-level information, often neglecting the middle ground of **semantic URL structures**, such as suspicious tokens, domain heuristics, or entropy scores. Second, although complex fusion or ensemble models often show improved accuracy, they tend to suffer from overfitting, poor scalability, or impractical latency.

3.0 Methodology

This section outlines the research design, data pre-processing techniques, synthetic data augmentation strategies, model development, and performance evaluation methods used in this study. The methodology is designed to evaluate the trade-offs between architectural complexity and performance in phishing URL detection, with a focus on simplifying models and optimizing data quality. The methodological workflow is illustrated in Figure 1.

3.1 The Dataset

The dataset employed in this study comprises a total of 11,430 records. It was curated for training and evaluating machine learning models in the context of phishing detection, with the primary goal of distinguishing between legitimate and malicious websites based on a wide array of syntactic, lexical, and structural characteristics extracted from URLs and their associated web content(Abdelhakim & Salima, 2021).



3.2 Synthetic Minority Over-sampling Technique (SMOTE)

As class imbalance often affects the performance of machine learning models, Synthetic Minority Over-sampling Technique (SMOTE) (Elreedy & Atiya, 2019) is a widely used data augmentation method designed to mitigate class imbalance in machine learning datasets. When one class (the majority) dominates another (the minority), models tend to bias predictions toward the majority



class, degrading performance on the minority class. SMOTE counteracts this by generating synthetic minority-class samples, thereby balancing the dataset and enhancing model performance. Data balancing with SMOTE was used in this study to compare its impact with label noise correction using Cleanlab.

3.3 Conditional Tabular Generative Adversarial Network (CTGAN),

The Conditional Tabular Generative Adversarial Network (CTGAN) is a synthetic data generation technique introduced by (Xu et al., 2019). It enhances the traditional GAN architecture(Goodfellow et al., 2020) to better handle the generation of structured tabular data. It ensures that the synthetic data not only mirrors the marginal distributions of the original dataset but also retains the conditional relationships among different features. CTGAN begins by selecting a condition from the actual dataset, which is then combined with random noise and fed into the conditional generator. This strategy allows the model to preserve the attribute dependencies present in the original data (Lei Xu et al., 2020).

3.4 Confidence Learning with Cleanlab

To address the challenge of **label noise**, which can significantly degrade model performance, this study employed the Cleanlab framework to automatically identify and remove potentially mislabelled examples from the training data. The process is presented in Algorithm 1. The method began by loading the data and encoding the target feature (Line 3 and 4 of Algorithm 1). The Algorithm then proceeds with the encoding of the remaining features (Line 5 of Algorithm 1). Then, a baseline classification model was built (Line 6 of Algorithm 1). The baseline model plays a foundational and diagnostic role. It serves as the primary tool through which Cleanlab estimates the reliability of each labelled instance in the dataset. It estimates the probability that a given sample's label is incorrect based on the model's understanding of the data distribution(Northcutt, Athalye, et al., 2021). In this study, Logistic Regression was used as the baseline model. Five (5) cross-validated probability estimates were used to ensure that the detection of label issues was based on fair and generalizable model behaviour (Line 7 of Algorithm 1). The labels with noise are detected and removed (Line 8 and 9 of Algorithm 1). The cleaned dataset is then saved to a file. The label correction was applied to the three different datasets: (i) raw dataset, (ii) balanced dataset using SMOTE, and (iii) augmented dataset using CTGAN. The operation resulted in producing three (3) cleaned datasets: (i) Cleaned Raw, Cleaned SMOTE, and (iii) Cleaned CTGAN.

Algorithm 2: Label Noise Correction with Cleanlab

- 1. **Input:** raw dataset
- 2. **Output:** cleaned_dataset
- 3. Load dataset
- 4. Encode target labels
- 5. Set up preprocessing pipeline:

preprocessor ← ColumnTransformer with:

- StandardScaler for numeric_features
- OneHotEncoder for categorical_features
- 6. Build classification pipeline:

model pipeline ← Pipeline with:



- 'preprocessor': preprocessor
- 'classifier': LogisticRegression(max_iter=1000)
- 7. Perform cross-validated prediction:

 predicted_probabilities ← cross_val_predict(model_pipeline, X, y, cv=5)
- 8. Detect potential label issues
- 9. Remove noisy records
- 10. Save cleaned dataset

3.5 Training the models

3.5.1 Feedforward Neural Network Architecture (FFN)

In this study, a Feedforward Neural Network (FNN) was implemented due to its proven capability in modelling complex nonlinear relationships between input features and target labels in structured datasets(Lecun et al., 2015). Prior to feeding the data into the model, features were standardized using the StandardScaler method, which transforms each feature to have zero mean and unit variance. The network consists of three hidden layers, each composed of fully connected (dense) neurons. The first layer includes 256 neurons, followed by 128 neurons in the second layer and 64 neurons in the third. Each layer applies the Rectified Linear Unit (ReLU) activation function to introduce non-linear transformations and enhance model expressiveness. To mitigate overfitting(Ioffe & Szegedy, 2015), each dense layer is followed by a Batch Normalization layer and a Dropout layer. Dropout randomly disables a fraction of neurons during training, preventing co-adaptation of features (SrivastavaNitish et al., 2014). Dropout rates were set to 0.3 for the first two layers and 0.2 for the third, reflecting a decreasing regularization strategy as the network deepens.

The final layer consists of a single neuron with a sigmoid activation function, producing a probability output between 0 and 1. The model was compiled using the binary cross-entropy loss function, which is appropriate for binary classification problems, and optimized using the Adam optimizer (Kingma & Ba, 2015), known for its robustness and adaptive learning rate properties.

3.5.2 DNN-BiLSTM

This study replicated the hybrid deep learning model that integrates a Deep Neural Network (DNN) with a Bidirectional Long Short-Term Memory (BiLSTM) network as proposed in (Ozcan et al., 2023). For this architecture, the features fed were the raw URL and the set of manually engineered features. These features capture statistical, structural, and lexical characteristics of URLs and domains, such as token counts, entropy values, and the presence of certain keywords or patterns. The target variable is transformed into binary format using label encoding, with "phishing" represented as 1 and "legitimate" as 0. To ensure consistent feature scale and improve convergence speed during training, all numerical features are standardized using z-score normalization.

The raw URL strings, were processed through a **character-level tokenizer.** Unlike word-level tokenization, which may miss obfuscated character patterns used in phishing attacks, character-level tokenization enables the model to detect subtle manipulations and irregular character sequences(Correa Bahnsen, 2018). Each URL is converted into a sequence of integers and padded to a fixed length of 75 characters to standardize input dimensions for the sequential model.



The architecture is composed of two parallel branches: (i) 1. DNN Branch (Processing Hand-Crafted Features) and (ii) BiLSTM Branch (Processing Character-Level Embeddings). The first branch (DNN branch) begins with a dense layer comprising 64 neurons activated by the ReLU function, followed by a dropout layer with a rate of 0.3 to reduce overfitting. Another layer in the first branch is the second dense layer with 32 neurons to further abstract the learned representations.

The second branch (BiLSTM branch) receives raw URL sequences in the form of character indices. These are passed through an **embedding layer**, which transforms each character index into a 128-dimensional vector, thereby capturing distributed representations of characters based on usage context. The embedded sequences are then fed into a **Bidirectional LSTM layer** with 64 units. This recurrent layer processes the sequence in both forward and backward directions, enabling the model to capture patterns that may emerge from any part of the URL string. The outputs of the DNN and BiLSTM branches are combined, creating a unified feature vector that combines high-level semantic signals with low-level sequential patterns. This merged representation is passed through an additional dense layer of 32 neurons with ReLU activation, followed by another dropout layer to further improve generalization. The final layer consists of a

The model is compiled using the binary cross-entropy loss function, appropriate for two-class problems, and trained using the Adam optimizer, known for its adaptive learning rate and computational efficiency(Kingma & Ba, 2015). The training process spans 10 epochs with a batch size of 32 and includes a validation split to monitor performance.

single neuron activated by the sigmoid function, producing a probability score for binary

In summary, in the DNN-BiLSTM hybrid architecture, the DNN branch learns from hand-crafted semantic features, while the BiLSTM branch processes character-level embedding of URLs to capture syntactic irregularities and sequential patterns.

3.5.3 Semantic NLP

classification.

This model builds upon the previous DNN-BiLSTM design by incorporating lexical representations of tokenized URL segments as part of what is here referred to as Semantic NLP features. These Semantic NLP features are extracted from URLs by decomposing them into meaningful tokens using common delimiters such as slashes, dots, and hyphens. The resulting tokens are vectorised using TF-IDF, which measures the relative importance of each term based on its frequency and uniqueness across the corpus. By retaining only the top 100 tokens, the model captures essential lexical indicators of phishing behaviour, such as misleading subdomains, obfuscated brand names, and suspicious keyword combinations.

These semantic features were combined with hand-crafted features to form a rich structured input. This combined feature set is normalized and passed into a deep neural network, which constitutes the DNN branch of the model. The DNN is thus responsible for learning high-level patterns from both quantitative behaviour, represented by hand-crafted features, and semantic word cues from the URL tokens.



In parallel, the model processes the raw URL strings using character-level tokenization on the BiLSTM branch. The outputs of the Semantic NLP + hand-crafted DNN branch and the BiLSTM branch are combined, fused through an additional dense layer, and passed into a sigmoid-activated output neuron for binary classification. The model is trained using binary cross-entropy loss, optimized via Adam.

3.5.4 Transformer architecture

This model added a URL Transformer encoder to the DNN-BiLSTM architecture. The URL Transformer block defines multi-head self-attention, residual connections, and feed-forward layers, resembling the encoder module of the original Transformer architecture (Vaswani et al., 2017). The sequence is passed through two BiLSTM layers: the first with 128 units returning sequences, and the second with 64 units reducing it to a fixed-length output vector. This two-stage BiLSTM stack captures both local and long-range dependencies in the URL string, a critical advantage when detecting manipulations that occur across various positions in the URL.

The outputs of the DNN branch and the BiLSTM branch are concatenated to form a unified latent representation. This combined vector is passed through a dense layer with 64 GELU-activated neurons, followed by dropout. The final classification is performed using a sigmoid-activated neuron that outputs the probability of the instance being phishing or legitimate. The model is compiled using binary cross-entropy loss and optimized with the Adam optimizer, utilizing a custom exponential decay learning rate schedule. This schedule starts with a learning rate of 0.001 and decays over time, facilitating better convergence during prolonged training. To avoid overfitting and ensure optimal performance on phishing detection (class 1), early stopping is configured to monitor validation recall with a patience of five epochs. Furthermore, class weights are applied to slightly prioritize the minority class, addressing mild label imbalance.

3.6 Evaluation

In the context of this study, the evaluation process involves various metrics and techniques to measure the model's predictive accuracy and generalization capabilities.

Precision: Calculates the proportion of true positive predictions among all positive predictions. It's a measure of the model's ability to avoid false positives. The formula is given as:

Precision =
$$\frac{TP}{TP+FP}$$

Where TP means True Positive and FP means False Positive

Recall (Sensitivity): Calculates the proportion of true positive predictions among all actual positives. It's a measure of the model's ability to capture all positives. The formula is given as:

$$Recall = \frac{TP}{TP + FN}$$

Where FN means False Negative

F1-Score: Harmonic mean of precision and recall, providing a balance between the two metrics. Useful when the class distribution is imbalanced. The formula is:

$$F1 = \frac{2 \ X \ precision \ X \ recall}{precision + recall}$$

Runtime. Runtime refers to the total amount of time a model takes to complete a specific task, such as training or inference. In the context of phishing URL detection, runtime is typically measured in seconds (s) and serves as an essential metric for evaluating a model's computational efficiency and practicality.



4.0 Results and Discussions

This section presents a comprehensive analysis of experimental results evaluating the performance, computational efficiency, and robustness of four machine learning models across diverse dataset conditions. The investigation focuses on three critical dimensions: (1) model effectiveness on noisy versus cleaned datasets, measured by F1-scores; (2) computational runtime efficiency; and (3) the trade-offs between training time and classification accuracy, particularly in the context of phishing detection.

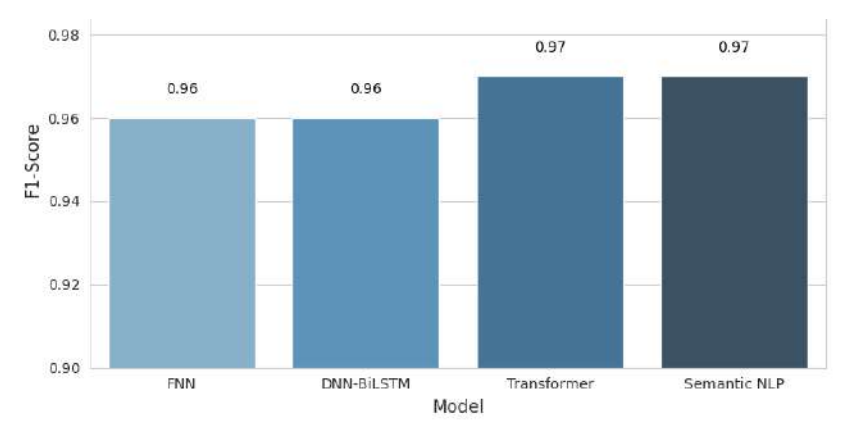


Figure 2: Comparison of FNN, DNN-BiLSTM, Transformer, and Semantic NLP before label noise correction using the F1-score metric

The bar graph, in Figure 2 provides a quantitative comparison of four models: Feedforward Neural Network (FNN), Deep Neural Network with Bidirectional Long Short-Term Memory (DNN-BiLSTM), Transformer, and Semantic NLP, using the F1-score metric. The results reveal distinct disparities in the models' ability to handle noise, with scores as follows: FNN: 0.96, DNN-BiLSTM: 0.96, Transformer: 0.96, and Semantic NLP: 0.97.

Semantic NLP emerged as the top-performing model, achieving an F1-score of 0.97. This superior performance can be attributed to its focus on contextual and semantic understanding, which enables it to discern meaningful patterns despite noise. By leveraging advanced linguistic features, Semantic NLP mitigates the distortions introduced by noisy data, making it particularly effective for tasks requiring nuanced interpretation.



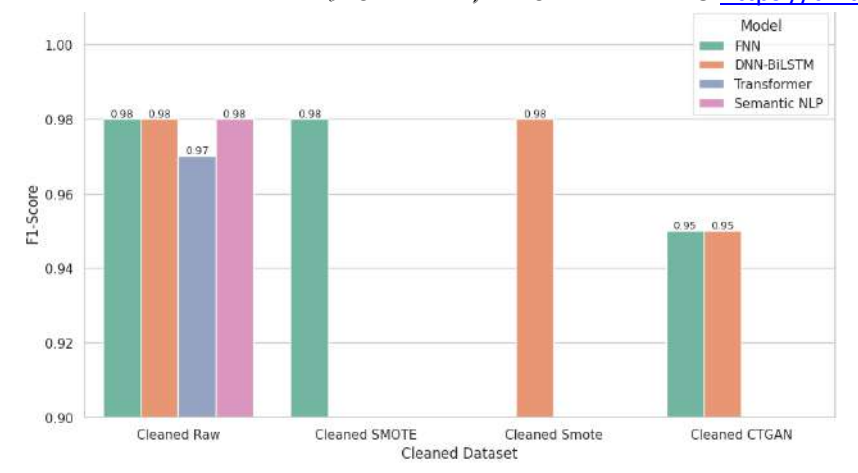


Figure 3: Comparison of FNN, DNN-BiLSTM, Transformer, and Semantic NLP after label noise correction on three datasets: (i) Raw dataset, (ii) Dataset balanced with SMOTE, and (iii) Dataset augmented with CTGA- using the F1-score metric

The graph in Figure 3 shows that the FNN consistently outperformed other models across all cleaned datasets, achieving the highest score (0.98) on the dataset with label noise corrected (Cleaned Raw). This suggests that for cleaned datasets, simpler architectures may sometimes outperform more complex ones. DNN-BiLSTM maintained strong performance, closely following FNN, indicating that its bidirectional processing remains effective even with cleaned data. The Transformer showed moderate performance, while Semantic NLP, despite its sophistication, ranked lowest in this comparison. The FNN's strong performance challenges the common assumption that complex models always outperform simpler ones.

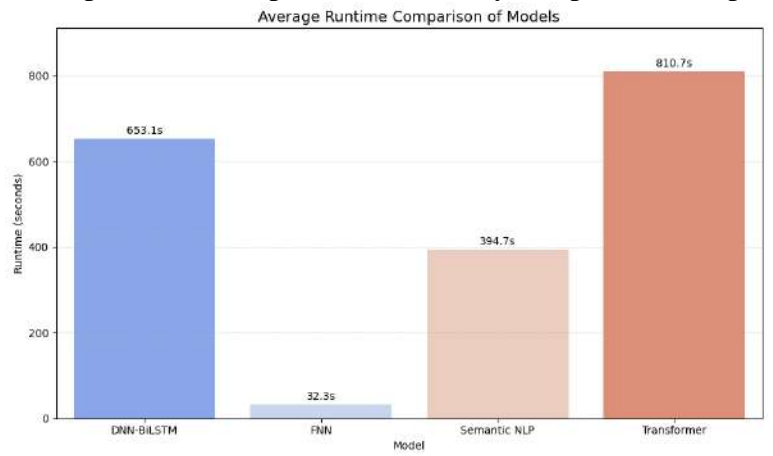


Figure 4: Comparison of computational efficiency of FNN, DNN-BiLSTM, Transformer, and Semantic NLP after label correction

The bar graph in Figure 4 shows the following results: DNN-BiLSTM: 653.1 seconds, FNN: 39.47 seconds, Semantic NLP: 32.3 seconds, Transformer: 810.7 seconds. Thus, FNN Semantic NLP, despite its advanced semantic processing capabilities, also demonstrates impressive efficiency. In contrast, DNN-BiLSTM and Transformer exhibited significantly higher runtimes (653.1 seconds and 810.7 seconds, respectively). The DNN-BiLSTM's bidirectional recurrent layers require sequential processing of data in both forward and backward directions, leading to increased



computational time. The Transformer, while powerful, suffers from the quadratic complexity of its self-attention mechanisms, particularly for longer input sequences, which explains its status as the slowest model in this comparison.

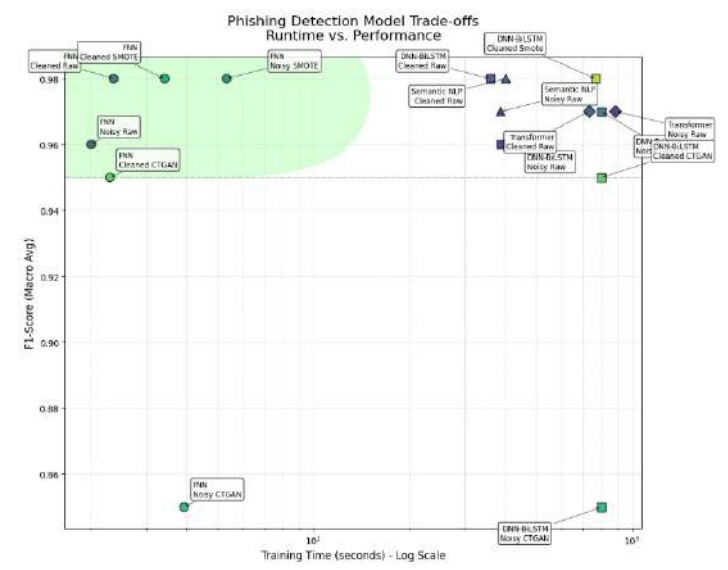


Figure 5: The trade-offs between model training time and classification performance for various phishing detection models and datasets

Figure 5 presents the trade-offs between model training time and classification performance for various phishing detection models and datasets. The x-axis, scaled logarithmically, quantifies the training duration in seconds, reflecting computational resource allocation. The y-axis represents the F1-Score, a robust metric for evaluating classification models, particularly in scenarios with imbalanced class distributions, as it harmonically averages precision and recall. The shaded light green region at the upper-left quadrant of the plot signifies the optimal zone. This area delineates models that concurrently achieve high F1-Scores (generally exceeding 0.95) and relatively expedient training times (approximately below 200 seconds). This zone represents the ideal balance between predictive accuracy and computational efficiency.

Notably, several FNN configurations, especially those trained on Cleaned Raw, Cleaned SMOTE, and Noisy SMOTE datasets, are situated within or in close proximity to this optimal zone. These models consistently yielded F1-Scores above 0.97 with training durations significantly less than 100 seconds. This finding underscores the potential of FNNs, when coupled with Confidence Learning, to serve as highly efficient and effective solutions for phishing detection. Models such as DNN-BiLSTM Cleaned Raw and Semantic NLP Noisy Raw demonstrate commendable F1-Scores (approaching 0.97-0.98), indicating strong classification capabilities. However, their placement further to the right on the x-axis reveals substantially longer training times, extending into several hundred seconds. This suggests that while these models offer high accuracy, their computational demands for training may be considerable.

Conversely, certain model-dataset combinations exhibit suboptimal F1-Scores. For instance, FNN Noisy CTGAN yields a very low F1-Score (around 0.85) despite a moderate training time. Even more critically, DNN-BiLSTM Noisy CTGAN not only demonstrates poor performance but also



incurs an exceedingly long training time, approaching 1000 seconds. Such instances highlight the critical interplay between model choice, data quality, and the efficacy of augmentation techniques.

4.2 Discussions

The effectiveness of CleanLab as a noise-removal tool becomes evident when evaluating its impact across various models and datasets, particularly on FNN and the replicated DNN-BiLSTM architecture. For instance, the FNN trained on noisy raw data achieved a baseline F1-score of 0.96. After applying CleanLab to this same dataset, the accuracy improved to 0.98, marking a 2% increase. This improvement demonstrates the value of label noise correction. This enhancement also becomes more notable when compared to the replicated DNN-BiLSTM architecture, which achieved 0.97 on the same cleaned dataset. Despite the architectural sophistication of the hybrid model, the cleaned FNN still outperformed it by a margin of 1%, indicating that data quality can rival-or even outweigh complex model when it comes to performance gains.

An even more dramatic effect of label cleaning is observed on synthetically augmented datasets, particularly those generated using CTGAN. CTGAN is known to introduce a high degree of variability, and occasionally noise, due to its generative adversarial nature. When FNN was trained on the raw CTGAN-generated dataset, it recorded a poor performance of 0.85, highlighting the detrimental effect of training on synthetic samples with noisy or ambiguous labels. However, after the data was cleaned using CleanLab, the model's performance surged to 0.95, reflecting a 10% absolute improvement. This underscores the critical importance of post-synthetic label verification when using generative data augmentation strategies.

Similarly, the replicated DNN-BiLSTM architecture showed improvement when trained on SMOTE-augmented data. On raw SMOTE data, it achieved an F1-score of 0.97. After applying CleanLab, this score nudged upward to 0.98. While the gain here is modest (1%), it confirms that even high-quality oversampling methods like SMOTE can benefit from noise filtering, especially by removing subtle outliers or mislabelled data that may otherwise misguide gradient updates during training.

5.0 Conclusion

This study demonstrates that a simple Feedforward Neural Network (FNN), when trained on a dataset with label noise corrected using the Cleanlab framework, can achieve performance comparable to or surpassing more complex deep learning architectures, such as the hybridized Deep Neural Network and Bidirectional Long Short-Term Memory (DNN-BiLSTM), DNN-BiLSTM with a transformer, and DNN-BiLSTM with semantic Natural Language Processing (NLP) features, in the task of phishing URL detection. The FNN achieved an impressive F1-score of 0.98 on the cleaned raw dataset, outperforming the more sophisticated models while requiring significantly lower computational resources, with a training time of approximately 39.47 seconds compared to over 600 seconds for DNN-BiLSTM and 810.7 seconds for the transformer-based model. The application of Cleanlab for label noise correction proved critical, enhancing model performance by up to 10% on synthetically augmented datasets like those generated by CTGAN. These findings challenge the prevailing trend of pursuing increasingly complex architectures for marginal performance gains, highlighting the importance of data quality over model complexity.



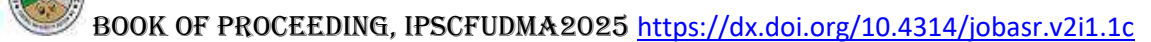
Future research could explore the generalizability of these findings across diverse datasets and cybersecurity tasks.

References

- Abdelhakim, H., & Salima, Y. (2021). Web page phishing detection. *Engineering Applications of Artificial Intelligence*.
- Ahammad, S. H., Kale, S. D., Upadhye, G. D., Pande, S. D., Babu, E. V., Dhumane, A. V., & Bahadur, M. D. K. J. (2022). Phishing URL detection using machine learning methods. *Advances in Engineering Software*. https://doi.org/10.1016/j.advengsoft.2022.103288
- Aljofey, A., Jiang, Q., Qu, Q., Huang, M., & Niyigena, J. P. (2020). An effective phishing detection model based on character level convolutional neural network from URL. *Electronics (Switzerland)*. https://doi.org/10.3390/electronics9091514
- Alsariera, Y. A., Balogun, A. O., Adeyemo, V. E., Tarawneh, O. H., & Mojeed, H. A. (2022). Intelligent tree-based ensemble approaches for phishing website detection. *Jestec.Taylors.Edu.MyYA Alsariera, AO Balogun, VE Adeyemo, OH Tarawneh, HA MojeedJ. Eng. Sci. Technol, 2022•jestec.Taylors.Edu.My, 17*(1), 563–0582. https://jestec.taylors.edu.my/Vol 17 Issue 1 February 2022/17 1 39.pdf
- Bahnsen, A. C., Bohorquez, E. C., Villegas, S., Vargas, J., & Gonzalez, F. A. (2017). Classifying phishing URLs using recurrent neural networks. *ECrime Researchers Summit, ECrime*. https://doi.org/10.1109/ECRIME.2017.7945048
- Ballesteros, M., Dyer, C., & Smith, N. A. (2015). Improved transition-based parsing by modeling characters instead of words with LSTMs. *Conference Proceedings EMNLP 2015: Conference on Empirical Methods in Natural Language Processing*. https://doi.org/10.18653/v1/d15-1041
- Balogun, A. O., Mojeed, H. A., Adewole, K. S., Akintola, A. G., Salihu, S. A., Bajeh, A. O., & Jimoh, R. G. (2021). Optimized Decision Forest for Website Phishing Detection. *Lecture Notes in Networks and Systems*. https://doi.org/10.1007/978-3-030-90321-3 47
- Correa Bahnsen, A. (2018). DeepPhish Simulating Malicious AI. *Proceedings of the Symposium on Electronic Crime Research, San Diego, CA, USA*.
- Elreedy, D., & Atiya, A. F. (2019). A Comprehensive Analysis of Synthetic Minority Oversampling Technique (SMOTE) for handling class imbalance. *Information Sciences*, *505*, 32–64. https://doi.org/10.1016/j.ins.2019.07.070
- Goodfellow, I., Pouget-Abadie, J., Mirza, M., Xu, B., Warde-Farley, D., Ozair, S., Courville, A., & Bengio, Y. (2020). Generative adversarial networks. *Communications of the ACM*, 63(11), 139–144. https://doi.org/10.1145/3422622
- Ioffe, S., & Szegedy, C. (2015). Batch normalization: Accelerating deep network training by reducing internal covariate shift. *32nd International Conference on Machine Learning, ICML 2015*, *1*, 448–456. http://proceedings.mlr.press/v37/ioffe15.html
- Karim, A., Shahroz, M., Mustofa, K., Belhaouari, S. B., & Joga, S. R. K. (2023). Phishing Detection System Through Hybrid Machine Learning Based on URL. *IEEE Access*. https://doi.org/10.1109/ACCESS.2023.3252366
- Kingma, D. P., & Ba, J. L. (2015). Adam: A method for stochastic optimization. 3rd International Conference on Learning Representations, ICLR 2015 Conference Track Proceedings.
- Lecun, Y., Bengio, Y., & Hinton, G. (2015). Deep learning. *Nature*, *521*(7553), 436–444. https://doi.org/10.1038/NATURE14539;SUBJMETA=117,639,705;KWRD=COMPUTER+SCIEN CE,MATHEMATICS+AND+COMPUTING
- Liu, D. J., Geng, G. G., & Zhang, X. C. (2022). Multi-scale semantic deep fusion models for phishing website detection. *Expert Systems with Applications*. https://doi.org/10.1016/j.eswa.2022.118305
- Northcutt, C. G., Athalye, A., & Mueller, J. (2021). Pervasive Label Errors in Test Sets Destabilize Machine Learning Benchmarks. *Advances in Neural Information Processing Systems*. https://arxiv.org/pdf/2103.14749



- Northcutt, C. G., Jiang, L., & Chuang, I. L. (2021). Confident learning: Estimating uncertainty in dataset labels. *Journal of Artificial Intelligence Research*. https://doi.org/10.1613/JAIR.1.12125
- Opara, C., Chen, Y., & Wei, B. (2024). Look before you leap: Detecting phishing web pages by exploiting raw URL and HTML characteristics. *Expert Systems with Applications*, 236. https://doi.org/10.1016/j.eswa.2023.121183
- Ozcan, A., Catal, C., Donmez, E., & Senturk, B. (2023). A hybrid DNN–LSTM model for detecting phishing URLs. *Neural Computing and Applications*. https://doi.org/10.1007/s00521-021-06401-z
- SrivastavaNitish, HintonGeoffrey, KrizhevskyAlex, SutskeverIlya, & SalakhutdinovRuslan. (2014). Dropout. *The Journal of Machine Learning Research*, *15*, 1929–1958. https://doi.org/10.5555/2627435.2670313
- Xu, L., Skoularidou, M., Cuesta-Infante, A., & Veeramachaneni, K. (2019). Modeling tabular data using conditional GAN. *Advances in Neural Information Processing Systems*, 32.
- Zhang, M., Gao, J., Lyu, Z., Zhao, W., Wang, Q., Ding, W., Wang, S., Li, Z., & Cui, S. (2020). Characterizing label errors: confident learning for noisy-labeled image segmentation. *SpringerM Zhang, J Gao, Z Lyu, W Zhao, Q Wang, W Ding, S Wang, Z Li, S CuiMedical Image Computing and Computer Assisted Intervention—MICCAI 2020: 23rd, 2020•Springer, 12261 LNCS,* 721–730. https://doi.org/10.1007/978-3-030-59710-8_70
- Zhu, E., Ju, Y., Chen, Z., Liu, F., Computing, X. F.-A. S., & 2020, undefined. (2020). DTOF-ANN: an artificial neural network phishing detection model based on decision tree and optimal features. *ElsevierE Zhu, Y Ju, Z Chen, F Liu, X FangApplied Soft Computing, 2020•Elsevier*, 95, 106505. https://doi.org/10.1016/j.asoc.2020.106505



JACOBI LAST MULTIPLIER APPROACH FOR LINEARIZATION OF THE MODIFIED EMDEN EQUATION

¹Orverem Joel Mvendaga

¹Department of Mathematics, Federal University Dutsin-Ma, Katsina State-Nigeria E-mail: orveremjoel@yahoo.com

ABSTRACT

This article linearizes the universal Modified Emden differential equation of the second order $y'' + \alpha yy' + \beta y^3 = 0$ with the constraint $\alpha^2 = 9\beta$ using the Jacobi Last Multiplier approach. The Jacobi Last Multiplier (JLM) is used to construct the equation's Lagrangian. This problem was previously examined by Orverem et al., (2021), who linearized the equation using the generalized Sundman transformation method. The results demonstrate that JLM makes linearizing the Modified Emden equation simpler and more direct.

KEY WORDS: Linearization; Modified Emden Equation; Differential Equation; Jacobi Last Multiplier.

1. INTRODUCTION

Carl Gustav Jacob Jacobi developed a traditional analytical technique in the 19th century called the Jacobi Last Multiplier (JLM) method. It offers a methodical way to identify Lagrangians and integrating factors for ordinary differential equations of second order. The approach is especially useful for researching nonlinear ODEs that are challenging to solve or linearize using conventional techniques.

The Jacobi's approach was used by Nucci & Tamizhmani, (2013) for determining the Lagrangians of any second-order differential equation, which involves calculating the Jacobi Last Multiplier. When there is a plentiful supply of symmetry, the use of the connections between a mechanical system's Lie symmetries, Jacobi Last Multiplier, and Lagrangian to create alternate Lagrangians and first integrals is achieved (Nucci & Leach, 2008). The example is a nonlinear oscillator of the Liénard type. They also provide examples of how a dynamical system's general solution and its first integrals might occasionally be incompatible.

To find the Lagrangians of the Painlevé equations, we apply a formula that Madhav Rao developed about 70 years ago that links the Jacobi Last Multiplier and its Lagrangian of a second-order ordinary differential equation (Choudhury et al., 2009). In fact, the Lagrangians of a large number of the Painlevé–Gambier classification equations are obtained using this method. The authors determine the associated Hamiltonian functions by applying the conventional Legendre transformation. It was discovered that these Hamiltonians were constants of motion, despite their typically non-standard shape. However, they used a new transformation to determine the relevant Lagrangians for second-order Liénard class equations. They identified the conserved quantity (first integral) arising from the related Noetherian symmetry and provide examples of some specific circumstances.

Some nonlinear oscillatory systems can be described using the modified Emden equation. Systems that display oscillations with amplitudes and frequencies that vary over time are relevant to both mechanical and electrical engineering. It can be used to investigate chaotic systems, where complex, erratic behaviors are produced over time by nonlinear interactions.

The nonlinear character of the modified Emden equation makes it extremely flexible and enables it to represent the intricacy of real-world systems in a wide range of fields. This study uses the Jacobi Last Multiplier technique to obtain the solution of the modified Emden differential equation.

2. METHOD OF JACOBI LAST MULTIPLIER



The Jacobi Last Multiplier (JLM) is a classical method for analyzing second-order nonlinear differential equations. It provides a systematic way to obtain a Lagrangian and, in some cases, helps to linearize or simplify the equation. For an equation of the form:

$$y'' = f(x, y, y'), \tag{1}$$

the Jacobi Last Multiplier M(x, y, y') satisfies:

$$M(y'' - f(x, y, y')) = \frac{dL}{dx'},\tag{2}$$

where L(x, y, y') is a Lagrangian function.

Given y'' = f(x, y, y'), of equation (1), the JLM satisfies

$$\frac{d}{dx}(\ln M) + \frac{\partial f}{\partial y'} = 0,\tag{3}$$

or equivalently,

$$\frac{dM}{dx} = -M \frac{\partial f}{\partial y'}. (4)$$

This is a first-order linear ordinary differential equation in *M*.

In summary, given a second-order ordinary differential equation in equation (1), compute

$$\frac{\partial f}{\partial y'}$$
.

Solve the JLM equation

$$\frac{d}{dx}(\ln M) = -\frac{\partial f}{\partial y'}.$$

Find the Lagrangian using

$$\frac{\partial^2 L}{\partial y'^2} = M.$$

Apply

$$\frac{d}{dx}\left(\frac{dL}{dy'}\right) - \frac{dL}{dy} = 0,$$

to verify the ordinary differential equation.

3. RESULTS AND DISCUSSIONS

Consider the Modified Emden Equation (MEE)

$$y'' + \alpha y y' + \beta y^3 = 0. \tag{5}$$

The aim is to linearize this equation using the Jacobi Last Multiplier (JLM) method under the special condition:

$$\alpha^2 = 9\beta. \tag{6}$$

Rewrite the modified Emden equation as:

$$y'' = -\alpha y y' - \beta y^3, \tag{7}$$

so that

$$f(x, y, y') = -\alpha yy' - \beta y^3. \tag{8}$$

The Jacobi Last Multiplier, denoted M(x, y), satisfies the partial differential equation:

$$\frac{d}{dx}(\ln M) + \frac{\partial f}{\partial y'} = 0,$$

that is, equation (3). Compute

$$\frac{\partial f}{\partial y'} = -\alpha y,\tag{9}$$

so that



$$\frac{1}{M}\frac{dM}{dx} = -\alpha y \Longrightarrow \frac{dM}{dx} = -\alpha yM.$$

Using the chain rule:

$$\frac{\partial M}{\partial x} + y' \frac{\partial M}{\partial y} = -\alpha y M. \tag{10}$$

Using method of characteristics, the characteristic equations are:

$$\frac{dx}{1} = \frac{dy}{y'} = \frac{dM}{-\alpha yM}.$$

Solving the third equation, one has that

$$\frac{dM}{M} = -\alpha y dx \Longrightarrow \ln M = -\alpha \int y(x) dx + C.$$

Thus, the JLM is:

$$M(x) = e^{-\alpha \int y(x)dx}. (11)$$

The Lagrangian L(x, y, y') satisfies:

$$\frac{\partial^2 L}{\partial v'^2} = M.$$

Integrating:

$$\frac{\partial L}{\partial y'} = My', \qquad L = \int My' \, dy' = \frac{1}{2} My'^2,$$

so that

$$L = \frac{1}{2}e^{-\alpha \int y(x)dx}y'^2. \tag{12}$$

Let us define a new variable:

$$u(x) = y(x)e^{\frac{\alpha}{2}\int y(x)dx}.$$
 (13)

Differentiate equation (13), we have

$$u' = e^{\frac{\alpha}{2} \int y(x) dx} \left(y' + \frac{\alpha}{2} y^2 \right).$$

After substitution into the modified Emden equation (MEE), and under the condition $\alpha^2 = 9\beta$, the equation becomes

$$u^{\prime\prime}=0, \tag{14}$$

which is the free particle equation — a linear second-order differential equation.

Thus, the Modified Emden-Type Equation

$$y'' + \alpha y y' + \beta y^3 = 0,$$

with

$$\alpha^2 = 9\beta$$
,

can be linearized to

$$u^{\prime\prime}=0$$
,

via the transformation

$$u = y. e^{\frac{\alpha}{2} \int y(x) dx},$$

and the Jacobi Last Multiplier

$$M = e^{-\alpha \int y(x)dx}$$

It is important to note that the Lagrangian $L(q_i, q'_i, t) = T - V$ (kinetic energy minus potential energy) is a key component of Lagrangian mechanics, which is a reformulation of Newtonian mechanics. Instead of providing vector equations, it offers a scalar function (Lagrangian), which is useful in non-Cartesian coordinates or systems with constraints.



4. CONCLUSION

The linearization of the extensively researched modified Emden equation (MEE) using the Jacobi Last Multiplier (JLM) method is covered in this study. The Jacobi Last Multiplier is used to construct the appropriate Lagrangian. The modified Emden equation is reduced to the second-order free particle linear equation with an appropriate transformation.

REFERENCES

- Choudhury, A. G., Guha, P., & Khanra, B. (2009). On the Jacobi Last Multiplier, integrating factors and the Lagrangian formulation of differential equations of the Painlevé Gambier classification. *Journal of Mathematical Analysis and Applications*, 360(2), 651–664. https://doi.org/10.1016/j.jmaa.2009.06.052
- Nucci, M. C., & Leach, P. G. L. (2008). The Jacobi Last Multiplier and its applications in mechanics. *PHYSICA SCRIPTA*, 065011(78), 1–6. https://doi.org/10.1088/0031-8949/78/06/065011
- Nucci, M. C., & Tamizhmani, K. M. (2013). Lagrangians for Dissipative Nonlinear Oscillators: the Method of Jacobi Last Multiplier Oscillators. *Journal of Nonlinear Mathematical Physics ISSN*:, 9251, 167–178. https://doi.org/10.1142/S1402925110000696
- Orverem, J. M., Haruna, Y., Abdulhamid, B. M., & Adamu, M. Y. (2021). Linearization of Emden Differential Equation via the Generalized Sundman Transformations. *Advances in Pure Mathematics*, 11, 163–168. https://doi.org/10.4236/apm.2021.113011



Role of Phytoestrogenic Plants in Tilapia Production: Leveraging *Eriosema psoraleoides* as a Biotechnological Approach for Sustainable Aquaculture Diversification in Nigeria

*Nwangwu, D.C.^{1,2}, Bake, G.G.², Sadiku, S.O.E² and Mann, A².

- 1. Fish Genetics and Biotechnology Programme, National Institute for Freshwater Fisheries Research, P.M.B. 6006, New Bussa, Nigeria
- 2. Water Resources, Aquaculture and Fisheries Technology Department, Federal University of Technology, P.M.B. 65, Minna, Nigeria.

Abstract

Tilapia species (especially Oreochromis niloticus - Nile tilapia) are ready to play a crucial role in diversifying Nigeria's aquaculture sector, currently dominated by catfish and their hybrids. However, prolific reproduction in tilapia leads to stunted growth and economic losses, limiting their commercial potential. While synthetic hormones like 17-alpha-methyltestosterone (17-α-MT) are commonly used for reproduction control in tilapia production, their environmental persistence and health risks necessitate sustainable alternatives. Phytoestrogenic plants particularly Eriosema psoraleoides (Canary pea) offer a promising, sustainable solution. The review integrates current knowledge on the efficacy of known phytoestrogenic plants in tilapia reproduction management, highlighting their mechanisms in altering sex hormone levels (estradiol, testosterone, vitellogenin) and gonadosomatic indices. E. psoraleoides stands out due to its unique prenylated flavonoids, which may simultaneously inhibit aromatase (CYP19a1a) and enhance androgenic pathways. Consequently, a research framework is suggested to validate its efficacy, with emphasis on (1) dose optimization for fecundity reduction without compromising growth, (2) dual estrogen-androgen modulation and (3) better palatability over bitter alternatives like Azadirachta indica (neem). In Nigeria, where tilapia farming is expanding, E. psoraleoides presents a locally available, environmentally friendly and cost-effective alternative to synthetic hormones. By integrating E. psoraleoides into tilapia feed, Nigeria tilapia farmers could achieve two crucial goals: (1) mitigating overpopulation in farmed tilapia, and (2) accelerating species diversification to strengthen food security. This review underscores the urgent need to explore and invest in locally available phytoestrogenic plant-based solutions specifically adapted to the unique challenges of farmed tilapia production.

Keywords: Phytoestrogens, *Eriosema psoraleoides*, Tilapia, Sustainable Aquaculture, Nigeria

Introduction

Aquaculture in Nigeria has undergone substantial expansion over the past two decades, positioning the country as the second-largest aquaculture producer in Africa. This growth has been largely driven by the dominance of African catfish (*Clarias gariepinus*) and its hybrids, prized for their rapid growth, adaptability, and market demand (Ogunji & Wuertz, 2023). However, the sector's over-reliance on catfish has raised concerns regarding genetic bottlenecks, market saturation, and heightened vulnerability to disease outbreaks, which threaten long-term sustainability (Ibidapo-Obe & Yussuf, 2024).

In response to these challenges, stakeholders have increasingly turned to tilapia species, particularly *Oreochromis niloticus* (Nile tilapia), as a viable alternative for diversifying Nigeria's aquaculture portfolio. Nile Tilapia is recognized for its resilience, efficient feed conversion, and broad consumer acceptance, making it a strong candidate for commercial expansion (Ragasa *et al.*, 2023). Nonetheless, its prolific reproductive capacity presents a significant constraint. In



uncontrolled culture systems, excessive breeding often results in overcrowding, stunted growth, and diminished economic returns, a factor that undermines production efficiency and profitability. To address these reproductive challenges, synthetic hormones such as 17α -methyltestosterone (MT) have been widely employed in tilapia aquaculture to produce monosex male populations, which generally exhibit superior growth performance. According to Mlalila *et al.* (2015), the effectiveness of MT is offset by concerns over its persistence in aquatic environments and the potential for endocrine-disrupting effects on non-target organisms. Silva *et al.* (2023) similarly emphasize that residues of synthetic steroids in culture systems pose risks to both ecosystems and public health. These challenges have stimulated interest in sustainable approaches, and recent reviews by Wokeh *et al.* (2021) and experimental evidence from Jamal *et al.* (2024) highlight the promise of plant-based alternatives capable of achieving reproductive control without the ecological risks associated with synthetic hormones.

Among the emerging candidates, phytoestrogenic plants have garnered attention for their ability to modulate hormonal pathways in fish (Ahmadifar *et al.*, 2025; Farooq *et al.*, 2025). *Eriosema psoraleoides* (Canary pea), a leguminous plant native to West Africa, has attracted interest due to its unique phytoestrogenic profile and local availability (Burkill, 1995). Preliminary studies indicate its potential to influence sex differentiation and suppress reproduction in tilapia, offering a natural and ecologically sound alternative to synthetic hormone treatments (Abaho *et al.*, 2023) This review explores the potential of *E. psoraleoides* as a sustainable alternative to synthetic hormones in tilapia farming. It integrates current knowledge on phytoestrogenic mechanisms, evaluates hormonal and physiological impacts, and proposes a research framework tailored to Nigeria's aquaculture landscape.

Conventional Reproduction Control in Tilapia

Oreochromis niloticus, commonly known as Nile tilapia, is widely acknowledged for its prolific reproductive capacity in tropical and subtropical environments. Although this trait is biologically advantageous, it presents significant challenges in aquaculture systems. As Syanya et al. (2025) observe, mixed-sex populations of O. niloticus often experience uncontrolled breeding, which leads to overcrowding, heightened competition for feed and space, and ultimately results in stunted growth and reduced market value. If left unmanaged, this reproductive efficiency can severely compromise production outcomes and threaten the economic sustainability of intensive aquaculture operations.

To address these reproductive constraints, aquaculturists have adopted various control strategies, with synthetic hormone treatment remaining the most widely practiced. Karaket *et al.* (2023) demonstrated that the application of androgens—particularly 17α -methyltestosterone (MT) during early developmental stages effectively induces masculinization in *O. niloticus*. This technique yields monosex male populations, which are preferred due to their superior growth rates and more uniform size distribution compared to females. The authors further note that this approach not only enhances growth performance but also alleviates reproductive pressure within the system, thereby improving overall operational efficiency.

Use of Synthetic Hormones

The administration of synthetic androgens, particularly 17α -methyltestosterone (MT), remains a widely practiced method for generating monosex male populations in *Oreochromis niloticus* culture. MT is typically delivered via feed during the critical developmental window (between 3 – 28 days post-hatch) when sex differentiation is most responsive to hormonal modulation. This principle has been substantiated in recent trials, where male ratios exceeding 95% were achieved,



alongside marked improvements in growth performance and feed conversion efficiency (Hassan et al., 2025).

Despite its effectiveness, concerns have emerged regarding the environmental persistence, bioaccumulation, and endocrine-disrupting potential of MT. Hassan *et al.* (2025) caution that although MT remains a potent tool for sex reversal, its unregulated use may pose risks to fish health, human consumers, and aquatic ecosystems. These findings highlight the need for dosage optimization, regulatory oversight, and the exploration of safer, alternative reproductive control strategies.

Environmental and Health Concerns

The application of synthetic hormones such as 17α-methyltestosterone (MT) in aquaculture has raised considerable environmental and public health concerns. These compounds are known to leach into adjacent water bodies, where they may affect non-target organisms and disrupt aquatic ecosystems. Residual hormones have been associated with altered reproductive behaviors and the emergence of intersex conditions in wild fish populations. Recent findings by Li *et al.* (2024) suggest that similar endocrine disruptions occur in *Oreochromis* spp. exposed to non-steroidal aromatase inhibitors, such as tamoxifen citrate, which are increasingly used as alternatives to MT. Beyond ecological implications, the improper handling and excessive use of MT present occupational hazards for aquaculture workers and potential health risks for consumers, especially in regions with limited regulatory oversight. In Nigeria, where small-scale and semi-intensive aquaculture systems are prevalent, the absence of standardized protocols for hormone administration exacerbates the risk of misuse and environmental contamination. These challenges underscore the urgent need for safer and more sustainable alternatives. Phytogenic agents have shown promise in aligning reproductive control strategies with ecological conservation and public health objectives (Ahmadifar *et al.*, 2025)

Regulatory and Ethical Perspectives on Synthetic Hormone Use in Aquaculture

The global use of synthetic hormones in aquaculture particularly 17α-methyltestosterone (MT) is under increasing regulatory scrutiny due to mounting concerns over environmental safety and consumer health. Regulatory bodies in the European Union, United States, and China have formally banned the use of MT in food fish production, citing its classification as an endocrine-disrupting compound and its potential to harm non-target aquatic organisms (Li *et al.*, 2024). Although Nigeria has yet to implement similar restrictions, growing awareness of sustainability and public health implications is expected to shape future policy, especially as aquaculture expands within smallholder and semi-intensive systems.

Ethical considerations are also gaining traction, particularly in the context of organic aquaculture and eco-labeling initiatives. Consumers are increasingly demanding transparency in production practices, and hormone-free fish products are becoming more desirable in global markets. The Food and Agriculture Organization (FAO) emphasizes in its *State of World Fisheries and Aquaculture 2020* report that sustainability and responsible sourcing are now central to aquaculture certification schemes. These frameworks prioritize environmental integrity, animal welfare, and food safety, and are influencing industry standards worldwide (Action, 2020; Fisheries, 2007). In response to these evolving expectations, interest is growing in plant-based reproductive modulators which offer promising efficacy without the ecological and ethical risks associated with synthetic hormone treatments.

Phytoestrogenic Plants as Sustainable Alternatives



The pursuit of sustainable and ecologically sound alternatives to synthetic hormones in aquaculture has intensified interest in phytoestrogenic plants—botanical sources rich in bioactive compounds capable of mimicking or modulating vertebrate sex hormones. These plants offer a promising pathway for reproductive control in *Oreochromis* spp. culture, particularly in regions such as Nigeria, where environmental safety, affordability, and local availability are critical considerations. As aquaculture continues to expand globally, the integration of plant-based feed ingredients containing phytoestrogens has gained relevance not only for their nutritional contributions but also for their endocrine-modulating potential. Nwangwu *et al.* (2024) demonstrated that *Jatropha curcas* seed meal, when processed and incorporated into tilapia diets, significantly suppressed reproduction while maintaining growth performance and feed efficiency, underscoring the viability of phytogenic agents as functional alternatives to synthetic sex reversal compounds

Understanding Phytoestrogens

Phytoestrogens are non-steroidal, polyphenolic compounds naturally synthesized by plants. Structurally analogous to 17β-estradiol, they possess the capacity to bind to estrogen receptors and influence endocrine signaling pathways. These compounds are broadly categorized into isoflavones, lignans, and coumestans, with isoflavones particularly genistein and daidzein being the most extensively studied due to their pronounced hormonal activity (Muhammad *et al.*, 2023). In aquatic organisms, phytoestrogens have been shown to alter sex differentiation, suppress gonadal maturation, and modulate circulating levels of sex steroids such as estradiol and testosterone (Shohreh *et al.*, 2024). Their presence in plant-based aquafeeds, especially those incorporating soybean derivatives, underscores the need for a nuanced understanding of their biological effects across fish species.

Mechanisms of Action in Fish

In aquaculture, phytoestrogens exert their influence through multiple mechanisms. First, they engage estrogen receptors, competing with endogenous estrogens to either mimic or antagonize hormonal signals. This receptor-mediated activity can result in feminization or masculinization depending on the compound, dosage, and species involved (Farooq *et al.*, 2025). Second, certain phytoestrogens inhibit aromatase (*CYP19a1a*), the enzyme responsible for converting androgens into estrogens. This inhibition shifts the hormonal equilibrium toward androgenic dominance, facilitating male-biased sex differentiation—a desirable outcome in tilapia production where males exhibit superior growth rates. Third, phytoestrogens can suppress vitellogenin synthesis, a yolk precursor protein regulated by estrogens and commonly used as a biomarker for estrogenic exposure. Reduced vitellogenin expression indicates reproductive suppression and supports the utility of phytoestrogens in early developmental interventions (Muhammad *et al.*, 2023).

Collectively, these mechanisms position phytoestrogenic plants as compelling candidates for sex control strategies in tilapia aquaculture. Their natural origin, relative safety, and compatibility with sustainable feed formulations align with the broader goals of environmentally responsible aquaculture, particularly in developing regions where synthetic hormone use is constrained by regulatory and ecological concerns.

Advantages of Plant-Based Alternatives

In contrast to synthetic hormones, phytoestrogenic plants offer a suite of strategic advantages that align with the principles of sustainable aquaculture. Environmentally, these compounds are naturally biodegradable and exhibit lower persistence in aquatic ecosystems, thereby minimizing the risk of endocrine disruption in non-target organisms. Their ecological compatibility makes



them particularly suitable for integration into semi-intensive and smallholder systems, where effluent management is often limited (Farooq *et al.*, 2025).

From a consumer standpoint, plant-based hormonal modulators resonate with the increasing demand for organic and hormone-free aquaculture products. As global markets shift toward transparency and sustainability, the use of phytogenic agents enhances certification potential and market acceptance, particularly within eco-labeling and organic aquaculture frameworks (Shohreh *et al.*, 2024). These trends are reinforced by evolving ethical standards that prioritize environmental integrity, animal welfare, and food safety.

Economically, the use of phytoestrogenic plants offers distinct advantages in regions such as Nigeria, where many effective species including *Eriosema psoraleoides*, *Carica papaya*, and *Azadirachta indica* are indigenous and readily available. This localization reduces dependency on imported inputs and supports economic resilience by enabling smallholder farmers to adopt reproductive control strategies without incurring prohibitive costs. The ease of cultivation or wild harvesting further enhances the cost-effectiveness of these plants, making them accessible to resource-constrained producers and compatible with low-input production models (Muhammad *et al.*, 2023).

Collectively, these benefits underscore the potential of phytoestrogens as strategic tools for advancing sustainable aquaculture development in Nigeria and other tropical regions. Their integration into Tilapia production systems could mitigate the ecological and ethical concerns associated with synthetic hormone use, while fostering inclusive, environmentally responsible growth across the sector.

Proposed Research Framework

To validate and optimize the application of *Eriosema psoraleoides* and other phytoestrogenic plants in tilapia aquaculture, a structured research framework is essential. This framework should address key biological, nutritional, and ecological dimensions to ensure efficacy, safety, and scalability across diverse production systems.

Dose Optimization

Establishing effective concentrations of *E. psoraleoides* extracts is critical to achieving reproductive suppression without compromising somatic growth. Controlled trials should be conducted across different developmental stages, particularly during the early post-hatch window when sex differentiation is most plastic. This is to determine timing sensitivity and hormonal responsiveness. Dose-response studies will help identify thresholds that balance reproductive control with growth performance, minimizing adverse physiological effects.

Dual Hormonal Modulation

The phytoestrogenic profile of *E. psoraleoides* suggests potential for dual modulation of endocrine pathways. Investigations should focus on the compound's ability to suppress estrogenic activity while enhancing androgenic signals. Molecular assays targeting gene expression in aromatase (*CYP19a1a*) and androgen receptor (AR) pathways will provide insights into the mechanistic basis of sex differentiation and reproductive suppression. These studies will also clarify whether *E. psoraleoides* act primarily through receptor binding, enzymatic inhibition, or transcriptional regulation — key factors in designing targeted interventions.

Palatability and Feed Integration

For practical adoption, the palatability of *E. psoraleoides*-based feed formulations must be assessed relative to other phytoestrogenic plants such as *Carica papaya* and *Azadirachta indica*.



Comparative trials should evaluate feed acceptance, growth performance, and nutrient utilization across different inclusion levels. Developing standardized feed formulations that incorporate *E. psoraleoides* extracts, either as whole plant material or purified compounds, will facilitate consistent application and dosage control. These formulations should be tested under semi-intensive and smallholder conditions to ensure relevance to Nigeria's aquaculture landscape.

Implications for Nigerian Aquaculture

The integration of *Eriosema psoraleoides* into tilapia farming aligns closely with Nigeria's strategic objectives for sustainable aquaculture development. Its indigenous status reduces reliance on imported inputs, thereby enhancing local resource utilization and economic resilience. Moreover, its biodegradable nature and low ecological footprint support long-term ecosystem health, addressing growing concerns over environmental degradation linked to synthetic hormone use

Species diversification remains a critical priority for Nigerian aquaculture, which has historically been dominated by *Clarias gariepinus*. By improving the viability and manageability of *Oreochromis niloticus*, farmers can reduce monoculture dependency and expand market offerings, contributing to a more balanced and resilient aquaculture sector. Enhanced reproductive control through plant-based modulators also supports food security by enabling more predictable yields and efficient resource management - key factors in addressing Nigeria's protein deficit and malnutrition challenges1.

Furthermore, the economic empowerment of smallholder farmers is a central benefit of adopting *E. psoraleoides*. Its local availability and ease of cultivation make it a low-cost solution that is accessible to producers operating in semi-intensive systems. By reducing input costs and improving production outcomes, *E. psoraleoides* can contribute to poverty alleviation and inclusive growth in rural aquaculture communities.

Future Directions and Recommendations

To fully harness the potential of *E. psoraleoides*, a coordinated research and policy agenda is essential. First, standardization efforts should focus on developing protocols for extract preparation, dosage calibration, and feed formulation to ensure consistency and safety across production systems. Second, field validation through multi-site trials is necessary to assess efficacy under diverse environmental and operational conditions, particularly within Nigeria's varied agroecological zones.

Policy support will play a pivotal role in promoting plant-based alternatives and regulating synthetic hormone use. Regulatory frameworks should incentivize sustainable practices, establish safety thresholds, and integrate phytogenic agents into national aquaculture guidelines. Finally, stakeholder engagement is critical. Collaborative efforts involving farmers, researchers, extension agents, and policymakers will ensure that innovations are contextually relevant, socially accepted, and economically viable.

Conclusion

The prolific reproductive nature of tilapia presents a persistent challenge to commercial aquaculture in Nigeria. While synthetic hormones such as 17α -methyltestosterone have demonstrated efficacy in reproductive control, their environmental persistence and potential health risks necessitate the exploration of safer alternatives. *Eriosema psoraleoides*, with its unique hormonal properties and indigenous availability, offers a promising solution that aligns with ecological sustainability and economic accessibility.

By integrating *E. psoraleoides* into tilapia feed, Nigerian farmers can achieve dual objectives: mitigating overpopulation and accelerating species diversification. This review highlights the



urgent need to invest in plant-based reproductive modulators tailored to the ecological and economic realities of Nigerian aquaculture. Such innovations will not only enhance production efficiency but also contribute to the broader goals of food security, environmental stewardship, and rural development.

REFERENCES

- Abaho, I., Gabriel, N. N., & Izaara, A. A. (2023). Use of plant extracts to control reproduction in tilapia production systems: An Emerging Eco-Friendly Innovation. In *Emerging Sustainable Aquaculture Innovations in Africa* (pp. 167–196). Springer.
- Action, S. (2020). World fisheries and aquaculture. Food and Agriculture Organization, 2020, 1–244.
- Ahmadifar, E., Fallah, H. P., Chandran, D., Mohammadzadeh, S., Dehghani, M., Guerreiro, I., Abaho, I., Yousefi, M., & Abdel-Latif, H. M. (2025). Botanical Interventions for Controlling Reproduction in Fish–an Overview. *Annals of Animal Science*, 25(3), 921–928.
- Burkill, H. (1995). The useful plants of west tropical Africa, vol. 3, Families J-L, 857. *Royal Botanic Gardens, Kew, UK*.
- Farooq, S., Bhat, N. M., Dar, S. A., & Malik, M. A. (2025). Phytoestrogens in aquaculture: friend or foe to fish growth and reproductive health? *Blue Biotechnology*, 2(1), 15.
- Fisheries, F. (2007). The state of world fisheries and aquaculture. 2006.
- Hassan, H. U., Ali, A., Al Sulivany, B. S., Kabir, M., Kanwal, R., Ahmed, M. Z., Ghaffar, R. A., Ijaz, M. Z., Rafiq, N., & Mahwish, M. (2025). Effects of Tribulus terrestris extract and 17 α-methyl testosterone on masculinization, growth, economic efficiency and health assessment of Nile tilapia (Oreochromis niloticus). *Aquaculture International*, *33*(2), 156.
- Ibidapo-Obe, E., & Yussuf, K. (2024). SPECIES DIVERSIFICATION, A POSITIVE TREND TOWARD NIGERIA'S AQUACULTURE SUSTAINABILITY: A REVIEW. Federal Polytechnic Ilaro Journal of Pure And Applied Sciences, 6(1).
- Jamal, R., Asad, F., Naz, S., & Hussain, S. M. (2024). Comparative assessment of natural and synthetic reproductive inhibitors in Oreochromis niloticus. *International Journal of Agricultural and Biological Engineering*, 17(5), 284–292.
- Karaket, T., Reungkhajorn, A., & Ponza, P. (2023). The optimum dose and period of 17α-methyltestosterone immersion on masculinization of red tilapia (Oreochromis spp.). *Aquaculture* and Fisheries, 8(2), 174–179.
- Li, T., Xiong, Z., Liu, Y., Zhao, H., Rong, W., Chen, Y., Chen, G., Cao, L., Liu, Q., & Song, J. (2024). Mechanism of vitamin C alleviating the immunotoxicity of 17α-methyltestosterone in Carassius auratus. *BMC genomics*, 25(1), 1068.
- Mlalila, N., Mahika, C., Kalombo, L., Swai, H., & Hilonga, A. (2015). Human food safety and environmental hazards associated with the use of methyltestosterone and other steroids in production of all-male tilapia. *Environmental Science and Pollution Research*, 22(7), 4922–4931.
- Muhammad, N. P., Nirmal, T., Prabhakaran, A., & Varghese, T. (2023). Phytoestrogens as Endocrine-Disrupting Agents in Aquaculture. In *Xenobiotics in Aquatic Animals: Reproductive and Developmental Impacts* (pp. 213–231). Springer.
- Nwangwu, D. C., Bake, G. G., Orire, A. M., Ibiyo, L. M. O., & Yisa, M. (2024). Role of phytoestrogenic plants in smart and sustainable tilapia aquaculture in Nigeria. In *Futuristic Trends in Agriculture Engineering & Food Sciences* (Vol. 3, pp. 1–15). IIP Series.
- Ogunji, J., & Wuertz, S. (2023). Aquaculture development in Nigeria: The second biggest aquaculture producer in Africa. *Water*, 15(24), 4224.



- Ragasa, C., Onoja, A., Siriwardena, S., Ansa, E., & Popoola, O. (2023). Stakeholders Consultation on the National Fisheries Fisheries and Aquaculture Policy (2024-2028).
- Shohreh, P., Mohammadzadeh, S., Mood, S. M., Ahmadifar, E., Naiel, M. A., & Chandran, D. (2024). The potentials of phytoestrogen compounds in aquaculture—a review. *Annals of Animal Science*, 24(3), 695–705.
- Silva, R. C., Britto, D. M. C., Santos, C. A., Giordani, S. C. O., & Pedreira, M. M. (2023). Sexual differentiation and sex reversal in tilapia (Oreochromis niloticus) by hormone 17 α methyltestosterone similar to that used in cultivation systems. *Aquaculture*, 574, 739624.
- Syanya, F. J., Mahadevan, H., & Khanna, A. N. (2025). The effects of a non-steroid aromatase inhibitor on hybrid red tilapia masculinization, growth, reproductive hormone profile, and economic efficiency in aquaculture. *Aquaculture International*, 33(2), 160.
- Wokeh, O. K., Orose, E., Wokeh, O., & Orose, E. (2021). Use of dietary phytochemicals as control for excessive breeding in Nile Tilapia (Oreochromis niloticus): a review. *GSC Biological and Pharmaceutical Sciences*, 17(2), 152–159.

MOLECULAR DOCKING, DRUG-LIKENESS AND SWISSADME EVALUATIONS OF SOME POLYPHENOLS WITH FTO INHIBITORY PROPERTIES

¹ Sada Maryam H., Bello Oluwasesan M. and ² Sani Suleiman
 ¹Department of Chemistry, Faculty of Physical Sciences, Federal University Dutsinma, Katsina State, PMB 5001, Nigeria.

Chemistry Unit, School of General Studies, Federal University of Transportation Daura, Katsina State, PMB 1050 Nigeria.

*Corresponding author's email: mhassansada@fudutsinma.edu.ng

ABSTRACT

The orthodox approach to investigating lead compounds is a time-consuming and tedious one that generally yields few results. An alternate route to drug discovery via the interactions of two or more complexes is offered by molecular docking analysis. A few chosen polyphenols were subjected to molecular docking studies with the FTO protein target in order to anticipate their SwissADME characteristics, drug-likeness and predicted biological activities using PASS. The UCSF Chimera was used for the docking investigations, which examined the molecular interactions between the ligands and the target protein, sesamin, pinoresinol and chondrillasterol were the compounds with higher docking scores according to the docking study. It was discovered that the molecular weight (sesamin; MW of 345.34, pinoresinol; 358.39; chondrillasterl; 419.69 g/mol respectively) the number of H-bond acceptor; (s; 6; p; 6; c; 1) and donors (s;0; p;2 c; 1) respectively appeared within permissible bounds, the TSPA of the compounds all fully complied with the Lipinski rule limitations. With the exception of chondrillasterol, the compounds (sesamin, pinoresinol and Ononin) exhibit strong gastrointestinal absorption, BBB penetration, and inhibition of permeability glycoprotein (P-gp) substrate. They are also cytochrome CYP3A5 inhibitors. Also According to the results of PASS, pinoresinol and ononin have the highest predicted biological activities; Pinoresinol have been predicted to have antioxidant (0.632), free radical scavenger (0.526), CYP3A5 (0.509) substrate, anti-carcinogenic (0.576) and for ononin, has predicted activity (0.540) for antibacterial, (0.634) antifungal, (0.939) anti-ineffective, (0.616) anti-inflammatory, (0.707) antioxidant, (0.726) free radical scavenger, (0.521) CYP3A, (0.912) anticarcinogenic and (0. 615) anti-diabetic. This indicates the potential of the pinoresinol and ononin for the biological activities and for their multiple medicinal properties such as antioxidant, free radical scavenging, anti-inflammatory, and cyto-protective activities. These findings might influence future FTO agent optimization.



Keywords: Molecular docking, Drug-likeness, ADME, 3LMF protein.

INTRODUCTION

Due to the availability of chemical diversity, secondary metabolites, such as plant extracts in the form of pure chemicals or standardized extracts, present countless prospects for the identification of novel medications (Badock et al., 2024). Numerous compounds found in plants used in traditional medicine have the potential to be used in the treatment of chronic illnesses. Plants contain chemical molecules called active ingredients that have specific physiological effects on human bodies. Among the most beneficial are calcium, phosphorus, and flavonoids as well as polyphenols (Badock et al., 2024). Over 60% to 80% of people worldwide rely on complementary and integrative medicine, according to WHO data, which amply illustrates the importance of traditional medicine in contemporary healthcare. Plants high in polyphenols have been shown to reduce inflammation and act as antioxidants, which helps to treat a wide range of illnesses (Adamu et al., 2023). Given the indisputable proof of the effectiveness of plant-based chemicals, especially secondary metabolites), both in the avoidance and management of illnesses in humans. The bacterial community in the human gut may be impacted by the prolonged consumption of plant products and specific phytochemicals with antimicrobial qualities because polyphenolic compounds, the most abundant secondary metabolites in plants, are potent antimicrobial agents (Stefaniu and Pirvu, 2022).

Fat mass and obesity-associated protein (FTO) is a dioxygenase enzyme that acts on N6-methyladenosine (m6A) and N6,2'-O-dimethyladenosine (m6Am) in eukaryotic mRNA to cause a most common internal alteration. Additionally, it catalyzes the demethylation of thymidine and uracil DNA bases. A portion of the physiological function of FTO-dependent methyladenosine control has been identified. This metabolic alteration has drawn a lot of interest. Numerous researches have demonstrated on the correlation between FTO gene polymorphism and obesity with increased body mass (Ruud et al., 2019). The widespread inactivation of FTO reduces adiposity and protects against diet-induced obesity, while overexpressing FTO in mice results in an increase in body mass and fat (Fischer et al., 2009).

A relatively new bioinformatics method called "molecular docking" has been extensively researched to examine how pharmaceuticals interact molecularly with their target protein, or receptor (Trott and Olson 2009). A global source of databases on the dimensional structure of biological macromolecules is the Protein Data Bank (PDB). Drug compounds can be found in the open-source chemistry database PubChem. A software suite called AutoDock Vina is designed to forecast the ideal conformations for bindings between ligands and proteins (Vina et al., 2020). The purpose of this work is to forecast potential ligand orientation, binding affinity, and physical interactions between and FTO.

Materials and Method

Preparation of Proteins receptor

The RCSB (Research Collaboratory for Structural Bioinformatics) PDB (Protein Data Bank) was the source of the 3D structures of the two FTO proteins (receptors) that were employed; PDB IDs for these proteins are 3LFM and 1GNG (https://www.rcsb.org/).Prior to molecular docking, the protein underwent the following pretreatment procedures: all ions, water molecules, and internal ligands were eliminated, and polar hydrogen atoms and Gasteiger charges were added to the protein system. Using the UCSF Chimera software version 1.16



(https://www.rbvi.ucsf.edu/chimera/), this procedure was carried out, and the produced protein was stored in a PDB file for additional (Rakshit et al., 2023).

Preparation of Ligand

The open-source chemical database PubChem (https://pubchem.ncbi.nlm.nih. gov/) provided the 3D structures of the selected polyphenol compounds sesamin, pinoresinol, chondrillasterol, and ononin. The compounds were prepared for ligands by adding hydrogen atoms and Gasteiger charges along with the conventional MCFA using UCSF Chimera software version 1.16 (https://www.rbvi.ucsf.edu /chimera/). The structures (.PDB) were then saved for molecular docking with FTO (Mandal and Mandal, 2024).

Molecular Docking

UCSF Chimera version 1.16 (https://www.cgl.ucsf.edu/chimera/) was used to do the molecular docking in order to identify the protein-ligand interaction and confirm the binding affinity in terms of the ligands' binding energy against the FTO. Auto Dock Vina was used for this purpose. The structures (PDB files) were uploaded into the AutoDock vina platform in order to dock the ligands with the protein. Blind docking was used to attach one ligand per analysis. In order to enable unrestricted mobility of the ligands during docking and recognition of the protein's binding sites, a grid box covering the complete protein structure was constructed. For every ligand, the docked complex which showed the lowest binding energy and the best ligand poses with zero RMSD was chosen. Using BIOVIA Discovery Studio v21.1.0.20298 (https://www.3ds.com/products-services/biovia/products/molecular-modelingsimulation/biovia discovery-studio/visualization/), the protein-ligand docked complex produced by molecular docking was visualized for intermolecular interaction analysis, taking into account the bond/interaction types (formed between ligand and receptor residues) and bond distances (Sarkar et al., 2022).

Pharmacological analysis of the ligands

Chemo informatics is frequently employed to predict the relative properties of molecules' Absorption, Distribution, Metabolism, Excretion, and Toxicity (ADME-Tox) as part of the search for new drugs. This helps to improve the molecules' pharmacokinetic properties by removing those that would not be good drug candidates. Therefore, we transformed the compounds in our study into SMILES format and applied the pkCSM website, which offers ADMET information, to every molecule. In addition, for a drug to be effective and bio-available, it must also have other characteristics, and it must also follow rules which are called Lipinski's rules which were calculated by using the Swissadme server (http://www.swissadme.ch/). (Mandal and Mandal, 2024; Lipinski et al., 2012; Daina et al., 2016).

PASS (Prediction of Activity Spectra for Substances) is a computer program that predicts different kinds of biological activity with an average accuracy above 95%, and can be used to assess the total biological potential of drug-like substances based on their SMILES by using version 2.0 (Sucularlı et al., 2022), http://www.way2drug.com/passonline/) (Daina and Zoete, 2017).

Results and Discussion Molecular docking analysis



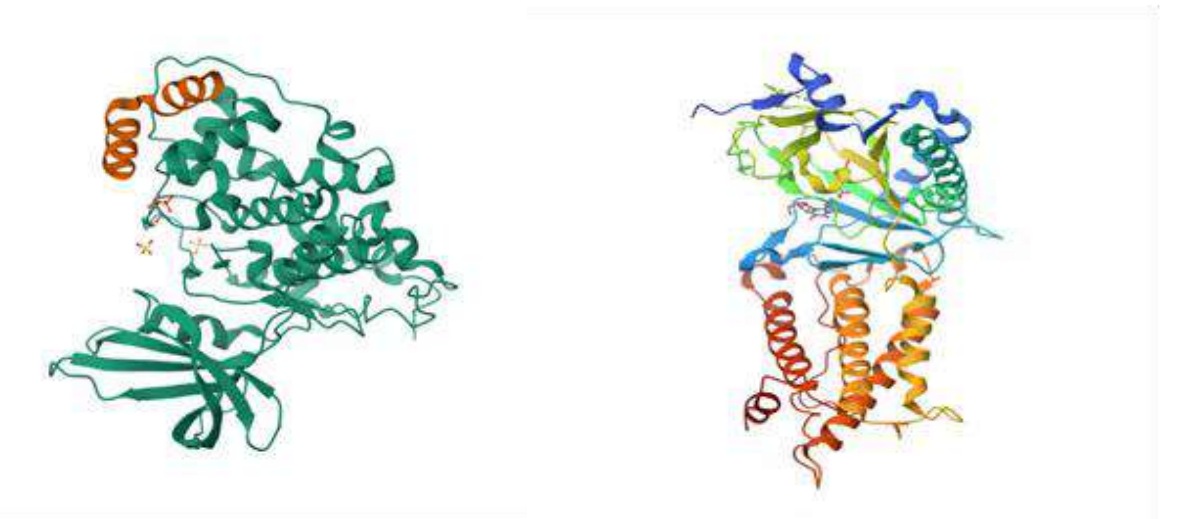


Fig. 1. Fat mass and obesity-associated protein (FTO). 3-D model of 1GNG and 3LFM respectively retrieved from protein data bank (https://www.rcsb.org/structure/4IE7).

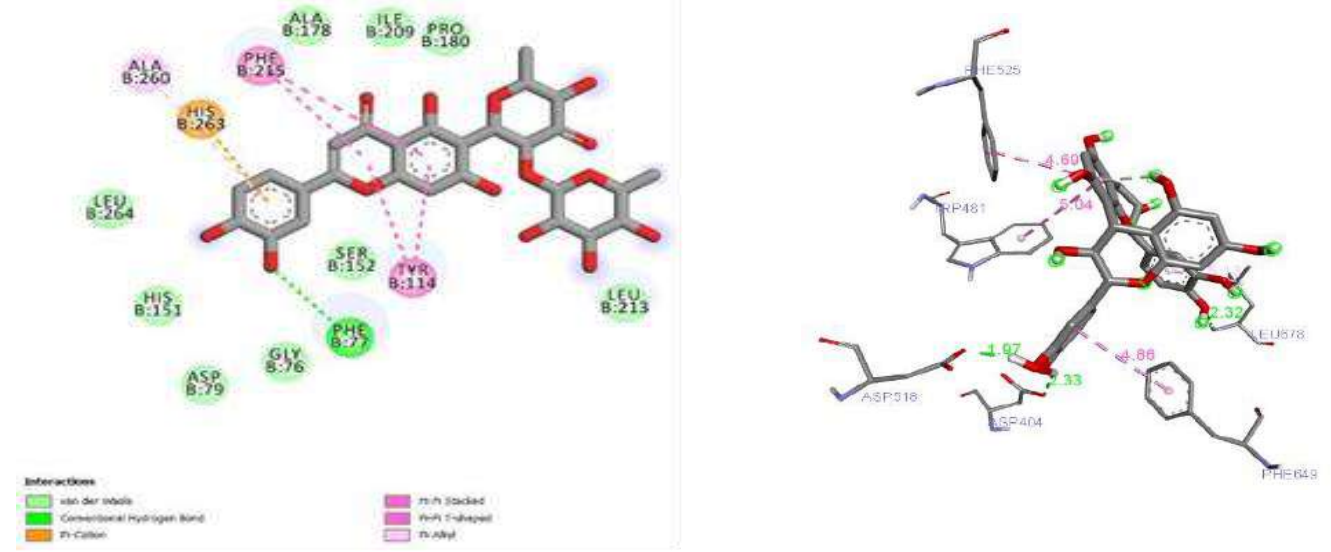


Fig. 2. Molecular docking analysis of FTO– Sesamin complex. 3-D interaction diagram showing FTO amino acid residues interacting with Sesamin and 2-D interaction diagram showing FTO amino acid residues with different bond interactions against Sesamin. FTO, fat mass and obesity-associated protein; 1GNG, Sesamin.



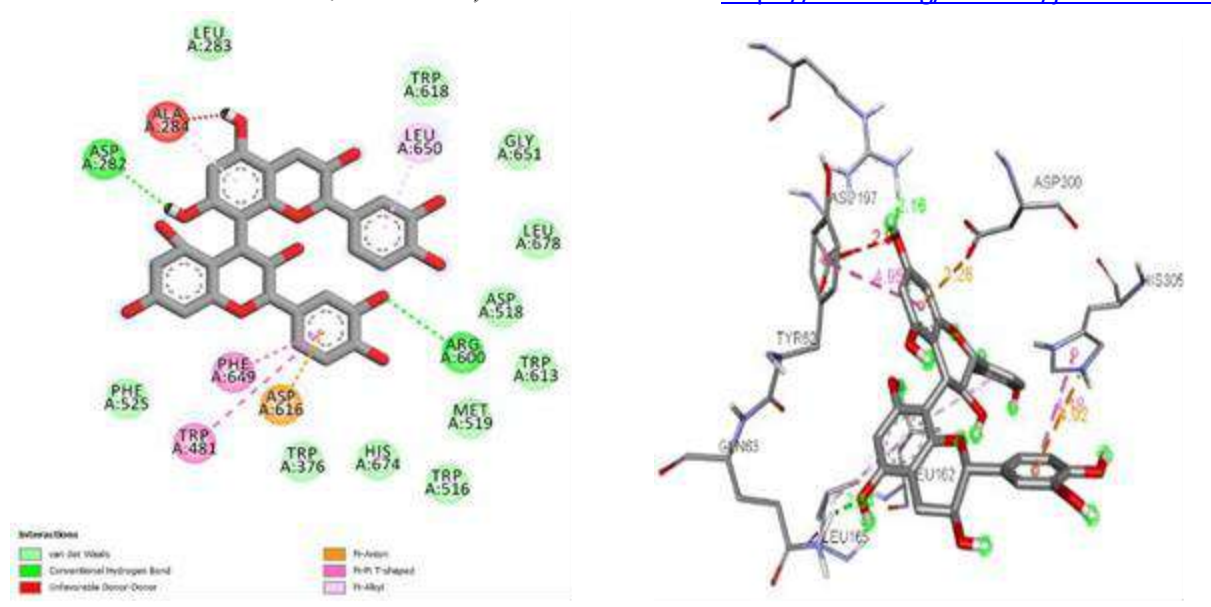


Fig. 3. Molecular docking analysis of FTO– pinoresinol complex. 3-D interaction diagram showing FTO amino acid residues interacting with Pinoresinol and 2-D interaction diagram showing FTO amino acid residues with different bond interactions against Pinoresinol. FTO, fat mass and obesity-associated protein; 1GNG, Pinoresinol.

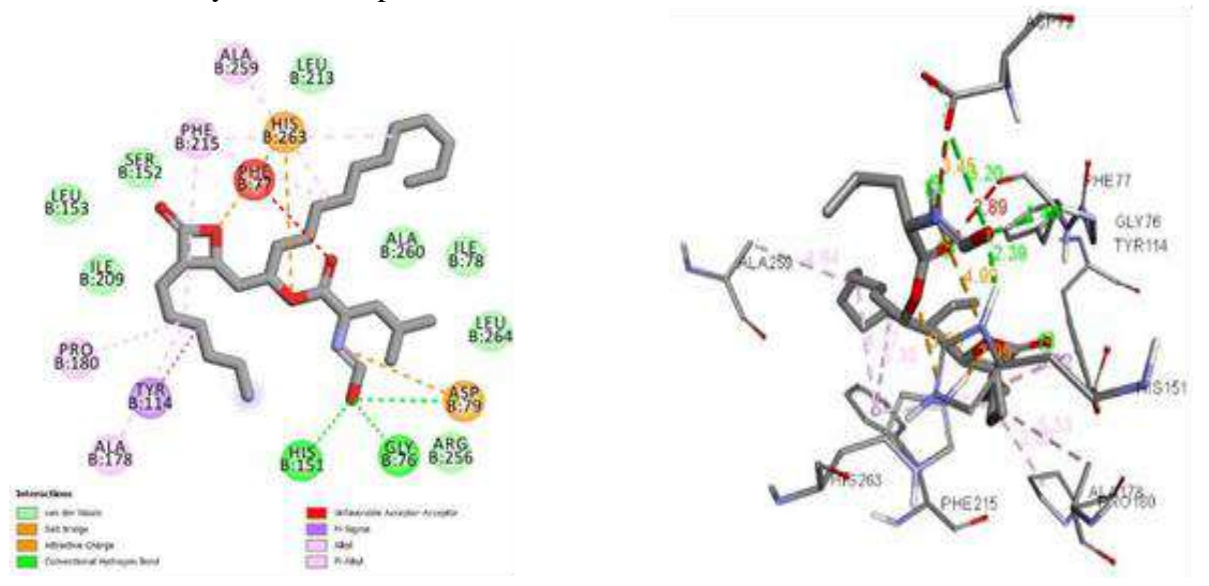


Fig. 4. Molecular docking analysis of FTO– Chondrillasterol complex. 3-D interaction diagram showing FTO amino acid residues interacting with Chondrillasterol and 2-D interaction diagram showing FTO amino acid residues with different bond interactions against Chondrillasterol. FTO, fat mass and obesity-associated protein; 3LFM, Chondrillasterol



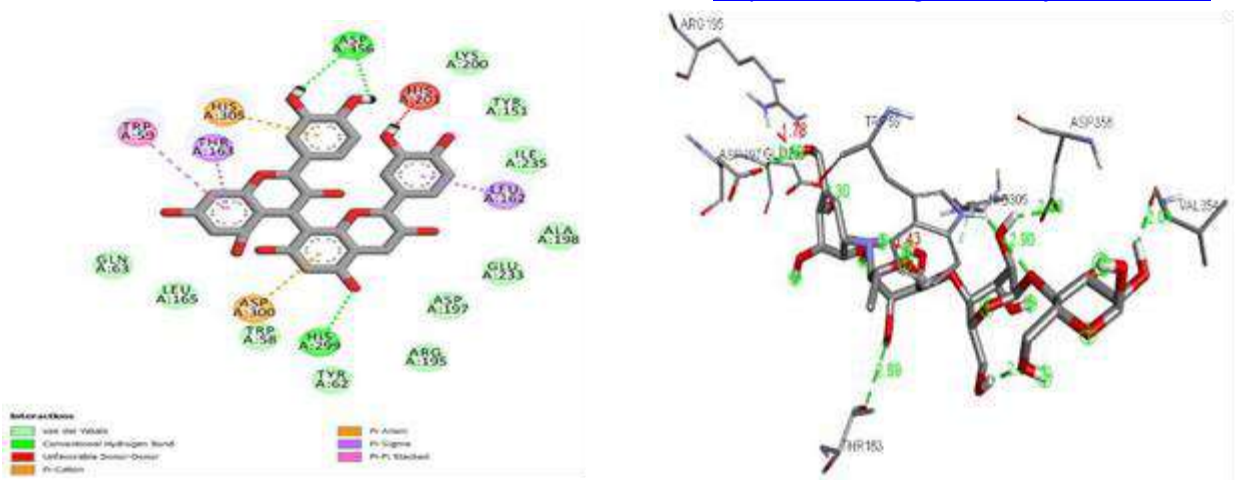


Fig. 5. Molecular docking analysis of FTO– Ononin complex. 3-D interaction diagram showing FTO amino acid residues interacting with Ononin and 2-D interaction diagram showing FTO amino acid residues with different bond interactions against Ononin. FTO, fat mass and obesity-associated protein; 3LFM, Ononin

Table 1: Molecular docking interactions between obesity-associated protein (FTO) and polyphenols ligands with binding energy. The involved FTO residues and bond distances are shown.

Compound	Hydrogen bond	Distance	Hydrophobic	Binding energy	
r	,	(A^0)	interaction	(Kcal/mol)	
Sesamin	PHE77	2.33	ALA260,	-9.9	
			PHE215, TYR114		
Pinoresinol	ASP282	2.16	LUE650, PHE649,	-9.0	
	ARG600	2.34	TRP481		
Chondrillasterol	HIS151	2.39	TYR114,ALA259,	-8.8	
	GLY76	2.45	ALA178,		
			PRO180, PHE215		
Ononin	ASP356	2.38	LEU162,	-7.8	
	HIS299	2.90	THR163, TRP59		

In the present study, certain compounds (sesamin, pinoresinol, chondrillasterol, and ononin) were docked against FTO proteins 1GNG and 3LFM, respectively. Table 1 displays the results for the complexes under study in terms of distance, binding energy, H-bond, and hydrophobic interactions.

Fig. 1 and Table 1 show the 2D and 3D molecular docking interactions between FTO (1GNG) and sesamin molecule had hydrophobic interactions with ALA260 (Pi-alkyl), PHE215, TYR114 (Pi-pi stacked and T-shaped), and HIS263 (Pi-cation). It also had H-bonding with PHE77 (convectional hydrogen bond). Furthermore, (Table 1 and Fig. 2) The docked complex of FTO (1GNG) and pinoresinol involved the formation of interactive bonds such as hydrogen bonding (ASP282, ARG600), electrostatic pi anion (ASP616), and hydrophobic interaction involving the amino acid residues LUE650 (pi-alkyl), PHE649, and TRP481 (pi-pi T-shaped). Moreover, the interaction connections that formed in the FTO (3LFM) and chondrillasterol docking complex (Figure 3 and Table 2) include H-bonding with HIS151, GLY76 (convectional hydrogen bond),



HIS263, ASP79 (attractive charge), hydrophobic interaction are TYR114 (pi sigma), ALA259, ALA178, PRO180, PHE215 (Alkyl and Pi-alkyl). Also for the interactive bonds, that were developed in the docking complex of FTO (3LFM) and Ononin (Fig.4 and Table 2) include H-bonding with ASP356, HIS299 (convectional H-bond), electrostatic interaction with ASP300, HIS305 (pi cation and pi-anion), hydrophobic interaction are LEU162, THR163 (pi-sigma), TRP59 (pi-pi stacked). As represented in our study (Table 2), the FTO residues with ligands interactions formed H-bonding and hydrophobic interactions.

We observed that every molecule exhibited hydrogen bonds, which are thought to be one of the key components of protein-ligand stability. Nevertheless, additional interactions, such as hydrophobic contacts, support the efficacy of these chemicals against FTO and are consistent with the literature's findings that sesamin, pinoresinol and ononin reduce body weight and control lipid metabolism (Hajji et al., 2022). Further research revealed that polyphenols, which are well-known to be useful in the treatment and prevention of diabetes, also hasten weight loss. Additionally, British researchers have demonstrated that polyphenols may combat obesity by controlling lipid metabolism and preventing the differentiation of adipocytes), which are demonstrated by some docking results similar to the docking results for this studies of the three compounds (Ononin, Chondrillasterol, and Pinoresinol) (Table 1).

(Hajji et al., 2022

Table 2: Lipinski's role of all compounds in the dataset

Compounds	Molecular weight (g/mol)	Log P	H-bond acceptors	H-bond donor	Rotatable bonds
Sesamin	345.34	2.79	6	0	2
Pinoresinol	358.39	2.26	6	2	4
Chondrillasterol	419.69	6.87	1	1	5
Ononin	430.40	0.98	9	4	5

Table 3: Results of the ADME test of all compounds

Compounds	GI absorptio n	BBB permean t	CYP3A 4 inhibito r	Pgp substrat e	XLOPG 3	Bioavailabilit y score
Sesamin	High	Yes	Yes	No	2.68	0.55
Pinoresinol	High	Yes	Yes	Yes	2.28	0.55
Chondrillastero	Low	No	No	No	8.30	0.55
l						
Ononin	High	No	Yes	Yes	0.99	0.55

GI- gastrointestinal, BBB blood-brain barrier

ADMET

This is the first study to use in-silico analysis to describe the physicochemical and ADME properties of certain polyphenols. One of the primary reasons for medication failure in clinical phase trials related to drug development is inadequate pharmacokinetic profiles (absorption,



metabolism, distribution, and excretion) (Imam et al., 2021). It's interesting to note that in-silico computer models offer reliable substitutes for forecasting ADME in the early stages of medication development (Imam et al., 2021).

Computer modeling can also be used to predict the biological activity and decrease the toxicity profile of medications based on their concentration and accessibility at therapeutic targets. Molecular structure is used in in-silico models to assess the drug's oral bioavailability, and substructures are used to identify molecules that are most likely to be hazardous, unstable, reactive, or prone to interfere with biological reactions (Adamu et al., 2023).

It can be observed from Table 2 that all polyphenols compounds except chondrillasterol respect the Lipinski rules, where all values of log P<5, Molecular weight<500, HBA<10, HBD<5, RB<10. Sesamin, pinoresinol, and ononin are predicted by the ADME properties of the polyphenols listed in the result (table 3) section to be easily absorbed through the gastrointestinal tract, while chondrillasterol is not; however, more in-silico analysis is required to explain this discrepancy. It's interesting to note that two of the polyphenols, chondrillasterol and sesamin, do not inhibit CYP3A4 and act as substrates for P-gp, a member of the ATP-binding cassette transporters, which is responsible for the active efflux of small molecules across biological membranes. For instance, from the brain or the wall of the gastrointestinal tract to the lumen. Predicting whether small compounds would be a substrate for P-gp and CYP3A4 inhibitor, which was discovered in two; pinoresinol and ononin, is therefore crucial for drug discovery (Adamu et al., 2023)

Additionally, a molecule's potential to be an oral medication candidate based on its bioavailability was assessed using the drug-likeness metric. Moreover, because of their high expected bioavailability index (1 to 10), they are anticipated to exhibit good drug-likeness. Table Three Additionally, every polyphenol

The ratio of a compound's steady-state concentration in the brain to the blood is known as the blood-brain barrier (BBB). Conversely, to prevent negative CNS effects, medications with a peripheral action must have a restricted capacity to penetrate the blood-brain barrier (BBB) (Hajji et al., 2022). The chemical biotransformation of a drug in the body, which is vital to the conversion of drug molecules, is indicated by the enzymatic metabolism. Drug metabolism is significantly influenced by the cytochrome CYP (Abdelrheem et al., 2021).

Table 4: Results of predicted Biological activity of all test compounds

	Prediction confidence of approved compounds (= Pa- Pi)									
Name of Compounds	Antibacterial	Antifungal	Anti-infective	Anti- inflammatory	Antioxidant	Free radical scavenger	CYP3A substrate	CYP3A5 substrate	Anticarcinoge nic	Antidiabetic
Sesamin	0.091	0.006	0.233	0.164	0.449	0.206	0.178	0.407	0.160	0.158
Pinoresinol	0.204	0.247	0.188	0.483	0.632	0.526	0.239	0.509	0.576	0
Chondrillasterol	0.049	0.532	0	0.227	0.157	0	0.839	0.684	0.193	0
Ononin	0.540	0.634	0.939	0.616	0.707	0.726	0.521	0.305	0.912	0.615

Pa = probability to be active, Pi = probability to be inactive



Table 4, showing the calculated confidence of Pa for antibacterial, antifungal, anti-infective, anti-inflammatory, antioxidant, free radical scavenging activity, anti-diabetic, CYP3A substrate, CYP3A5 substrate and anti-carcinogenic for this study (Loewy et al., 2018; Aljarbou et al., 2020). Also According to the results of PASS, Pinoresinol have been predicted to have antioxidant (0.632), free radical scavenger (0.526), CYP3A5 (0.509) substrate, anti-carcinogenic (0.576), for chondrillasterol, has antifungal (0.532), CYP3A (0.839) and CYP3A5 substrate (0.684), for ononin, has all the predicted activity (0.540) for antibacterial, (0.634) antifungal, (0.939) anti-ineffective, (0.616) anti-inflammatory, (0.707) antioxidant, (0.726) free radical scavenger, (0.521) CYP3A, (0.912) anticarcinogenic and (0.615) anti-diabetic

This showed that the selected compounds: pinoresinol have been predicted to have antioxidant, free radical scavenger, CYP3A5 substrate, anti-carcinogenic, for chondrillasterol, has antifungal, CYP3A and CYP3A5 substrate, for ononin, has all the predicted activity except for CYP3A5 substrate. The above mentioned compounds in tables showed confidence values of ≥0.500 of the predicted biological activities are considered active. This indicates the potential of the compounds for the biological activities (Mathew et al., 2013). Polyphenols like ononin and pinoresinol are known for their multiple medicinal properties such as antioxidant, free radical scavenging, anti-inflammatory, and cyto-protective activities. (Idoko et al., 2023; Ayman et al., 2019; Tony et al., 2018).

Conclusion

The study of these polyphenols' docking, drug-likeness, SwissADME and PASS (predicted biological activity) predictions showed many molecular interactions between the compounds and the proteins they were trying to target. Numerous hydrogen bonds, Vander Waals interactions and other hydrophobic interactions are present in the interactions. Since three of the compounds were determined to be consistent with Lipinski's RO5, they were considered the most active compounds. Their SwissADME experiments showed that, with the exception of sesamin, all three compounds had high gastrointestinal absorption and were determined to be CYP3A4 inhibitors in addition to having a strong blood-brain barrier (BBB) penetration. The compounds exhibited conventional ranges for log skin permeability, number of rotatable bonds, and P-gp substrate inhibition. The predicted biological activities showed that pinoresinol and Ononin have the highest activities which shows the have stronger ability for biological activity and can be used in drug discovery When creating theoretical compounds and optimizing drugs generally, these features can be taken into consideration.

References

- Abdelrheem, D.A.; Rahman, A.A.; Elsayed, K.N.M.; Abd El-Mageed, H.R.; Mohamed, H.S.; Ahmed, S.A. (2021) Isolation, Characterization, in Vitro Anticancer Activity, Dft Calculations, Molecular Docking, Bioactivity Score, Drug-Likeness and Admet Studies of Eight Phytoconstituents from Brown Alga Sargassum Platycarpum. Journal of Molecular Structure, 1225, 129245, https://doi.org/10.1016/j.molstruc.2020.129245.
- Adamu U. M., Renggasamy R., Stanslas J., Abdull Razis A. F., Fauzi F. M., Mulyani S. WM., Ramasamy R., (2023) In-silico Prediction Analysis of Polyphenolic Contents of Ethanolic Extract of Moringa oleifera Leaves. *Mal J Med Health Sci* 19(SUPP16): 9-15.
- Ahmed M. Z., Hameed S., Ali M., Hizbullah S., Zaheer A., (2021) In Silico Molecular Docking Analysis of Limonene with The Fat Mass and Obesity-Associated Protein by Using Autodock Vina, *Scientific Journal of Informatics*, Vol. 8, No. 1. p-ISSN 2407-7658



- Aljarbou F, Almobarak A, Binrayes A, Alamri HM. (2022) *Salvadora persica*'s Biological Properties and Applications in Different Dental Specialties: A Narrative Review. Evidence-Based Complement Altern Med.
- Ayman MM, Rene JHB, Mansur AS, Omnia EH. (2019) Beneficial Effects of Citrus Flavonoids on Cardiovascular and Metabolic Health. Oxid Med Cell Longev.; 2019:5484138
- Badock, E.A., Niang, L., Dramé, A., Nkounkou-Loumpangou, C., Touré, O., Sokhna, O., Ayessou, N.C. and Cissé, M. (2024) Phytochemical Screening and Assays of Phenolic Compounds in Senna occidentalis L. Leaf and Seed Extracts. Food and Nutrition Sciences, 15, 499-508. https://doi.org/10.4236/fns.2024.157033
- Daina A. and Zoete V., (2016) A BOILED-Egg to predict gastrointestinal absorption and brain penetration of small molecules, ChemMedChem. 11: 1117–1121, https://doi.org/10.1002/cmdc.201600182.
- Daina A., Michielin O., Zoete V., (2017) SwissADME: a free web tool to evaluate pharmacokinetics, drug-likeness and medicinal chemistry friendliness of small molecules, Sci. Rep. 7: 42717, https://doi.org/10.1038/srep42717.
- Fischer J et al., (2009) "Inactivation of the Fto Gene Protects from Obesity," Nature, vol. 458, no. 7240, pp. 894–898.
- Hajji H., Tabti K., En-nahli F., Bouamrane S., Lakhlifi T., Ajana M. A., Bouachrine M., (2022) In Silico Investigation on the Beneficial Effects of Medicinal Plants on Diabetes and Obesity: Molecular Docking, Molecular Dynamic Simulations, and ADMET Studies *Biointerface research of applied chemistry*, Vol 11, 5 : 6933 6949 https://doi.org/10.33263/BRIAC115.69336949
- Idoko A, Parker JE, Njoku O U.(2023) Ethylacetate Flavonoid Biocompounds of Honey with Mitigating Anti-hyperlipidemic and Antioxidant Properties in Carbohydrate and Lipid Enriched Diets Obese Rats. Ann Res Rev Biol. 38(9):1-23.
- Iman Zolkiffly SZ, Stanslas J, Hamid HA, Mehat MZ. Ficus deltoidea: (2021) Potential Inhibitor of ProInflammatory Mediators in LipopolysaccharideInduced Activation of Microglial Cells. Journal of Ethnopharmacology. :114309
- Lipinski C. A., F. Lombardo, B.W. Dominy, P.J. Feeney, (2012) Experimental and computational approaches to estimate solubility and permeability in drug discovery and development settings, Adv. Drug Deliv. Rev. 64: 4–17, https://doi.org/10.1016/j.addr.2012.09.019.
- Loewy ZG, Galbut S, Loewy E, Felton DA. (2018) Influence of the Oral Microbiome on General Health. In: Bhardwaj SB, editor. Oral Microbiology in Periodontitis. IntechOpen.
- Mathew B, Suresh J, Anbazhagan S. (2013) Synthesis and PASS-assisted in silico approach of some novel 2-substituted benzimidazole bearing a pyrimidine-2, 4, 6(trione) system as mucomembranous protector. J Pharm BioAllied Sci. 5(1):39–43
- Rakshit G. and Jayaprakash V., (2023) Tuberculosis and HIV responses threatened by nCOVID-19: a situation prompting an in silico investigation of reported MbtA inhibitors for combined inhibition of SARS-CoV-2 and HIV-TB co-infection, Struct. Chem. 34 : 655–679, https://doi.org/10.1007/s11224-022-02013-y.
- Ruud J et al., (2019) "The Fat Mass and Obesity-Associated Protein (FTO) Regulates Locomotor Responses to Novelty Via D2R Medium Spiny Neurons," Cell Rep., vol. 27, no. 11, pp. 3182-3198.e9.
- Sarkar A., Agarwal R., Bandyopadhyay B., (2022) Molecular docking studies of phytochemicals from Terminalia chebula for identification of potential multi-target inhibitors of SARS-CoV-



- 2 proteins, J. Ayurveda Integr. Med. 13 : 100557, https://doi.org/10.1016/j.jaim.2022.100557.
- Stefaniu, A.; Pirvu, L.C. (2022) In Silico Study Approach on a Series of 50 Polyphenolic Compounds in Plants; A Comparison on the Bioavailability and Bioactivity Data. *Molecules*, 27, 1413. https://doi.org/10.3390/molecules27041413
- Tony S, Renti E, Marimpola S, Laksmi A. (2018) Docking Evaluation of Catechin and its Derivatives on Fat Mass and Obesity-Associated (FTO) Protein For Anti-Obesity Agent. J Appl Pharm Sci. 8(08):063-068.
- Trott O and Olson A. O., (2009) "AutoDock Vina: Improving the Speed and Accuracy of Docking with A New Scoring Function, Efficient Optimization, and Multithreading," J. Comput. Chem., vol. 31, no. 2
- Vina D., Albumin H. S, Octanoate S., and Vina A., (2020) "How to Perform Docking in A Specific Binding Site Using AutoDock Vina?," pp. 1–13.



The Stability of out-of-plane equilibrium points in the photogravitational Elliptic Restricted Three-Body Problem (ER3BP) with triaxiality surrounded by a belt Isah Ndama¹ and Tyokyaa K. Richard².

1. Department of Mathematics, Faculty of sciences, Niger state College of Education, Minna, Nigeria.

e-mail:

2. Department of Mathematics, Faculty of Physical sciences, Federal University Dutsin-Ma, Katrsina State, Nigeria.

e-mail:rtkanshio6@gmail.com

Abstract

The paper investigates the motion of an infinitesimal particle near the out-of-plane equilibrium points in the elliptic restricted three body problem (ER3BP) when the primaries are triaxial rigid bodies with the smaller primary a source of radiation and surrounded by a belt. It is observed that there exist two out-of-plane equilibria which lie in the $\xi\zeta$ - plane in symmetrical positions with respect to the orbital plane. The parameters involved in the system affect their positions. The position changes with an increase in triaxiality, radiation and belt. The position and stability of the out-of-plane equilibrium points are investigated numerically using two binary systems (Xi-Bootis and Kruger 60) and they are found to be unstable.

Keywords: Triaxiality; Radiation; Elliptic restricted three body problem; Stability; gravitational potential from the belt; binary systems.

1. Introduction

In celestial mechanics the three-body problem is one of the most important areas of research, most especially in the field of astrodynamics and astrophysics. Renowned mathematicians and scientists have obtained interesting and significant results in an attempt to understand and predict the motion of natural bodies.

The restricted three-body problem is a configuration involving two massive bodies called the primaries and a particle of negligible mass, called the third body (infinitesimal particle, test particle). It explains the motion of the infinitesimal particle in the vicinity of the primaries which move in circular or elliptic orbits around their common centre of mass due to their mutual gravitational attraction. It possesses three collinear points $L_{1,2,3}$ and two triangular points $L_{4,5}$. They lie on the orbital plane of motion of the primaries. The latter are conditionally stable, while the former are unstable.

In the classical restricted three-body problem (CR3BP) only gravitational forces influence the motion of the particle. The photogravitational restricted three-body problem (R3BP) problem arises when one of the participating bodies or both are intense emitters of radiation. It is inadequate to consider only the gravitational force in some solar or stellar dynamic problems. For instance, gravity is not only the dominant force present when a star collides with a particle, but also the repulsive forces of radiation pressure (Radsviesky, 1950). Due to the importance of this force, several authors (Chermikov, 1970; Simmons et.al. 1985; Das et.al.2009; Singh and Umar 2012; Abouelmagd 2013; Ammar 2008) studied its influence on the stability of infinitesimal mass in their papers.



In addition to this force, many authors have extended the work to include the role played by the shape of bodies (triaxiality, oblateness and so on). These two Pertubing forces (triaxiality and oblateness) have been studied extensively by researchers in the R3BP.

The first to point out the existence of out-of-plane equilibrium points was (Radvieskii, 1950) who studied the case of sun planet-particle and Galaxy-kernel-sun-particle and found the two equilibrium points $L_{6.7}$ on the $\xi\zeta$ -plane to be symmetrical with respect to the orbital plane.

Doukos and Markellos (2006) determined the out-of-plane points numerically by approximation with power series expansion. They showed that the out-of-plane points exist, but they are unstable. A generalized out-of-plane model was studied by Hussain and Umar (2019) in which the primary is oblate and the secondary is triaxial and radiating in the ER3BP, it is observed that the out-of-plane equilibrium points $L_{6,7}$ area affected by the oblateness of the primary, radiation pressure and triaxiality of the secondary, semi-major axis and eccentricity.

It was also established by Singh and Umar (2013) that the position and stability of out-of-plane points in ER3BP are greatly affected by oblateness and radiation pressure of the primaries and the eccentricity of their orbits. Singh and Tyokyaa (2021) examined the motion of a test particle around the out-of-plane libration points in the er3bp with oblateness up to zonal harmonics J_4 . It is found that their positions are affected by the oblateness of the primaries, the semi-major axis and eccentricity of their orbits.

Several authors such as (Singh, 2012; Singh and Amuda 2015; Naraya and Nutan, 2014; Zotos 2018) have studied the out-of-plane points under the influence of radiation pressure or PR-drag or oblateness or in combination of one of these forces and they all found the out-of-plane equilibrium points unstable in the CR3BP or ER3BP. The basins of attraction around the out-of-plane points in the Copenhagen R3BP was determined by Zotos (2018) using a multivariate version of the Newton-Raphson interactive method.

The discovery of many extra solar planetary systems revealed the presence of belts of dust particles that are regarded as the young analogues of Kuiper belt. (Aumman et al. 1984) and Jiang & Yeh (2003) studied the effects of belts on planetary orbits and observed that the planets might prefer to stay near the inner part instead of outer part of the belt. Later the R3BP was modified in their paper Jiang & Yeh (2004) to include the effect of additional gravitational force from the belt on the infinitesimal mass, which results in the formation of new libration points.

Singh and Taura (2014b) studied the model of restricted three-body problem when the two primaries are oblate spheroids and radiating with the gravitational potential from a belt. They obtained in addition to the usual five libration points two new collinear points as a result of the potential from the belt. The influence of the belt and non-sphericity of the primaries on the infinitesimal mass was studied by Singh and Taura (2014c). They did analytic and numerical treatment of motion of a dust grain particle around triangular equilibrium points when the bigger primary is triaxial and the smaller one an oblate spheroid with a potential from the belt. They found that triangular points are stable for $0 < \mu < \mu_c$ and unstable for $\mu_c \le \mu \le \frac{1}{2}$, where μ_c is the critical mass ratio. It was also observed that the potential from the belt increase the range of stability. Singh and Tyokyaa (2023) studied the collinear investigation of albedo effects in the elliptic restricted three-body problem with an oblate primary, a triaxial secondary and a potential due to belt. The result revealed that, as the half distance between the mass dipoles and oblateness of the primary increase, the region of stability of the collinear positions decreases for the aforementioned binary systems.

The case when the more massive primary is a triaxial body and less massive one an oblate spheroid emitting radiation enclosed by a circumbinary disc (belt) in the presence of Poyting-Robertson



drag (P-R Drag) force was investigated by Singh and Amuda (2019). They observed that the potential from the belt is a stabilizing force as it can change an unstable condition to a stable one even when the mass parameter exceeds the critical mass value ($\mu > \mu_c$).

In this paper our aim is to investigate the effect of triaxiality and radiation pressure of the smaller primary together with the potential of the belt enclosing them on the stability of a test particle around the out- of- plane equilibrium points in the ER3BP.

2. Location and Linear stability of out-of-plane triangular equilibrium points

The equation of motion of an infinitesimal particle in the ER3BP when the primaries are triaxial and smaller one radiating, with a gravitational potential from a belt, in a dimensionless rotating coordinate system (ξ, η, ζ) are as follows:

$$\xi'' - 2\eta' = \Omega_{\xi}
\eta'' + 2\xi' = \Omega_{\eta}
\xi'' = \Omega_{\zeta}$$

$$\Omega = (1 - e^{2})^{-1/2} \left[\frac{1}{2} (\xi^{2} + \eta^{2}) + \frac{1}{n^{2}} \left\{ \frac{(1 - \mu)}{r_{1}} + \frac{(1 - \mu)(2\sigma_{1} - \sigma_{2})}{2r_{1}^{3}} - \frac{3(1 - \mu)(\sigma_{1} - \sigma_{2})\eta^{2}}{2r_{1}^{5}} - \frac{3(1 - \mu)\sigma_{1}\zeta^{2}}{2r_{1}^{5}} + \frac{\mu(2\sigma_{3} - \sigma_{4})q_{2}}{2r_{2}^{3}} - \frac{3\mu\sigma_{3}q_{2}\zeta^{2}}{2r_{2}^{5}} + \frac{M_{b}}{\left[r^{2} + \left(c + \sqrt{\zeta^{2} + d^{2}}\right)^{2}\right]^{1/2}} \right\} \right]$$
(2)

$$r_1^2 = (\xi + \mu)^2 + \eta^2 + \zeta^2$$

$$r_2^2 = (\xi + \mu - 1)^2 + \eta^2 + \zeta^2$$

$$n^2 = \frac{1}{a} \left[1 + \frac{3}{2} e^2 + \frac{3}{2} (2\sigma_1 - \sigma_2) + \frac{3}{2} (2\sigma_3 - \sigma_4) + \frac{2M_b r_c}{[r_c^2 + T^2]^{3/2}} \right]$$
(4)

r is the radial distance of the infinitesimal mass and is given by $r^2 = \xi^2 + \zeta^2$, where c and d are the parameters which determine the density profile of the belt Miyamoto and Nagai (1975) and (Kushvah, 2008) r_c is the distance of any out-of-plane point from the origin and T is their sum, r_1 and r_2 are distances of the bigger and smaller primaries from the infinitesimal particle, respectively. q_1 and q_2 are their mass reduction factor (radiation factor), while (σ_1, σ_2) and (σ_3, σ_4) denote their triaxiality, respectively. n is the mean motion, a and e are the semi major axis and the eccentricity of the elliptic orbis respectively.

The equilibrium points are the solutions of the system of equations $\Omega_{\xi} = \Omega_{\eta} = \Omega_{\zeta} = 0$, i.e.

$$\left[\xi - \frac{1}{n^2} \left\{ \frac{(1-\mu)(\xi+\mu)}{r_1^3} + \frac{3(1-\mu)(2\sigma_1-\sigma_2)}{2r_1^5} - \frac{15(1-\mu)(\xi+\mu)\sigma_1}{2r_1^7} \eta^2 - \frac{15(1-\mu)(\xi+\mu)\sigma_1\zeta^2}{2r_1^7} + \frac{\mu(\xi+\mu-1)q_2}{r_2^3} + \frac{1}{r_2^3} + \frac{1}{$$

$$\frac{3\mu(\xi+\mu-1)(2\sigma_{3}-\sigma_{4})q_{2}}{2r_{2}^{5}} - \frac{15\mu(\xi+\mu-1)\sigma_{3}}{2r_{2}^{7}}q_{2}\eta^{2} - \frac{15\mu(\xi+\mu-1)\sigma_{3}q_{2}\zeta^{2}}{2r_{2}^{7}} + \frac{M_{b\,\xi}}{\left[\xi^{2}+\left(c+\sqrt{\zeta^{2}+d^{2}}\right)^{2}\right]^{3/2}}\right\} = 0$$
(5)





$$\Omega_{\eta} = (1 - e^{2})^{-1/2} \eta \left[1 - \frac{1}{n^{2}} \left\{ \frac{(1 - \mu)}{r_{1}^{3}} + \frac{3(1 - \mu)(2\sigma_{1} - \sigma_{2})}{2r_{1}^{5}} + \frac{3(1 - \mu)(\sigma_{1} - \sigma_{2})}{r_{1}^{5}} - \frac{15(1 - \mu)(\sigma_{1} - \sigma_{2})}{2r_{1}^{7}} \eta^{2} - \frac{15(1 - \mu)\sigma_{1}\zeta^{2}}{2r_{1}^{7}} + \frac{\mu q_{2}}{r_{2}^{3}} + \frac{3\mu(2\sigma_{3} - \sigma_{4})q_{2}}{2r_{2}^{5}} + \frac{3\mu(\sigma_{3} - \sigma_{4})}{r_{2}^{5}} q_{2} - \frac{15\mu(\sigma_{3} - \sigma_{4})}{2r_{2}^{7}} q_{2}\eta^{2} - \frac{15\mu\sigma_{3}q_{2}\zeta^{2}}{2r_{2}^{7}} + \frac{M_{b}}{\left[\xi^{2} + \left(c + \sqrt{\zeta^{2} + d^{2}}\right)^{2}\right]^{3/2}}\right\} = 0 \qquad (6)$$

$$\Omega_{\zeta} = (1 - e^{2})^{-1/2} \left[-\frac{\zeta}{n^{2}} \left\{ \frac{(1 - \mu)}{r_{1}^{3}} + \frac{3(1 - \mu)(2\sigma_{1} - \sigma_{2})}{2r_{1}^{5}} + \frac{3(1 - \mu)\sigma_{1}}{r_{1}^{5}} - \frac{15(1 - \mu)(\sigma_{1} - \sigma_{2})}{2r_{1}^{7}} \eta^{2} - \frac{15(1 - \mu)\sigma_{1}\zeta^{2}}{2r_{1}^{7}} + \frac{\mu q_{2}}{r_{2}^{3}} + \frac{3\mu(2\sigma_{3} - \sigma_{4})}{2r_{2}^{5}} q_{2} + \frac{3\mu\sigma_{3}}{r_{2}^{5}} q_{2} - \frac{15\mu(\sigma_{3} - \sigma_{4})}{2r_{2}^{7}} q_{2}\eta^{2} - \frac{15\mu\sigma_{3}q_{2}\zeta^{2}}{2r_{2}^{7}} + \frac{M_{b}\left[c(\zeta^{2} + d^{2})^{-1/2} + 1\right]}{\left[\xi^{2} + \left(c + \sqrt{\zeta^{2} + d^{2}}\right)^{2}\right]^{3/2}}\right\} = 0 \qquad (7)$$

The out-of-plane equilibrium points are the solution of above equations, when

$$\xi \neq 0$$
, $\eta = 0$ and $\zeta \neq 0$

From (7) with $\zeta \neq 0$ we get:

$$\frac{(1-\mu)}{r_{1}^{3}} + \frac{3(1-\mu)(2\sigma_{1}-\sigma_{2})}{2r_{1}^{5}} + \frac{3(1-\mu)\sigma_{1}}{r_{1}^{5}} - \frac{15(1-\mu)\zeta^{2}}{2r_{1}^{7}} + \frac{\mu q_{2}}{r_{2}^{3}} + \frac{3\mu(2\sigma_{3}-\sigma_{4})}{2r_{2}^{5}} q_{2} + \frac{3\mu\sigma_{3}}{r_{2}^{5}} q_{2} - \frac{15\mu\sigma_{3}q_{2}\zeta^{2}}{2r_{2}^{7}} + \frac{\mu q_{2}}{r_{2}^{5}} + \frac{\mu q_{2}}{2r_{2}^{5}} + \frac{\mu q_{2}}{2r_{2}^{5}} + \frac{3\mu(2\sigma_{3}-\sigma_{4})}{2r_{2}^{5}} q_{2} - \frac{15\mu\sigma_{3}q_{2}\zeta^{2}}{2r_{2}^{7}} + \frac{\mu q_{2}}{2r_{2}^{7}} + \frac{\mu q_{2}}{2r_{2}^{5}} + \frac{\mu q_{2}}{2r_{2}^{5$$

Let $Q_1 = (1 - \mu)$ and $Q_2 = \mu q_2$, then (8) becomes:

$$\frac{Q_1}{r_1^3} + \frac{3Q_1(2\sigma_1 - \sigma_2)}{2r_1^5} + \frac{3Q_1\sigma_1}{r_1^5} - \frac{15Q_1\sigma_1\zeta^2}{2r_1^7} + \frac{Q_2}{r_2^3} + \frac{3Q_2(2\sigma_3 - \sigma_4)}{2r_2^5} + \frac{3Q_2\sigma_3}{r_2^5} - \frac{15Q_2\sigma_3\zeta^2}{2r_2^7} + \frac{M_b \left[c(\zeta^2 + d^2)^{-1/2} + 1\right]}{\left[\xi^2 + \left(c + \sqrt{\zeta^2 + d^2}\right)^2\right]^{3/2}} = 0$$
(9)

Also from (5) we write:

$$n^{2}\xi - \frac{Q_{1}(\xi+\mu)}{r_{1}^{3}} - \frac{3Q_{1}(\xi+\mu)(2\sigma_{1}-\sigma_{2})}{2r_{1}^{5}} + \frac{15Q_{1}(\xi+\mu)\sigma_{1}\zeta^{2}}{2r_{1}^{7}} - \frac{Q_{2}(\xi+\mu-1)}{r_{2}^{3}} - \frac{3Q_{2}(\xi+\mu-1)(2\sigma_{3}-\sigma_{4})}{2r_{2}^{5}} + \frac{15Q_{2}(\xi+\mu-1)\sigma_{3}\zeta^{2}}{2r_{2}^{7}} - \frac{M_{b\xi}}{\left[\xi^{2} + \left(c + \sqrt{\zeta^{2} + b^{2}}\right)^{2}\right]^{3/2}}$$

$$(10)$$

Expanding (10) we obtained:

$$\xi \left\{ 1 - \frac{1}{n^2} \left(\frac{Q_1}{r_1^3} + \frac{3Q_1(2\sigma_1 - \sigma_2)}{2r_1^5} - \frac{15Q_1\sigma_1\zeta^2}{2r_1^7} + \frac{Q_2}{r_2^3} + \frac{3Q_2(2\sigma_3 - \sigma_4)}{2r_2^5} - \frac{15Q_2\sigma_3\zeta^2}{2r_2^7} + \frac{Q_2}{2r_2^7} + \frac{Q_2}{2r_2^7} \right) \right\} - \frac{\mu}{n^2} \left(\frac{Q_1}{r_1^3} - \frac{15Q_1\sigma_1\zeta^2}{2r_1^7} + \frac{Q_2}{r_2^3} - \frac{15Q_2\sigma_3\zeta^2}{2r_2^7} + \frac{3Q_1(2\sigma_1 - \sigma_2)}{2r_1^5} + \frac{3Q_2(2\sigma_3 - \sigma_4)}{2r_2^5} \right) + \frac{1}{n^2} \left(\frac{Q_2}{r_2^3} + \frac{3Q_2(2\sigma_3 - \sigma_4)}{2r_1^5} - \frac{15Q_2\sigma_3\zeta^2}{2r_2^7} \right) = 0 \tag{11}$$
From (9) we have



$$\frac{15Q_{1}(\sigma_{1}-\sigma_{2})\zeta^{2}}{2r_{1}^{7}} + \frac{15Q_{2}(\sigma_{3}-\sigma_{4})\zeta^{2}}{2r_{2}^{7}} \\
= \frac{Q_{1}}{r_{1}^{3}} + \frac{3Q_{1}(2\sigma_{1}-\sigma_{2})}{2r_{1}^{5}} + \frac{3Q_{1}\sigma_{1}}{r_{1}^{5}} + \frac{Q_{2}}{r_{2}^{3}} + \frac{3Q_{2}(2\sigma_{3}-\sigma_{4})}{2r_{2}^{5}} + \frac{3Q_{2}\sigma_{3}}{r_{2}^{5}} \\
+ \frac{M_{b}\left[c(\zeta^{2}+d^{2})^{-1/2}+1\right]}{\left[\xi^{2}+\left(c+\sqrt{\zeta^{2}+d^{2}}\right)^{2}\right]^{3/2}}$$

$$\zeta^{2} = \frac{2r_{1}^{7} r_{2}^{7}}{15Q_{1}(\sigma_{1} - \sigma_{2}) r_{2}^{7} + 15Q_{2}(2\sigma_{3} - \sigma_{4})r_{1}^{7}} \left\{ \frac{Q_{1}}{r_{1}^{3}} + \frac{3Q_{1}(2\sigma_{1} - \sigma_{2})}{2r_{1}^{5}} + \frac{Q_{2}}{r_{2}^{3}} + \frac{3Q_{2}(2\sigma_{3} - \sigma_{4})}{2r_{2}^{5}} + \frac{3Q_{1}\sigma_{1}}{r_{1}^{5}} + \frac{3Q_{2}\sigma_{3}}{r_{2}^{5}} + \frac{3Q_{2}\sigma_{3}}{r_{2}^{5}$$

$$\frac{M_{b}\left[c\left(\zeta^{2}+d^{2}\right)^{-1/2}+1\right]}{\left[\xi^{2}+\left(c+\sqrt{\zeta^{2}+d^{2}}\right)^{2}\right]^{3/2}}\right\} \tag{12}$$

Substituting (9) into (11) and solving we obtained:

$$\begin{split} \xi \left\{ 1 - \frac{1}{n^2} \left(-\frac{3Q_1\sigma_1}{r_1^5} - \frac{3Q_2\sigma_3}{r_2^5} + \frac{M_b}{\left[\xi^2 + \left(c + \sqrt{\zeta^2 + d^2}\right)^2\right]^{3/2}} - \frac{M_b \left[c + \left(\zeta^2 + d^2\right)^{-1/2} + 1\right]}{\left[\xi^2 + \left(c + \sqrt{\zeta^2 + d^2}\right)^2\right]^{\frac{3}{2}}} \right) \right\} \\ - \frac{\mu}{n^2} \left(-\frac{3Q_1\sigma_1}{r_1^5} - \frac{3Q_2\sigma_3}{r_2^5} - \frac{M_b \left[c + \left(\zeta^2 + d^2\right)^{-1/2} + 1\right]}{\left[\xi^2 + \left(c + \sqrt{\zeta^2 + d^2}\right)^2\right]^{3/2}} \right) \\ + \frac{1}{n^2} \left(-\frac{Q_1}{r_1^3} - \frac{3Q_1(2\sigma_1 - \sigma_2)}{2r_1^5} - \frac{3Q_1\sigma_1}{r_1^5} - \frac{3Q_2\sigma_3}{r_2^5} + \frac{15Q_1\sigma_1\zeta^2}{2r_1^7} - \frac{M_b \left[c + \left(\zeta^2 + d^2\right)^{-1/2} + 1\right]}{\left[\xi^2 + \left(c + \sqrt{\zeta^2 + d^2}\right)^2\right]^{3/2}} \right) = 0 \end{split}$$

$$\xi = \frac{\frac{Q_{1}}{r_{1}^{3}} + \frac{3Q_{1}(2\sigma_{1} - \sigma_{2})}{2r_{1}^{5}} + \frac{3Q_{1}\sigma_{1}(1 - \mu)}{r_{1}^{5}} + \frac{3Q_{2}Q_{1}\sigma_{3}}{r_{2}^{5}} - \frac{15Q_{1}\sigma_{1}\zeta^{2}}{2r_{1}^{7}} + \frac{M_{b}Q_{1}\left[c + \left(\zeta^{2} + d^{2}\right)^{-1/2} + 1\right]}{\left[\xi^{2} + \left(c + \sqrt{\zeta^{2} + d^{2}}\right)^{2}\right]^{3/2}}}{n^{2} + \frac{3Q_{1}\sigma_{1}}{r_{1}^{5}} + \frac{3Q_{2}\sigma_{3}}{r_{2}^{5}} + \frac{M_{b}}{\left[\xi^{2} + \left(c + \sqrt{\zeta^{2} + d^{2}}\right)^{2}\right]^{3/2}} + \frac{M_{b}\left[c\left(\zeta^{2} + d^{2}\right)^{-1/2} + 1\right]}{\left[\xi^{2} + \left(c + \sqrt{\zeta^{2} + d^{2}}\right)^{2}\right]^{3/2}}}$$

$$\xi = \frac{(1-\mu)\left\{\frac{1}{r_{1}^{3}} + \frac{3(2\sigma_{1}-\sigma_{2})}{2r_{1}^{5}} + \frac{3Q_{1}\sigma_{1}}{r_{1}^{5}} + \frac{3Q_{2}\sigma_{3}}{r_{2}^{5}} - \frac{15\sigma_{1}\zeta^{2}}{2r_{1}^{7}} + \frac{M_{b}\left[c + (\zeta^{2} + d^{2})^{-1/2} + 1\right]}{\left[\xi^{2} + \left(c + \sqrt{\zeta^{2} + d^{2}}\right)^{2}\right]^{3/2}}\right\}}{n^{2} + \frac{3Q_{1}\sigma_{1}}{r_{1}^{5}} + \frac{M_{b}}{r_{2}^{5}} + \frac{M_{b}\left[c \left(\zeta^{2} + d^{2}\right)^{-1/2} + 1\right]}{\left[\xi^{2} + \left(c + \sqrt{\zeta^{2} + d^{2}}\right)^{2}\right]^{3/2}} + \frac{M_{b}\left[c \left(\zeta^{2} + d^{2}\right)^{-1/2} + 1\right]}{\left[\xi^{2} + \left(c + \sqrt{\zeta^{2} + d^{2}}\right)^{2}\right]^{3/2}}$$

$$(13)$$

We use the initial approximation $\xi_o = (1 - \mu)$ and $\zeta_o = \sqrt{3(2\sigma_3 - \sigma_4)}$ to obtain the positions of out-of-plane equilibrium points L_{6,7} with the aid of the software package MATHEMATICA 10.4 in the form of power series to third order term in $(2\sigma_3 - \sigma_4)$ from (12) and (13) as:



$$\xi_{0} = \frac{(-1+\mu) - 3\sqrt{3}(-1+\mu) (2-3e^{2} - 2a + (2\sigma_{2} - \sigma_{1})(3-3a) \times (2\sigma_{3} - \sigma_{4})^{3/2}}{2(a\mu q_{2})}$$

$$-9 \left(\sqrt{3} (1+\mu) (2+3a (2+15(2\sigma_{2} - \sigma_{1})) (2\sigma_{3} - \sigma_{4})^{5/2} - 27 (-1+\mu)(2+3e^{2} - 2a)\right)$$

$$4(a\mu q_{2})$$

$$+(2\sigma_{1}-\sigma_{2})(-3+6a)(-1+\mu)q_{2})(4(\sigma^{2}\mu^{2}q_{2}^{2})^{-1}(2\sigma_{3}-\sigma_{4})^{3}+0(2\sigma_{3}-\sigma_{4})^{7/2}$$

$$\zeta_{o} = \sqrt{3}\sqrt{(2\sigma_{3}-\sigma_{4})} - \frac{9(-1+\mu)(2+9(2\sigma_{1}-\sigma_{2})}{10\mu q_{2}}(2\sigma_{3}-\sigma_{4})^{2} + \frac{81(-1+\mu)}{20\mu q_{2}}$$

$$(14)$$

$$(2\sigma_1 - \sigma_2)q_2(2\sigma_3 - \sigma_4)^3 - 0(2\sigma_3 - \sigma_4)^{7/2}$$
(15)

The equilibrium points $(\xi_0, 0, \pm \zeta_0)$ given by equations (14) and (15) are called the out-of-plane equilibrium points and are denoted by L₆ and L₇ respectively.

2.1 Linear stability of out-of-plane equilibrium points

The stability of these equilibrium points is determined by the eigen-values of the characteristic equation (16). If the roots of the characteristic equation are pure imaginary roots or complex roots with negative real parts the equilibrium point will be stable otherwise it will be unstable. Near any one of the out-of-plane equilibrium points the characteristic equation of the system can be written as:

$$\lambda^{6} + \left(4 - \Omega^{0}_{\xi\xi} - \Omega^{0}_{\eta\eta} - \Omega^{0}_{\zeta\zeta}\right)\lambda^{4} + \left(\Omega^{0}_{\eta\eta}\Omega^{0}_{\zeta\zeta} + \Omega^{0}_{\xi\xi}\Omega^{0}_{\zeta\zeta} + \Omega^{0}_{\xi\xi}\Omega^{0}_{\eta\eta} - 4\Omega^{0}_{\zeta\zeta} - (\Omega^{0}_{\xi\zeta})^{2}\right)\lambda^{2} - \left(\Omega^{0}_{\xi\xi}\Omega^{0}_{\eta\eta}\Omega^{0}_{\zeta\zeta} - (\Omega^{0}_{\xi\zeta})^{2}\Omega^{0}_{\eta\eta}\right) = 0$$
(16)

The superscript O denotes that the partial derivatives are evaluated at the out-of-plane point (ξ_o, o, ζ_o) where we have:

$$\Omega^{0}_{\xi\xi} = (1 - e^{2})^{-1/2} \left[1 + \frac{1}{n^{2}} \left\{ \frac{3Q_{1}(\xi_{0} + \mu)^{2}}{r_{10}^{3}} - \frac{Q_{1}}{r_{10}^{3}} + \frac{15Q_{1}(\xi_{0} + \mu)^{2}(2\sigma_{1} - \sigma_{2})}{2r_{10}^{7}} - \frac{3Q_{1}}{2r_{10}^{5}} + \frac{105Q_{1}(\xi_{0} + \mu)^{2}\sigma_{1}\zeta_{0}^{2}}{2r_{10}^{9}} - \frac{15Q_{1}\sigma_{1}\zeta_{0}^{2}}{2r_{10}^{7}} + \frac{3Q_{2}(\xi_{0} + \mu - 1)^{2}}{r_{20}^{5}} - \frac{Q_{2}}{r_{20}^{5}} + \frac{15Q_{2}(\xi_{0} + \mu - 1)^{2}(2\sigma_{3} - \sigma_{4})}{2r_{20}^{7}} - \frac{3Q_{1}}{2r_{20}^{5}} - \frac{3Q_{2}}{2r_{20}^{7}} + \frac{105Q_{2}(\xi_{0} + \mu - 1)^{2}\sigma_{3}\zeta_{0}^{2}}{2r_{20}^{7}} + \frac{3M_{b}\xi_{0}^{2}}{\left[\xi_{0}^{2} + \left(c + \sqrt{\zeta_{0}^{2} + d^{2}}\right)^{2}\right]^{5/2}} - \frac{M_{b}}{\left[\xi_{0}^{2} + \left(c + \sqrt{\zeta_{0}^{2} + d^{2}}\right)^{2}\right]^{5/2}} \right\}$$

(17)

$$\Omega^{0}_{\eta\eta} = (1 - e^{2})^{-1/2} \left[1 - \frac{1}{n^{2}} \left\{ \frac{Q_{1}}{r_{10}^{3}} + \frac{3Q_{1}(2\sigma_{1} - \sigma_{2})}{2r_{10}^{5}} - \frac{15Q_{1}\sigma_{1}\zeta_{0}^{2}}{2r_{10}^{7}} + \frac{Q_{2}}{r_{20}^{3}} + \frac{3Q_{2}(2\sigma_{3} - \sigma_{4})}{2r_{20}^{5}} - \frac{15Q_{2}\sigma_{3}\zeta_{0}^{2}}{2r_{20}^{7}} - \frac{15Q_{2}\sigma_{3}\zeta_{0}^{2}}{2r_{20}^{7}} - \frac{3M_{b}\eta_{0}^{2}}{\left[\xi_{0}^{2} + \left(c + \sqrt{\zeta_{0}^{2} + d^{2}}\right)^{2}\right]^{\frac{5}{2}}} + \frac{M_{b}}{\left[\xi_{0}^{2} + \left(c + \sqrt{\zeta_{0}^{2} + d^{2}}\right)^{2}\right]^{3/2}} \right\} \right]$$

$$\Omega^{0}_{\zeta\zeta} = (1 - e^{2})^{-1/2} \left[\frac{1}{n^{2}} \left\{ -\frac{Q_{1}}{r_{10}^{3}} + \frac{3Q_{1}\zeta_{0}^{2}}{r_{10}^{5}} - \frac{3Q_{1}(2\sigma_{1} - \sigma_{2})}{2r_{10}^{5}} + \frac{15Q_{1}(2\sigma_{1} - \sigma_{2})\zeta_{0}^{2}}{2r_{10}^{7}} - \frac{3Q_{1}\sigma_{1}}{r_{10}^{5}} + \frac{15Q_{1}\sigma_{1}\zeta_{0}^{2}}{r_{10}^{7}} + \frac{45Q_{1}\sigma_{1}\zeta_{0}^{2}}{2r_{10}^{7}} - \frac{105Q_{1}\sigma_{1}\zeta_{0}^{4}}{2r_{10}^{9}} - \frac{Q_{2}}{r_{20}^{3}} + \frac{3Q_{2}\zeta_{0}^{2}}{r_{20}^{5}} - \frac{3Q_{2}(2\sigma_{3} - \sigma_{4})}{2r_{20}^{5}} + \frac{15Q_{2}(2\sigma_{3} - \sigma_{4})\zeta_{0}^{2}}{2r_{20}^{7}} - \frac{3Q_{2}\sigma_{3}}{r_{20}^{5}} + \frac{15Q_{2}\sigma_{3}\zeta_{0}^{2}}{2r_{20}^{7}} + \frac{15Q_{2}\sigma_{3}\zeta_{0}^{2}}{2r_{20}^{7}} + \frac{15Q_{2}\sigma_{3}\zeta_{0}^{2}}{r_{20}^{5}} + \frac{15Q_{2}\sigma_{3}\zeta_{0}^{2}}{2r_{20}^{7}} + \frac{15Q_{2}\sigma_{3}\zeta_{0}^{2}}{r_{20}^{7}} + \frac{15Q_{2}\sigma_{3}\zeta_{0}^{2}}{r_{20}^{7}}$$



BOOK OF PROCEEDING, IPSCFUDMA2025 https://dx.doi.org/10.4314/jobasr.v2i1.1c

$$\frac{45Q_{2}\sigma_{3}\zeta_{o}^{2}}{2r_{20}^{7}} - \frac{105Q_{2}\sigma_{3}\zeta_{o}^{2}}{2r_{20}^{9}} - \frac{M_{b}\left[c(\zeta_{0}^{2}+d^{2})^{-1/2}+1\right]}{\left[\xi_{0}^{2}+\left(c+\sqrt{\zeta_{0}^{2}+d^{2}}\right)^{2}\right]^{\frac{3}{2}}} + \frac{M_{b}c^{2}\zeta_{0}^{2}\left[\left(\zeta_{0}^{2}+d^{2}\right)^{-3/2}\right]}{\left[\xi_{0}^{2}+\left(c+\sqrt{\zeta_{0}^{2}+d^{2}}\right)^{2}\right]^{\frac{3}{2}}} + \frac{3M_{b}\zeta_{0}^{2}\left[c(\zeta_{0}^{2}+d^{2})^{-1/2}+1\right]^{2}}{\left[\xi_{0}^{2}+\left(c+\sqrt{\zeta_{0}^{2}+d^{2}}\right)^{2}\right]^{\frac{3}{2}}} + \frac{3M_{b}\zeta_{0}^{2}\left[c(\zeta_{0}^{2}+d^{2})^{-1/2}+1\right]^{2}}{\left[\xi_{0}^{2}+\left(c+\sqrt{\zeta_{0}^{2}+d^{2}}\right)^{2}\right]^{\frac{3}{2}}} + \frac{3M_{b}\zeta_{0}^{2}\left[c(\zeta_{0}^{2}+d^{2})^{-1/2}+1\right]^{2}}{\left[\xi_{0}^{2}+\left(c+\sqrt{\zeta_{0}^{2}+d^{2}}\right)^{2}\right]^{\frac{3}{2}}} + \frac{3M_{b}\zeta_{0}^{2}\left[c(\zeta_{0}^{2}+d^{2})^{-1/2}+1\right]^{2}}{\left[\xi_{0}^{2}+\left(c+\sqrt{\zeta_{0}^{2}+d^{2}}\right)^{2}\right]^{\frac{3}{2}}} + \frac{3M_{b}\zeta_{0}^{2}\left[c(\zeta_{0}^{2}+d^{2})^{-1/2}+1\right]^{2}}{\left[\xi_{0}^{2}+\left(c+\sqrt{\zeta_{0}^{2}+d^{2}}\right)^{2}\right]^{\frac{3}{2}}} + \frac{3M_{b}\zeta_{0}^{2}\left[c(\zeta_{0}^{2}+d^{2})^{-1/2}+1\right]^{2}}{\left[\xi_{0}^{2}+\left(c+\sqrt{\zeta_{0}^{2}+d^{2}}\right)^{2}\right]^{\frac{3}{2}}} + \frac{3M_{b}\zeta_{0}^{2}\left[c(\zeta_{0}^{2}+d^{2})^{-1/2}+1\right]^{2}}{\left[\xi_{0}^{2}+\left(c+\sqrt{\zeta_{0}^{2}+d^{2}}\right)^{-1/2}+1\right]}\right]$$

$$\left[\xi_{0}^{2}+\left(c+\sqrt{\zeta_{0}^{2}+d^{2}}\right)^{-1/2}+1\right]$$

The effect of triaxiality, belt and radiation pressure on the locations and stability of out-of-plane equilibrium points are analyzed using the values of the parameters of the binary system (xi-Bootis and Kruger-60) with the aid of mathematical software MATHEMATICA 10.4.and are presented in Table 2- 6.

The numerical data of the binary system xi-Bootis and Kruger-60 are presented below:

Table 1: Numerical data for the Binary System

Binary	Masses	s (MO)	Eccentricity	Semi-major	Luminosity		Spectral
system			(e)	axis (a)	LO		Types
	M_1	M_2			L_1	L_2	
Xi Bootis	0.9	0.66	0.5117	4.9044	0.49	0.061	G8/k4
Kruger	0.271	0.176	0.4100	2.3830	0.01	0.0034	M3/M4
60							

Source: NASA ADS

Table 2: The effect of triaxiality on the location and stability of out-of-plane equilibrium points of xi-Bootis for e = 0.5117, a = 0.7304, $\mu = 0.4231$, $q_2 = 0.9998$.

S/no	Triaxiality			Out-of plane points		Roots of the characteristic equation			
	σ_1	σ_2	σ_3	σ_4	ξ	$\pm \zeta$	$\lambda_{1,2}$	$\lambda_{3,4}$	$\lambda_{5,6}$
1.	0.015	0.011	0.002	0.001	0.466009	0.265523	±610.224	-173.012± 175.323 <i>i</i>	173.012± 175.323 <i>i</i>
2.	0.02	0.015	0.003	0.002	0.477622	0.257321	±814.001	-172.807± 177.887 <i>i</i>	172.807± 177.887 <i>i</i>
3.	0.03	0.019	0.004	0.003	0.49838	0.246711	±998.013	-169.557± 178.39i	169.557± 178.39i
4.	0.04	0.02	0.005	0.004	0.526424	0.206453	±1522.48	-165.09± 179.832 <i>i</i>	165.09± 179.832 <i>i</i>



0.05 0.03 0.006 0.005

0.005 0.528303 0.204726 ± 1321.43

-162.88± 180.378i 162.88± 180.378i

192



Table 3: The effect of belt (M_b) on the location and stability of out-of-plane equilibrium points of xi-Bootis for e = 0.5117, a = 0.7304, $\mu = 0.4231$ $q_1 = 0.9988$, $q_2 = 0.9998$. $\sigma_1 = 0.02$, $\sigma_2 = 0.015$, $\sigma_3 = 0.003$, $\sigma_4 = 0.002$

S/no	M_b	Out-of plane points		Roots of the characteristic equation			
1	0.02	ξ 0.520081	±ζ 0.211443	$\lambda_{1,2} \pm 47.114534$	$\lambda_{3,4}$ ±113.35634i <i>i</i>	λ _{5,6} ±33.3587	
22	0.03	0.512573	0.211498	±47.244377	±120.48473i	±34.33589	
3	0.04	0.510623	0.221980	±48.257841	±120.67357i	±34.367635	
4	0.05	0.510327	0.222246	±48.264759	±121.24245ii	±35.40873	
5	0.06	0.509117	0.2235341	± 49.266985	±122.1156i	±35.50873i	

Table 4: The effect of triaxiality on the location and stability of out-of-plane equilibrium points of Kruger 60 for e = 0.4100, a = 0.5894, $\mu = 0.3937$ and $q_2 = 0.9996$

	Triaxiality		Out-of-plane points		Roots of the characteristic equation				
S/No	σ_1	σ_2	σ_3	σ_4	ξ	$\pm \zeta$	$\lambda_{1,2}$	$\lambda_{3,4}$	$\lambda_{5,6}$
1.	0.02	0.002	0.002	0.001	0.946635	0.220887	-37.25764± 21.3724 <i>i</i>	0±41.8365 <i>i</i>	$37.25764 \pm 21.3724i$
2.	0.03	0.025	0.003	0.002	0.947233	0.220663	-38.6453 <u>+</u>	0±43.2243 <i>i</i>	38.6453±
							-22.19753		-22.19753
3.	0.04	0.035	0.004	0.003	0.947834	0.220247	-51.478± 28.1867 <i>i</i>	0±51.3443 <i>i</i>	51.478± 28.1867 <i>i</i>
4.	0.05	0.045	0.005	0.004	0.950755	0.219965	-100.255± 55.1194i	0±113.603 <i>i</i>	100.255± 55.1194i
5.	0.06	0.055	0.006	0.005	0.955314	0.218754	-134.56± 62.55370i	0±154.122 <i>i</i>	134.56± 62.55370i



Table 5: The effect of belt (M_b) on the location and stability of out-of-plane equilibrium points of Kruger-60 for e=0.4100, $\alpha=0.5894$, $\mu=0.3937$, $q_2=0.9996$. $\sigma_1=0.02$, $\sigma_2=0.015$, $\sigma_3=0.003$, $\sigma_4=0.002$

S/no	M_b	Out-of plane points		Roots of the cha	n	
1	0.001	ξ 0.223211	±ζ 0.194723	$\lambda_{1,2}$ ± 46.473223	λ _{3,4} ±69.2802	λ _{5,6} ±56.4778i
2	0.002	0.223200	0.194841	± 46.55631	±75.5432	±62.3342i
3	0.003	0.223230	0.194981	± 46.50467	±76.775	±71.6184i
4	0.004	0.223245	0.195274	±46.36982	±76.4643	±89.6221
5	0.005	0.223297	0.195613	± 46.27746	±111.675	±94.3398

Table 6: The Combined effect of the pertubations on the location and stability of out-of-plane equilibrium points for e=0.3, a=0.34

(a) S/no.	r	Tr	iaxiality		Radiation Factor	Belt	Mass ratio
	σ_1	σ_2	σ_3	σ_4	q_2	M_b	μ
1.	0.002	0.001	0.0002	0.0001	0.9972	0.001	0.0375
2.	0.003	0.002	0.0003	0.0002	0.9976	0.002	0.0380
3.	0.004	0.003	0.0004	0.0003	0.9980	0.003	0.0385
4.	0.005	0.004	0.0005	0.0004	0.9984	0.004	0.0390
5.	0.006	0.005	0.0006	0.0005	0.9988	0.005	0.0395
(b)							
, ,	out-of-plan	ne points		The char	racteristic Root	S	
	ξ	±ζ	$\lambda_{1,2}$		$\lambda_{3,4}$	$\lambda_{5,6}$	
0.567	412	0.185532	±197.9	63 ±	17.4552	±77.3282 <i>i</i>	
0.567	395	0.193443	±211.	495 <u>+</u>	70.5671	±83.8671 <i>i</i>	
0.567	382	0.206738	±258.7	57 ±2	70.4693	±83.7942i	

0.567374	0.215372	±567.09	±71.3939	±80.133 <i>i</i>
0.567367	0.220541	±667.430	±101.4056	±22.4906 <i>i</i>

3. Discussion and Conclusion

The motion of a third body under the influence of triaxiality and a radiating smaller primary together with a circumbinary disc has been described in equation (1)-(4). The positions of out-of-plane equilibrium points are given in equation (14) and (15) and are obtained numerically by approximating the series expansion in the triaxiality coefficient to third order term with the aid of the software MATHEMATICA 10.4. The stability of these points are determined numerically using equation (16). Table 1 shows the properties of the binary system (Kruger-60 and Xi-bootis) used in demonstrating the dynamics of the particle under investigation. The effect of triaxiality on the location and stability of out-of-plane equilibrium points of Xi-bootis is shown on Table 2. Due to increase of triaxiality the infinitesimal mass moves away from the barycenter along the ξ -axis while

 ζ -axis it moves towards the origin this shows that the particle is unstable, which is shown by the characteristic roots of the system which are complex or real roots. The equilibrium points are stable only if the six roots λ_i (i=1,2,3,4,5,6) are purely imaginary roots or complex roots with negative real parts and are unstable if λ_i (i=1,2,3,4,5,6) are complex or real roots (Szehebely,1967).

Table 3 shows the point $L_{6,7}$ shifts towards the axis (origin), with an increase in gravitational potential from the belt of Xi-Bootis. An increase in the triaxiality factor of Kruger-60 (Table 4) moves $L_{6,7}$ away from the origin, while in the case of belt (Table 5) the point moves towards the origin. The combined effect of all the parameters are shown in Table 6. Table 6a contains the arbitrary values for the parameters and Table 6b shows their effects on out-of- plane points and their stability, As can be seen in Table 6a the out-of- plane equilibrium points shifts towards the ζ -axis with increasing values of all parameters together and they are unstable. The effects of triaxiality and the belt on the two above systems can be observed in Table 2-6. These Tables shows that with increasing values of triaxiality and belt the out-of-plane points (in the both system) move towards the ζ axis and they are unstable since the six roots λ_i (i=1,2,3,4,5,6) are not purely imaginary roots or complex roots with negative real parts. This instability has been confirmed by (Douskos & Markellos (2006); Kushvah (2008); Singh & Umar (2013))

We have established the existence of out of plane equilibrium points and their stability in the framework of (ER3BP) when the primaries are triaxial, with only the smaller primary radiating and surrounded by a belt. It is found that the positions are affected by triaxiality, radiation and the belt. The out-of-plane equilibrium points are unstable.

References

Abouelmagd EI (2013) The effect of photogravitational force and oblateness in the pertubed restricted three-body problem. Astrophy Space Sci 346(1):51-69.

Ammar MK (2008) The Effect of Solar Radiation Pressure on Lagragian Points in the Elliptic Restricted Three-Body Problem. Astrophys Space Sci **313**:393-408

Aumann HH, Beichman CA, Gillet FC, De-long T, Houck JR, Low FT, Neugebanar G, Walker RG, Wesselius PR (1984) Discovery of a shell around Alpha Lyrae. Astrophy J 278: 123-127.



Chermikov YA (1970) The photogravitational restricted three-body problem Sov Astron 14:176-181 Das MK, Pankaj N, Mahajan T, Yuasa M (2008) Effect of radiation on the stasbility of equilibrium points in the stellar binary system:RW-Monocerotis,kruger 60. Astrophys space sci 314:261-274

Douskos CN, Markellos VV (2006) Out-of-Plane equilibrium points in restricted three-body problem with oblateness Astron Astrophys 446:357-360.

Hussain AA,Umar A (2019) Generalized "Out-Of-Plane" Equilibrium Points in the Frame of Elliptic restricted three-body problem: Impact of oblate primary and Luminuos Triaxial Secondary. Adv Asron http://doi.org/10.1155/2019/3278946

Jiang IG, Yeh LC (2003) Birfurcation for dynamical systems of planet-belt interaction. Int J of Birf Chaos 13:No.3 617-630.

Jiang IG, Yeh LC (2004) The modified restricted three-body problem. Rev Mex AA (Serie de Conferencias) 21:152-155

Kushvah, B.S. (2008) Linear Stability of Equilibrium Points in the Generalized Photogravitational Chermnykh's Problem. Astrophys Space Sci 318:41-50.

Miyamoto M, Nagai P (1975) Three Dimensional Models for the distribution of mass galaxies. ,Astron Soc of Japan 27: 533-543.

Narayan A, Nutan S (2014) Stability of triangular Lagragian points in the elliptic restricted three-body problem under radiating binary system. Astrophys Space *Sci.*53: 457-464

Radzievskii VV (1950) The restricted problem of three bodies taking account of light pressure. Astron J 27: 250.

Simmons JFL,McDornald JC,Brown JC (1985) The restricted three-body problem with radiation Pressure. Cel Mech Dyn Astron5:145-187

Singh J, Amuda TO (2019) Stability Analysis of Triangular equilibrium points in restricted three-body problem under effect of circumbinary disc,radiation and drag forces. Astrophys astron 40: 5 http://doi.org/10.1007/s 12036-019-9537-6

Singh J, Amuda TO (2015) Out-Of-Plane Equilibrium Points in the photogravitational CR3BP with Oblateness and PR Drag.J Astrophys astron 36:2 DoI 10.1007/s12036-015-9336-v

Singh J (2012) Motion around the Out-Of-Plane Equilibrium Points of the pertubed restricted three-body problem Astrophys Space Sci 342: 303-308

Singh J Umar A (2013) On Out-Of-Plane Equilibrium Points in the Elliptic restricted three-body with radiating and oblate primaries. Astrophys Space Sci 344 13-19

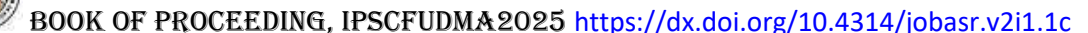
Singh J Taura JJ (2014b) Combine effect of oblateness, radiation and a cluster of material points on the stability of triangular libration points in the restricted three-body problem J Astrophys Astron 351: 2.

Singh J Taura JJ (2014b) Effects of triaxiality, oblateness and gravitational pontetial from a belt on the linear stability of $L_{4,5}$ in the restricted three-body problem. Astrophys Astron 35 (4):729-743

Singh J. and Tyokyaa K.R (2021). The Motion of Out-of-Plane Equilibrium Points in the Elliptic Restricted Three-Body Problem at J4. *International Frontier Science Letters. ISSN: 2349-4484, Vol. 17, pp 1-11 doi:10.18052/www.scipress.com/IFSL.17.1 CC BY 4.0. Published by SciPress Ltd, Switzerland, 2021*

Singh J. and Tyokyaa K.R (2023). Albedo effects in the ER3BP with an oblate primary, a triaxial secondary and a potential due to belt. Scientific reports (2023)13:4286, https://doi.org/10.1038/s41598-023-30671-3, www.nature.com/scientificreports/Springer.

Zotos EE (2018) On the Newton-Raphson basins of convergence of the Out-Of-Plane equilibrium points in the Copenhagen problem with oblate primaries. Int. J non-linear mech DOI:10.1016/j.ijnonlinmec.2018.05.002



Evaluation of Cancer Risk Associated with Natural Radioactivity in Soil and Plant Samples from Federal University Dutsin-Ma, Katsina State, Nigeria Namadi A. Z.¹, Agu M. N.² and Ugbe R. U.³

1Department of Physics, Faculty of Physical Sciences, Federal University Dutsin-Ma 2Department of Physics, Faculty of Science, Nigerian Defence Academy, Kaduna 3Groundwater Department, National Water Resources Institute, Kaduna. *Corresponding Author Email: nabdulrahman@fudutsinma.edu.ng

Abstract

This study investigates the cancer risk associated with natural radioactivity in soil and vegetation samples from the Federal University Dutsin-Ma (FUDMA), Katsina State, Nigeria. A total of 10 soil and 10 plant samples were collected across various campus locations. Gamma spectrometric analysis using a NaI(Tl) detector quantified the activity concentrations of Ra-226, Th-232, and K-40. The results revealed that average concentrations of Ra-226 and Th-232 in soil (33.43 Bq/kg and 43.16 Bq/kg, respectively) exceeded global averages, while K-40 remained significantly lower. Corresponding vegetation samples showed reduced radionuclide levels, indicating selective uptake. Radiological hazard indices including absorbed dose, annual effective dose, and excess lifetime cancer risk (ELCR) were calculated. The highest soil ELCRγ (5.04) was observed at the Faculty of Physical Sciences, while the highest in plants (1.76) occurred at the Faculty of Life Sciences. Despite the lower risk from vegetation, the cumulative exposure from both sources may pose long-term health hazards. The study emphasizes the need for regular environmental radiation assessments, informed land use planning, and public sensitization to ensure safety and compliance with international radiation protection standards.

Keywords: Natural radioactivity, Radionuclides, Cancer risk, Gamma spectrometry, FUDMA, Environmental radiation, ELCR

Introduction

Natural radioactivity is a pervasive environmental phenomenon originating from the decay of primordial radionuclides, predominantly U-238 series, Th-232 series, and K-40, which are naturally embedded within the Earth's crust (Beogo et al., 2022; Ehsan et al., 2020). Their concentrations in soil, water, and air vary based on geological and geographical factors (Beogo et al., 2022; Souffit et al., 2022). Human activities and construction materials can also augment and redistribute these radionuclides, affecting background radiation and human exposure (Eštoková et al., 2022; Fohlmeister & Hoffmann, 2023; Kocsis et al., 2021; Verde et al., 2022). Hence, localized assessments are essential for accurate evaluation (Aguko et al., 2020). Radiation exposure, even at low doses, poses recognized health risks and has been linked to malignancies such as leukemia and lung, pancreatic, hepatic, skin, and kidney cancers, as well as non-carcinogenic effects like cataracts and sterility (Alimam & Auvinen, 2025; Ehsan et al., 2020; Kendall et al., 2021; Reddy et al., 2022; Simon et al., 2022; Zhu et al., 2020). In Nigeria, cancer cases are rising, especially in low- and middle-income regions (Akinwande et al., 2023). Increased use of diagnostic imaging further emphasizes the need for environmental radiation monitoring (Abdulkadir, 2020; Aladeniyi et al., 2022; Rahman, 2020). Soil is a primary reservoir for radionuclides, exposing humans via external gamma radiation and internal routes like inhalation or ingestion through contaminated food chains (Abdelfadeel et al., 2023; Eke et al., 2022; Ononugbo & Anekwe, 2020; Salminen-Paatero & Paatero, 2021; Yang et al., 2022). To evaluate such risks, concentrations of Ra-226, Th-232, and K-40 are measured using gamma-ray spectrometry (Bangou et al., 2021; Barba-Lobo et



al., 2021; Pavel et al., 2025). Radiological indices like radium equivalent activity and excess lifetime cancer risk are then calculated (Chussetijowati et al., 2022; Coulibaly et al., 2023; Saudi et al., 2022). This study assesses cancer risk from natural radioactivity in soil and plants at Federal University Dutsin-Ma, Nigeria.

Materials and Methods

Study Area

Dutsin-Ma is a Local Government Area in Katsina State, North-Western Nigeria. It lies on latitude 12°26'N and longitude 07°29'E. It is bounded by Kurfi and Charanchi LGAs to the north, Kankia LGA to the East, Safana and Dan-Musa LGAs to the West, and Matazu LGA to the Southeast.

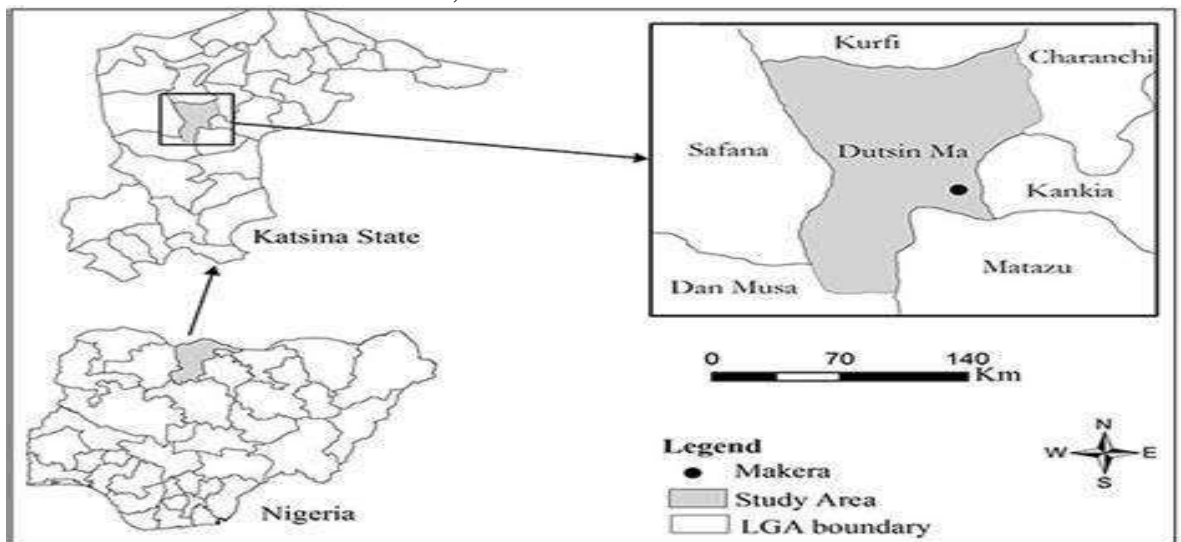


Figure 1: Geographical of Map of Nigeria, indicating Katsina state and Dutin-Ma (Oyebamiji et al., 2019)

The Federal University Dutsin-Ma was established on 7th February, 2011 along with eight other Federal Universities to tackle the challenges of inadequate enrolment space for eligible University applicants in some educationally less privileged states who don't have Federal Universities. With the support of the State Government, the permanent as well as the take-off site were identified; with the take-off site located in Dutsin-Ma town while the main campus at Kilometer-Sixty Katsina-Kankara road in Dutsin-Ma Local Government Area of Katsina State (FUDMA, 2015).







Plate 1: Satellite View of Federal University Dutsin-Ma main Campus (Google maps, 2024; modified) Materials

Materials used in gamma spectroscopy

Soil and vegetation samples, Polythene Bag, Hand auger, Digger, shovel, surgical gloves, drilling machine, indelible ink, masking tape, tissue paper, candle wax, plastic container, sieve, hydraulic pressure system, geographical positioning (GPS), gamma spectrometry system (Sodium iodide activated with thallium).

Methods

Soil sample collection

Soil samples were collected within the university. The soil samples were taken using a mechanical hand auger to a depth of 5-10 cm. At each sampling location, soil sample was taken into labeled plastic bags. One kilogram (1 kg) of each sample was collected for analysis.

Vegetation sample collection

In locations where soil samples were collected, vegetation samples were collected with each sample collected within a grid area of 1 m x 1 m. The samples were also packaged in plastic bags and labelled with identification marks. The coordinates of each sampling location that corresponded to the soil samples earlier discussed were recorded for traceability (Kamunda, 2017).

Sample preparation for gamma radioactivity measurements

The sample preparation method was adopted from Ibeanu, (1999). Each of the soil sample as well as the plant sample was sealed in a polyethylene bag, firmly tied and labelled to avoid cross contamination of the samples. Samples were spread on cardboard sheets and "all foreign materials" were removed. The samples were then oven dried at a temperature of 110°C for 12-18 hours. The samples were then grinded into a fine powder and sieved using 2 mm sieve. The homogenized samples were filled into 25 g plastic containers (7.2 cm diameter by 6 cm height) which were hermetically sealed with the aid of PVC tape to prevent the escape of airborne ²²²Rn and ²²⁰Rn from the samples. The dimensions of the plastic containers were chosen in such a way that it suited the optimal soil mass of 350 g for analysis of bulk samples. The samples were then sealed and stored for over 24 days to allow secular equilibrium to be reached between radon and its daughters. The IAEA reference materials for gamma spectrometry (RGK-1, IAEA-448 and RGTh-1) were prepared exactly as the



samples.

Gamma spectrometric analysis

The NaI(TI) detector, situated at low background laboratory of the Center for Energy Research and Training, Ahmadu Bello University, Zaria, was used for the gamma spectrometric measurements. The detector has a 6 cm thick lead shield, cadmium lined assembly with copper sheets for the detection of background radiation. The detector has pulse resolving time of about 0.25 s, an incorporated preamplifier and a 1 kV external source which permits its use for high counting rates. The detector was coupled to a computer based multichannel analyser Maestro program from ORTEC for the acquisition and analysis of the gamma spectra. The detector was calibrated with the prepared IAEA reference materials RGK-1, IAEA-448 and RGTh-1 for the quantitative determination of ⁴⁰K, ²³⁸U and ²³²Th respectively in the soil samples. Each of the prepared samples was counted for 30,000 seconds in the outlined detector geometry in order to mitigate the influence of background radiation from radioactive contaminants within the shielding materials of the detector assembly. The spectral energy windows used for the analysis of the NORMs were presented in Table 2.1. The obtained data in counts per second were converted to conventional units of Bq/kg using calibration factors to determine the activity concentration of ²²⁶Ra (²³⁸U), ²³²Th and ⁴⁰K.

Table 1: Spectral energy used in the gamma spectrometric analysis

Element analysed	Isotope used	Gamma energy (keV)	Energy windows (keV)
40 K	40 K	1460.0	1380-1510
²²⁶ Ra	²¹⁴ Bi	1764.0	1690-1820
²³² Th	²⁰⁸ Tl	2614.5	2590-2710

Computation of Cancer Risk Due To NORMs Absorbed Dose

The absorbed dose at 1 meter above the ground both outdoor (D_{out}) and indoor (D_{in}) were calculated from the measured specific activities of 226 Ra, 232 Th and 40 K (Bqkg⁻¹) in soil using Equations 1 and 2 respectively (Ramasamy, 2009; UNSCEAR, 2000; European Commission, 1999).

$$D_{out} (nGyh^{-1}) = 0.462A_{Ra} + 0.604A_{Th} + 0.0417A_K$$
 1

$$D_{in} (nGyh^{-1}) = 0.92A_{Ra} + 1.1A_{Th} + 0.081A_K$$

where A_{Ra} , A_{Th} and A_K are the activity concentrations (in Bqkg⁻¹) of ²²⁶Ra, ²³²Th and ⁴⁰K in the samples, respectively. The numerical values 0.462, 0.604 and 0.041 in nGyh⁻¹Bq⁻¹kg⁻¹ are conversion factors of γ -radiation emanating from ²²⁶Ra, ²³²Th and ⁴⁰K outdoor respectively, while 0.92, 1.1 and 0.081 in nGyh⁻¹Bq⁻¹kg⁻¹ are conversion factors of γ -radiation emanating from ²²⁶Ra, ²³²Th and ⁴⁰K indoor respectively.

Annual effective dose due to external gamma radiation (AED $_{\gamma}$)

The annual effective dose is of two types. The outdoor annual effective dose (E_{out}) and indoor annual effective dose (E_{in}). The Total annual effective doses due to external radiation from 226 Ra, 232 Th and 40 K in Bqkg⁻¹ (AED $_{\gamma}$) were evaluated by summing up outdoor and indoor effective doses. It was assumed that 137 Cs, 90 Sr and 235 U radioactivity decay series have no noticeable contribution to the total dose from environmental background (Qureshi *et al.*, 2014). Equations 3, 4 and 5 were used in evaluating E_{out} , E_{in} and AED_{γ} (Hafezi *et al.*, 2005; Ramasamy *et. al.*, 2009 UNSCEAR, 2000).



$E_{out}(mSvyr^{-1}) = D_{out} \times 8760 \times 0.2 \times 0.7 \times 10^{-6}$	3
$E_{in}(mSvyr^{-1}) = D_{in} \times 8760 \times 0.8 \times 0.7 \times 10^{-6}$	4
$AED_{v}(mSvyr^{-1}) = E_{out} + E_{in}$	5

where D is dose rate in nGyh⁻¹, the value 8760 are the hours in a year, the conversion coefficient from the absorbed dose in the air to the effective dose is 0.7 SvGy⁻¹, outdoor and indoor occupancy factors are 0.2 and 0.8 respectively (UNSCEAR, 2000).

Excess life cancer risk due to external gamma radiation (ELCR_γ)

The excess life cancer risk (ELCR $_{\gamma}$) was computed using the result of annual effective doses E_{in} and E_{out}. Life expectancy (LE) which according to (Statista, 2023) in Nigeria is 59.93 for men, 63.75 for Women and 61.84 average and Risk factor (RF). ELCR_{out}, ELCR_{in} and ELCR $_{\gamma}$ were all evaluated using Equations 6, 7 and 8 respectively (Qureshi *et al.*, 2014; ICRP, 2007).

$ELCR_{out} = E_{out} \times LE \times RF$	6
$ELCR_{in} = E_{in} \times LE \times RF$	7
$ELCR_{\gamma} = ELCR_{out} + ELCR_{in}$	8

Results

Table 2a: Activity concentrations of 226 Ra, 232 Th and 40 K in soil samples from FUDMA main

campus and worldwide average.

S/No.	Sample ID	Area	A adiavidas a am a amdurad	dan (Dalra-1)	
	_	Location	Activity concentrat	Activity concentration (Bqkg ⁻¹)	
			²²⁶ Ra	²³² Th	40 K
1.	SS-A01	University Gate	33.01±2.78	34.05±2.46	143.13±4.96
2.	SS-A02	Senate Building	47.86 ± 2.20	64.57±2.24	234.84±4.94
3.	SS-A03	University Library	28.05 ± 2.78	53.67 ± 2.51	209.36±5.55
4.	SS-A04	University Clinic	30.21 ± 2.68	35.88 ± 1.26	81.56±4.88
5.	SS-A05	Faculty of Physical Sciences	37.97 ± 3.54	47.81 ± 2.41	154.96±2.89
6.	SS-A06	Faculty of Life Sciences	24.48 ± 1.27	27.48 ± 1.53	129.08±3.27
7.	SS-A07	Faculty of Health Sciences	42.94±5.57	45.61 ± 2.01	193.98 ± 2.52
8.	SS-A08	Faculty of Engineering	20.36 ± 2.47	51.78 ± 2.14	174.50 ± 2.95
9.	SS-A09	Female Hostel	46.22 ± 3.38	49.74±3.71	196.33±3.03
10.	SS-A10	Male Hostel	23.16±2.12	21.03±1.46	125.49 ± 2.47
		MINIMUM	20.36 ± 2.47	21.03±1.46	81.56±4.88
		MAXIMUM	47.86 ± 2.20	64.57 ± 2.24	234.84±4.94
		AVERAGE	33.43	43.16	164.32
		WORLDWIDE AVERAGE	30.00	35.00	400.00

Table 2a presents the activity concentrations of natural radionuclides ²²⁶Ra, ²³²Th, and ⁴⁰K in soil samples collected from various locations within the FUDMA main campus. The measured concentrations ranged from 20.36 to 47.86 Bq/kg for ²²⁶Ra, 21.03 to 64.57 Bq/kg for ²³²Th, and 81.56 to 234.84 Bq/kg for ⁴⁰K. The highest values for all three radionuclides were recorded at the Senate Building, indicating a potential concentration of naturally occurring radioactive materials (NORMs) in that area. The average activity concentrations across all samples were 33.43 Bq/kg for ²²⁶Ra, 43.16 Bq/kg for ²³²Th, and 164.32 Bq/kg for ⁴⁰K. When compared to the global averages reported by UNSCEAR 30 Bq/kg for ²²⁶Ra, 35 Bq/kg for ²³²Th, and 400 Bq/kg for ⁴⁰K the FUDMA campus shows slightly elevated levels of ²²⁶Ra and ²³²Th, but significantly lower levels of ⁴⁰K.



These findings suggest the local geology is moderately enriched in uranium and thorium series radionuclides, while potassium-bearing minerals may be less prevalent.

Table 2b: Activity concentrations of ²²⁶Ra, ²³²Th and ⁴⁰K in vegetation samples from FUDMA

main campus and worldwide average.

S/No.	Sample ID	Area Location	Activity concentration (Bqkg ⁻¹)			
			²²⁶ Ra	²³² Th	40 K	
1.	VS-A01	University Gate	32.98±2.79	30.86±1.49	48.01±4.40	
2.	VS-A02	Senate Building	14.46±1.51	16.67±1.51	25.04±3.00	
3.	VS-A03	University Library	43.91 ± 2.48	32.85 ± 3.59	56.10±4.51	
4.	VS-A04	University Clinic	26.09±3.61	33.88 ± 4.45	30.95±3.30	
5.	VS-A05	Faculty of Physical Sciences	22.81±1.26	19.74 ± 2.85	75.61 ± 4.04	
6.	VS-A06	Faculty of Life Sciences	34.93±2.16	49.90±2.63	34.48±3.14	
7.	VS-A07	Faculty of Health Sciences	13.73±1.09	36.34 ± 2.20	29.08±2.20	
8.	VS-A08	Faculty of Engineering	19.10±1.41	50.96±3.37	19.63±1.96	
9.	VS-A09	Female Hostel	26.49 ± 2.87	32.27±3.31	24.06±2.51	
10.	VS-A10	Male Hostel	16.10±2.33	27.57 ± 2.17	30.02±3.73	
		MINIMUM	13.73±1.09	16.67±1.51	19.63±1.96	
		MAXIMUM	43.91±2.48	50.96±3.37	75.61 ± 4.04	
		AVERAGE	25.06	33.10	37.30	
		WORLDWIDE AVERAGE	30.00	35.00	400.00	

Table 2b illustrates the activity concentrations of the same radionuclides ²²⁶Ra, ²³²Th, and ⁴⁰K but in vegetation samples collected from corresponding locations. Here, the activity concentrations ranged from 13.73 to 43.91 Bq/kg for ²²⁶Ra, 16.67 to 50.96 Bq/kg for ²³²Th, and 19.63 to 75.61 Bq/kg for ⁴⁰K. The highest concentration of ²²⁶Ra was found at the University Library, while ²³²Th peaked at the Faculty of Engineering, and ⁴⁰K was highest at the Faculty of Physical Sciences. The average values 25.06 Bq/kg for ²²⁶Ra, 33.10 Bq/kg for ²³²Th, and 37.30 Bq/kg for ⁴⁰K are lower than both the soil values and global averages. These results reflect the selective uptake of radionuclides by plants, which depends on several factors including root depth, soil-to-plant transfer coefficients, species-specific absorption traits, and the chemical form of the radionuclides in the soil. Notably, ⁴⁰K, despite being essential for plant nutrition, remains significantly below the global average of 400 Bq/kg, hinting at limited availability or uptake from the soil.

Table 3a: Excess life cancer risk due to external gamma radiation (ELCR_y) for soil samples

S-No		ELCR _{out}	ELCR out	ELCR out	$ELCR_{in}$	ELCR _{in}	ELCR _{in}	
	Sample Location	(M)	(F)	(Av)	(M)	(F)	(Av)	ELCRγ
1.	University Gate (SS)	1.88	2.14	2.08	1.33	1.42	1.37	3.45
2.	Senate Building	0.99	1.13	1.09	2.25	2.40	2.33	3.42
3.	University Library	2.20	2.51	2.43	1.71	1.82	1.76	4.19
4.	University Clinic	1.21	1.38	1.34	1.26	1.34	1.30	2.64
5.	Faculty of Physical Sciences	2.96	3.38	3.28	1.71	1.82	1.76	5.04
6.	Faculty of Life Sciences	1.37	1.56	1.52	1.09	1.16	1.13	2.65
7.	Faculty of Health Sciences	1.15	1.31	1.27	1.78	1.89	1.83	3.10
8.	Faculty of Engineering	0.80	0.91	0.88	1.54	1.64	1.59	2.47
9.	Female Hostel	0.96	1.09	1.06	1.91	2.03	1.97	3.03



10.	Male Hostel	1.18	1.34	1.30	0.92	0.98	0.95	2.25
	MINIMUM	0.80	0.91	0.88	0.92	0.98	0.95	1.83
	MAXIMUM	2.96	3.38	3.28	2.25	2.40	2.33	5.61
	AVERAGE	1.47	1.68	1.62	1.55	1.65	1.60	3.22

Table 3a estimates the Excess Lifetime Cancer Risk (ELCRγ) from soil exposure, considering both outdoor and indoor scenarios for males and females. The ELCR_{out} values ranged from 0.88 to 3.28, while ELCR_{in} values ranged from 0.95 to 2.33. Combined, the total ELCR ranged from 1.83 to 5.61, with the Faculty of Physical Sciences recording the highest risk and the Faculty of Engineering the lowest. The average ELCR across all soil samples was 3.22. the relatively elevated values observed at academic and residential areas warrant ongoing monitoring and possibly public sensitization regarding cumulative exposure risks.

Table 3b: Excess life cancer risk due to external gamma radiation (ELCR $_\gamma$) for vegetation samples

sampes								
Serial		ELCR _{out}	ELCR _{out}	ELCR _{out}	ELCR _{in}	ELCR _{in}	ELCR _{in}	
No	Sample Location	(M)	(W)	(Av)	(M)	(W)	(Av)	ELCRγ
1.	University Gate	0.17	0.18	0.18	1.13	1.20	1.16	1.34
2.	Senate Building	0.10	0.11	0.11	0.58	0.62	0.60	0.70
3.	University Library	0.20	0.22	0.21	1.37	1.45	1.41	1.62
4.	University Clinic	0.17	0.18	0.18	1.06	1.13	1.09	1.27
5.	Faculty of Physical Sciences	0.14	0.15	0.14	0.82	0.87	0.85	0.99
6.	Faculty of Life Sciences	0.20	0.22	0.21	1.50	1.60	1.55	1.76
7.	Faculty of Health Sciences	0.14	0.15	0.14	0.92	0.98	0.95	1.09
8.	Faculty of Engineering	0.17	0.18	0.18	1.26	1.34	1.30	1.48
9.	Female Hostel	0.17	0.18	0.18	1.02	1.09	1.06	1.23
10.	Male Hostel	0.14	0.15	0.14	0.79	0.84	0.81	0.95
	MINIMUM	0.10	0.11	0.11	0.58	0.62	0.60	0.70
	MAXIMUM	0.20	0.22	0.21	1.50	1.60	1.55	1.76
	AVERAGE	0.16	0.17	0.17	1.05	1.11	1.08	1.24

Table 3b provides the ELCR γ for vegetation samples. The values were uniformly lower than their soil counterparts, ranging from 0.70 to 1.76. The highest ELCR was found at the Faculty of Life Sciences, while the Senate Building showed the lowest. The average ELCR from vegetation was 1.24. While these levels are within safe limits, the potential for bioaccumulation over time and introduction into the food web cannot be overlooked. Continuous observation is important, especially for plants used in food, medicine, or grazing. The data suggest that, although less significant than soil, vegetation still contributes to long-term cancer risk and should be factored into comprehensive radiological assessments.



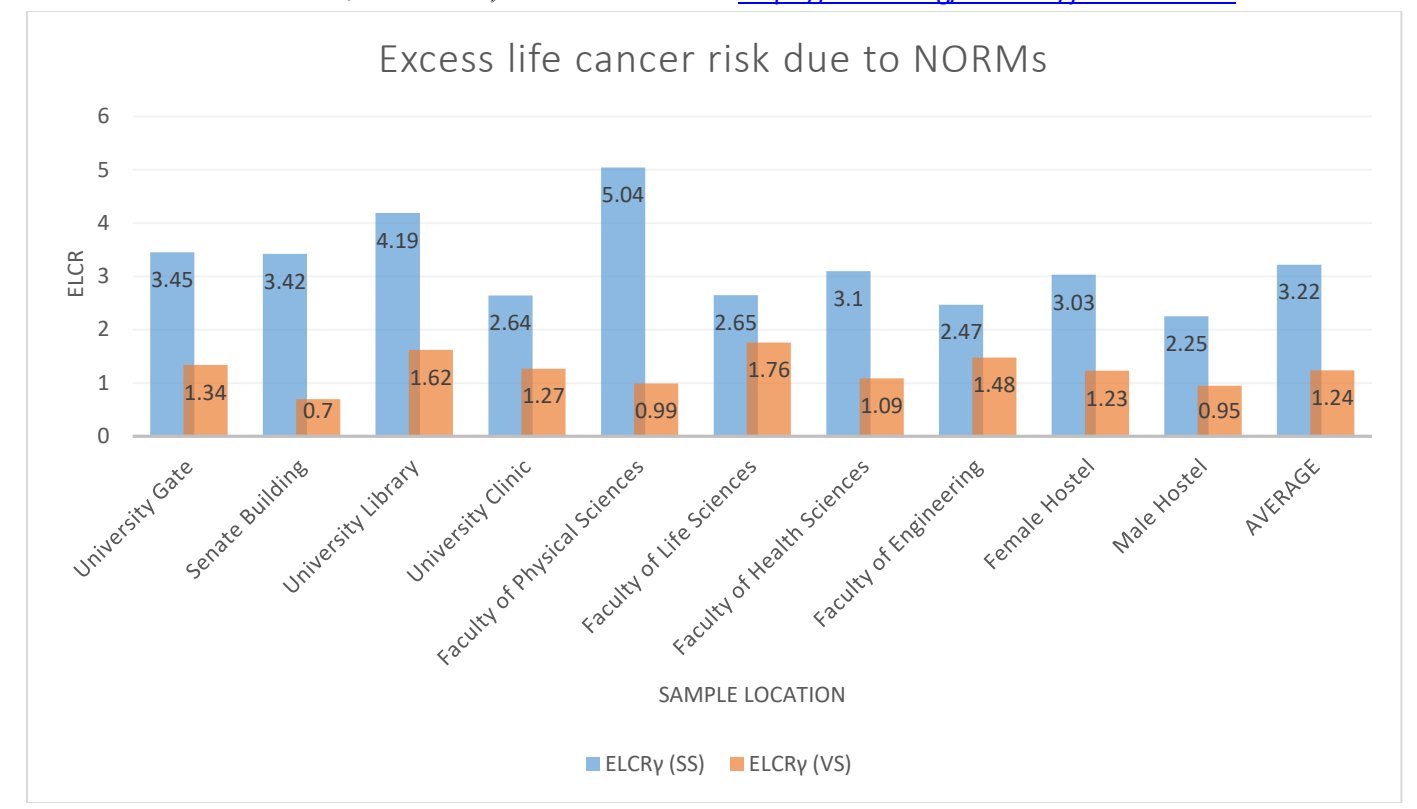


Figure 3: Excess life cancer risk due to external gamma radiation (ELCR $_{\gamma}$) for soil and vegetation samples

Figure 3. compares ELCR values from both soil (SS) and vegetation (VS). From the figure, it is evident that soil consistently poses a higher cancer risk due to its higher radionuclide content and prolonged proximity to human activity. Locations like the Faculty of Physical Sciences and University Library stand out, with ELCRγ values approaching 5.04 and 4.19 respectively. In contrast, vegetation at the same locations yielded considerably lower risks, further emphasizing the predominance of soil in terrestrial exposure. The graphical data simplifies the complex numerical results into an intuitive format that can support decision-making, especially in the context of land management and environmental health policy on campus.

Conclusion

The study revealed elevated concentrations of Ra-226 and Th-232 in soil and plant samples within the FUDMA main campus, with activity levels exceeding global averages in several locations. Calculated radiological indices, particularly excess lifetime cancer risk (ELCR), suggest potential long-term health implications, especially in soil-exposed areas. Although vegetation posed lower risks, its role in internal exposure through bioaccumulation remains relevant. These findings highlight the importance of consistent environmental monitoring and risk mitigation strategies to safeguard public health and ensure compliance with international radiological safety standards.

Recommendations

- 1. Establish routine radiological monitoring programs across FUDMA and similar institutions to track changes in background radiation levels.
- 2. Conduct periodic health surveillance of residents, especially those frequently exposed to high-risk zones such as the Faculty of Physical Sciences.



- 3. Promote soil management practices that limit radionuclide mobility and uptake by edible plants within the university community.
- 4. Integrate radiological safety education into environmental and health-related university curricula to raise awareness among students and staff.
- 5. Collaborate with national regulatory agencies to enforce radiation safety guidelines and facilitate intervention in identified high-risk zones.

References

- Adadey, S. M., Languon, S., Ayee, R., Ntumy, M. M., Nettey, O., Abrahams, A. J., & Tagbor, D.. Incidence and mortality of cancer in the Volta Region of Ghana (Adadey et al., 2020). *PLoS ONE*, 15.
- Aguko, W. O., Kinyua, R., & Githiri, J.. Natural Radioactivity and Excess Lifetime Cancer Risk Associated with Soil in Kargi Area, Marsabit-Kenya (Aguko et al., 2020). *Journal of Geoscience and Environment Protection*, 8, 127–143.
- Aladeniyi, K., Olowookere, C. J., Khandaker, M. U., Sanusi, A. J., Alabi, O. M., & Usman, I.. Evaluation of Radiological Health Risks in Popularly Consumed Brands of Sachet Water in Nigeria (Aladeniyi et al., 2022). *Applied Water Science*, 12.
- Akinwande, A. M., Ugwuanyi, D. C., Chiegwu, H. U., & Amakom, C. M.. Radiotherapy services in low resource settings: The situation in Nigeria (Akinwande et al., 2023). *Frontiers in Oncology*, 13.
- Beogo, C. E., Cissé, O., & Zougmoré, F.. Assessment of radiological hazards from soil samples in the Northeastern area of Burkina Faso (Beogo et al., 2022). *Radiochimica Acta*, 110.
- Borba-Lobo, A., San Miguel, E. G., Lozano, R. L., & Martín-Delgado, J. M.. A general methodology to determine natural radionuclides by well-type HPGe detectors (Barba-Lobo et al., 2021). *Journal of Radioanalytical and Nuclear Chemistry*, 329, 211–217.
- Chussetijowati, J., Seno, H., & Muliawan, D.. Environmental Radioactivity Concentrations and Assessment of Radiological Hazards in Soil Around Bandung Nuclear Area (Chussetijowati et al., 2022). *Jurnal Sains Dirgantara*, 19, 108–117.
- Coulibaly, A., Kpeglo, D. O., & Darko, E. O.. Assessment of Radiological Hazards in Some Foods Products Consumed by the Malian Population Using Gamma Spectrometry (Coulibaly et al., 2023). *Journal of Radiation Research and Applied Sciences*, 16, 100494.
- Djeufack, L. B., Bineng, G. S., Modibo, O. B., & Ndountchi, T. J.. Correlation between Ground \$^{222}\$Rn and \$^{226}\$Ra and Long-Term Risk Assessment at the at the Bauxite Bearing Area of Fongo-Tongo, Western Cameroon (Djeufack et al., 2022). *Physical Sciences Research International*, 10, 10–19.
- Ehsan, M. S., Rahman, M. F., Tabassum, N., Rahman, S., Hossain, M., & Rahman, M. M.. The Activity Concentration of Radionuclides (\$^{226}\$Ra, \$^{232}\$Th and \$^{40}\$K) in Soil Samples and Associated Health Hazards in Natore, Kushtia and Pabna District of Bangladesh (Ehsan et al., 2020). *Journal of Nuclear and Atomic Physics*, 5.
- Eke, B. C., Amakom, C. M., Ukewuihe, U. M., & Ukwuoma, E. I.. Radiological Dose Assessment due to the Presence of Norms in the Top Soil of the Imo State Polytechnic, Imo State Nigeria (Eke et al., 2022). *Journal of Environmental and Public Health*, 2022.
- Faruwa, A. R., Qian, W., Agbele, A. T., & Adedeji, O. A.. AIRBORNE RADIOMETRIC MAPPING FOR NATURAL RADIATION ASSESSMENT OVER OKITIPUPA SOUTHEAST BELT OF THE BITUMINOUS SAND FIELD OF NIGERIA (Faruwa et al., 2020). *Journal of Geoscience and Environment Protection*, 8, 160–169.



- Jain, S.. Radiation in medical practice & health effects of radiation (Jain, 2021). *Journal of the Royal College of Physicians of Edinburgh*, 51, 260–267.
- Kamdem, F. E., Samba, O. N., Takam, C. A., & Kengne, S. G.. Optimization of pediatric CT scans in a developing country (Kamdem et al., 2021). *Insights into Imaging*, 12.
- Kassim, A. M., Nawar, S., & Mouazen, A. M.. Potential of On-the-Go Gamma-Ray Spectrometry for Estimation and Management of Soil Potassium Site Specifically (Kassim et al., 2021). *Sensors*, 21, 3042.
- Kendall, G. M., Little, M. P., & Wakeford, R.. A review of studies of childhood cancer and natural background radiation (Kendall et al., 2021). *Journal of Radiological Protection*, 41, R1–R30.
- Kocsis, E., Tóth-Bodrogi, E., Peka, A., Somlai, J., & Szabó, S. A.. Radiological impact assessment of different building material additives (Kocsis et al., 2021). *Journal of Radioanalytical and Nuclear Chemistry*, 329, 1121–1132.
- La Verde, G., Artiola, V., Raulo, A., & Bacci, S.. Radiological Impact of Building Material: Characterization of a Village Entirely Built out of Stone in Tuscany, Italy (Verde et al., 2022). *International Journal of Environmental Research and Public Health*, 19, 12513.
- Muhammad, K. A.. Quality Assurance in Medical Imaging: A Review of Challenges in Nigeria (Abdulkadir, 2020). *Annals of Health Research*, 6, 16–23.
- Naskar, N., Lahiri, S., Mitra, S., & Basu, P.. Radiogenic quality assessment of ground and riverine water samples collected from Indian Sundarbans (Naskar et al., 2020). *Environmental Science and Pollution Research*, 27, 32306–32314.
- Nugraha, E. D., Hosoda, M., Kusdiana, K., Shiroya, Y., & Fukushi, M.. Comprehensive exposure assessments from the viewpoint of health in a unique high natural background radiation area, Mamuju, Indonesia (Nugraha et al., 2021). *Scientific Reports*, 11.
- Ononugbo, C. P., & Anekwe, U. L.. Background Gamma Radiation in Nigerian Market Environment (Ononugbo & Anekwe, 2020). *Asian Journal of Applied Sciences*, 8.
- Oshima, M., Goto, J., Haraga, T., Koizumi, M., & Hagiwara, M.. Application of multiple γ-ray detection to long-lived radioactive nuclide determination in environmental samples (Oshima et al., 2020). *Journal of Radioanalytical and Nuclear Chemistry*, 324, 795–802.
- Pavel, A. B., Ujeniuc, S., Iordache, G., & Dinescu, L.. Gamma-Ray Analysis of Reed Samples from the Danube Delta (Pavel et al., 2025). *Journal of Environmental Radioactivity*, 275, 107436.
- Rašeta, D., Petrinec, B., Babić, D., & Radolić, V.. Application of a new in situ calibration technique for gamma spectrometry and comparison of in situ and laboratory measurements (Rašeta et al., 2021). *Journal of Radioanalytical and Nuclear Chemistry*, 328, 351–361.
- Reddy, A., Conde, C., Peterson, C., & Patel, P.. Residential radon exposure and cancer (Reddy et al., 2022). *Seminars in Oncology Nursing*, *38*, 151296.
- Salminen-Paatero, S., & Paatero, J.. Transfer of Natural Radionuclides in Terrestrial Food Chains—A Review of Investigations in Finland (Salminen-Paatero & Paatero, 2021). *Foods*, 10.
- Saudi, H. A., Abedelkader, H. T., Issa, S. A., & Hussein, M. A.. An In-Depth Examination of the Natural Radiation and Radioactive Dangers Associated with Regularly Used Medicinal Herbs (Saudi et al., 2022). *Acta Scientific Medical Sciences*, 6, 11–22.
- Simon, S. L., Kendall, G. M., & Bouffler, S.. The Evidence for Excess Risk of Cancer and Non-Cancer Disease at Low Doses and Dose Rates (Simon et al., 2022). *Radiation Research*, 198, 615–624.



- Souffit, G. D., Saïdou, S., Modibo, O. B., & Ndountchi, T. J.. Risk Assessment of Exposure to Natural Radiation in Soil Using RESRAD-ONSITE and RESRAD-BIOTA in the Cobalt-Nickel Bearing Areas of Lomié in Eastern Cameroon (Souffit et al., 2022). *Toxics*, 10, 577.
- Usman, R. L., Hudu, A., Ubaidullah, A., & Ibrahim, M. A., Fertility Cancer and Hereditary Risks in Soil Sample of Nasarawa, Nasarawa State, Nigeria (Usman et al., 2021). *Journal of Medical and Biomedical Studies*, 5, 101–105.
- Wu, Z., Wang, B., Sun, J., Zhang, C., & Zhang, R.. In-situ γ-ray analysis of ground surface radioactivity using portable HPGe γ spectrometer (Wu et al., 2022). *Journal of Radioanalytical and Nuclear Chemistry*, 331, 2901–2909.
- Yang, B., Tuo, F., Zhou, Q., Zhang, J., Li, Z., & Pang, C.. Dietary exposure of radionuclides and heavy metals in adult residents in a high background natural radiation area using duplicate diet method (Yang et al., 2022). *Scientific Reports*, 12.
- Zlobina, A., Farkhutdinov, I., Carvalho, F. P., & Al-Ameri, A.. Impact of Environmental Radiation on the Incidence of Cancer and Birth Defects in Regions with High Natural Radioactivity (Zlobina et al., 2022). *Applied Sciences*, 12, 8683.
- Zhu, Y., McKeon, T. P., Tam, V., & Huang, J. Y.. Geographic Differences in Lung Cancer Incidence: A Study of a Major Metropolitan Area within Southeastern Pennsylvania (Zhu et al., 2020). *Cancers*, 12.



Toxicity and Reproductive Effects of *Moringa oleifera* Leaves Extracts on *Drosophila melanogaster*

Abdulsalam Abdullahi Dabo¹, Bulus Caleb Laraps¹, Kobbe Amina Isa¹

¹Department of Science Laboratory Technology, Federal Polytechnic Bauchi, Bauchi State, Nigeria.

 $Correspondence: \underline{abduldabo94@outlook.com}, \underline{aadabo.slt@fptb.edu.ng}$

Phone: 08063267828

Abstract

Moringa oleifera, widely recognized for its nutritional and medicinal properties, is commonly consumed as a cooked aqueous extract, yet its toxicity remains underexplored. This study evaluates the acute toxicity and reproductive effects of cooked *Moringa oleifera* leaf aqueous and ethanolic extracts using *Drosophila melanogaster* as a model organism. The percentage yield of aqueous and ethanolic extracts was determined, followed by assessment of the median lethal dose (LD50) and eclosion rates. The aqueous extract yielded 9.50%, while the ethanolic extract yielded 4.02%. The 7-day LD50 was 154.3 mg/10 g diet for the aqueous extract and 431 mg/10 g diet for the ethanolic extract. Eclosion assays revealed that aqueous extracts (250–1250 mg/10 g) had a nonsignificant (p > 0.05) positive effect on reproductive performance, with the highest emergence at 1250 mg/10 g (137 \pm 14.5 flies). Conversely, ethanolic extracts (250–750 mg/10 g) significantly reduced eclosion rates (p < 0.05) compared to the control. These findings suggest that cooked *Moringa oleifera* aqueous leaf extracts are less toxic and potentially safer for therapeutic applications at doses below 154.3 mg/10g.

Keywords: *Moringa oleifera*, *Drosophila melanogaster*, toxicity, LD₅₀, eclosion assay, aqueous extract, ethanolic extract

Introduction

Moringa oleifera Lam., a member of the Moringaceae family, is a fast-growing tree known as the "Miracle Tree" due to its diverse nutritional, therapeutic, and prophylactic properties (Kumari, 2016). Native to northwest India, it is now cultivated across tropical and subtropical regions, valued for its leaves, pods, and seeds, which are used in traditional medicine and nutrition (Arora et al., 2013). The leaves, rich in vitamins, minerals, and bioactive compounds, are commonly consumed cooked to treat ailments such as diabetes, infections, and malnutrition (Gyamfi, 2016). However, the toxicity of cooked Moringa oleifera leaf extracts has not been adequately assessed, raising concerns about their safety, particularly due to potential toxic phytochemicals like saponins or alkaloids (Stohs & Hartman, 2015).

Drosophila melanogaster, a well-established model organism in toxicological studies, offers a robust platform for evaluating the safety and biological effects of natural compounds (Abolaji et al., 2015). Its short life cycle, genetic similarity to mammals, and complex physiological systems make it ideal for studying toxicity and reproductive outcomes (Nichols et al., 2022). The use of *D. melanogaster* in toxicological research has been validated for assessing plant-derived compounds, providing insights into their safety and efficacy (Pandey & Nichols, 2011). This study aims to determine the percentage yield, median lethal dose (LD50), and eclosion effects of cooked *Moringa oleifera* leaf aqueous and ethanolic extracts in *D. melanogaster*, contributing to the understanding of their safety for medicinal applications.



Materials and Methods

Sample Collection and Preparation

Fresh *Moringa oleifera* leaves were collected from the Federal Polytechnic Bauchi Staff Quarters, Nigeria. The leaves were hand-picked, cleaned, cooked for 45 minutes, and air-dried under shade for one week. The dried leaves were grounded into a fine powder and stored in airtight jars for further processing.

Maceration and Extraction

For ethanolic extraction, 50 g of powdered cooked *Moringa oleifera* leaves were mixed with 500 mL of 60% ethanol in a 1-liter jar. The mixture was stirred intermittently over three days, filtered using Whatman filter paper, and the filtrate was evaporated to obtain a dry extract (Feng et al., 2021). The aqueous extract was prepared similarly, using distilled water as the solvent.

Determination of Percentage Yield

The percentage yield of each extract was calculated using the formula:

$$\%Yield = \frac{Wieght \ of \ Extract}{Weight \ of \ Sample} \ x \ 100$$

An empty beaker was weighed, followed by the beaker containing the extract, to determine the extract weight (Wang, 2009).

Acute Toxicity Assay

Serial concentrations of aqueous and ethanolic extracts (250–1250 mg/10 g diet) were mixed into the *D. melanogaster* diet. Adult flies were exposed to these diets, and mortality was recorded daily for seven days. The LD₅₀ was calculated using probit analysis with GraphPad Prism software (Feng et al., 2021).

Eclosion Assay

Following the 7-day toxicity assay, flies were allowed to lay eggs, and the number of emerged flies was recorded after 13 days by counting pupal cases. Data were analyzed using GraphPad Prism to assess the reproductive impact of the extracts (Wang, 2009).

Statistical Analysis

Data were analyzed using GraphPad Prism, with results expressed as mean \pm standard deviation. Significance was determined using one-way ANOVA, with p < 0.05 considered statistically significant.

Results

Percentage Yield

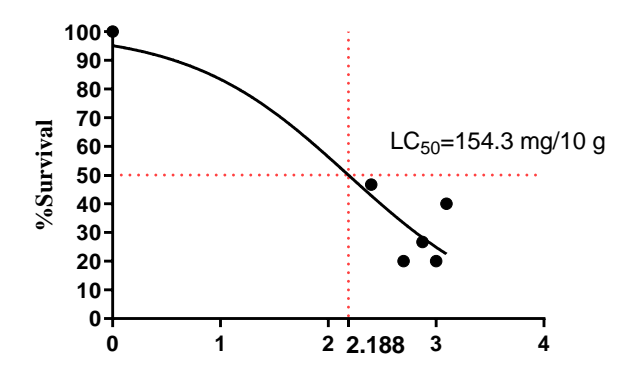
The percentage yield of the aqueous extract was 9.50% (4.75 g from 50 g), while the ethanolic extract yielded 4.02% (2.01 g from 50 g) (Table 1).

Sample	Initial weight of sample (g)	Weight of extract sample (g)	Percentage yield (%)
Ethanolic extract	50	2.01	4.02
Aqueous extract	50	4.75	9.50



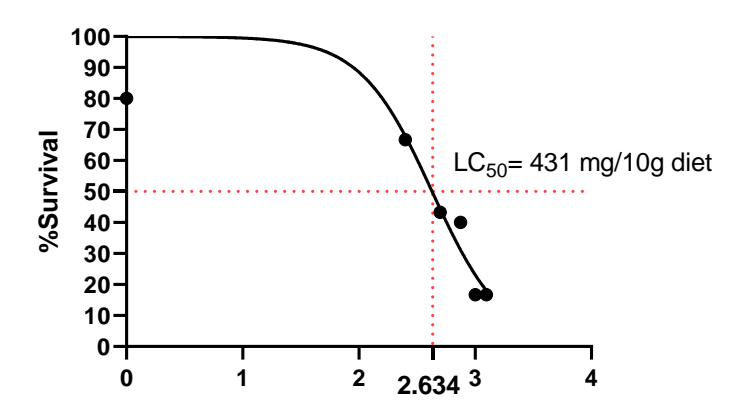
Acute Toxicity (LD50)

The 7-day LD₅₀ for the aqueous extract was 154.3 mg/10 g diet, while the ethanolic extract had an LD₅₀ of 431 mg/10 g diet, indicating lower toxicity for the ethanolic extract (Fig 1& 2).



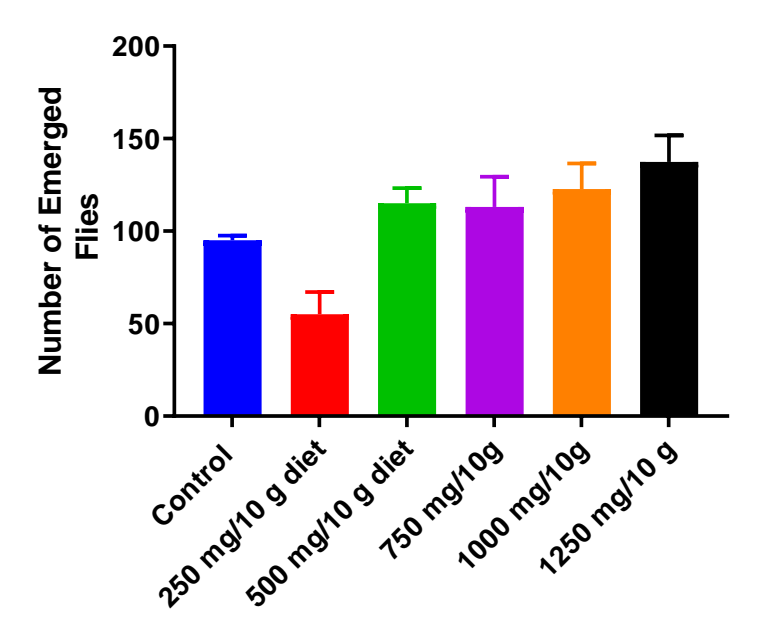
Log Concentration of Moringa Leaf Aqueous Extract

Fig 1: -day LD₅₀ of *Moringa oleifera* leaf aqueous extract in *D. melanogaster*



Log Concetration(mg/10g) of Ethanolic Extract of cooked Moringa Leave

Fig 2: -day LD₅₀ of *Moringa oleifera* ethanolic leaf extract in *D. melanogaster*



Concentration of M. oleifera Aqueous Leaf Extract

Fig 3: Number of emerged young flies from eggs of adult fruit flies administered *Moringa* oleifera aqueous leaf extracts

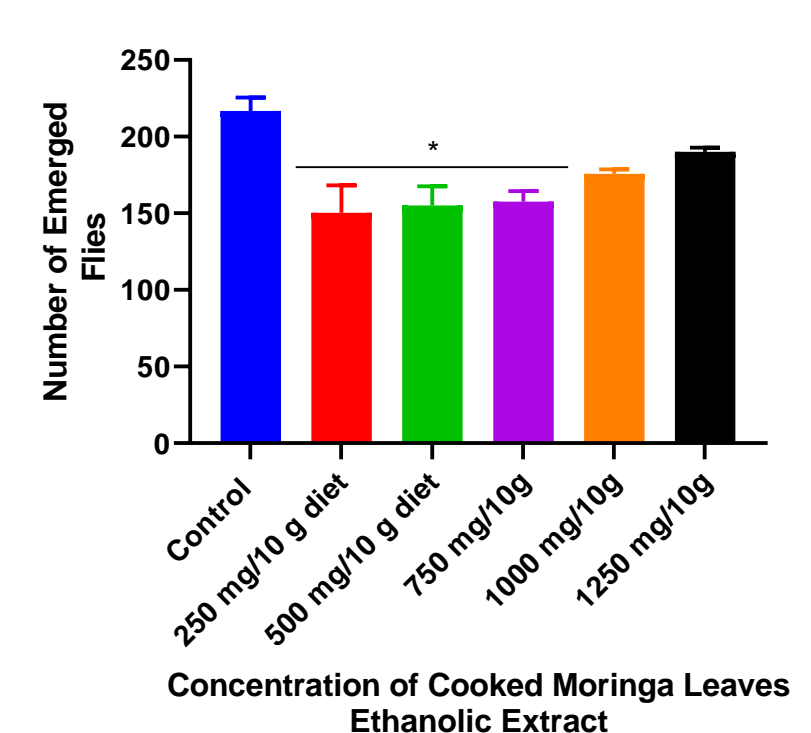


Fig 4: Number of emerged young flies from eggs of adult fruit flies administered cooked *Moringa oleifera* ethanolic leaf extracts



Discussion

This study provides novel insights into the safety and reproductive effects of cooked *Moringa* oleifera leaves extracts in *D. melanogaster*. The higher yield of the aqueous extract (9.50%) compared to the ethanolic extract (4.02%) suggests that water is a more efficient solvent for extracting bioactive compounds from cooked *Moringa* oleifera leaves, possibly due to the polarity of its phytochemicals (Silva et al., 2017). This aligns with previous studies reporting higher yields for aqueous extractions of plant materials, attributed to the solubility of polar compounds like flavonoids and glycosides (Ezeonu & Ejikeme, 2016; Fawole et al., 2010).

The LD₅₀ values indicate that the aqueous extract (154.3 mg/10 g) is more toxic than the ethanolic extract (431 mg/10 g). This difference may be attributed to the presence of water-soluble compounds, such as saponins or cyanogenic glucosides, which could exert toxic effects at lower concentrations (Lorent et al., 2014; Nahrstedt & Davis, 2003). The lower toxicity of the ethanolic extract suggests that ethanol may extract less toxic or different bioactive compounds, such as phenolic acids, which have been shown to have lower toxicity in *D. melanogaster* (Stohs & Hartman, 2015). Further phytochemical analysis is needed to identify the specific compounds responsible for these effects, as recommended by previous studies on *Moringa oleifera* (Leone et al., 2016).

The eclosion assay revealed contrasting effects of the extracts on D. melanogaster reproductive performance. The aqueous extract showed a dose-dependent, non-significant increase in emerged flies, with the highest number (137 ± 14.5) at 1250 mg/10 g. This suggests a potential stimulatory effect on reproduction, possibly due to the nutritional benefits of Moringa oleifera leaves, which are rich in proteins, vitamins, and minerals (Gyamfi, 2016). In contrast, the ethanolic extract significantly reduced eclosion rates (p < 0.05), particularly at lower concentrations (250 mg/10 g), indicating potential reproductive toxicity. This could be linked to ethanol-extracted compounds, such as polyphenols, which may disrupt developmental processes by inducing oxidative stress or interfering with gene expression (Hättenschwiler & Vitousek, 2020; Pandey & Nichols, 2011). The significant decline in eclosion with ethanolic extracts compared to the control highlights the need for caution in their therapeutic use.

These findings underscore the importance of evaluating the safety of commonly consumed herbal extracts, particularly when processed (e.g., cooked). The lower toxicity and potential reproductive benefits of the aqueous extract suggest it may be safer for medicinal applications, but doses below 154.3 mg/10 g are recommended for further studies. The ethanolic extract's higher LD50 but adverse reproductive effects indicate that its use should be approached with caution, pending further toxicological and phytochemical investigations.

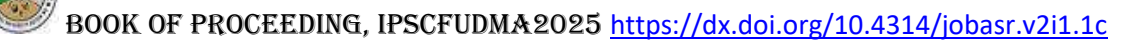
Conclusion

Cooked *Moringa oleifera* aqueous leaf extracts exhibit lower toxicity (LD₅₀: 154.3 mg/10 g) and a non-significant positive effect on *D. melanogaster* reproductive performance, suggesting potential safety and therapeutic value at doses below 1000 mg/10 g. In contrast, ethanolic extracts are less toxic (LD₅₀: 431 mg/10 g) but significantly impair eclosion rates, indicating potential reproductive toxicity. These results highlight the need for careful dose optimization and further studies to elucidate the bioactive compounds responsible for these effects.



References

- Abolaji, A. O., Kamdem, J. P., Lugokenski, T. H., Farombi, E. O., Souza, D. O., da Silva Loreto, E. L., & Rocha, J. B. T. (2015). Ovotoxicants 4-vinylcyclohexene 1,2-monoepoxide and 4-vinylcyclohexene diepoxide disrupt redox status and modify different electrophile sensitive target enzymes and genes in *Drosophila melanogaster*. **Redox Biology**, 5, 328–339. https://doi.org/10.1016/j.redox.2015.06.001
- Arora, D. S., Onsare, J. G., & Kaur, H. (2013). Bioprospecting of *Moringa* (Moringaceae): Microbiological perspective. **Journal of Pharmacognosy and Phytochemistry**, 1(6), 193–215.
- Ezeonu, C. S., & Ejikeme, C. M. (2016). Qualitative and quantitative determination of phytochemical contents of indigenous Nigerian softwoods. **New Journal of Science**, 2016, 1–9. https://doi.org/10.1155/2016/5601327
- Fawole, O. A., Amoo, S. O., Ndhlala, A. R., Light, M. E., Finnie, J. F., & Van Staden, J. (2010). Anti-inflammatory, anticholinesterase, antioxidant and phytochemical properties of medicinal plants used for pain-related ailments in South Africa. **Journal of Ethnopharmacology**, 127(2), 235–241. https://doi.org/10.1016/j.jep.2009.11.015
- Feng, R. F., Wang, N., & Kou, J. J. (2021). Sulfated modification, characterization, and potential bioactivities of polysaccharide from *Ziziphus jujuba*. **Natural Product Communications**, 16(10), 1–14. https://doi.org/10.1177/1934578X211045672
- Gyamfi, E. T. (2016). Nutritional and medicinal properties of *Moringa oleifera* leaves. **Journal of Food Science and Nutrition**, 2(1), 23–30.
- Hättenschwiler, S., & Vitousek, P. M. (2020). The role of polyphenols in terrestrial ecosystem nutrient cycling. **Trends in Ecology & Evolution,** 15(6), 238–243. https://doi.org/10.1016/S0169-5347(00)01861-9
- Kumari, D. J. (2016). *Moringa oleifera*: The miracle tree. **International Journal of Herbal Medicine**, 4(3), 45–50.
- Leone, A., Spada, A., Battezzati, A., Schiraldi, A., Aristil, J., & Bertoli, S. (2016). *Moringa oleifera* seeds and oil: Characteristics and uses for human health. **Molecules**, 21(12), 1681. https://doi.org/10.3390/molecules21121681
- Lorent, J. H., Quetin-Leclercq, J., & Mingeot-Leclercq, M. P. (2014). The amphiphilic nature of saponins and their effects on artificial and biological membranes and potential consequences for red blood and cancer cells. **Organic & Biomolecular Chemistry,** 12(44), 8803–8822. https://doi.org/10.1039/C4OB01652A
- Nahrstedt, A., & Davis, R. H. (2003). Occurrence, variation, and biosynthesis of the cyanogenic glucosides linamarin and lotaustralin in species of the Heliconiini (Insecta: Lepidoptera). **Comparative Biochemistry and Physiology Part B: Comparative Biochemistry**, 75(1), 65–73. https://doi.org/10.1016/0305-0491(83)90043-4
- Nichols, C. D., Torres, J., & Horowitz, L. (2022). *Drosophila melanogaster* as a model for neuropharmacology. **Journal of Neurogenetics,** 36(1), 12–20. https://doi.org/10.1080/01677063.2022.2030345
- Pandey, U. B., & Nichols, C. D. (2011). Human disease models in *Drosophila melanogaster* and the role of the fly in therapeutic drug discovery. **Pharmacological Reviews**, 63(2), 411–436. https://doi.org/10.1124/pr.110.003293
- Silva, G. O., Abeysundara, A. T., & Aponso, M. M. (2017). Extraction methods, qualitative and quantitative techniques for screening of phytochemicals from plants. **American Journal of Essential Oils and Natural Products**, 5(2), 29–32.
- Stohs, S. J., & Hartman, M. J. (2015). Review of the safety and efficacy of *Moringa oleifera*. **Phytotherapy Research**, 29(6), 796–804. https://doi.org/10.1002/ptr.5325
- Wang, L. (2009). Effect of nano-packing on preservation quality of Chinese jujube (*Ziziphus jujuba* Mill. var. inermis (Bunge) Rehd). **Food Chemistry**, 114(2), 547–552.



LOCATION OF NON-COLLINEAR EQUILIBRIUM POINTS IN THE PHOTOGRAVITATIONAL RESTRICTED 2 + 2 BODY PROBLEM WITH OBLATENESS AND CIRCUMBINARY DISC

¹Kamfa A Salisu & ²Umar Aishetu

¹Departement of Mathematical Science, Federal University of Health Sciences, Azare, Bauchi State, Nigeria

²Departement of Mathematics, Faculty of Physical Sciences, Ahmadu Bello University, Zaria, Nigeria

E-mail: kamfa.salisu@fuhsa.edu.ng umaraishetu33@yahoo.com

Abstract

We have studied the combined effects of the oblateness, radiation pressure and circumbinary disc on the locations of the equilibrium points in the restricted 2+2 body problem. This system holds eight non – collinear equilibrium points in the framework of 2+2 body problem. The asphericity and luminosity of the primary bodies together with the circumbinary disc are found to impact immensely on the positions.

Keywords: Restricted 2+2 body problem – Photogravitational – Circumbinary disc – Oblateness

1. Introduction

The dynamics of the combined system of two primaries and two minor bodies called the restricted 2+2 body problem (R2+2BP) is considered. Two point masses, $M_1 \ge M_2$ are assumed to move on circular keplerian orbits about their centre of mass, while the two minor bodies (m_1 and m_2) << M_2 , move in the gravitational field of the primaries (M_1 and M_2) while mutually attracting each other but not perturbing the primaries. The problem is to describe the motion of the minor bodies. The R2+2BP admits fourteen equilibrium solutions in the plane of motion of the primaries; six of these are located about the collinear points, while the other eight are in the neighborhood of the triangular points (Whipple 1984).

The shape of the celestial bodies is importance since most of the celestial bodies are not spherical, they are either oblate, triaxial or prolate. Many researchers have considered variants of the restricted three - body problem by taking radiation pressure and oblateness in to consideration some of them are Singh and Taura (2014), Kushva (2008), Singh and Umar (2012), Singh and Taura (2013). The inclusion of the circumbinary disc surrounding some of the celestial bodies have to be considered, since some of the steller system have planet formation occurring around young stars in discs that are rich in gas and dust. It is also found that debris disc or circumstellar disc exist around many nearby stars (e.g. Kepler 16, HD 98800, ϵ - Eradani e.t.c). Many researchers have studied the effect of the circumbinary disc in the R3BP (Singh and Taura 2013; Umar et al. 2021a; Umar et al. 2021b; Jiang and Yeh 2006;). They found that the circumbinary disc produce significant changes in the equilibrium positions.

Whipple and Szebehely (1984) generalized the study of the restricted three - body problem to the restricted problem of n + v bodies. They derived the integral of the system for n = 2 and $v \ge 1$, by considering only gravitational forces. In the same year, Whipple (1984) studied the existence and stability of the equilibrium points of the restricted problem of 2 + 2 bodies, He found fourteen equilibrium points of the restricted problem of 2 + 2 bodies, six are collinear with the centres of mass of the primary bodies and the rest are non - collinear. Croustalloudi and Kalvouridis (2013) investigated numerically the new aspect of the 2 + 2 body problem including the parametric



variation of the equilibrium states of the minor bodies and their attracting regions. The positions and linear stability of the equilibrium points in the restricted 2 + 2 body problem under the effect of straight segment was discussed by Denesh et al. (2020). They found that the length parameter l has a subsequent effect on the locations of all the equilibrium points.

Recently, Mahato et al. (2022) have studied the effects of planetesimal belt on the locations and stability of the collinear and non - collinear equilibrium points in the perturbed R2+2BP. Later, Kumar and Aggrawal (2022) studied analytically and numerically the effects of oblateness and straight line segment on the positions and linear stability of equilibrium points in the R2+2BP. They found that, all the fourteen equilibrium points are affected by the oblateness and length of the primary bodies. And also, the equilibrium points were found to slightly perturb the positions of the equilibrium points.

The present paper aim is to determine the positions of the Non - collinear equilibrium points in the restricted problem of 2 +2 bodies when both primaries are oblate and luminous primary surrounded by a circumbinary disc. Such systems can be found in the Steller systems like HD98800B, Kepler 47, and HW vir.

This paper is organized as follows; the formulation of the equations of motion of the restricted 2 +2 body problem is presented in Section 2. In Section 3 locates the equilibrium points. The numerical application is in section 4: discussion is carried out in section 5; section 6 concludes the research.

2. Equations of Motion

The model consists of two primaries P_i , i = 1, 2, with masses M_1 , M_2 ($M_1 \ge M_2$), which revolve in circular orbits around their centre of mass, and of two minor bodies Q_i , i = 1, 2, with masses m_i , i = 1, 2, such that $m_i << M_j$, i, j = 1, 2. The minor bodies move under the combined action of the primaries and their mutual attraction. The aim of the problem is to describe the dynamical behavior of this pair of minor bodies.

The equations of motion of the two minor bodies under the perturbing effects of oblateness and radiation pressure of both primaries and circumbinary disc in the restricted 2 + 2 body problem in a synodic coordinate system *oxyz* are presented as follows:

Where:

$$\mu = \frac{M_2}{M_1 + M_2}, \quad \mu_i = \frac{m_i}{M_1 + M_2},$$



$$r_c^2 = 1 - \mu + \mu^2, \quad R_i^2 = x_i^2 + y_i^2,$$

$$r_{1i}^2 = (x_i - \mu)^2 + y_i^2 + z_i^2,$$

$$r_{2i}^2 = (x_i - \mu + 1)^2 + y_i^2 + z_i^2,$$

$$r^2 = (x_1 - x_2)^2 + (y_1 - y_2)^2 + (z_1 - z_2)^2$$

The radiation factors of the bigger and smaller primaries are given by q_1 , q_2 respectively, with $q_1 = 1 - p_1$, $0 < p_1 << 1$ where $p_1 = \frac{F_{p_1}}{F_{g_1}}$, and where F_p is the radiation pressure force which changes with distance by the same law as the gravitational attraction force and F_g acts opposite to

it. The oblateness coefficients as A_i , $0 < A_i = \frac{AE_i^2 - AP_i^2}{5R^2} << 1$, i = 1, 2 for more massive and less massive primaries, respectively. Where AE_1 and AE_2 are equatorial radii and AP_1 and AP_2 are polar radii of m_1 and m_2 respectively.

The potential from the circumbinary disc $\frac{M_b}{\left(R_i^2 + T^2\right)^{\frac{1}{2}}}$, where M_b is the total mass of the disc, and

the parameter *T* determine the density profile of the disc (Miyamoto & Nagai 1975, Singh and Taura 2013, Umar et al. 2021).

The mean motion n is given by;

The inean motion
$$n$$
 is given by,
$$n^2 = 1 + \frac{3}{2} \left(A_1 + A_2 \right) + \frac{2M_b r_c}{\left(r_c^2 + T^2 \right)^{\frac{3}{2}}}$$
(Singh and Taura 2013)

(3)

Where r_c the radial distance of the infinitesimal body in the classical restricted three – body problem and is given by $r_c^2 = 1 - \mu + \mu^2$

2.1 Jacobi Constant

From equation (1) we obtain the energy integral of the problem as

$$2U - \sum_{i=1}^{2} \mu_{i} \begin{pmatrix} \dot{x}_{i}^{2} + \dot{y}_{i}^{2} + \dot{z}_{i}^{2} \end{pmatrix} = C$$
 (4)

Where C is known as Jacobi's constant.

3 Non-collinear Equilibrium Solutions

At equilibrium points the velocity and acceleration are zero that is

$$U_{x_1} = U_{y_1} = U_{z_1} = U_{x_2} = U_{y_2} = U_{z_2} = 0$$
, and $U_{x_1x_1} = U_{y_1y_1} = U_{z_1z_1} = U_{x_2x_2} = U_{y_2y_2} = U_{z_2z_2} = 0$ since $\mu_1 \neq 0$ and $\mu_2 \neq 0$, we have

$$n^{2}x_{1} - \frac{(1-\mu)(x_{1}-\mu)q_{1}}{r_{11}^{3}} - \frac{\mu(x_{1}-\mu+1)}{r_{21}^{3}} - \frac{3(1-\mu)(x_{1}-\mu)A_{1}q_{1}}{2r_{11}^{5}} - \frac{3\mu(x_{1}-\mu+1)A_{2}}{2r_{21}^{5}} - \frac{\mu_{2}(x_{1}-x_{2})}{r^{3}} - \frac{M_{b}x_{1}}{(R_{1}^{2}+T^{2})^{\frac{3}{2}}} = 0$$

(5)



$$n^{2}y_{1} - \frac{(1-\mu)y_{1}q_{1}}{r_{11}^{3}} - \frac{\mu y_{1}}{r_{21}^{3}} - \frac{3(1-\mu)y_{1}A_{1}q_{1}}{2r_{11}^{5}} - \frac{3\mu y_{1}A_{2}}{2r_{21}^{5}} - \frac{\mu_{2}(y_{1}-y_{2})}{r^{3}} - \frac{M_{b}y_{1}}{(R_{1}^{2}+T^{2})^{\frac{3}{2}}} = 0$$
 (6)

$$n^{2}x_{2} - \frac{(1-\mu)(x_{2}-\mu)q_{1}}{r_{12}^{3}} - \frac{\mu(x_{2}-\mu+1)}{r_{22}^{3}} - \frac{3(1-\mu)(x_{2}-\mu)A_{1}q_{1}}{2r_{12}^{5}} - \frac{3\mu(x_{2}-\mu+1)A_{2}}{2r_{22}^{5}}$$

$$-\frac{\mu_1(x_2 - x_1)}{r^3} - \frac{M_b x_2}{\left(R_2^2 + T^2\right)^{\frac{3}{2}}} = 0$$
(7)

$$n^{2}y_{2} - \frac{(1-\mu)y_{2}q_{1}}{r_{12}^{3}} - \frac{\mu y_{2}}{r_{22}^{3}} - \frac{3(1-\mu)y_{2}A_{1}q_{1}}{2r_{12}^{5}} - \frac{3\mu y_{2}A_{2}}{2r_{22}^{5}} - \frac{\mu_{1}(y_{2}-y_{1})}{r^{3}} - \frac{M_{b}y_{2}}{(R_{2}^{2}+T^{2})^{\frac{3}{2}}} = 0$$
 (8)

The non-collinear equilibrium points in the presence of one infinitesimal mass m_3 are obtained by solving equations (5) and (6) neglecting second and higher order terms of oblateness and gravitational potential from the disc as:

$$x_{L_{4.5}} = \mu - \frac{1}{2} + \left(\frac{p_1}{3} - \frac{A_1 - A_2}{2}\right)$$

$$y_{L_{4.5}} = \pm \frac{\sqrt{3}}{2} \left(1 - \frac{2(p_1)}{9} - \frac{A_1 + A_2}{3} - \frac{4M_b(2r_c - 1)}{9(r_c^2 + T^2)^{\frac{3}{2}}}\right)$$

The positions of the non-collinear equilibrium points L_4 and L_5 are influenced by the oblateness and gravitational potential from the disc.

The non- collinear equilibrium points of R2+2BP in the presence of both the infinitesimal masses m_i i = 1,2 can be found by solving equations (5), (6), (7) and (8) following the approach of Whipple (1984):

$$x_{i}^{k_{1}} = x_{L_{k}} \pm \frac{\alpha_{k} \mu_{3-i}}{\left[\left(\mu_{1} + \mu_{2} \right)^{2} \left(\Omega_{xy}^{L_{k}} \alpha_{k} + \Omega_{yy}^{L_{k}} \right) \right]^{\frac{1}{3}} \left(1 + \alpha_{k}^{2} \right)^{\frac{1}{2}}}$$

$$y_{i}^{k_{1}} = y_{L_{k}} \pm \frac{\mu_{3-i}}{\left[\left(\mu_{1} + \mu_{2} \right)^{2} \left(\Omega_{xy}^{L_{k}} \alpha_{k} + \Omega_{yy}^{L_{k}} \right) \right]^{\frac{1}{3}} \left(1 + \alpha_{k}^{2} \right)^{\frac{1}{2}}}$$

$$(9)$$

For i=1,2; K=4 at L_4 and K=5 at L_5 , and

$$x_{i}^{k_{1}} = x_{L_{k}} \pm \frac{\beta_{k} \mu_{3-i}}{\left[\left(\mu_{1} + \mu_{2} \right)^{2} \left(\Omega_{xx}^{L_{m}} + \frac{\Omega_{xy}^{L_{k}}}{\beta_{m}} \right) \right]^{\frac{1}{3}} \left(1 + \frac{1}{\beta_{m}^{2}} \right)^{\frac{1}{2}}}$$

$$y_{i}^{m_{1}} = y_{L_{m}} \pm \frac{\mu_{3-i}}{\left[\left(\mu_{1} + \mu_{2} \right)^{2} \left(\Omega_{xx}^{L_{k}} + \frac{\Omega_{xy}^{L_{m}}}{\beta_{m}} \right) \right]^{\frac{1}{3}} \left(1 + \frac{1}{\beta_{m}^{2}} \right)^{\frac{1}{2}}}$$

$$(10)$$

For i=1,2; K=4 at L_4 and K=5 at L_5 , where



$$\alpha_k = \frac{\left(-1\right)^{k+1} + \left(-1\right)^k \sqrt{1 + 12(\mu - 0.5)^2}}{2\sqrt{3}(\mu - 0.5)}$$

$$\beta_k = \frac{\left(-1\right)^{k+1} - \left(-1\right)^k \sqrt{1 + 12(\mu - 0.5)^2}}{2\sqrt{3}(\mu - 0.5)}$$

Where Ω_{xx}^0 , Ω_{xy}^0 and Ω_{yy}^0 are second order partial derivatives of Ω evaluated at the non-collinear equilibrium points L_4 and L_5 for the present model. The restricted problem of 2+2 bodies under the combined effect of oblateness of the primaries, radiation pressure and circumbinary disc eight non-collinear equilibrium points are obtained and denoted as follows:

$$\left(IxL_{m-}^{n}, IyL_{m-}^{n} \right)$$

$$\left(IxL_{m+}^{n}, IyL_{m+}^{n} \right)$$

$$\left(PxL_{m-}^{n}, PyL_{m-}^{n} \right)$$

$$\left(PxL_{m+}^{n}, PyL_{m+}^{n} \right)$$

$$\left(PxL_{m+}^{n}, PyL_{m+}^{n} \right)$$

4. Numerical Application

The non-collinear equilibrium points given by (9) and (10) of the problem are obtained numerically for the triple—star system Gliese 667. Table 1 contains numerical data about the system (source: NASA ADS).

Table 1: Numerical data for the system

Binary System	Ma	asses (M	I_{\square}	Masses (M_{earth})		Luminosity $(L_{_{\!\square}})$		
	$M_1 M_2$	M_3		$m_1 m_2$		$L_1 L_2 L_2$		
Gliese 667	0.73	0.69	0.33	3.7	5.68	0.31	0.19	0.014



Table 2: Effect of perturbation on non – collinear equilibrium points L_4 of Gliese 667 when $\mu_1 = 0.000011952$, $\mu_2 = 7.7856 \times 10^{-6}$ and T = 0.11

Cases	μ	$q_{_1}$	$A_{\rm l}$	A_2	M_{b}	IxL_{4-}^1	IyL_{4-}^1	IxL_{4+}^{1}	IyL_{4+}^1
						IxL_{4-}^2	IyL_{4-}^2	IxL_{4+}^2	IyL_{4+}^{2}
1	0.485915	1	0	0	0	-0.01444483205	0.8554684403	-0.01383516795	0.8766923673
						-0.01458387903	0.8497654536	-0.01368612097	0.8823853540
2	0.485915	1	0	0	0.01	-0.01435017245	0.8514247058	-0.01392982755	0.8723564081
						-0.0145767259	0.8458239913	-0.0137932741	0.8779571225
3	0.485915	0.996005	0	0	0	-0.01428941051	0.8539855809	-0.01377058949	0.8751659298
						-0.01441823192	0.8481918464	-0.01362176808	0.8808586643
4	0.485915	1	0.01	0	0	-0.01934354573	0.852534447	-0.01882645427	0.8737428579
						-0.01948190435	0.8468596934	-0.01868809565	0.8794176114
5	0.485915	1	0	0.001	0	-0.01384470226	0.8550850883	-0.01332529774	0.876388369
						-0.01398367979	0.8493849503	-0.01318632021	0.882088507
6	0.485915	0.996005	0.01	0.0002	0.01	-0.01917352744	0.8469475407	-0.01930920058	0.8413829321
						-0.01866647256	0.8677443036	-0.01853079942	0.8733089122
	0.485915	0.996005	0.01	0.02	0.01	-0.009271175331	0.8413282445	-0.008768824669	0.8619320644
						-0.009405589751	0.8358152618	-0.008634410249	0.8674450471
	0.485915	0.996005	0.01	0.2	0.01	0.08074683377	0.7901053601	0.08121316623	0.8092319003
						0.08062205677	0.7849876546	0.08133794323	0.8143496059
7	0.485915	0.996005	0.001	0.001	0.01	-0.01427452239	0.8492738694	-0.01376547761	0.8701522470
						-0.01441072795	0.8436874231	-0.01362927205	0.8757386933
	0.485915	0.996005	0.10	0.001	0.01	-0.06376346571	0.8211485186	-0.06327653429	0.8411199212
						-0.06389375439	0.8158047524	-0.06314624561	0.8464636874
	0.485915	0.996005	0.20	0.001	0.01	-0.1137540668	0.7926665001	-0.1132859332	0.8118669128
						-0.1138793257	0.7875290284	-0.1131606743	0.8170043845
8	0.485915	0.996005	0.01	0.001	0.001	-0.01877753133	0.8503637439	-0.01826246867	0.8714889444
						-0.01891534711	0.8447112550	-0.01812465289	0.8771414333
	0.485915	0.996005	0.01	0.001	0.1	-0.01874093985	0.8099395530	-0.01829906015	0.8280631679
						-0.01885917401	0.8050902011	-0.01818082599	0.8329125198
	0.485915	0.996005	0.01	0.001	0.3	-0.01869598815	0.7270863019	-0.01834401185	0.7415225454
						-0.01879016677	0.7232235832	-0.01824983323	0.7453852641



5. Discussion

The system (1) represents the equations of motion of the two minor bodies, when the primaries are oblate and radiation pressure of the bigger primary surrounded by a circumbinary disc in the framework of 2+2 body problem. From (9) and (10), locations of the non-collinear equilibrium points are determined and found to be significantly affected by oblateness, radiation pressure of the bigger primary and circumbinary disc. It is verified that, our results are in conformity with Whipple (1984) in the absence of all perturbations in the present study. The results of Singh and Taura (2013) are in agreement with ours when we consider only one minor body in the present study and r_1^2 and r_2^2 become $r_1^2 = (x - \mu)^2 + y^2$ and $r_2^2 = (x - \mu + 1)^2 + y^2$ respectively. This fact agrees with Kalvouridis (1997) in the absence of circumbinary disc in the present study.

Table 1 shows the positions of the non-collinear equilibrium points, the problem possess eight equilibrium points which are affected by oblateness and radiation of the bigger primary together with the circumbinary disc.

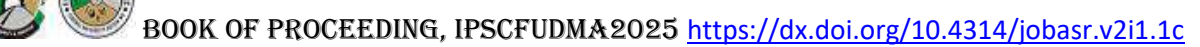
Table 1 shows that with the variation in oblateness of the bigger primary causes $\left(IxL_{4\pm}^{1},IyL_{4\pm}^{1}\right)$ and $\left(IxL_{4\pm}^{2},IyL_{4\pm}^{2}\right)$ a shift away from the bigger primary and it also reveals that $\left(IxL_{4\pm}^{1},IyL_{4\pm}^{1}\right)$ and $\left(IxL_{4\pm}^{2},IyL_{4\pm}^{2}\right)$ as a result of increase in circumbinary disc, a significant shift toward the origin is observed.

References

- Croustalloudi, M., N. and Kalvouridis, T., J. (2013). The restricted 2 + 2 body problem; parametric variation of the equilibrium states of the minor bodies and their attracting regions, Hindawi publishing corporation, Astronomy and astrophysics.
- Chenciner, A. (2007). Scholarpedia, 2(10), 2111.
- Govind, M.; Pal, A.K.; Alhowaity, S.; Abouelmgd, E. I.; Kushvah, B. S. (2022). Effect of the planetesimaal belt on the dynamics of the restricted problem of 2+2 Bodies. Appl.sc. 12, 424.
- Kumar, D., Aggarwal, R. and Kaur, B. (2020). An Insight on the restricted problem of 2 +2 bodies with straight segment, *Astronomische Nachricher*
- Kushvah, B. S (2008). Linear stability of equilibrium points in the generalized photogravitational Chermnykh's problem. Astrophysic space Sci, 318: 41 50
- Kumar, D. and Aggarwal, R. (2022). Restricted 2+2 body problem with oblateness and straight segment. Astrophys. Astr. 43:36
- Singh, J. and Umar, A. (2012). On the Stability of Triangular Equilibrium Points in the Elliptic R3BP under radiating and oblate primaries, *Astrophysics and Space Science*, 341: 349 358.
- Singh, J. and Taura, J. J. (2013). *Motion in the generalized restricted three-body problem*. Astrophys. Space Sci. 343, 95.



- Singh, J. and Taura, J.J. (2014). Stability of triangular equilibrium points in the photogravitation R3BP with oblateness and potential from a belt Astrophys. 35, 107 119
- Szebehely, V. (1967). *Theory of orbits: The restricted problem of three bodies*. Academic press, San Diego.
- Umar, A., Kamfa A. S., and Bashir, U., (2021a). Perturbation due to a circumbinary disc around L_{4,5} in the photogravitational elliptic restricted three body problem, *International letter of chemistry, physics and Astronomy*, **87**: 22 36 https://doi:10.18052/www.scipress.com/ILCPA.87.22
- Umar, A., Kamfa A. S., and Bashir, U., (2021b). Stability of libration points around L_{4,5} with oblateness primaries and circumbinary disc in elliptic restricted three body problem, *KASU Journal of Mathematical Sciences (KJMS)*.
- Valtonen, M. and Karttunen, H. (2006). The three-body problem. Cambridge University Press.
- Whipple, A., L. (1984). Equilibrium solutions of the restricted problem of 2 +2 bodies, *celestial Mechanics* 33(1984) 271 -294. 0008-8714/84/0333-0271\$03.60
- Whipple A., L. and Szebehely, V. (1984). The restricted problem of *n*+*v* bodies, *Celestial Mechanics* 32 (1984), 137 -144, 0008 8714/84/0322 -0137\$1.20
- Yen, L. C and Jiang, I. G (2006) On the chermnykh like problems: II. The equilibrium points. Astrophysics Space sci. 306: 189 200



Phyto-Pharmacological Activities of *Phyllantus amarus***: A Brief Overview** ^{1,2}Garba, I. L., ²Garga, M. A., and ¹Okunola, O. J.

¹Department of Chemistry, Federal University Dutsin-Ma, Katsina State, Nigeria.

²National Biotechnology Development Agency, Bio-resources Development Centre, Katsina, Nigeria.

Corresponding author's email:iladan34@gmail.com +2348034708230

Abstract

This study provides an overview of the phyto-pharmacological activities of *Phyllanthus amarus*. The plant is reported to have a lot of phytochemicals including alkaloids, flavonoids, terpenoids, saponins, and tannins etc. which are responsible for its pharmacological activities. Examining its medicinal properties reveals a spectrum of bioactive compounds with potent anti-inflammatory, antiviral, antileptospira, hepatoprotective effects, nephrotic effects, and other pharmacological effects. The plant's diverse therapeutic potential extends to many medicinal applications, making it a subject for various health applications. Understanding the multi-faceted phytochemistry and pharmacology of *Phyllanthus amarus* is crucial for harnessing its beneficial effects in the development of therapeutic functions. More than 510 compounds have been isolated, the majority of which are lignins, triterpenoids, flavonoids, and tannins. The researches of their remarkable antiviral, antioxidant, antidiabetic, and anticancer activities have become hot topics.

Keywords: Hepatoprotective, Antiviral, Anti-leptospira, Pharmacology.

Introduction

Herbs have long been essential to human health and are used to cure a wide range of illnesses (Verma et al., 2014). Since 80% of people worldwide still primarily rely on herbal remedies, the World Health Organization (WHO) has mandated that countries support and incorporate traditional medicine into their national healthcare systems (Salisu et al., 2022). Therefore, it is encouraged to use medicinal plants and herbs to treat both infectious and non-infectious disorders. The plant Phyllanthus amarus (PA) belongs to the Euphorbiaceae family, which includes about 800 species that grow in tropical and subtropical regions of the globe. In Nigeria a country with three major languages, which involve Hausa, Igbo and Yoruba. Phyllanthus amarus (PA) is called "Geron tsuntsaye" (Hausa), "Eyin Olobe" (Yoruba), and "Ngwu" (Igbo) (Zubair et al., 2016). PA is an annual glabrous herb that branches, growing to a height of 30 to 60 cm. Its leaves are subsessile, elliptic-oblong, obtuse, and round in base. Its branching leaves are slender and leaf-bearing. The auxiliary flowers are yellowish, whitish, or greenish. The male flowers are grouped in groups of one to three, while the females are solitary. Fruits resemble longitudinal parallel ribs on the back and are depressed-globose in shape (Vermaet al., 2014).





Figure 1: Phyllantus amarus (Patel et al., 2011)

The study of phytochemistry, a subfield of chemistry that evaluates the chemical makeup of plants and plant products (natural products chemistry), has revealed that many of the chemicals found in plants, such as lignans, carbohydrates, alkaloids, glycosides, terpenoids, and other secondary metabolites, are either therapeutically active or inactive (Ghosh et al., 2022). Flavonoids, one of the secondary metabolites found in PA, are polyphenolic compounds with different classes including flavones, chalcones, catechins, and their derivatives; in humans, they help prevent and treat a variety of pathologies that have been scientifically documented (Agatiet al., 2012). Alkaloids, yet another secondary metabolite found in plants in PA, exhibit a range of pharmacological actions. Numerous alkaloids, such as securinine, epibubbialine, isobubbialine, and others, are found in PA. The compounds primarily carry out various antibacterial and other pharmacological actions (Ghosh et al., 2022). Using various methodologies, some additional phytochemicals found in PA are home to several classes of secondary metabolites that have been identified and demonstrated to have the rapeutic benefits all around the world (Ghosh et al., 2022). Numerous medicinal uses for PA's therapeutic properties have been demonstrated, including hepatoprotective, antiviral, anti-inflammatory, anti-oxidant, anti-leptospira, anti-malaria, and antidiabetic benefits among others (Islam et al., 2008).

Antiviral Activity

There have been reports of *Phyllanthus amarus* having antiviral properties against HIV, hepatitis B, and other viruses. The most effective mediators of the antiviral action were found to be ellagitannins, specifically geranin and corilagin. *In vitro*, tests were used to determine the methanolic extracts of PA's roots and leaves inhibitory effect on the NS3 and NS5B enzymes of the hepatitis C virus (Patel *et al.*, 2011).

Anti-SARS-CoV2 (Covid-19)

A selected group of researchers have reported on the possibility of PA in inhibiting COVID-19 following the 2019/2020 pandemic. One study used molecular dynamics simulations to test 198 bioactive compounds from five chosen medicinal plants, including PA, which was previously shown to have antiviral properties against SARS-Cov-2 protease and two co-receptors.



Astragalidin was found to be a superior candidate among the evaluated compounds for COVID-19 inactivation, suggesting that it would be a good option for the activity (Adejoro *et al.*, 2020).

Antiamnesic Activity

In male Swiss albino mice, the effects of an aqueous extract of PA's leaves and stems were assessed for cognitive abilities and brain cholinesterase activity. Both young and old mice's memory scores improved in a dose-dependent manner when given PA at 50, 100, or 200 mg/kg. Additionally, PA effectively corrected the amnesia brought on by diazepam (1 mg/kg, i.p.) and scopolamine (0.4 mg/kg, i.p.). Remarkably, there was a decrease in brain cholinesterase activity by phyllanthin, an active ingredient of PA. The positive control was piracetam 400 mg/kg, intraperitoneally (Joshi and Parle, 2007).

Figure 2: Chemical Structure of Phyllanthin Compound (Source: Huang et al., 2001) Anticancer Activity

The MTS (3-(4,5-dimethyl thiazole-2-yl)-5(3-carboxymethoxyphenyl)-2-(4-sulfopheny)-2H-tetrazolium) reduction test was used to screen for cytotoxicity of the crude extracts (aqueous and methanolic) and their two fractions of PA. According to Patel *et al.* (2011), it was demonstrated to suppress the growth of MCF-7 (breast carcinoma) and A549 (lung carcinoma) cells, with IC50 values ranging from 56 to 126 μ g/mL and 150-240 μ g/mL for methanolic and aqueous extracts, respectively.

Figure 3: Showing the structure of Tetrazolium compound as Anticancer Agent (Source: Huang et al., 2001)

Anti-leptospiral Activity

Leptospirosis is a serious disease that affects people worldwide and is primarily contracted through exposure to animal feces or environments contaminated with urine. By using the tube dilution technique or the microdilution test, PA's anti-leptospiral action has been studied. The outcome



shows that the entire plant extract of PA, both in a methanolic and aqueous form, inhibits leptospira (Chandan and Sirasakthivelan, 2012). The underneath figure showed antileptospiral agent known as niranthin.

Figure 4: Niranthin Compound Isolated from *Phyllantus amarus* (Source: Huang et al., 2001)

Hepatotoxicity Effect of *Phyllanthus amarus*

According to early research, the main lignin found in large quantities in PA leaves, phyllathin, is what reduces liver toxicity (Ogunmoyole et al., 2020). When the herb powder was administered to rats with ethanol-induced fatty liver, the efficiency of PA was seen. One study's findings demonstrated that giving mice aqueous leaf extracts of PA for a week significantly reduced the cytotoxic effects of lead nitrate and aluminum sulfate (Ghosh et al., 2022). The following structures are compounds isolated from PA that have hepatoprotective activities.

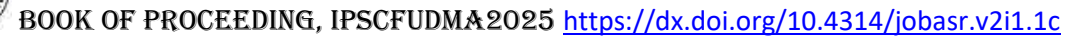
Figure 5: Showing Hepatoprotective Isolated Compounds (1) niranthin, (2) hypophyllanthin, and (3) nirtetralin. (Source: Huang et al., 2001)

Effects of PA on Kidneys

The effects of oral administration of *Phyllantus amarus* aqueous extract, which is extensively used in African ethnomedical practice to treat urological disorders and kidney stones, on the kidneys of adult Wistar rats were meticulously examined in terms of histology. For 28 days, the rats in the treatment groups were given oral doses of 500 mg/kg and 1000 mg/kg body weight of PA aqueous extract. The kidneys were closely examined on the 29th day following the rats' sacrifice. According to the histological results, treated kidney sections displayed different degrees of tubular necrosis, mild-to-severe chronic inflammatory cell infiltration, and blood vessel hypertrophy in comparison to the control sections. According to the study's conclusion, adult Wistar rats' kidneys are negatively impacted by PA extracts in some ways (Eweka and Enogieru, 2011). Additionally, it was discovered that PA extract has a strong and efficient non-concentration-dependent inhibitory effect on the development of calcium oxalate crystals, which are the precursors of the majority of kidney stones (Calixto, 2000). Kidney stone removal with PA has been proven to be 94% successful (Eweka and Enogieru, 2011).

Phyllanthus amarus as anti-asthma

Phyllanthin and hypophyllathin were detected in the methanolic extract of PA by HPLC analysis, with retention times of 25.243 and 26.832 minutes, respectively. The findings of this study



demonstrated that, in a maurine model of asthma, the presence of phyllanthin and hypophyllathin in PA reduces the Th2 response in OVA-induced AHR by altering endogenous markers. Phyllanthin and hypophyllathin, therefore, may provide a novel therapeutic strategy for the treatment of asthma (Wu *et al.*, 2018).

Antidiabetic Activity of PA

Monitoring hypo- and hyperglycemia is critical for the management of diabetes. A study conducted on 21 diabetic individuals who were not insulin-dependent and were administered aqueous extracts of PA demonstrated the plant's efficacious hypoglycemic properties. Additionally, it was discovered that methanolic extracts of PA exhibited antioxidant activity and, when given for 15 days to rats with alloxan-induced diabetes, produced a significant (p<0.001) drop in blood sugar (Ghosh *et al.* 2022). Aqueous preparations of the whole PA plant were tested for their hypoglycemic properties in diabetic Wistar rats who had been given alloxan. After 24 hours of oral treatment, the extracts at a dose of 260 mg/kg significantly (p<0.05) reduced blood glucose levels by 112%. At doses of 130 to 260 mg/kg of extract, there was a substantial (p<0.01) drop in blood glucose levels of 81 and 61% (day 7) respectively (Patel *et al.*, 2011).

Conclusion

Decades of thorough clinical trials and the necessity to standardize *Phyllanthusamarus's* therapeutic potential have prompted an extensive scientific study on the plant. The plant may have significant biological medicinal potential, according to a compilation of studies on PA. It is firmly believed that all of the detailed information about PA included in this overview offers insight into how this plant can be used to treat a variety of illnesses and also investigates its potential applications in the pharmaceutical industry.

Reference

- Adejoro, I. A., Babatunde, D. D., and Tolufashe, G. F. (2020). Molecular Docking and Dynamic Simulations of some Medicinal Plants Compounds against SARS-Cov-2: An *in silicoistudy, Journal of Taibah University Science*, 14(1): 70-1563 DOI: 10.1080/16583655.2020.1848049
- Agati, G., Azzarello, E., Pollastri, S., and Tattini, M. (2012). Flavonoids as Antioxidants in Plants: Location and Functional Significance, *Journal of Plant Science*, 196: 67-76
- Calixto, J. B. (2000). Efficay, Safety, Quality Control, Marketing and Regulatory Guidelines for Herbal Medicines (Phytotherapeutic Agents), *Brazilian Journal of Medicines and Biological Research*, 3: 179-189.
- Chandan, S., Sirasakthivelan, P. (2012). Screening of Antibacterial Activity of the Medicinal Plant *Phyllanthus amarus* against UTI causing Bacterial Pathogens, *Applied Journal of Hygiene* 1(3): 19-24
- Eweka, A. O. and Enogieru, A. (2011). Effects of Oral Administration of *Phyllanthus amarus* Leaf Extracts on the Kidneys of Adult Wistar Rats: A Histological Study, *African Journal of Traditional and Complementary Alternative Medicine*, 8(3):307-311 DOI: 10.4314/ajtcam.v8i3.65294.
- Ghosh, A. B. M., Banerjee, A. and Chathopadhyay, S. (2022). An Insight into the Potent Medicinal Plant, *Phyllanthus amarus* Schum. and Thonn., *Journal of The Nucleus*, 65: 437-472
- Huang, R., Huang, Jun-Chih, Y., C., Chen, Feng-Lin H., and Chungming C. (2003) Screening of 25 Compounds Isolated from *Phyllanthus* Species for Anti-Human Hepatitis B Virus *In Vitro*, *Phytother. Res.* 17: 449–453
- Islam, A., Mazumder, U. K., Gupta, M., and Ghosal, S. (2008). Phyto-Pharmacology of *Phyllanthus amarus*, an overview, *Pharmacologyonline*, 3: 202-209.



- Joshi, H., Parle, M. (2007). Pharmacological Evidences for Antamnesic Potentials of *Phyllanthus amarus* in mice, *African Journal of Biomedical Research*, 10: 165-173.
- Ogunmoyole, T., Awodooju, M., Idowu, S., and Daramola, O. (2020). *Phyllanthus amarus* Extract Restored Deranged Biochemical Parameters in Rat Model of Hepatotoxicity and Nephrotoxicity, PMCID: PMC7753912, 6(12): 1-10 DOI: 10.1016/j.heliyon.2020. e05670.
- Patel, J. R., Tripathi, P., Sharma, V., Chauhan, N. S., and Dixit, V. K. (2011). Phyllanthus amarus: Ethnomedicinal uses, Phytochemistry and Pharmacology: A Review, *Journal of Ethnopharmacology*, 138: 286-313.
- Salisu, A., M. Y. Iliyasu, M. R. Sahal, I. Titus, S. Isma'il, R. D. Umar, H. Tahir, Z. M. Kabeer, A. H. Idris, H. S. Musa and Agbo, E. B. (2022). Antimicrobial Potential of Syzygiumaromaticium (CLOVE) Extracts on Multidrug-Resistant (MDR) Uropathogenic Bacteria Isolated from Clinical Specimens in Bauchi, Nigeria, *Journal of Advances in Medical and Pharmaceutical Sciences*, 24(11-12): 41-57, 2022; Article no.JAMPS.95522 ISSN: 2394-1111
- Wu, W., Li, Y., Jiao, Z., Zhang, L., Wang, X. and Qin, R. (2018). Phyllanthin and hypophyllathin from *Phyllanthus amarus* ameliorate immune inflammatory response in Ovalbumin-induced asthma: Role of IgE, NrF2, iNos, TNF-α, and IL's, Immunopharmacological and Immunotoxicology, 41(1): 1-10 DOI: https://doi.org/10.1080/08923973.2018.1545788.
- Zubair, M., F., Atolani, O., Ibrahim, S., O., Adebisi, O., O., Hamid, A., A., and Sowunmi, R., A. (2017). Chemical Constituents and Antimicrobial Properties of Phyllanthus amarus (SCHUM & THONN), *Bayero Journal of Pure and Applied Sciences*, 10 (1): 238-246.

Appreciation

The LOC Committee express our deepest gratitude to the Vice Chancellor of the University, Invited guests, and to the members of the Local Organizing Committee, whose meticulous planning and hard work have brought this event to fruition. Our sincere appreciation also goes to our generous sponsors and supporting institutions, whose invaluable contributions have provided the necessary resources to make this conference a reality.

Finally, to the countless volunteers and contributors, your selfless efforts and enthusiasm have been instrumental in ensuring the smooth execution of every aspect of this event.

Thank you all for your indispensable support.

Bashir Ahuome Abubakar Secretary, LOC.